



HAL
open science

Wetting, Adhesion and friction investigations of hetero-chemical smooth patterned surfaces

Imed Eddine Ben Ali

► **To cite this version:**

Imed Eddine Ben Ali. Wetting, Adhesion and friction investigations of hetero-chemical smooth patterned surfaces. Material chemistry. Université de Lyon, 2017. English. NNT : 2017LYSE1250 . tel-01723791

HAL Id: tel-01723791

<https://theses.hal.science/tel-01723791>

Submitted on 5 Mar 2018

HAL is a multi-disciplinary open access archive for the deposit and dissemination of scientific research documents, whether they are published or not. The documents may come from teaching and research institutions in France or abroad, or from public or private research centers.

L'archive ouverte pluridisciplinaire **HAL**, est destinée au dépôt et à la diffusion de documents scientifiques de niveau recherche, publiés ou non, émanant des établissements d'enseignement et de recherche français ou étrangers, des laboratoires publics ou privés.



THESE de DOCTORAT DE L'UNIVERSITE DE LYON
opérée au sein de
L'Université Claude Bernard Lyon 1

Ecole Doctorale 34
Matériaux de Lyon

Spécialité de doctorat :
Discipline : Physico-Chimie des matériaux

Soutenue publiquement le 28/11/2017, par :
Imed Eddine Ben Ali

Wetting, Adhesion and friction
investigations of hetero-chemical
smooth patterned surfaces

Devant le jury composé de :

ESPUCHE Éliane	Université Claude Bernard Lyon 1	Présidente
CHAPEL Jean-Paul	Université de Bordeaux	Rapporteur
VONNA Laurent	Université de Haute-Alsace	Rapporteur
MONTEUX Cécile	ESPCI Paris	Examinatrice
CASSAGNAU Philippe	Université Claude Bernard Lyon 1	Directeur de thèse
AL AKHRASS Samer	Université Claude Bernard Lyon 1	Co-directeur de thèse
SCHEIBERT Julien	Ecole Centrale de Lyon	Invité

UNIVERSITE CLAUDE BERNARD - LYON 1

Président de l'Université

Président du Conseil Académique

Vice-président du Conseil d'Administration

Vice-président du Conseil Formation et Vie Universitaire

Vice-président de la Commission Recherche

Directrice Générale des Services

M. le Professeur Frédéric FLEURY

M. le Professeur Hamda BEN HADID

M. le Professeur Didier REVEL

M. le Professeur Philippe CHEVALIER

M. Fabrice VALLÉE

Mme Dominique MARCHAND

COMPOSANTES SANTE

Faculté de Médecine Lyon Est – Claude Bernard

Faculté de Médecine et de Maïeutique Lyon Sud – Charles Mérieux

Faculté d'Odontologie

Institut des Sciences Pharmaceutiques et Biologiques

Institut des Sciences et Techniques de la Réadaptation

Département de formation et Centre de Recherche en Biologie Humaine

Directeur : M. le Professeur G.RODE

Directeur : Mme la Professeure C. BURILLON

Directeur : M. le Professeur D. BOURGEOIS

Directeur : Mme la Professeure C. VINCIGUERRA

Directeur : M. X. PERROT

Directeur : Mme la Professeure A-M. SCHOTT

COMPOSANTES ET DEPARTEMENTS DE SCIENCES ET TECHNOLOGIE

Faculté des Sciences et Technologies

Département Biologie

Département Chimie Biochimie

Département GEP

Département Informatique

Département Mathématiques

Département Mécanique

Département Physique

UFR Sciences et Techniques des Activités Physiques et Sportives

Observatoire des Sciences de l'Univers de Lyon

Polytech Lyon

Ecole Supérieure de Chimie Physique Electronique

Institut Universitaire de Technologie de Lyon 1

Ecole Supérieure du Professorat et de l'Education

Institut de Science Financière et d'Assurances

Directeur : M. F. DE MARCHI

Directeur : M. le Professeur F. THEVENARD

Directeur : Mme C. FELIX

Directeur : M. Hassan HAMMOURI

Directeur : M. le Professeur S. AKKOUCHE

Directeur : M. le Professeur G. TOMANOV

Directeur : M. le Professeur H. BEN HADID

Directeur : M. le Professeur J-C PLENET

Directeur : M. Y.VANPOULLE

Directeur : M. B. GUIDERDONI

Directeur : M. le Professeur E.PERRIN

Directeur : M. G. PIGNAULT

Directeur : M. le Professeur C. VITON

Directeur : M. le Professeur A. MOUGNIOTTE

Directeur : M. N. LEBOISNE

Dedication

To

My parents Lilia and Ammar,

And my brother and sister Zied and Hend,

For their love and support and for always encouraging me to excel

Acknowledgements

Throughout the course of my graduate career, there are many people whose influence and help I would like to acknowledge. I would first like to thank my dissertation advisors, Dr. Samer AL AKHRASS and Prof. Philippe CASSAGNAU, for their support, mentorship, and trust in my abilities. In particular, he gave me the freedom to pursue problems and their solutions that were of interest to me. To

Dr. Julien SHEIBERT, Dr. Riad SAHLI, Dr. Gael PALLARES and Matthieu GUIBERT for their assistance and collaboration in the JKR conception and friction measurements at LTDS and Dr. Armand FAHS for his help in the FFM measurements and to Pierre ALCOUFFE, Laurent, Ali, Thiery, Ali, Nadia, Sabine, Olivier, Gisèle, Eric and Sylvie For their help.

I would also like to acknowledge the many colleagues and friends who helped me to make the most of my time in graduate school. I would especially like to thank all my IMP colleagues and friends especially (my office : Nico, Fab, Tica, Bap, Mira , Mo et Ori) my friends (Marine.F, Dj Sheik, Mél, Guillaume & Marie , Gautier, Yann, Alice, Jiji, Christoche, Michael, Thibaud, Anais, Laurent, Bryan, Marjo, Amani, Jimmy, Clémence, Math & Ju). A Special thanks to my friends (Khalil, Sofiane, Samir, Adlen, Halim, Walid, Moez, Malek, Ibrahim and Selim).

My graduate school experience was also certainly more enjoyable thanks to the many wonderful friendships that I made.

My family deserves my utmost thanks and appreciation for molding me as a person throughout my life. I would like to thank my parents, my brother and my big sister for serving as excellent role models, showing me the rewards of hard work, persistence, and the joys of family.

Summary

Micro and Nanoscale surface patterns were considered as potential templates and building blocks for Micro/nanotechnology. As for materials in general, these micro /nano-scale surface structures have been of increasing research interest in recent years, due to their unique properties. They are expected to exhibit novel and significantly improved physical, chemical, mechanical and other properties, as well as to offer opportunities for manifestation of new phenomena and processes. In the present PhD work, we propose a multiple scale analysis of the adhesion, friction and wetting behaviors for different patterned interfaces. In a first chapter, we developed a general methodology to design well-defined surfaces combining micro-contact printing (μ CP), self-assembled monolayers (SAMs) and polymer grafting techniques. Then we study the wettability of a patterned solid surface. Where, the stick-slip regime, and the effect of the patterning at the mesoscale was investigated. Furthermore, we concentrate on the dependence of adhesion and friction between a polymer and a rigid tip on the composition of the patterned substrates using a JKR, FFM and friction machines. Intriguingly, the uses of these approaches did not provide us with a clear answer to our bewilderment. Therefore, in the third chapter, we adopted the approach of the dewetting of thin polymer film on top of patterned surfaces. We study the impact of the solid/liquid boundary condition on the evolution of the rim instability during the course of dewetting. The last chapter details the investigation of the predominant aspect between the chemistry introduced on the surface and the mechanical proprieties of the substrate.

Résumé

Les surfaces texturées sont devenues, ces dernières années, des substrats de choix pour de nombreuses applications. En effet, la texturation des surfaces, de l'échelle nanométrique à l'échelle microscopique, permet d'accroître les propriétés d'adhérence ou de renforcer la résistance mécanique intrinsèque. Dans ce travail de thèse nous proposons une étude sur l'influence des textures chimiques sur le comportement tribologique, adhésif et sur la mouillabilité des substrats. Dans le premier chapitre, on propose une stratégie de micro-texturation des surfaces basées sur la technique de microcontact-printing et le greffage de chaînes de polymères de géométries/formes contrôlées. En outre, on a notamment étudié de manière approfondie la mouillabilité des surfaces texturées afin de comprendre les effets de diminution de taille des textures sur le comportement adhésif. Dans les expériences d'adhésion et frottement, un dispositif de type JKR (pour Johnson, Kendall et Roberts), une machine de frottement et une FFM ont été utilisés permettant d'observer le contact entre une sphère élastique et une pointe rigide avec un plan texturé tout en contrôlant la force entre les surfaces. En outre l'utilisation de ces différentes approches ne nous a pas finalement donné des explications satisfaisantes sur les mécanismes agissant sur les phénomènes interfaciaux. De ce fait, l'utilisation du démouillage de films minces de PS et de PDMS sur

des surfaces texturées nous as permis de suivre l'évolution de l'instabilité du bourrelet à l'interface. Enfin, dans le dernier chapitre, nous avons étudié les différents aspects prédominants des phénomènes interfaciaux sur des surfaces homogènes.

TABLE OF CONTENTS

GENERAL INTRODUCTION 8

CHAPTER 1 11

LITERATURE REVIEW 11

I-WETTING-ADHESION AND FRICTION ON PATTERNED SURFACES 12

I-1-Basic concepts 12

 I-1.1-Surface Force 12

 I-1.2-Surface Energy 13

 I-1.3-Surface tension 13

I-2-Adhesion and contact Mechanics 14

 I-2.1-Hertez Model 14

 I-2.2-Johnson-Kendall-Roberts (JKR) Model 15

 I-2.3-Derjaguin-Muller-Toprov (DMT) Model 17

 I-2.4-Adhesion Between polymeric surfaces 17

 I-2.5-Capillary Force 17

 I-2.6-Wettability and work of adhesion 18

 I-2.7-Surface Wetting Properties 19

I-3-Friction 21

 I-3.1-Amontons’ Laws of Friction 21

 I-3.2-The Basic model of friction 21

 I-3.3-The geometrical or mechanistic model 21

 I-3.4-The molecular or adhesive model 22

 I-3.5-The deformation or ploughing model 22

 I-3.6-Interfacial friction 23

I-4-Surface Texturing Effects on friction and adhesion 23

 I-4.1-Adhesion on Physically Patterned Substrates 23

 I-4.2-Adhesion on Chemically Patterned Substrates 25

 I-4.3-Friction on Physically Patterned Substrates 26

 I-4.4-Friction on Chemically Patterned Substrates 27

II-DEWETTING AS AN INVESTIGATIVE TOOL FOR STUDYING THE MECHANICAL PROPERTIES OF THE SURFACE 28

II-1-Thin polymer Film 29

 II-1.1-Stability of supported thin films 29

II-2-Hydrodynamics in thin liquid films 30

 II-2.1-Navier-Stokes equation 30

 II-2.2-Boundary conditions at interfaces 31

 II-2.3-Thin film equation (Newtonian liquids) 32

 II-2.4-Equations of motion 32

II-3-Dewetting of viscoelastic polymer thin films 32

II-4-Dewetting on patterned substrates 35

 II-4.1-Dewetting on Physically Patterned Substrates 35

 II-4.2-Dewetting on chemically patterned substrates 37

III-CONCLUSION 39

CHAPTER 2 41

WETTING AND ADHESION INVESTIGATIONS OF PATTERNED SURFACES 41

 I-INTRODUCTION 42

 II-EXPERIMENTAL 42

Table of Contents

II.1-Sample Fabrication	42
II.1.1-Photo lithography.....	43
II.1.2-Fabrication of PDMS stamps.....	43
II.1.3-Substrate Cleaning.....	44
II.1.4-Contact-printing of organosilane.....	44
II.1.5-Adsorption of PDMS on patterned surface (MTS/PDMS).....	45
II.1.6-Adsorption of PDMS on activated Si-wafer.....	46
II.1.7-Self-assembled monolayer on activated Si-wafer.....	46
II-2-Experimental device: Design and construction of a Mini micro-contact printer (MμCP)	46
II-2.1-Dewetting of Thin Polymer Film.....	47
II-2.2-Stamp Size.....	48
II-3-Experimental device: Design and construction of a JKR Machine	50
II-3.1-Brief outline of the classical JKR test.....	52
II-4-AFM device PEAKFORCE QNM	54
III-RESULTS AND DISCUSSION	56
III-1-Patterns effect on the wetting behavior	56
III-1.1- Wettability of smooth Substrates.....	57
III-1.2-Circular micro-structured Substrates (MTS/Si-OH).....	59
III-1.3-Wettability of MTS/Si-OH patterned system.....	61
III-1.4-Anisotropy wetting.....	64
III-1.5- Control of Adhesion by Contact Line pinning and depinning.....	64
III-2-Patterns effect on the adhesive behavior	67
III-2.1-Adhesion measurements using the JKR machine.....	67
III-2.1.a- JKR Adhesion measurements on smooth Substrates.....	67
III-2.1.b- JKR Adhesion measurements on MTS/Si-OH linear patterned system.....	71
III-2.1.c- JKR Adhesion measurements on MTS/PDMS linear patterned system.....	74
III-2.2-Adhesion measurements using the AFM PeakForce QNM.....	76
III-2.2.a- AFM Adhesion measurements on smooth non-patterned substrates.....	77
III-2.2.1.b- AFM Adhesion measurements on MTS/SiOH patterned surfaces.....	80
III-2.2.1.c- AFM Adhesion measurements on MTS/PDMS patterned surfaces.....	81
III-2.2.1.d- Multiscale comparative adhesive studies.....	83
IV- CONCLUSION	84
CHAPTER 3	86
FRictional BEHAVIOR OF PATTERNED SURFACES	86
I-INTRODUCTION	87
II-EXPERIMENTAL	87
II-1-Friction machine	88
II-1.1- Friction Force Microscopy FFM device.....	90
III-RESULTS AND DISCUSSION	91
III-1- Friction measurements at Macro-Scale	92
III-1.1- Friction measurements on smooth Substrates.....	92
III-1.2-Friction measurements on MTS/Si-OH patterned surfaces.....	96
III-1.3- Friction measurements on MTS/PDMS patterned surfaces.....	98
III-2-Friction measurements using the FFM	101
III-2.1- FFM Friction measurements on smooth substrates.....	101
III-2.2 - FFM Friction measurements on MTS/Si-OH patterned substrates.....	104
III-2.3- FFM Friction measurements on MTS/PDMS patterned substrates.....	107
IV-CONCLUSION	110
CHAPTER 4	112

DEWETTING AS AN INVESTIGATIVE TOOL FOR STUDYING THE INTERFACIAL FRICTION OF PATTERNED SURFACES.....	112
I-INTRODUCTION	113
<i>I-1-Introduction to polymer</i>	113
I-1.1-Structure of polymers.....	113
I-1.2-Dispersity of molar masses—Average malar masses	114
I-1.3-Description of a random polymer chain	114
I-1.4-Dynamic of polymer (viscoelastic polymers)	116
I-1.5-Polystyrenes	118
I-1.6-Polydimethylsiloxane.....	119
<i>I-2-Liquid jets — Rayleigh-Plateau instability.....</i>	119
I-2.1-Impact of viscosity.....	121
I-2.2-Droplet detachment	121
II-RESULTS AND DISCUSSION.....	122
<i>II-1-Dewetting Experiments Using a viscoelastic liquid.....</i>	122
II-1.1-Dewetting Dynamics.....	127
II-1.2-Regimes of the rim instability.....	129
II-1.3.a-First stage: Rim growth:.....	130
II-1.3.b-Second stage: swelling regime:	130
II-1.3.a-1-undulation:	130
II-1.3.a-2- bulging	132
II-1.3.c-Third regime: Fingering instability	133
II-1.3.d-Forth regime: Droplet detachment	135
II-1.3.d-1-Primary droplets.....	135
II-1.3.d-2-Secondary droplets.....	137
II-1.4-Thickness effect on the dewetting dynamics	137
II-1.4-1-Finger thread	142
II-1.5-Rim instability on the circular geometry	143
II-1.5.1-Impact of the geometry.....	146
<i>III-2-Dewetting Experiments Using a Newtonian Fluid on a MTS/PDMS patterned system.....</i>	148
III-2.1-Dewetting Dynamics.....	149
III-CONCLUSIONS.....	158
CHAPTER 5	160
DEWETTING AND FRICTION MEASUREMENTS ON HOMOGENEOUS DEFORMABLE SUBSTRATES	160
I-INTRODUCTION	161
<i>I-1-Dewetting Dynamics</i>	161
I-1.1-Stages of dewetting.....	161
I-1.2-Driving forces.....	162
<i>I-2-Dissipation mechanisms.....</i>	163
I-2.1-Viscous dissipation: No-slip boundary condition.....	163
I-2.2-Full slippage: Friction at the solid/liquid interface	164
II-EXPERIMENTAL	165
<i>II.1-Sample Fabrication.....</i>	165
II.1.1-Polydimethylsiloxane monolayer	165
II.1.2-Cross-linked PDMS with varying thicknesses	165
II.1.3- Cross-linked PDMS for thicker films (>1,8 μm).....	166
III-RESULTS AND DISCUSSION.....	166
<i>III-1-Friction measurements at macro scale.....</i>	166

Table of Contents

III-1.1-Smooth Substrates	166
III-2-Dewetting Experiments Using a Newtonian Fluid PDMS.....	172
III-2.1-Dewetting Dynamics.....	173
III-2.3-Interfacial friction behaviour	179
IV-CONCLUSION.....	182
GENERAL CONCLUSION.....	184
BIBLIOGRAPHY	188

Table of Contents

General Introduction

As the size of engineered devices has been reduced to the microscale and smaller, the friction and adhesion caused by surface forces acting on these structures have proven to be detrimental to their operation. In recent years, surface texturing was introduced as a way of controlling friction and adhesion. Nowadays, surface texturing delineates a scientific and technological open-frontier where the area of micro-fabrication converge to surface science committed to study and demonstrate the various mechanisms of integrated micro-effects resulting in a macro-benefit that optimizes performances. Tribologists have been investigated the impact of micro-texturing on mating surfaces since the 60s, demonstrating by means of various experimental approaches and theoretical models that the presence of artificially created micro irregularities can significantly affect sliding behaviours and enhancing the different tribological proprieties.

Hence, many studies have investigated the effect of surface texturing on the performance of a variety of mechanical systems. It was found that surface texturing has great potential for improving the tribological performance in terms of reducing the wear, friction, and lubrication consumption.

However, compared to the topographical method, the chemical approach on micro-surface texturing can be considered as an unexplored approach. In fact, chemical texturing has several unique potential advantages for tribological applications that involve ultra-smooth surfaces. Where the combination of surface-texturing, self-assembled monolayer and grafting techniques can alter the surface wetting properties and thus change the tribological properties. Therefore, the fundamental issue of this variety of chemical texturing is the way the chemistry, topology and surface fraction can affect or be used to adjust the interfacial behaviour. These heterogeneous surfaces can also provide a model system for the understanding on the fundamental level recurrent interface phenomena and processes (wetting, dewetting, nucleation, etc.).

Thereby, we propose with this work a multiple scale analysis of adhesion, friction and wetting proprieties of different patterned interfaces.

In a first chapter, a bibliographic review briefly surveys the principles of adhesion and friction phenomena. The effects of surface texturing on the tribological performances were provided. Then, the fundamentals of thin liquid film and the dewetting scenario on chemically and topographically patterned surfaces were presented.

General Introduction

In a second chapter, various heterogeneous silane/polymer deposition methods were explored, including micro contact printing with hand pressure and micro contact printing using the mini (μ CP) machine followed by polymer grafting. Then, the wettability of a patterned solid surface, consisting of periodic patterns of alternating hydrophobic and hydrophilic stripes with a large wettability contrast (about 70°) was studied. As following, the stick-slip regime, and the effect of the patterning at the mesoscale were investigated. Furthermore, we concentrate on the dependence of adhesion and friction between a polymer and a rigid tip on the composition of the patterned substrates using a JKR, FFM and friction machines.

In the third chapter, we sought to explore the effect of the chemistry and the pattern size on the frictional response between a polymer and a rigid tip on the composition of the patterned substrates. Both a macro-friction test and a FFM measurement were employed to characterize the frictional response of an (hydrophobic/ hydrophilic) mixed silane (MTS/Si-OH) system and a (hydrophobic/ hydrophobic) mixed polymer and silane (MTS/PDMS) covered surfaces. Therefore, we are interested in the following questions: How does a smooth non-patterned surface with the same interfacial chemistry slide, or more generally, what is the frictional response at different scales? What is the value of the friction coefficient at such interfaces? And what are the consequences of the variation of the chemistry and pattern sizes of hydrophobic/ hydrophilic (MTS/Si-OH) system or hydrophobic/ hydrophobic (MTS/PDMS) covered surfaces on the frictional behavior at macro and nanoscales? After a brief description of our experimental conditions, we present the experimental results, which are discussed in light of the results described in the first chapter.

In the fourth chapter, we adopted the approach of the dewetting of thin polymer film on top of patterned surfaces, to investigate the interfacial friction response of the surface at the melt-substrate interface. We studied the impact of the solid/liquid boundary condition on the evolution of the rim instability during the course of dewetting. Then, we focused on how the alternation of hydrophobic and hydrophilic stripes with a large wettability contrast affects the evolution of the rim and the dynamics of dewetting. Despite that, the characteristics of the rim instability are observed in three dimensions, this chapter concentrates on the in-plane rim instability. Then, the effect of film thickness on the dewetting dynamics and the rim instabilities was investigated. Furthermore, we investigated the dewetting of a PDMS film on a hydrophobic/ hydrophobic (MTS/PDMS) covered surface as a mean to extract quantitative information of the interfacial friction.

The fifth chapter details the investigation of the predominant aspect between the chemistry introduced on the surface and the mechanical proprieties of the substrate. Thereby, we used friction experiments and autophobic dewetting of a thin PDMS polymer as mean to extract quantitative information of the interfacial friction. In one hand, we measured in situ the contact angle and the slippage length at the

General Introduction

melt-substrate interfaces and in the other hand, we explored the correlation between both micro and macros scales analysis bringing to light the impact of the mechanical proprieties of the surface on the frictional response.

Chapter 1

Literature review

TABLE OF CONTENTS

I-WETTING-ADHESION AND FRICTION ON PATTERNED SURFACES	12
<i>I-1-Basic concepts</i>	12
I-1.1-Surface Force	12
I-1.2-Surface Energy	13
I-1.3-Surface tension	13
<i>I-2-Adhesion and contact Mechanics</i>	14
I-2.1-Hertz Model	14
I-2.2-Johnson-Kendall-Roberts (JKR) Model	15
I-2.3-Derjaguin-Muller-Toprov (DMT) Model	17
I-2.4-Adhesion Between polymeric surfaces	17
I-2.5-Capillary Force	17
I-2.6-Wettability and work of adhesion	18
I-2.7-Surface Wetting Properties	19
<i>I-3-Friction</i>	21
I-3.1-Amontons' Laws of Friction	21
I-3.2-The Basic model of friction	21
I-3.3-The geometrical or mechanistic model	21
I-3.4-The molecular or adhesive model	22
I-3.5-The deformation or ploughing model	22
I-3.6-Interfacial friction	23
<i>I-4-Surface Texturing Effects on friction and adhesion</i>	23
I-4.1-Adhesion on Physically Patterned Substrates	23
I-4.2-Adhesion on Chemically Patterned Substrates	25
I-4.3-Friction on Physically Patterned Substrates	26
I-4.4-Friction on Chemically Patterned Substrates	27
II-DEWETTING AS AN INVESTIGATIVE TOOL FOR STUDYING THE MECHANICAL PROPERTIES OF THE SURFACE	28
<i>II-1-Thin polymer Film</i>	29
II-1.1-Stability of supported thin films	29
<i>II-2-Hydrodynamics in thin liquid films</i>	30
II-2.1-Navier-Stokes equation	30
II-2.2-Boundary conditions at interfaces	31
II-2.3-Thin film equation (Newtonian liquids)	32
II-2.4-Equations of motion	32
<i>II-3-Dewetting of viscoelastic polymer thin films</i>	32
<i>II-4-Dewetting on patterned substrates</i>	35
II-4.1-Dewetting on Physically Patterned Substrates	35
II-4.2-Dewetting on chemically patterned substrates	37
III-CONCLUSION	39

In this chapter, the principles of adhesion and friction phenomena were introduced. The effect of surface texturing on the tribological performances were provided. Then, the fundamentals of thin liquid film and the dewetting scenario on chemically and topographically patterned surfaces were presented.

I-Wetting adhesion and friction on patterned surfaces

In the following sections, various approach of adhesion and friction phenomena were reviewed.

I-1-Basic concepts

Understanding the mechanical behavior at small scales therefore requires a clear understanding of the basic phenomena related to surface energies and surface forces.

I-1.1-Surface Force

The intermolecular and surface forces can be attractive or repulsive and their range of action and magnitude can be very contrasting. The types of forces performing between two surfaces depend on the nature of the interacting surfaces and medium between them. The main types of nonspecific intermolecular and surface forces are listed in table1 [1]

Type of Interaction	Key aspects
van der Waals (WDS)	A force existing between all bodies and usually acts as an attractive force but can be sometimes repulsive.
Electrostatic (coulomb, ionic, double layer)	A force existing between charged molecules/surfaces in liquid and can be attractive or repulsive.
Steric	A quantum mechanical force that is normally short range and increases very sharply as the two molecules get close (depending on geometry/shape or conformation of the interacting molecules).
Thermal fluctuation (i.e., osmotic, entropic, protrusion)	A temperature-dependent force associated with entropic confinement of molecular groups. Usually repulsive
Hydrophobic	It is an attractive interaction between hydrophobic molecules or surfaces in water and it's typically a long range force

Solvation	Forces associated with local structuring of solvent molecules between interacting surfaces. For water, it is generally termed as hydration force.
Hydrogen bonding	An electrostatic attractive interaction involving positively charged H atoms covalently bonded to electronegative atoms (e.g., N, O).

Table 1 The main types of nonspecific intermolecular and surface forces.

I-1.2-Surface Energy

The term surface energy is in fact the cause of some bewilderment, as it can have several interpretations. At first, in all cases where it is used to define a material property, it is not an energy, but an energy per unit surface area (i.e., with units of J/m^2 , for example). Clearly, the pure surface energy is not an intrinsic material property as it depends on the total amount of surface present for the specific sample of interest. The terminology is also slightly confusing, since several terms are generally used for liquids versus solids. For solids, one speaks naturally of the surface energy, surface free energy, or the excess surface free energy, whereas for liquids one uses surface tension. In all cases, all of these terms attribute to the extra energy per unit area required to form a surface of a condensed phase (solid or liquid) that is exposed to an esoteric phase (gas or vacuum). This will have units of free energy per unit area, or equivalently, a force per unit length. Generally, we shall abide by frequent practice and refer to the surface free energy per unit area as the surface energy in the case of solids, and the surface tension in the case of liquids. Note that, if both phases are condensed (that is, solid–solid, solid–liquid, liquid–liquid) then we refer to the interface free energy [1, 2].

I-1.3-Surface tension

The reversible thermodynamic work per unit needed to form the free surface is what we define as the surface tension[1]. It is usually denoted by the symbol γ , and is given by

$$\gamma = \frac{dW}{dA} \quad (1.1)$$

Where W is the work and A is the surface area. The surface tension will typically be bigger for stronger bonding: regular values are $10 - 20 \text{ mJ}/m^2$ for fluorocarbons, $20 - 40 \text{ mJ}/m^2$ for hydrocarbons, $73 \text{ mJ}/m^2$ for water, $485 \text{ mJ}/m^2$ for mercury. As the temperature soars, the surface tension of most liquids goes down, attaining zero at the temperature of evaporation. The appellation tension implies that a force exists, and undeniably, this is a real tensile force confined to the surface region. For a liquid, the force is isotropic and operates within the plane of the surface. This is what causes liquid droplets to take the rounded shapes, because that is the minimum surface area configuration for a given volume. The

tensile force appears because, compared with atoms in the bulk, the atoms at the surface are lacking bonds with neighbors outside of the volume of the liquid.

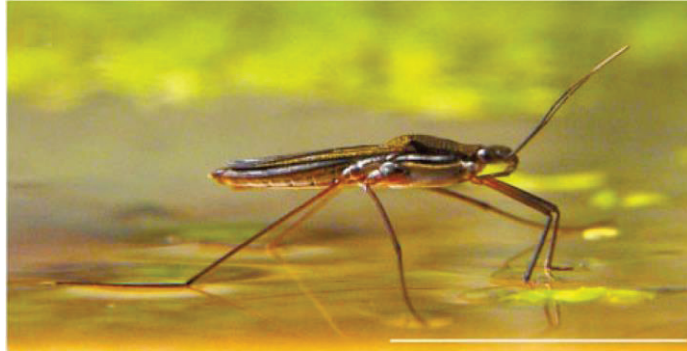


Figure 1. 1 A water strider. The membrane-like nature of water due to its surface tension is clearly seen. The behavior is assisted by the hydrophobic nature of the insect's tentacles.

Because of the tensile force, one can consider that the surface is operating as a stretched elastic membrane, an effect that is easily noticed, for example, when light objects that repel water rest on the water surface, enabling the water strider insect (Fig.1.1) to skim, instead of having to swim [3]!

I-2-Adhesion and contact Mechanics

Adhesion is the mechanism of attraction between two particles or surfaces that leads them into contact. For the attracted particles or surfaces of the same material, this process is commonly termed to as cohesion. Although at first glance there might not be any direct connection between tribology and adhesion (while one deal with surfaces in relative motion, the other tends to bring them into contact), adhesion play a decisive part in tribological phenomena, especially friction and wear. Adhesion also plays a crucial part in a broad range of practical applications from adhesives, to cold welding of metals, to biomedical applications. Research on creating enhanced adhesives in automotive and aerospace industries has continued for years. Therefore, the classical theoretical models for the adhesion or contact of two elastic surfaces are reviewed, which are commonly known as contact mechanics theories for analyzing surface deformations, stress distribution, and strength of the adhesion between two surfaces in contact.

I-2.1-Hertz Model

The deformation of two elastic surfaces in contact was first analyzed by Hertz in 1886 [4]. Hertz presumed that no adhesion was present between the two contacting surfaces, and studied the stress distribution and contact geometry of two spheres as a function of compressive load (F_L). Based on the Hertz theory, the radius a of contact area under compressive load F_L is given by Equation 1.2 for two spheres of radii R_1 and R_2 , Young's moduli E_1 and E_2 , and Poisson ratio ν_1 and ν_2 , where R and K are given by Equation 1.3 and Equation 1.21:

$$a^3 = \frac{RF_{\perp}}{K}, \quad (1.2)$$

$$\frac{1}{R} = \frac{1}{R_1} + \frac{1}{R_2}, \quad (1.3)$$

$$\frac{1}{K} = \frac{3}{4} \left[\frac{1 - \nu_1^2}{E_1} + \frac{1 - \nu_2^2}{E_2} \right]. \quad (1.4)$$

and the pressure or normal stress distribution within the contact area is given by:

$$P(x) = \frac{3Ka(1 - x^2)^{1/2}}{2\pi R}, \quad (1.5)$$

Where $x = r/a$ (see Fig. 1.1). Conferring to Equation 1.5, pressure at the center of contact region ($x = 0$) is $P(0) = (3F_a/2\pi a^2)$ that is 1.5 times of the mean pressure across the contact area. Hertz studied the contact of glass spheres by using an optical microscope and verified his theory experimentally. Based on the Hertz theory, there is infinite repulsion between the surfaces at $D = 0$; thus, all along the unloading process, the surfaces separate when contact area diminish to zero as the compressive load decreases to zero (see Eq. 1.2).

I-2.2-Johnson-Kendall-Roberts (JKR) Model

The key issue of the Hertz theory is that it neglects the surface energy in the contact of two surfaces. For the first time, in 1921, Griffith mentioned the role of surface energy in elastic contact and fracture of solids [5]. He declared that during the formation of a crack in an elastic body, work must be done to overcome the attractive forces between the molecules of the two sides of the crack. Furthermore, he specified that if the width of a crack is greater than the radius of the molecular action, the molecular attractions are negligible across the crack except near its end. Hence, Griffith stated that the conventional theory of elasticity is able of analyzing the stresses correctly at all points of an elastic body except those close to the end of a crack where molecular attractions cannot be ignored. For the same reason, there was a lot of discussion about the stress distribution and surface deformation at the edge of contact region until almost five decades after Griffith's paper (see Fig. 1.2) [6-11]. Although Griffith pointed out that surface forces deform the crack and alter the energy balance of the system, he did not quantify the model. The Hertz theory failed to predict the contact mechanics experiments performed by Johnson et al. using glass and rubber spheres: at low loads, the contact area was proved to be much bigger than that predicted by the Hertz theory and during the unloading process the contact radius attained a fixed value before detachment [12]. Almost a century after the Hertz model, in 1971, Johnson, Kendall, and Roberts (JKR) suggested a model for contact of elastic surfaces

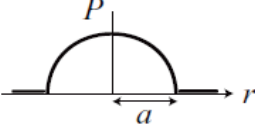
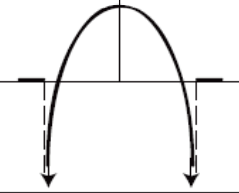
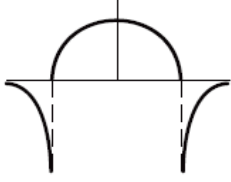
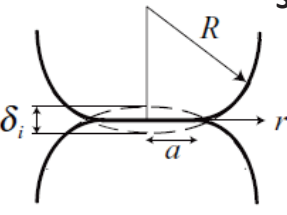
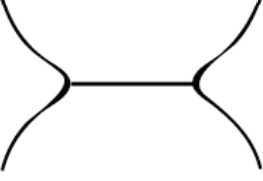
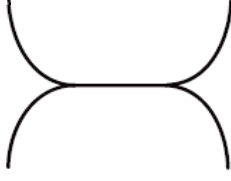
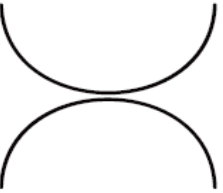
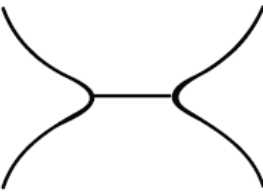
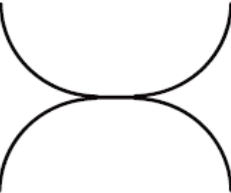
Hertz	JKR	DMT
Stress distribution under compressive load		
		
Shape under compressive load		
		
Shape under zero load		
		
Adhesion Force		
0	$3\pi\gamma R$	$4\pi\gamma R$

Figure 1. 2 The main features of classical contact mechanics theories Hertz, JKR and DMT.

which takes into account the role of surface forces [12]. They studied the contact between two elastic spheres and declared that equilibrium condition can be achieved when Equation 1.6 is satisfied:

$$\frac{dU_T}{Da} = 0. \quad (1.6)$$

The total energy of the system U_T consists of three terms: the stored elastic energy, the mechanical energy under the applied load, and the surface energy. The suitable expressions for these three components were derived and put into Equation 1.6 to obtain the relation shown in Equation 1.7, where W_{ad} is the adhesion energy and $W_{ad} = 2\gamma$ for two surfaces of the same materials:

$$a^3 = \frac{R}{K} \left(F_{\perp} + 3\pi R W_{ad} + \sqrt{6\pi R F_{\perp} W_{ad} + (3\pi R W_{ad})^2} \right). \quad (1.7)$$

When $W_{ad} = 0$ (non-adhesive), The Equation 1.7 (JKR theory) reduces to Equation 1.2 (Hertz theory). At zero load ($F_{\perp}=0$), the contact area is finite and given by:

$$a^3 = \frac{6\pi R^2 W_{ad}}{K}. \quad (1.8)$$

The adhesion force (or pull-off force) is the force needed to pull-off the spheres from adhesive contact. The corresponding adhesion force between the spheres based on JKR theory illustrated by:

$$F_{JKR} = \frac{3\pi R W_{ad}}{2}. \quad (1.9)$$

And the normal stress distribution within the contact area is given by Equation 1.10, where $x = r/a$ (see Fig1.1)

$$P(x) = \frac{2Ka}{2\pi R} (1 - x^2)^{1/2} - \left[\frac{3KW_{ad}}{2\pi a} \right]^{1/2} (1 - x^2)^{-1/2}. \quad (1.10)$$

I-2.3-Derjaguin-Muller-Toprov (DMT) Model

As presented in Equation 1.9, at the edge of contact region (i.e., $x = 1$), the normal stress is tensile and infinite in magnitude, which causes each surface to bend through a right angle along the contact edge. To resolve this dilemma, Derjaguin, Muller, and Toporov (DMT) [13] proposed another model for contact mechanics. According to DMT theory, adhesion emerges from attractive surface forces but the surface shape outside the contact area is assumed to be Hertzian and not deformed by the surface forces. The stress distribution within the contact area is also assumed to be the same as that in Hertz theory. In the DMT model, the contact radius is given by Equation 1.11 and the adhesion (pull-off) force is given by Equation 1.12:

$$a^3 = \frac{R}{K} (F_{\perp} + 2\pi R W_{ad}). \quad (1.11)$$

$$F_{DMT} = 2\pi R W_{ad}. \quad (1.12)$$

I-2.4-Adhesion Between polymeric surfaces

Adhesion is defined as the molecular attractive force acting between two surfaces of bodies in contact. The physical mechanisms of the adhesion force can be diverse and they include the van der waals, chemical, electrostatic, capillary, and other forces. In many cases, it is assumed that the total adhesion force is equal to the sum of these components, for example,

$$F_{adh} = F_{van\ der\ waals} + F_{covalent} + F_{electrostatic} + F_{Capillary}.$$

I-2.5-Capillary Force

Chapter 1 Literature review

Capillary adhesion is another element of the adhesion force; however, it has an utterly specific nature. The capillary forces emerge because of the interaction of liquid, gas, and solid molecules at the interface between them.

The most baltant illustration of the capillarity is the rise of water in a capillary tube, the surface tension, and filling the pores with water [14, 15]. When two solid surfaces in contact are placed in a humid environment, water vapor condenses and forms menisci at the contact region between the two surfaces [16]. The pressure inside the meniscus is decreased in comparison with the pressure outside in consonance with the Young–Laplace model, which relates the pressure drop to the curvature as:

$$\Delta P = \gamma \left(\frac{1}{R_1} + \frac{1}{R_2} \right), \quad (1.13)$$

Where ΔP is the pressure difference, γ is the surface tension, and R_1 and R_2 are radii of curvature. The decreased Laplace pressure inside menisci between two bodies or asperities results in an attractive force, which is equal to the pressure, drop times the area of the meniscus foundation.

I-2.6-Wettability and work of adhesion

If we observe a liquid drop on a solid surface, we can discern the presence of three different phases (Fig.1.3). Consequently, there are three surface tensions that need to be examined: liquid-gas, solid-gas and solid-liquid. Young’s equation (Young, 1805) gives the relation between the equilibrium contact angle θ_{eq} the drop makes with the surface and the three surfaces tension. Usually, we know $\gamma_{LV} \equiv \gamma$ by separate measurements.

$$\gamma_{SV} = \gamma_{SL} + \gamma \cos \theta_{eq} \quad (1.14)$$

The three phases, liquid, solid and gas are at least in mechanical equilibrium (force balance) with each other[17].

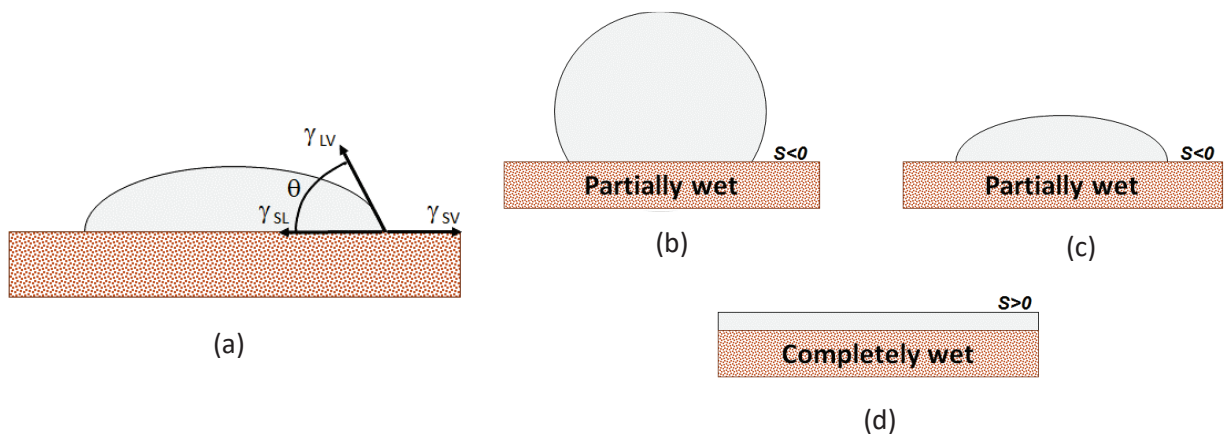


Figure 1. 3 (a) A small droplet in equilibrium over a horizontal surface: (b) and (c) correspond to partial wetting, the trend towards wetting being stronger in (c) than (b). (d) Corresponds to complete wetting $\theta_{eq} = 0$.

Chapter 1 Literature review

The discrimination between the diverse wetting states is mostly made by considering the equilibrium-spreading coefficient $S_{eq} \leq 0$, and that represents the surface free energy γ_{SV} relative to its value for complete wetting (Fig.1.4).

$$S_{eq} \equiv \gamma_{SV} - (\gamma_{SL} + \gamma) = \gamma(\cos \theta_{eq} - 1) \quad (1.15)$$

-If S_{eq} is negative, $\gamma_{SV} < \gamma_{SL} + \gamma$, means that wetting of the surface is unfavorable so the fluid will minimize its contact with the surface and form a compact liquid. Here we speak of partial wetting.

-If S_{eq} is positive, $\gamma_{SV} = \gamma_{SL} + \gamma$, the contact angle is zero indicates that wetting of the surface is favorable, and the fluid will spread over a large area on the surface. Here we speak of complete-wetting.

$$\cos \theta_{eq} = 1 + \left(\frac{S_{eq}}{\gamma}\right) \quad (1.16)$$

Young's equation received many criticisms specifically because it neglect the fact that the vapor of the liquid drop will be absorbed on the solid surface diminishing its surface energy and tension. Harkins and Livingston [18] stated the amount of reduction in terms of a spreading pressure, π_s ,

$$\pi_s = g_s - \gamma_{SV}. \quad (1.17)$$

where g_s belongs to the solid which is in contact with vacuum. Therefore, the true equilibrium of the three phase system is,

$$g_s - \pi = \gamma_{SL} + \gamma \cos \theta_{eq}. \quad (1.18)$$

When the liquid drop is separated from the solid (no absorbed vapor) to expose a unit area of the surface without any viscous or elastic deformation, the work of adhesion is given by,

$$W_a = \gamma + \gamma_{SV} - \gamma_{SL}. \quad (1.19)$$

It is the work necessary to obliterate the unite area of interface of surface energy γ_{SL} while creating two surfaces of unit area with energy γ_{SV} and γ . This is the Dupré equation:

$$W_a = \gamma(1 + \cos \theta_{eq}) + \pi \quad (1.20)$$

when π is negligible

$$W_a = \gamma(1 + \cos \theta_{eq}). \quad (1.21)$$

This is the well-known Young-Dupré equation [19] that expresses the work of adhesion in easily measurable quantities. This way the two unknowns, γ_{SV} and γ_{SL} can be neglected.

I-2.7-Surface Wetting Properties

One key problem in wetting is to study how the roughness and chemical inhomogeneity of a solid surface affect the apparent contact angle, namely the macroscopic angle between the liquid-air interface and the solid surface. To answer this question, there are two very well-known equations, namely the Wenzel equation [20] and the Cassie equation [21]. For the Wenzel state, the wetting behavior is such that the liquid fills the roughened surface completely, due to strong liquid/solid interaction. For the Cassie-Baxter state, the wettability of a surface is affected by a chemical heterogeneity. The Wenzel and Cassie-Baxter models are frequently referred to in literature for characterization and prediction of the wetting behavior of surfaces [22]. The Wenzel equation describes the apparent contact angle θ_{Wenzel} on a geometrically rough surface (Fig.1.4 (a)):

$$\cos \theta_{Wenzel} = r \cos \theta_Y. \quad (1.22)$$

where θ_Y is the Young's angle, and r is a roughness factor, which is the ratio of the actual area to the projected area of the surface. On the other hand, the Cassie-Baxter equation describes the apparent contact angle θ_{C-B} on a chemically patterned surface (Fig1.5 (b)):

$$\cos \theta_{C-B} = f_1 \cos \theta_{Y1} + (1 - f_1) \cos \theta_{Y2}. \quad (1.23)$$

where θ_{Y1} and θ_{Y2} are respectively the Young's angles of the two materials, f is the area fraction of material 1 on the surface.

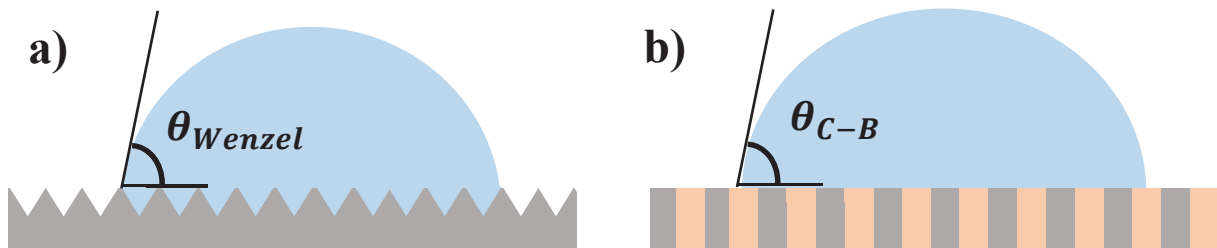


Figure 1. 4 The contact angle on geometrically and chemically rough surfaces. (a) Wenzel state (b) Cassie-Baxter state.

Although the two equations are widely used, their validity has been challenged recently [23-26]. The main problem is that the two equations are rarely consistent with experimental observations that the apparent contact angle is not unique on a rough surface. This phenomenon is very important in industrial applications and often referred to contact angle hysteresis. Obviously, the classical Wenzel and Cassie equations can not describe this phenomena [27-29]. It is believed that the non-ideality of the contact between solid and liquid causes contact angle hysteresis. That is, measured advancing contact angle is almost always larger than receding contact angle. In fact, thermodynamic irreversible nature of the surface alterations on the solid/liquid interface does not allow the liquid front retract on the same path it has passed in advancing. Metastable reorientation of the liquid molecules or clusters with different sizes again is the main reason behind the contact angle hysteresis caused by roughness.

I-3-Friction

I-3.1-Amontons' Laws of Friction

One of the first studies on friction was illustrated by Leonardo di Vinci (1452-1519). Whose friction experiments resulted in statements that are mostly known as the Amontons' law of friction, namely:

- The friction force is directly proportional to the applied load.
- The friction force is independent of the apparent contact area.
- Kinetic friction is independent of the sliding velocity.

The first law of Amontons' law is usually written as:

$$\mu = \frac{F_{\parallel}}{F_{\perp}}, \quad (1.24)$$

where F_{\parallel} is friction force, F_{\perp} is the normal load that press the surface together, and μ is the coefficient of friction. In order to make the results of different experiments comparable to each other, it is a common practice to report the results of friction experiments in terms of coefficient of friction rather than friction force itself. Euler was the first one who distinguished between two modes of friction: static friction and dynamic friction [30]. The force needed to initiate relative movement of two bodies originally at rest is referred to as static friction force. When two bodies are in motion against each other, the force that resists the movement is referred to as dynamic or kinetic friction. Generally, the kinetic friction is lower than the static friction, but the values may depend on the actual experimental conditions [31]. The role of surface texture in friction and the approach of asperity interaction were first introduced by Amontons in 1699 [32]. Later, in 1785, Coulomb studied the influence of surface area, nature of materials in contact, normal load, and contact time upon friction, mostly for wooden surfaces. Coulomb also studied the relationship between static and kinetic friction.

I-3.2-The Basic model of friction

In spite of about 500 years of scientific study on friction, a theory has not yet been developed which can describe all experimental data available and predict friction between any two surfaces. A wide range of materials already have been tested in friction experiments such as wood [32], metals [33, 34], crystalline solids [35, 36], polymers [37-39], and many more [40, 41]. As pointed out by Dowson [32], there have been several major models or approaches in the long history of friction study.

I-3.3-The geometrical or mechanistic model

In this model, asperity interaction and forces needed for asperities to slip over each other are considered the origin of the friction force. The work of early scientist, including Amontons' and Coulomb, who

believed in the mechanical view of friction, is broadly reviewed by Dowson [32]. Shortly, it was assumed that mechanical interlocking of asperities resists the motion of two bodies against each other and the work of frictional force is equal to the work done against the normal load in separating the asperities and sliding them over each other. Therefore, the effect of lubrication in shrinking friction was elucidated by the assumption that lubricants fill the irregularities and gaps between these asperities. However, the geometrical or mechanistic approach could not explain a variety of experimental observations. For example, friction between two highly polished smooth metallic surfaces is higher than unpolished surfaces because of cold welding of asperities. If the interlocking of asperities was the origin of friction, one should predict the unpolished surface to have higher friction. Another example is that adsorbed films and monolayers on different surfaces can greatly change the friction while actually preserving the same surface roughness.

I-3.4-The molecular or adhesive model

Ewing [31] and Hardy [42] were among the first to introduce that the origin of friction is the surface forces and molecular adhesion at the interface. According to Hardy, lubricants decrease the molecular field of force between the solid surfaces, which in turn reduces the friction. Prandtl [32] and Tomlinson [43] considered the role of adhesion in the friction mechanism and tried to analyze the friction at the molecular level. Conforming to Tomlinson when two surfaces sliding against each other, molecules will be forced into each other's atomic fields and then separated, which is accompanied by energy dissipation that was considered as the origin of the friction force. Derjaguin took into account the role of intermolecular forces, quantified the concept introduced by Tomlinson, and derived the following relation for friction force [44]:

$$\mu = \frac{F_{\parallel}}{A_{real}(P + P_0)} \quad (1.25)$$

Where A_{real} is the real contact area and P and P_0 are the mean stresses representing external forces (external load) and molecular adhesion, respectively.

I-3.5-The deformation or ploughing model

In the deformation or ploughing model, friction is associated to the force needed to shift hard asperities through or over another surface. Let A_0 be the sum of the area of indenting asperities perpendicular to the direction of sliding and H' be the mean stress needed to shear the junction; the friction force would be illustrated by:

$$F_{\parallel} = A_0 H' \quad (1.26)$$

Let H be the yield stress of the softer material and note that normal load is applied on real contact area, one would have:

$$F_{\perp} = A_{real}H. \quad (1.27)$$

Therefore, the coefficient of friction becomes:

$$\mu = \frac{F_{\parallel}}{F_{\perp}} = \frac{A_0H'}{A_{real}H} = \frac{A_0}{A_{real}}. \quad (1.28)$$

In Equation 1.28, it is considered that H is equal to H' , which is a realistic assumption in most cases [31]. In order to quantify the A_0/A_{real} ratio, the geometry of the asperities must be known.

I-3.6-Interfacial friction

The existence of systems with decreased liquid-solid interfacial friction that leads to a slip boundary condition has achieved substantial experimental confirmation only within the past few decades. Therefore, a surge of investigation have attempted to explore the nature of interfacial slip and the parameters that could affect the slip length. Surface force apparatus measurements have revealed many interesting properties of slip. SFA results have shown that the measured slip length can depend [45] on shear rate [46] or not depend on shear rate [47] depending on the liquid-solid system. As well, surface roughness of the substrate can reduce the effect of slip in certain cases. For partially wetting fluids, slip has been shown to be affected by the contact angle of the liquid on the substrate and the polarizability of the liquid molecules [48]. The dewetting of polymeric liquids has also been extensively used to study slip. Dewetting often occurs readily in slip systems, as the substrates are typically unfavorable for most polymeric liquids. The slip length primarily depends on the polymer-substrate combination [49]. Dewetting measurements have shown that the slip length measured is sensitive to the sample preparation and annealing procedure [50]. Recently, the effect of slip on droplet dynamics was examined. Slip at the liquid-solid interface influences both droplet shape and contact line movement [51].

I-4-Surface Texturing Effects on friction and adhesion

I-4.1-Adhesion on Physically Patterned Substrates

Several adhesion measurements were performed to evaluate the performance of different patterned substrates. In 2003, measurements on high AR polyimide pillars with low packing density and poorly defined tips showed that the pull-off force strongly increases with decreasing pillar spacing. The pillar diameter and height did not seem to strongly influence the pull-off force [52]. Crosby et al. [53] proved later that the adhesive properties of cylindrical polydimethylsiloxane (PDMS) patterns fabricated by molding show three regions of pull-off force evolution. These controversial results were resolved by a

Chapter 1 Literature review

systematic study on the influence of the geometrical aspect on adhesion by Greiner et al. [54]. They fabricated several PDMS pillar arrays with cylindrical geometry and different radii and heights and mentioned that the pull-off strength increases with shrinking pillar radius (Fig.1.5)

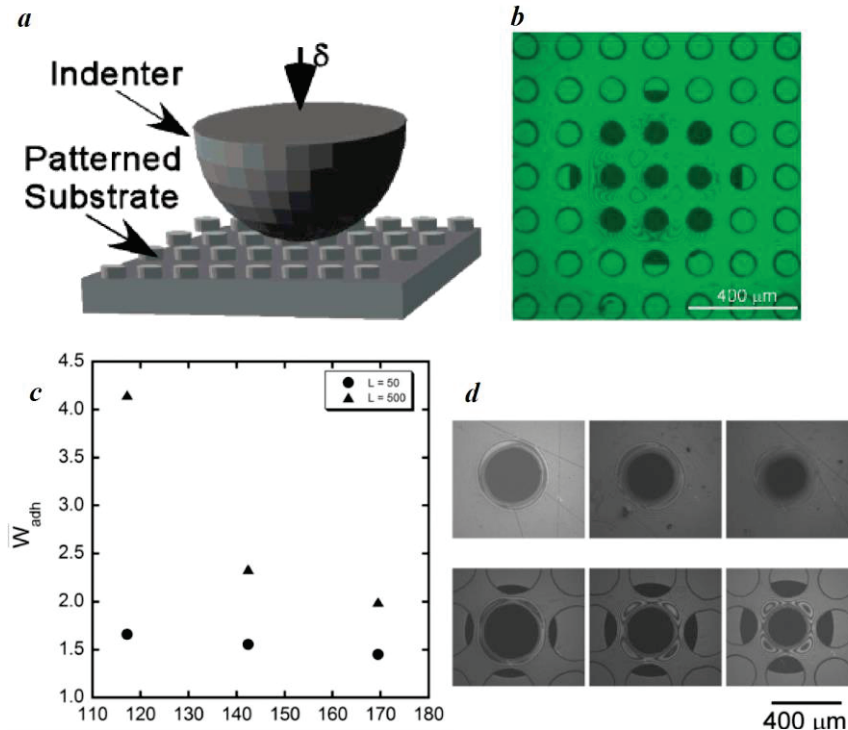


Figure 1.5 (a) Schematic of spherical probe contacting polymer surface decorated with low-aspect ratio posts. (b) Contact area image of spherical probe and patterned surface. (c-d) corresponds Normalized W_{adh} as a function of post radius, r_p , for two differently spaced patterns: $L = 50 \mu\text{m}$ and $L = 500 \mu\text{m}$. The patterns with $L = 50 \mu\text{m}$ have significantly lower values of W_{adh} . Maximum contact area images for $L = 500 \mu\text{m}$ (top) and $L = 50 \mu\text{m}$ (bottom) are on right.

Furthermore, Verneuil et al [55] investigated the adhesion between soft elastic substrates bearing surface microstructures (pillars and holes of different height) and a smooth lens of the same rubber using a home build JKR machine. In fact, compared to a homogenous surface, they illustrated the presence of a critical height h_c for the microstructures, generated by a competition between the adhesion energy and the elastic deformation energy necessary to invade the pattern. Hence, for $h < h_c$, the bead and the substrate are in intimate contact even when the applied force is zero, and for $h > h_c$, an air film remains intercalated in the microstructure (Fig.1.6), and the contact is limited to the top of the caps or between the holes. They mentioned that the transition between these two states could be induced by an augmentation of loading force.

Recently, several modified and complex geometries were studied to optimize the adhesive properties, varying from tilted pillars [56-58] over sub-surface patterns [59-61] and hierarchical geometries [62-64] to pillars with modified surface chemistry.

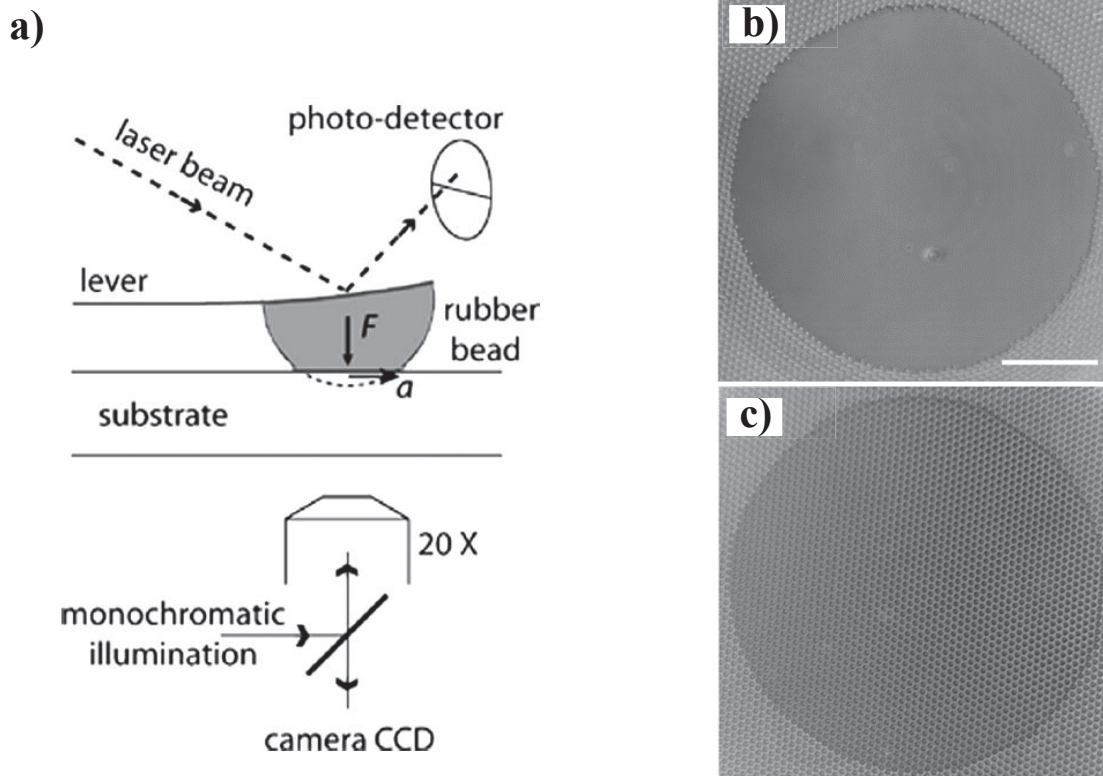


Figure 1.7 (a) Schematic representation of the experimental setup. (b-c) microscopy images of the contacts on substrates with holes of various depths and for a positive load $F = 0.6 \text{ mN}$. The contact is intimate for $h < h_c$ (b), and suspended for $h > h_c$. (c) The white bar represents 50 mm .

I-4.2-Adhesion on Chemically Patterned Substrates

The need of improved surfaces with specific tribological proprieties has stimulated the need and design of molecular assemblies capable to impart new functional surface properties to materials or improve those existing, for the control of their interface behaviors (adsorption, condensation, wetting, lubrication, adhesion, liquid flow). Self-assembled monolayers (SAMs) of either organosilanes have played and still continue to play a major role in the achievement of this goal, especially in fluidics and as lubrication coatings. Hence, Berg and Ramrus [65] studied the combination of an adhesion promoter with a second silane of different chemical functionality in order, to increase the number of potential applications. They used several methods to produce different mixed silane layers, including solution deposition, microcontact printing and vapor deposition. Thus, they determined the adhesion between polymers and heterogeneous micropatterned silanes using an AFM-PFM machine Fig.1.7).

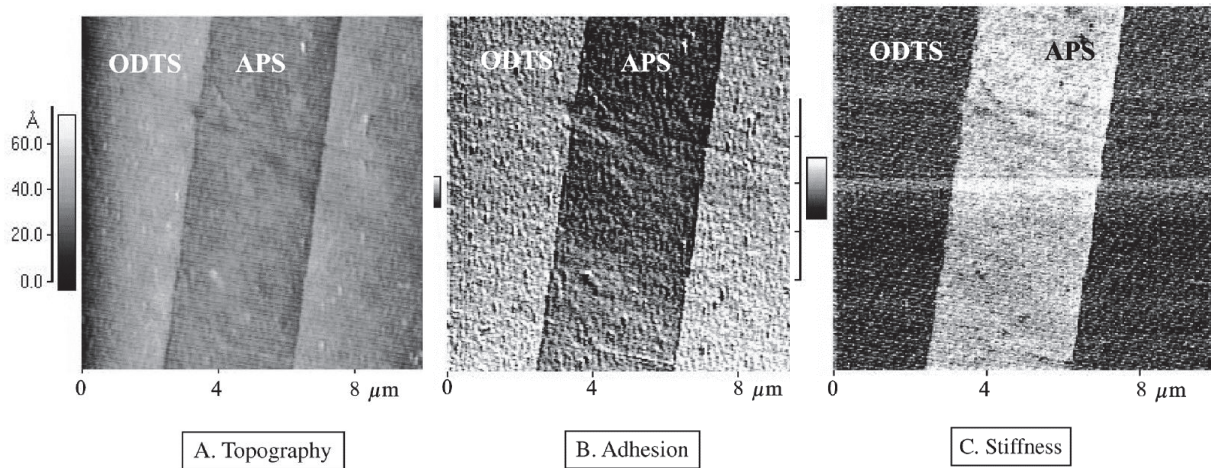


Figure 1. 7 AFM-PFM scans of a heterogeneous micro-contact printed pattern on a SiO₂ surface. The APS was solution deposited, followed by ODTS micro-contact printing. Scan width 10 μm.

I-4.3-Friction on Physically Patterned Substrates

Several studies have investigated the influences of surface texturing on the friction experimentally under different sliding conditions. Kovalchenko et al. [66] looked into the effects of laser surface texture on the lubrication regime transition. Specifically, the influences of the sliding speed, normal pressure, and the lubricant viscosity on the friction were tested. A pin-on-disk apparatus was used in this case, and the laser surface texturing had more impact on friction in cases of higher normal loads, higher sliding speed, and higher viscosity.

Pettersson and Jacobson [67] investigated the effects of the surface texturing of coated silicon under boundary and dry sliding conditions. Etched silicon samples were coated with either TiN or DLC. This study shows the crucial impact of the material interaction under oscillating sliding by a ball slider. Two texturing designs were investigated, grooves and square dimples as shown in Figure 1.8 [67]. The results of this study were compared to homogenous samples. Under boundary lubrication conditions, the DLC coating with square dimples showed stable low friction behavior, while the grooved texture showed high friction. The textured TiN coating behaved differently and showed unstable friction behavior on all texturing patterns. In dry sliding conditions, the DLC coating showed high friction when compared to the untextured surface. DLC has self-lubricating properties where a thin low friction tribofilm was formed on the surface. When the DLC coated sample was textured, the sharp edges of the pores scraped off the thin tribofilm causing the fluctuations in the friction behavior. On the other hand, the TiN textured samples showed low friction with both the square and groove patterns.

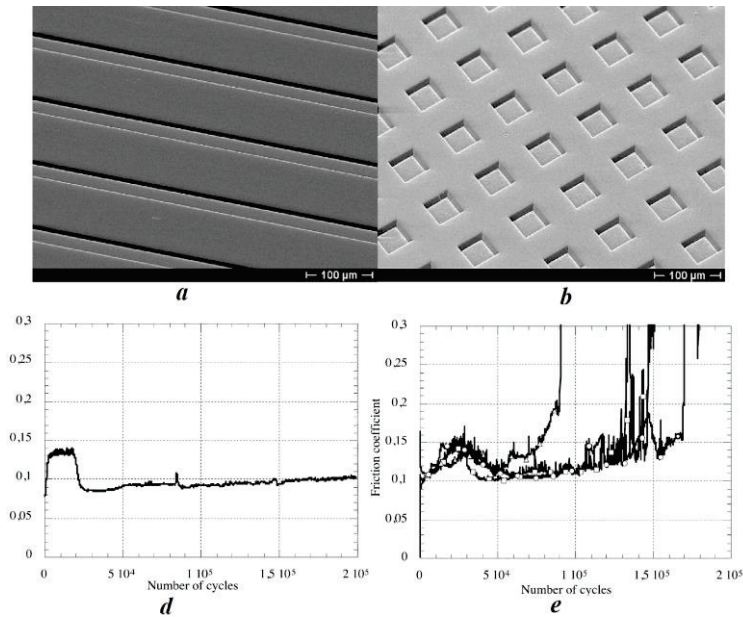


Figure 1. 10 The surface textures include (a) three groove widths and (b) three sizes of quadratic depressions, all with a 25% surface coverage (SEM). (d-e) show the friction coefficient in dry sliding between the steel ball and the TiN coated surfaces. (d) Two parallel tests on the flat surface. (e) All types of textured surfaces, including grooves (open circles) and a square depression (black squares) of three sizes each.

Suh and others [68-71] tested the effect of the width and orientation of undulations with respect to the sliding direction on the friction and wear, under boundary sliding conditions. Pin-on-disk tests were done, with the disks textured by abrasive machining. Grooves that were parallel to the sliding direction showed no improvement in either friction or wear. Yet, grooves perpendicular to the sliding direction decreased both the wear and friction.

I-4.4-Friction on Chemically Patterned Substrates

The tribological behavior of micro- and nanostructured organic molecular thin films was investigated and interpreted as a function of the topology and organization of the surface patterns: from geometrical and well-organized structures to more random ones. So far, little information is available in the literature on this influence of the topological organization. Recently, Ishida et al studied the frictional response of a patterned surface of alkylsilane and fluoroalkylsilane monolayers prepared with a series of chain lengths by a chemical vapor adsorption method. They investigated the tribological properties of the surface using a lateral force microscope (LFM) and friction tester. Where they found that even though the height difference between the two-components was less than 1 nm, friction force anisotropy between the parallel and perpendicular directions against the line pattern was observed Fig.1.9.

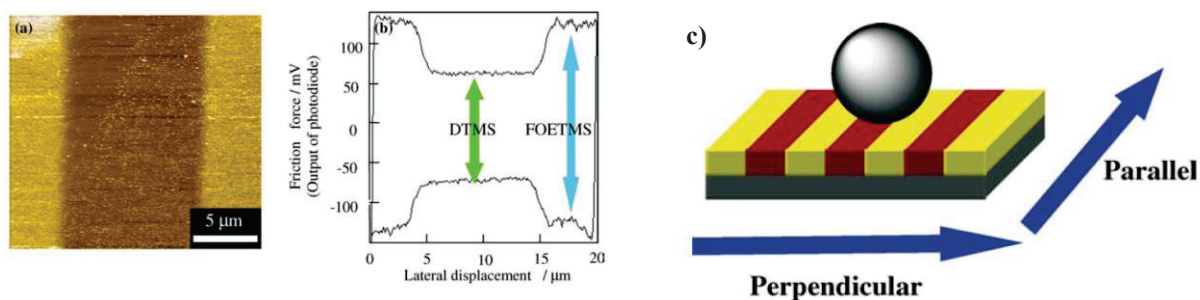


Figure 1. 12 (a) LFM image and (b) frictional curve of DTMS/FOETMS monolayer (c) Frictional direction of two-component micro patterned organosilane monolayer.

Mougin and Haidara [72] have also prepared striped micro patterned of methyl and hydroxyl terminated SAMs and studied correlation between friction and grafted mole fraction. Moreover, they found that the averaged frictional response of the surface is more sensitive to the chemistry and relative surface fraction of the molecular domains than to the size and distribution of patterns. In fact, they demonstrated that a regular increase of the tip/substrate friction on these (NH₂-CH₃)-patterned surfaces could be anchored to the increase the surface fraction of the hydrophilic molecular species (NH₂).

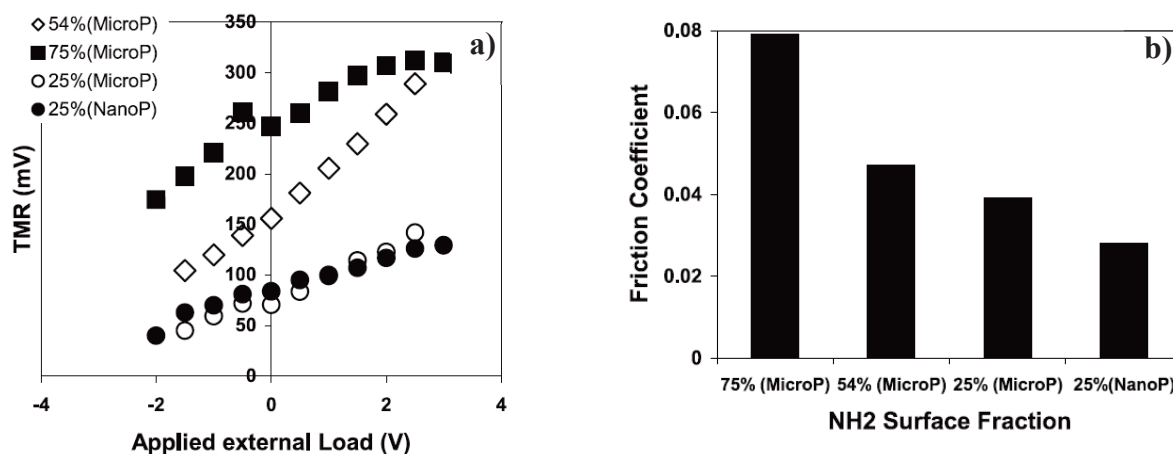


Figure 1. 10 (a) TMR (Trace minus Retrace) as a function of applied external load for different NH₂ surface fraction for micro and nano-patterned binary NH₂/CH₃ surfaces. (b) Friction coefficient versus NH₂ surface fraction for micro and nano-patterned binary NH₂/CH₃ surfaces.

The results show that the friction coefficient decreases linearly as the surface coverage of NH₂ for micro patterned surfaces (Fig.1.10). The friction forces increase with the magnitude of the adhesive interaction of the SAMs and the tip. As a result, the greater the surface fraction of NH₂ in the thin film, the friction response.

II-Dewetting as an investigative tool for studying the mechanical properties of the surface

Polymer thin films have proven to be an extremely intriguing test case for dewetting studies, for many reasons, amidst which are the ease of preparation and control of the samples, simple and precision of measurements, efficient relevance, and complexity of the systems. Therefore, in the following sections basic concepts from hydrodynamic theories in the bulk situation to corresponding models with regard to confinement are introduced. Depending on the type of liquid, viscous or even viscoelastic effects have to be considered and deviations from Newtonian behavior might become non-negligible. Since we concentrate in this section on polymer melts, viscosity and viscoelasticity can be varied by chain length and branching of the polymer. A key aspect of a liquid in motion is the velocity profile. Finally, several dewetting scenarios on chemically and physically patterned surfaces were introduced.

II-1-Thin polymer Film

While Miniaturization of functional devices needs the thickness of polymer films to attain values even smaller than the diameter of the undisturbed molecule, such films generally, reveal characteristic vigorously deviating properties from those these polymers display in the bulk. The situation can be described as a confined thin polymer film, where nearly the thickness film is to be smaller than the radius of gyration R_g of the polymer. The first studies to illustrate experiments on the dewetting of thin polymer film are due to G. Reiter [73]. Reiter noticed film rupture over (through) the evolution of holes and explained his results in terms of spinodal dewetting. Next study by Jacobs et al [74] showed that, by statistical sample analysis based on integral geometry, the rupture process was more possible to be based on heterogeneous nucleation. These intriguing observations have stimulated a profound search for a comprehensive explanation in the polymer film research community. There are several interesting reviews and books chapters, which compile the dynamic of confined polymer thin films [75-77].

II-1.1-Stability of supported thin films

Understanding the stability of a thin liquid film deposited on top of a substrate is crucial issue to foresee the behavior of the system. Bäümchen and Jacobs reviewed recent advances in this field illustrating an explicit link between the stability conditions and the dynamics and the final pattern obtained [49]. The stability of a thin film is controlled by the growth of the effective interface potential as a function of the film thickness. Thereby three cases are showed in Fig. 1.12, the stable, metastable and unstable. The function $\phi(h)$ is built from calculation of contribution between attractive and repulsive forces given in equation 1.29 for a system Si/SiO₂/layer/film. The index c represents a layer covering the substrate in case the Si-wafer is modified prior use.

$$\phi(h) = \frac{C_s}{h^8} - \frac{A_c}{12\pi h^2} + \frac{A_c - A_{SiO_2}}{12\pi(h + d_c)^2} + \frac{A_{SiO_2} - A_{Si}}{12\pi(h + d_c + d_{SiO_2})^2}. \quad (1.29)$$

As illustrated in Fig.1.12 by the curves of $\phi(h)$ a stable liquid film is attained if the effective interface potential is positive and monotonically decaying (curve (1) in Fig.1.11 a) the equilibrium film thickness h_{eq} is infinite and the liquid perfectly wets the substrate.

In case of a global minimum of $\phi(h)$, the system can minimize its energy and a finite value for h_{eq} results. Hence, the potential barrier that the system has to overcome to reduce its potential energy is what characterizes the metastable situation. which expose the contribution of van der Waals forces and repulsive forces as detailed in [49]. Further, the transition occurs when the second derivative of the effective interface potential crosses becomes negative ($\phi''(h) < 0$) Fig 1.11 b).

$$\phi(d_{eq}) = \gamma(\cos \theta_{eq} - 1). \quad (1.30)$$

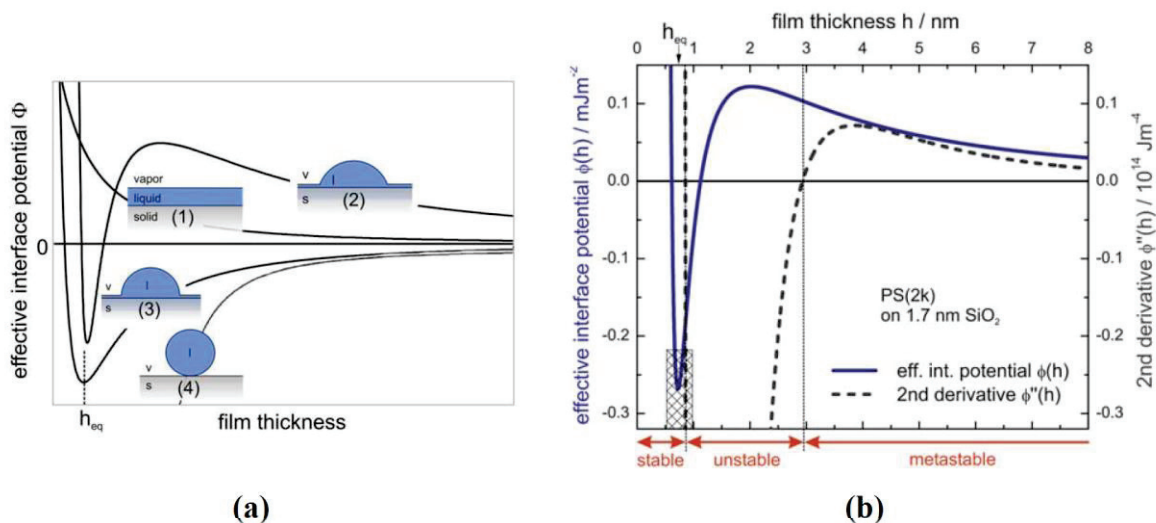


Figure 1. 11 (a) Different shapes of the effective interface potential $\phi(h)$ associated with different wetting conditions. Curve (1) characterizes a stable liquid film. Curve (2) represents a metastable, curve (3) and (4) an unstable situation. **(b)** Effective interface potential $\phi(h)$ (solid line) and its second derivative $\phi''(h)$ (dashed line) for a liquid polystyrene PS (2k) film prepared on a Si wafer with a 1.7nm SiO_2 layer. The sign reversal of $\phi''(h)$ characterizes the stability of the film. The hatched rectangle indicates typical experimental errors of the contact angle measurement and the determination of the equilibrium film thickness h_{eq} .

II-2-Hydrodynamics in thin liquid films

This part draws main lines in the basic theoretical concepts for hydrodynamics in thin liquid films.

II-2.1-Navier-Stokes equation

The Navier-Stokes equation (1.33) defines the fluid dynamics in confined geometries, which proposes that inertia of a small amount of a fluid equals the sum of external forces. According to conservation of mass, the equation of continuity can be formulated as

$$\partial_t \rho + \nabla \cdot (\rho \mathbf{u}) = 0, \quad (1.31)$$

with $\mathbf{u} = (u_x, u_y, u_z)$ is the velocity field of the fluid. Functioning under conditions of an incompressible liquid of density ρ , partially and temporally constant, implies a simplified version of equation 1.31: $\nabla \cdot \mathbf{u} = 0$. The conservation of momentum leads to the Navier-Stokes equation for incompressible fluids.

$$\rho \frac{\partial \mathbf{u}}{\partial t} + \rho(\mathbf{u} \cdot \nabla) \mathbf{u} = -\nabla p + \eta \nabla^2 \mathbf{u} + \rho \mathbf{f}. \quad (1.32)$$

With the pressure gradient ∇p and the volume force \mathbf{f} of external fields as driving forces for the liquid flow. For thin polymer films, inertia is small compared to viscosity ($Re \ll 1$), the terms on the left-hand side of equation 1.32 can be neglected, which leads to the Stokes equation

$$\mathbf{0} = -\nabla p + \eta \nabla^2 \mathbf{u} + \rho \mathbf{f}. \quad (1.33)$$

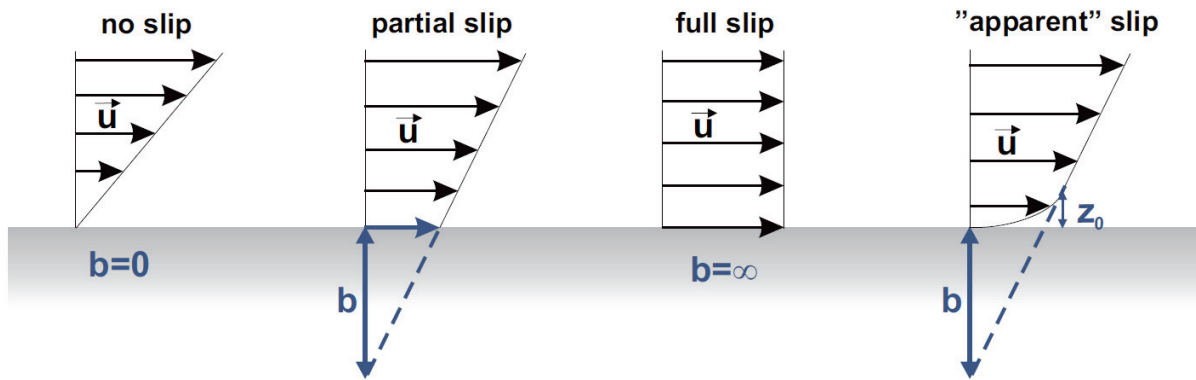


Figure 1.12 Different velocity profiles in the vicinity of the solid/liquid interface and illustration of the slip (extrapolation) length b . The situation of (apparent) slip is illustrated on the right: according to a thin liquid layer of thickness z_0 that obtains a significantly reduced viscosity, the slip velocity $u_x|_{z=0}$ is zero, but a substantial slip length is measured.

II-2.2-Boundary conditions at interfaces

In case of thin liquid films, the tangential flow velocity \mathbf{u}_{\parallel} differs from the bulk behavior assuming the no-slip boundary condition. As early as 1823, Navier states that the tangential velocity \mathbf{u}_{\parallel} grows proportionally to the strain rate tensor with the slip-length b acting as constant of proportionality (equation 1.34, with \mathbf{n} the normal component, perpendicular to the stress tensor) [78]. In the case of simple shear flow in x –direction, equation 1.35 illustrates that the slip length in fact evolves as the inverse of the friction coefficient ξ .

$$\mathbf{u}_{\parallel} = b \mathbf{n} \cdot \dot{\gamma} \quad (1.34)$$

$$b = \frac{u_x}{\partial_z u_z} \Big|_{z=0} = \frac{u_x \eta}{\sigma} = \frac{\eta}{\xi}. \quad (1.35)$$

Confining the motion of the fluid to the xz –plane in turn empowers an easy representation of flow profiles, as presented in Fig. 1.12, demonstrating both limiting cases, i. e. the no slip situation ($b = 0$) and plug flow ($b = \infty$). However, many experimental setup evidence an intermediate case, partial slip, where a non-zero slip length can be defined with the method described in the stability of supported thin films. Apparent slip illustrates the case where slip length is non negligible, but a zero dewetting velocity at $z = 0$ is obtained as a result of a thin layer of reduced viscosity for the height z_0 .

II-2.3-Thin film equation (Newtonian liquids)

The various velocity profiles noticed in the previous part result from fluid motion appearing under confinement far below the limit where bulk properties are observed. Gravitational forces are neglected for film thicknesses below the capillary length $l_c = \sqrt{\gamma/\rho g}$, normally in the millimeter range. Consecutively, intermolecular forces become more influential. Connected with the fact that the lateral length scale of the film thickness variations is much smaller than the film thickness, we obtain a simpler version of Navier-Stokes equations. The thin film equation for Newtonian fluids reads [79]

$$0 = -\nabla(p + \phi'(h)) + \eta \nabla^2 \mathbf{u}. \quad (1.36)$$

The disjoining pressure $\phi'(h)$ stands for the short-range forces as the spatial derivative of the effective interface potential $\phi(h)$, which represents the competition between short-range and long-range forces.

II-2.4-Equations of motion

Applying the Navier slip boundary (equation 1.35) to the Navier-Stokes equations (equations 1.33) together with the assumption of the lubrication approximation, the equation of motion for thin films in the three dimensions then reads

$$\partial_t = -\nabla \left[m(h) \nabla (\gamma \nabla^2 - \phi'(h)) \right] \quad (1.37)$$

$$\text{with } m(h) = \frac{1}{3\eta} (h^3 + 3bh^2).$$

The mobility coefficient $m(h)$ expresses motion at the solid/liquid interface conferring to the amount of slippage of the system. In the no-slip boundary condition the mobility of thin liquid film follows ($m(h) = h^3/3\eta$) whereas ($m(h) = bh^2/\eta$) if friction (ξ) at the solid/liquid interface is low.

II-3-Dewetting of viscoelastic polymer thin films

It is somewhat intriguing to notice similar dewetting phenomenon for viscoelastic films where, on the timescale of the experiment, the material cannot flow like a liquid, rather it behaves like an elastic body. Studies on thin polystyrene (PS) films at temperatures not too far above the glass transition temperature are of that kind, which contributed a lot for the study of thin polymer film properties through several papers presented specifically in the last years and still under an intense interest for investigation [80-87]. To study the dewetting phenomenon of highly elastic PS films, the mechanism of hole growth could be followed from the very early stages. Thus, to reduce the resistance from interfacial friction, the choice of highly non-wettable substrate can be achieved by using PDMS-coated Si-wafers.

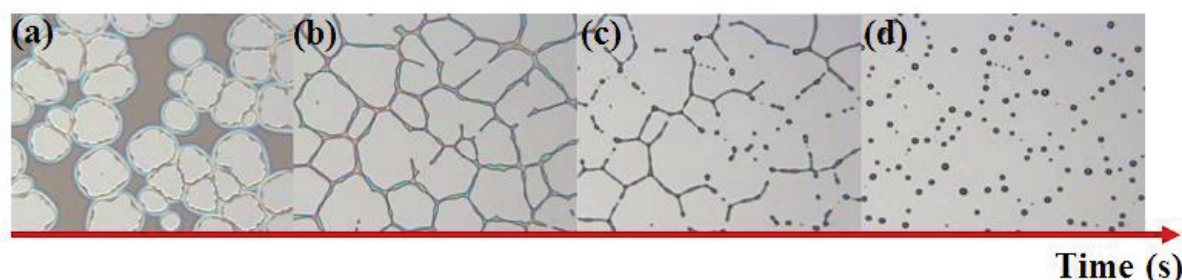


Figure 1. 13 Optical micrographs (size of each: $240 \times 200 \mu\text{m}^2$) showing dewetting of a thin film of polystyrene ($M_w = 4840 \text{ kg / mol}$, $h = 40 \text{ nm}$) nucleation and growth on a silicon substrate coated with a monolayer of adsorbed PDMS ($M_w = 139 \text{ kg/mol}$, thickness = 11 nm). The temperature of dewetting is $180 \text{ }^\circ\text{C}$. At the end, a multitude of dewetting droplets were arranged in polygons. The time between images is about 30 s.

Dewetting starts after heating the sample above the glass transition temperature of the polymer. Holes nucleate according to thermal activation or nucleation spots (dust particles, inhomogeneities of the substrate or of the polymer film) and evolve with time (Fig.1.13) the consecutive stages of dewetting are demonstrated by the arises of liquid ridges by coalescence of growing holes and traveling fronts. Very thin films in the range of several nanometers may become unstable and can dewet giving to thermally induced capillary modes that are heightened by forces contributing to the effective interface potential. This phenomenon is determined by the occurrence of a preferred wavelength and is termed spinodal dewetting. To analyze thin film flow with regard to the effect of slippage, especially nucleated holes enable an easy experimental access for temporal and spatial observation. While the liquid retract from the substrate and holes grow, a liquid rim arises at the three-phase contact line due to conservation of liquid volume. The formation of liquid bulges or "fingers" due to the fact that the liquid rim becomes unstable, similar to the instability of a cylindrical liquid jet that beads up into droplets (e.g. in case of a water tap). This phenomenon called the Rayleigh-Plateau instability Fig.1.13d. If two holes coalesce, a common ridge builds up, which in the end decays into single droplets due to the same mechanism. Generally, the last stage of dewetting is demonstrated by such equilibrium configuration of liquid droplets ideally of single curvature since the Laplace pressure should be same.

One of the first papers on viscoelastic dewetting of PS on PDMS coated Si-wafer was from Reiter [82]. AFM results for the early stages of hole formation obtained from the thinnest films showed most holes

were formed within a small time interval at the very beginning Fig.1.14. Intriguingly, these holes initially do not show any rim. Nonetheless, at the finale stage one could explicitly notice the formation of a rim. After 10 min of annealing at 105 °C the hole size of two different molecular weights (differing by nearly a factor of 30) thin polystyrene films appears nearly the same. Further, fairly thicker films were used in order to have fewer holes so that one can follow the different stages of hole growth up to much larger hole diameters. As the annealing time expanded, hole diameter became more larger.

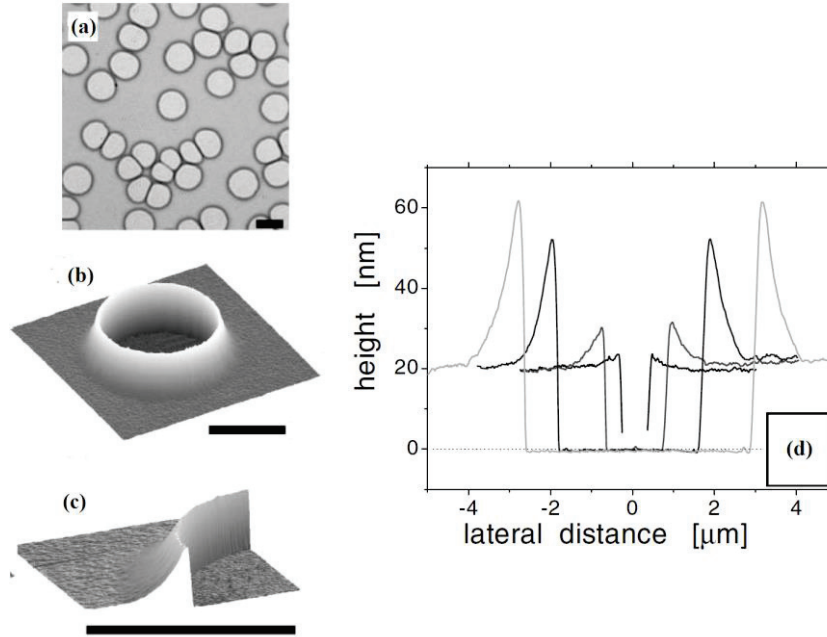


Figure 1. 14 Typical examples for holes and the corresponding rim formed in a 24 nm thick PS film. This film is thick enough for holes being separated by several mm on average. **(a)** Optical micrograph after annealing for 80 min at 120 °C. AFM images **(b)** and **(c)** focus on the asymmetric shape of the rim. The length of the bar represents 5 mm in each case. **(d)** Cross sections through holes in a 20 nm thick PS film after annealing for 1, 5, 40, and 80 min at 120 ±C, respectively. Note the highly asymmetric shape of the rim.

Such a transition is expected as soon as the viscous dissipation at the substrate-film interface is getting important. Initially the removed material (related to the dewetted hole radius, R has been redistributed within the film over a certain limit R_c which is characterized by film thickness h_0 and frictional properties:

$$R_c = \sqrt{bh_0} = \left(\frac{\eta h_0}{\xi}\right)^{1/2} \quad (1.38)$$

with ξ being the friction coefficient at the interface and η the viscosity of the film [85]. As the dewetted hole radius R gets larger than R_c , dissipation as well as friction at the substrate/film interface become important. Because of such friction, the velocity is damped over the distance R_c within the film. As a result, a highly asymmetric rim is observed, with a steep side reaching a height H next to the three-phase contact line and an approximately exponential decay on the other side, with a decay length R_c (Fig.1.15).

The highly asymmetric shape of the rim indicates that the polymer is not flowing like a liquid but rather behaves like a solid. For a viscous fluid, one could expect

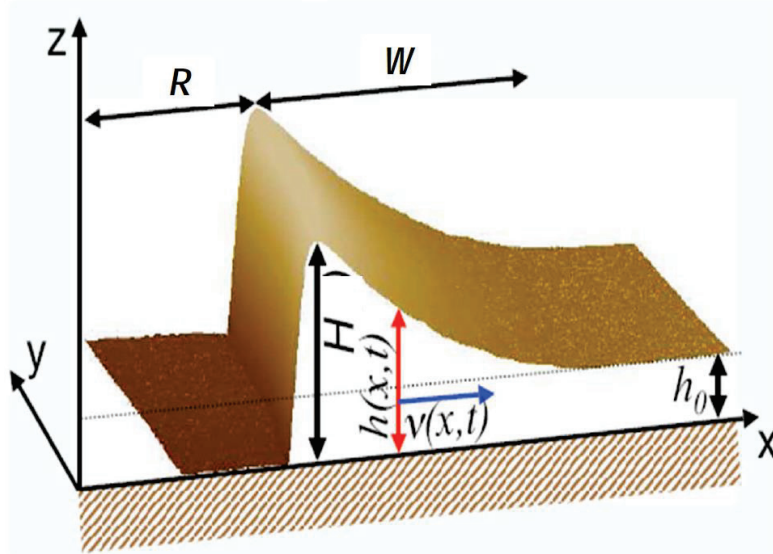


Figure 1. 15 3D-view (measured by AFM) of a section of a typical hole obtained by dewetting a polystyrene film on a PDMS-coated substrate at temperatures close to the glass transition of PS. $h(x, t)$ is the profile of the film, h_0 is the initial height of the film, H is the height of the front, R is the dewetted distance, W is the width of the rim, and $v(x, t)$ is the velocity inside the film.

equilibration of the Laplace pressure (which is proportional to curvature) through viscous flow during the experiment. This can lead to a more symmetric rim shape (mature rim). The asymmetric shape of the rim is a characteristic feature of dewetting of viscoelastic fluids at temperatures close to T_g , which changes further during the course of dewetting [87]. The transition from a highly asymmetric rim to a more symmetric mature rim shape illustrates the changeover from elasticity to viscosity dominated dewetting. All these experiments show that a thin film does not need to be purely liquid to dewett. In the following section different literatures, results on dewetting on chemically patterned surfaces are reviewed.

II-4-Dewetting on patterned substrates

Dewetted structures have been successfully adjusted by using either a chemically [45, 88-90], physically [91-93], or physico-chemically patterned substrates. The possibility of aligning the isotropic and randomly oriented dewetted patterns was first illustrated by Higgins and Jones by simply rubbing the substrate with a lens tissue before coating the film, resulting in the formation-aligned ridges on the substrate in the direction of rubbing [94]. The resulting directionality of the substrate influenced the dewetting pathway of the PMMA film and led to the formation of strongly anisotropic structures comprising a series of continuous lines running across the sample surface following the ridges [94].

II-4.1-Dewetting on Physically Patterned Substrates

Bao et al. [95] and recently, Ferrell and Hansford [96] have used dewetting during spin coating of a polymer solution on a topographically patterned substrate for fabricating micro- and nanoscale polymer patterns. Bao et al. directly spun coated MMA and polycarbonate (PC) solutions on physically patterned silica substrates coated with a higher surface-energy silane on the raised portions and a lower-surface energy silane over the recessed areas. The coated polymer preferentially wetted the higher-surface energy areas, leading to the creation of well-regulated structures [95]. The final pattern morphology was significantly affected by the geometry (height, lateral feature dimensions, and spacing) and polymer solution concentration [96].

Dewetting of a homopolymer film on a topographically patterned substrate was first presented by Rockfort et al., where striped substrates comprising periodically varying areas displaying polar (silicon oxide) and nonpolar (gold) interactions (stripe periodicity **170 nm**) were used to study dewetting of a **5 nm** -thick PS film. It shows that the PS film dewetted on the oxide stripes and segregated to the goldcoated zones, leading to the formation of strongly isotropic structures resembling the substrate pattern features [97]. Rehse et al. studied the stability of thin PS films of various molecular weights on regularly grooved silicon surfaces including triangular grooves or stripes with a mean stripe width of **250 nm** and a mean peak-to-valley height of 5 nm without any surface energy contrast Fig.1.16. [98]. The films, which were directly, spin coated on the patterned substrates showed a slight variation in thickness, in phase with the substrate geometry. Rupture in such a films debuted over the thinner areas above the stripes, resulting in the break-up of the initially continuous film, forming segregated and long strips of polymer filling the grooves [98]. Thus, the profile of the dewetted film replicated the inverse morphology of the substrate.

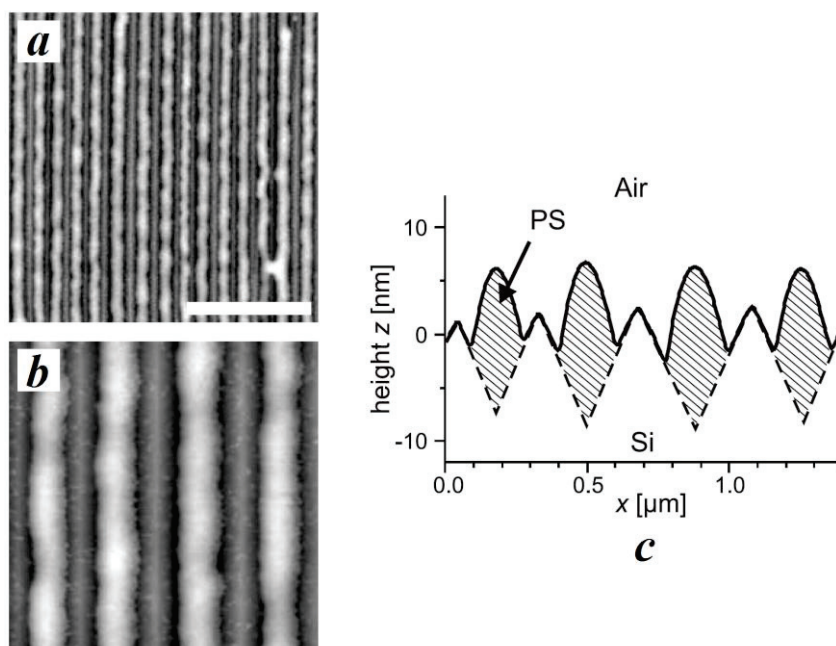


Figure 1. 20 (a) SFM Tapping ModeTM topography images of a thin PS film ($M_w = 100$ kDa, $t_{av} = 5$ nm) on a corrugated silicon substrate at 150°C for 3 h. (b) Average line scan along the horizontal taken from image. (c) The solid line is the experimental result. The dashed line depicts the position of the substrate surface.

Furthermore, the morphological growth and pattern formation of polymer thin films, with homogenous thickness on topographically patterned substrates with several geometries has been studied by Mukherjee et al.[99, 100]. They demonstrated that by adapting the transfer conditions like, the rate and angle of lift-off, it is feasible to control the initial morphology of the film with respect to the underlying substrate. As presented in Fig. 1.17, in the dewetting of a 24 nm -thick PS film on a patterned substrate, the final dewetted morphology comprises an array of droplets, the positioning of which depends entirely on the initial conformation of the films (Fig. 1.19) with respect to the substrate.

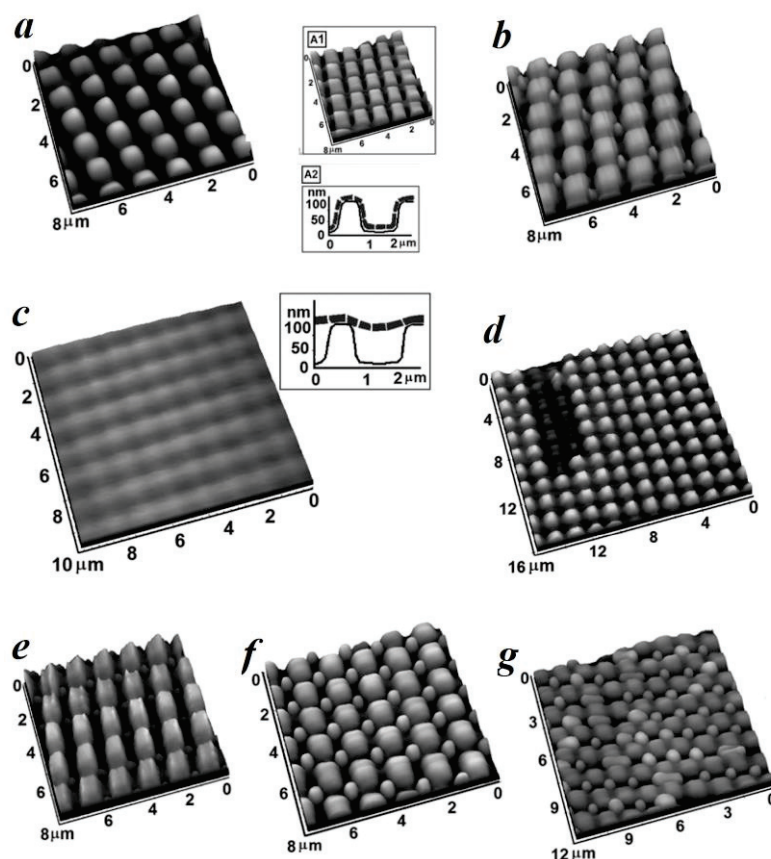


Figure 1. 17 (a) A floated PS film conformally adhering to a topographically patterned substrate, comprising an array of square pillars (inset **a₁**). Inset (**a₂**) shows the line profile of the substrate and the film. (b) A perfectly filled and ordered dewetted structure resulting from the dewetting of a 24 nm -thick film on the substrate shown in inset (**a₁**). (c) A 24 nm -thick floated PS film focally adhering to the same substrate as shown in (**a₁**). Inset shows the film (dashed line) in contact with the raised protrusions of the substrate only and freely hanging over other intervening areas. (d) The dewetted droplets are positioned on top of each pillar roof. (e) Imperfect ordering with some missing droplets for an 11 nm film, (f) perfectly ordered but underfilled structure formation for a 17 nm -thick film, and (g) distorted, overfilled structure with occasional oversized or interconnected droplets for a 31 nm -thick PS film.

II-4.2-Dewetting on chemically patterned substrates

While rubbing-based techniques are useful in demonstrating conceptually that isotropic dewetted structures can indeed be aligned [101], it is not feasible to obtain patterns with a high degree of accuracy in terms of periodicity, fidelity, precise control of morphology, and long-range order by merely extending any of these processes. An efficient method in this case is to use chemically patterned

substrates for dewetting a polymer thin film [96, 101-108]. Such substrates are typically processed by any of the existing lithography techniques, and thus pattern-directed ordering of dewetted structures is regarded as a hybrid approach, combining both top-down lithography and self-organization techniques. The ordering of dewetted structures on a chemically patterned substrate, comprising microcontact printed patches of hydrophilic 11-mercaptopundecanoic acid (MUA) on a gold-coated glass substrate was first illustrated by Meyer and Braun [107, 108]. The dewetting of a PS thin film on such a surface was seen to initiate only over the MUA patterns, which acted as preferred nucleation sites [107]. The dewetted structures aligned proportionally with the chemical patterns on the substrate [107, 108]. It was subsequently shown by Sehgal et al. that even on a chemically patterned substrate, the degree of ordering of the dewetted structures depends greatly on the commensuration between the initial film thickness and the periodicity of the patterned substrate. They described the dewetting of PS thin films on chemically patterned substrates comprising arrays of progressively narrower stripes (1–15 μm) of alternating $-\text{CH}_3$ (lower surface energy) and $-\text{COOH}$ (higher surface energy) end-terminated self-assembled monolayers (SAMs) [90] Fig1.18.

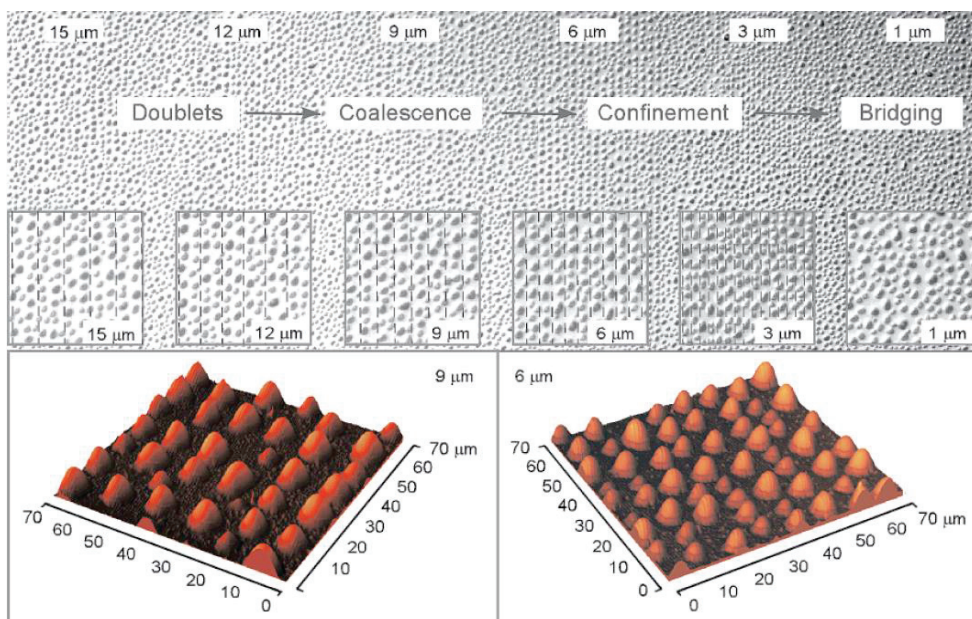


Figure 1. 18 Library of the late stage morphology of the droplet arrays with pattern dimension. OM images and insets show transition from the doublet state (15-12 μm), to coalescence (9 μm), confinement (6 and 3 μm), and a heterogeneous morphology (1 μm) with bridging over multiple bands. Dashed lines (insets) indicate registry with the underlying chemical pattern period. AFM images (9 and 6 μm) highlight control of droplet size and spatial position.

AL Akhrass et al. [88] have recently shown how a simple dewetting process of a thin polymer film on a chemically patterned substrate can transform a smooth layer of material into various structures. For this purpose, a combinatorial increasing of thickness was used. Fig 1.19 summarizes the variation of the dewetted pattern of hexagonally arranged non-wettable circular patches into a sequence of ordered three-dimensional topographies. Where holes followed by droplets with the shape of a spherical cap and finally toroids were generated. They demonstrated that the critical aspect responsible for this sequence

is the dewetted fluid collected the rim, characterized mainly by its width w . Thus, w may be considered as the crucial criterion determining the final 3D morphology. Further they showed that the volume V of the rim is exclusively determined by the dewetted distance and the thickness h of the film [88].

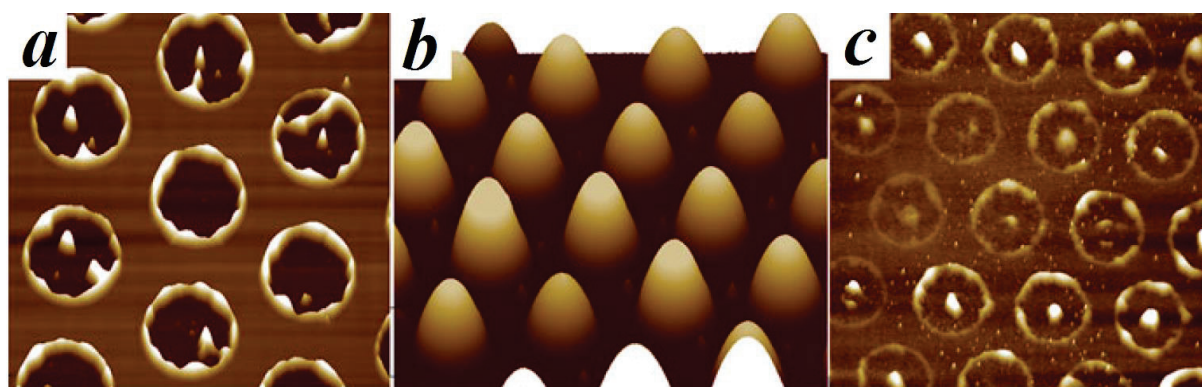


Figure 1. 19 (a) Topographic AFM image ($25 \times 25 \mu\text{m}^2$) of holes formed in a ca. 15 nm thick *PS120k* film. The height range is 100 nm . Holes are circular with both a diameter and a surface distribution identical to that of the imprinted domains pattern. (b) Topographic AFM image ($30 \times 30 \mu\text{m}^2$) of droplets formed in a ca. 50 nm thick *PS120k* film. The height range is 250 nm . The circular droplets with a diameter identical to that of the imprinted domains are distributed regularly on the substrate. (c) Topographic AFM image ($30 \times 30 \mu\text{m}^2$) of patterns formed in a ca. 90 nm thick *PS120k* film. The height range is 40 nm . Circular toroids with a diameter identical to that of the imprinted domains are distributed regularly on the substrate. These toroids at the periphery of the imprinted domains were generated by polymers remaining after dewetting at the boundaries of the domains.

III-Conclusion

We propose with this chapter a detailed analysis of a various approach of adhesion and friction phenomena. The effect of surface texturing on the mechanical behavior at the surface and the different approach used to chemically pattern the surface were provided. Then, a complete understanding of the thin liquid film principals and the dewetting phenomena on patterned surfaces were introduced. Basic concepts from hydrodynamic theories in the bulk situation and the frictional behavior at the interfaces were also reviewed. Hence, based on the above-mentioned literature, micro surface texturing has proven to be an effective means of enhancing the frictional and adhesion performances. Most of the studies investigated the effects of physically micro patterned surface with a very limited number of studies tackling the chemically patterned substrate. In this thesis, our goal was to gain a better understanding in the molecular mechanisms responsible for adhesion, friction and wetting at patterned interfaces. At first, we developed a general methodology to design well-defined surfaces combining micro-contact printing (μCP), self-assembled monolayers (SAMs) and polymer grafting techniques not only to control the geometrical and mechanical properties of surface, but also to precisely tune the surface energy using a broad range of functionalities. Then we used different characterizations approach from nano, micro and macro scale to investigate the mechanical behavior of this chemically patterned substrate. Therefore, Wettability, friction and adhesion measurements was carried out using a JKR apparatus, Friction machine, AFM and finally using the simplest technique the dewetting of thin polymer film. In the following chapter, we discuss the impact of chemically patterns geometry on the wettability and the

Chapter 1 Literature review

adhesion behavior at the surface. Furthermore, we introduce a novel set of experiments, which helps to consider whether the combination of surface patterning, self-assembled monolayer and grafting techniques can alter the surface wetting properties and thus change the tribological properties.

Chapter 2

Wetting and adhesion investigations of patterned surfaces

TABLE OF CONTENTS

I-INTRODUCTION	42
II-EXPERIMENTAL	42
<i>II.1-Sample Fabrication</i>	42
II.1.1-Photo lithography.....	43
II.1.2-Fabrication of PDMS stamps	43
II.1.3-Substrate Cleaning.....	44
II.1.4-Contact-printing of organosilane.....	44
II.1.5-Adsorption of PDMS on patterned surface (MTS/PDMS).....	45
II.1.6-Adsorption of PDMS on activated Si-wafer	46
II.1.7-Self-assembled monolayer on activated Si-wafer	46
<i>II-2-Experimental device: Design and construction of a Mini micro-contact printer (MμCP)</i>	46
II-2.1-Dewetting of Thin Polymer Film.....	47
II-2.2-Stamp Size	48
<i>II-3-Experimental device: Design and construction of a JKR Machine</i>	50
II-3.1-Brief outline of the classical JKR test	52
<i>II-4-AFM device PEAKFORCE QNM</i>	54
III-RESULTS AND DISCUSSION.....	56
<i>III-1-Patterns effect on the wetting behavior</i>	56
III-1.1- Wettability of smooth Substrates.....	57
III-1.2-Circular micro-structured Substrates (MTS/Si-OH)	59
III-1.3-Wettability of MTS/Si-OH patterned system.....	61
III-1.4-Anistropy wetting	64
III-1.5- Control of Adhesion by Contact Line pinning and depinning	64
<i>III-2-Patterns effect on the adhesive behavior</i>	67
III-2.1-Adhesion measurements using the JKR machine	67
III-2.1.a- JKR Adhesion measurements on smooth Substrates.....	67
III-2.1.b-JKR Adhesion measurements on MTS/Si-OH linear patterned system.....	71
III-2.1.c- JKR Adhesion measurements on MTS/PDMS linear patterned system.....	74
III-2.2-Adhesion measurements using the AFM PeakForce QNM.....	76
III-2.2.a- AFM Adhesion measurements on smooth non-patterned substrates.....	77
III-2.1.b- AFM Adhesion measurements on MTS/SiOH patterned surfaces.....	80
III-2.1.c- AFM Adhesion measurements on MTS/PDMS patterned surfaces.....	81
III-2.1.d-Multiscale comparative adhesive studies.....	83
IV- CONCLUSION	84

Chapter 2 Wetting and Adhesion Investigations of patterned surfaces

I-Introduction

In the last decades, surface texturing has proved to be a promising tool for controlling wettability [109-111] [1–4] and adhesion properties [65]. However, many challenges must still be tackled. In particular, there is still a lack of understanding on the role played by patterns on the wetting and adhesive phenomena arising from the interaction with the solid substrate. In fact, the problem of the contact line dynamics and drop motion on structured substrates has been investigated in a number of theoretical and numerical studies [112-115]. Thiele and coworkers [114, 116, 117], mentioned that the depinning process corresponding to the loss of stability of drops moving over a heterogeneous pattern has been studied in the limit of small contact angles and small wettability contrasts, with the emergence of a stick-slip motion during which the contact line jumps from one wetting defect to another [118, 119]. From the experimental side, the sliding of a drop on a chemically striped surface has been studied [113, 120, 121]. Nevertheless, knowing that a second patterned functionality may affect the macroscopic wetting. Another potential challenge can be advance: adhesion, where one component could be an adhesion promoter, while the second component conferred an additional property. In fact, the optimal feature size, shape and coverage needed to generate a specific surfaces for a particular applications has not yet been investigated.

This chapter has first sought to introduce the textured surfaces preparations and the multiple-scale approaches used to characterize wetting and adhesive properties of these samples. Secondly, the study has sought to explore the dynamics of a sessile drop on patterned solid surface, consisting of a periodic array of alternating hydrophobic and hydrophilic stripes with a large wettability contrast (about 70°). Hence, the stick-slip regime, the role of the energy balance, and the effect of the patterning at the mesoscale was investigated. Thirdly, in this research we explored the dependence of adhesion between a polymer and a rigid tip on the composition of the patterned substrates. Both a JKR test and an AFM test were employed to characterize the adhesion of an (hydrophobic/ hydrophilic) mixed silane (MTS/Si-OH) and a (hydrophobic/ hydrophobic) mixed polymer and silane (MTS/PDMS) covered surfaces.

II-Experimental

II.1-Sample Fabrication

The method for fabrication of micro-patterned surfaces is based on conventional molding of lithographically patterned templates contains two fabrication steps; photo lithography is used to fabricate a patterned template and modeling to transfer the pattern from the template to the sample material. The complete process of this conventional process is described in the following Fig.2.1.

Chapter 2 Wetting and Adhesion Investigations of patterned surfaces

First, a silicon wafer is coated with a photo resist. This resist is UV-exposed through a lithographic mask. Depending on the chemical properties of the photo resist, the pattern on the mask is transferred to the photo resist as a positive or a negative pattern. After several heat treatments, the resist is developed. This results in a patterned template that can be used as a mold. An optional step is a surface modification of the template after lithography, e.g. silanization with a fluorosilane, to prevent sticking of the sample material to the template during the following molding step. PDMS (Sylgard 184, Dow Corning) solution is then poured onto the template and cured to form an elastomer stamp. After inking, the stamp was brought into contact with the silicon substrate and withdrawn after a contact period; a patterned surface is obtained which can be processed further.

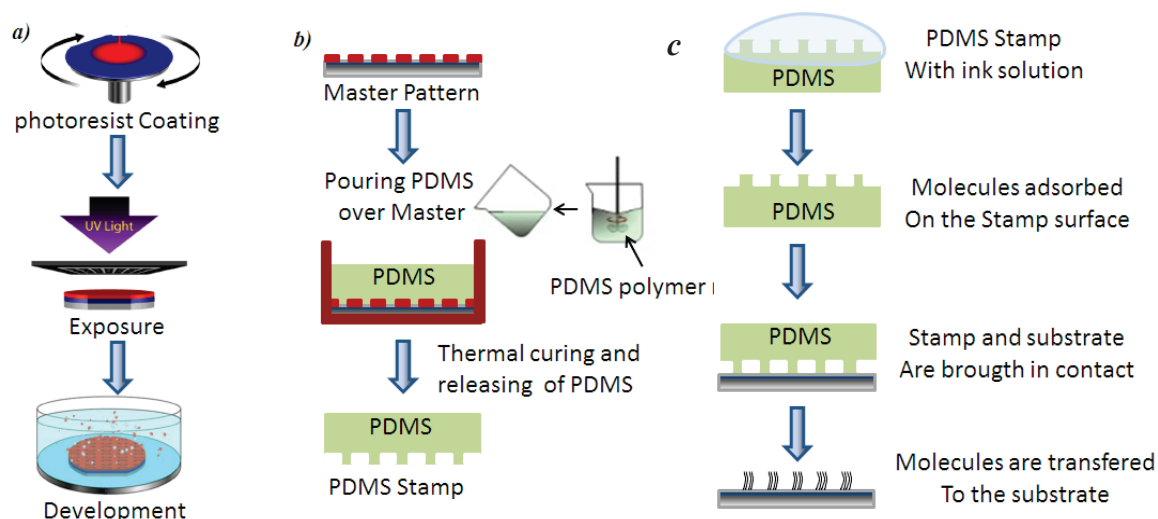


Figure 2. 1 (a) Master pattern development process using a photoresist. (b) Subsequent generation of the PDMS replication stamp. (c) Printing of self-assembled monolayers of trichlorosilane on the surface using μ CP.

II.1.1-Photo lithography

Photo lithography was performed in the clean room of the LTDS, École Centrale de Lyon, France. The negative photo-resist SU8 and the SU8-developer were purchased from MicroChem, USA. The SU8 was spin-coated onto polished silicon wafers (provided by Sil'tronix-ST, France) in a spin-coater. After thermal evaporation of the solvent in the resist, the coated wafers were exposed through a mask in a Mask-Aligner using a broad band UV-source. Then another heat treatment the samples were developed and rinsed in isopropanol. All thermal treatments were performed on a contact heating plate.

II-1.2-Fabrication of PDMS stamps

The stamps were fabricated from silicone elastomers. The elastomer was generated by mixing the Sylgard 184 elastomer base and curing agent according to a 10:1 ratio of pre-polymer and cross-linker. The mixture was then poured into an aluminum weighing dish containing a master template placed on the bottom of the dish. For stamps with a completely flat surface, the master was a piece of silicon wafer treated with FTS (as described below). Then, the mixture was cured at 130°C for 4 h, which is known

Chapter 2 Wetting and Adhesion Investigations of patterned surfaces

to be sufficient to achieve a polymerization state allowing reproducible adhesion measurements. Finally the elastomeric stamps were peeled away from the masters Fig.2.2.

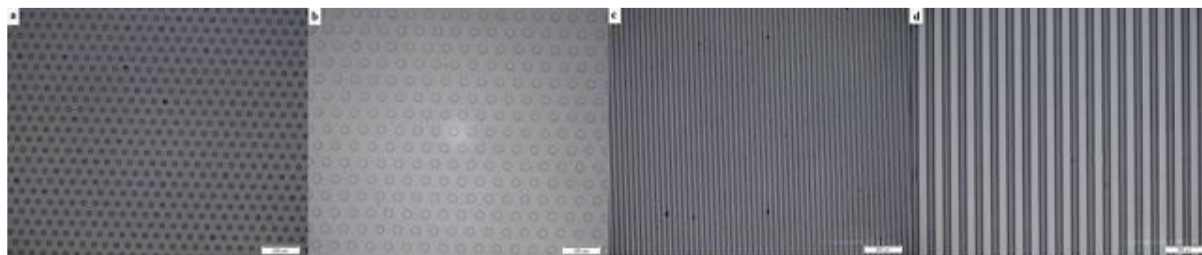


Figure 2. 2 Optical microscopic images of the PDMS stamps used for μ CP experiments. (a) 16 μ m spherical stamp, (b) 113 μ m spherical stamp, (c) 10 μ m linear stamp and (d) 45 μ m linear stamp.

II-1.3-Substrate Cleaning

Surface activation step is commonly used for cleaning, more importantly to create reactive silanol functional groups for subsequent surface functionalizations. Silicon wafers and glass slides were selected as substrates. Prior to μ CP, monolayer or grafting preparation, the silicon wafers were treated in boiling piranha solution (solution of 3:1 concentrated H_2SO_4 and 30% H_2O_2) for 30 min at 50°C. Then the silicon wafers were removed from the cleaning solution, rinsed with high purity water and dried in a stream of nitrogen until they appeared dry just prior to use for μ CP, SAM deposition or grafting technique.

II-1.4-Contact-printing of organosilane

For contact printing of MTS onto a silicon wafer, a 2 mM solution of MTS was prepared in HPLC-grade Toluene. After cleaning the PDMS stamp by toluene followed by drying under stream of nitrogen it was inked by the mixture prepared for about 20 seconds to spread the solution thoroughly over the surface of the stamp then it was dried under a stream of nitrogen. After drying, the stamp was brought into contact with the cleaned and oxidized silicon wafer for 20 s (under the pressure of the mini micro-contact printer device) and removed. Then, it was sonicated in toluene inside an ultrasonic cleaner for 2 min. The modified substrates were then dried with N_2 gas and characterized within 4 h. This same procedure was followed for each sample of silicon wafer by using different shaped and sized stamps Fig.2.3.

Chapter 2 Wetting and Adhesion Investigations of patterned surfaces

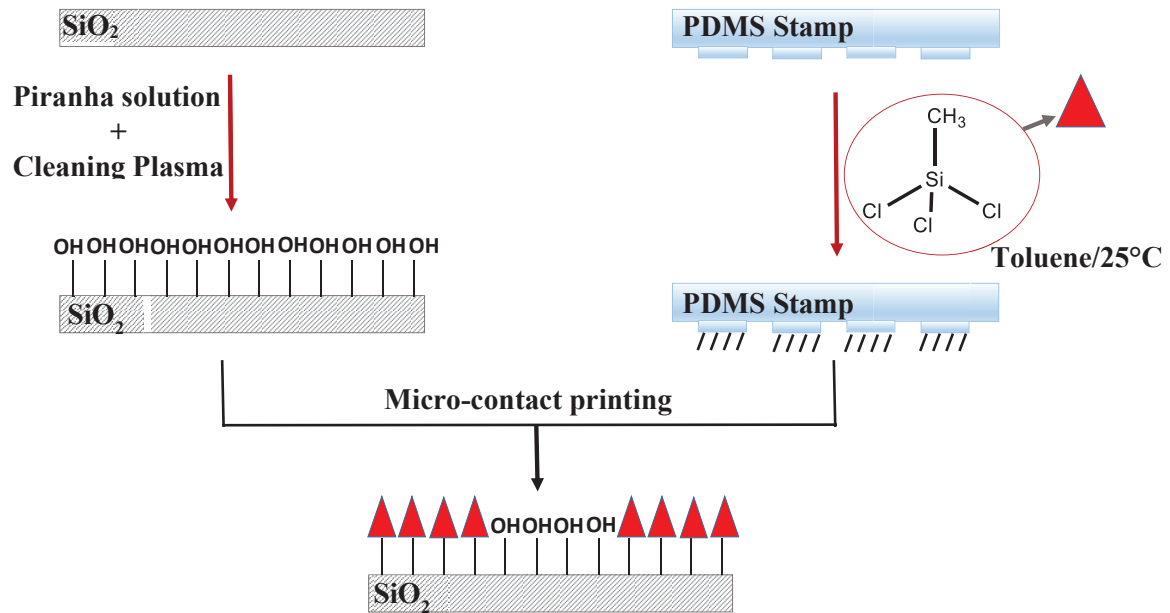


Figure 2. 3 Schematic outline of the procedure for patterning of alkylsiloxanes on the silicon surface.

These samples are used at first for the characterization of the patterning approach. Secondly, they were used for the preparation of (MTS/PDMS) textured systems.

II-1.5-Adsorption of PDMS on patterned surface (MTS/PDMS)

Considering the remaining unexposed area. PDMS ($M_w = 139 \text{ kg/mol}$) pre-polymer solution (in the form of a viscous liquid) obtained by diluting uncured PDMS by heptane solution was layered over the substrate surface and spin coated at 2000 rpm for 30 seconds. This causes the solution to spread uniformly in a thin film, typical thickness of spin coated films were (200-500) nm. Then the samples were placed in heater at 130°C for 4 hours after that the samples removed and cleaned in heptane solution for 2 hours to remove unphysisorbed PDMS that remained free after heating in order to have a homogenous uniform film of 11 nm thickness. In this case, even though the SAM and PDMS have the same surface functional property covered by $-\text{CH}_3$ group, but the viscoelastic properties of PDMS may cause different adhesion and friction characteristics. The experimental procedure is outlined in schematic form in Fig.2.4, micro-contact printed silicon surfaces were obtained by patterning of hydrophobic methyl alkyl silane onto hydrophilic surface region, and then another viscous PDMS (hydrophobic) was applied onto the remaining bare hydroxylated surface regions that created a monolayer of irreversible adsorbed PDMS with.

Chapter 2 Wetting and Adhesion Investigations of patterned surfaces

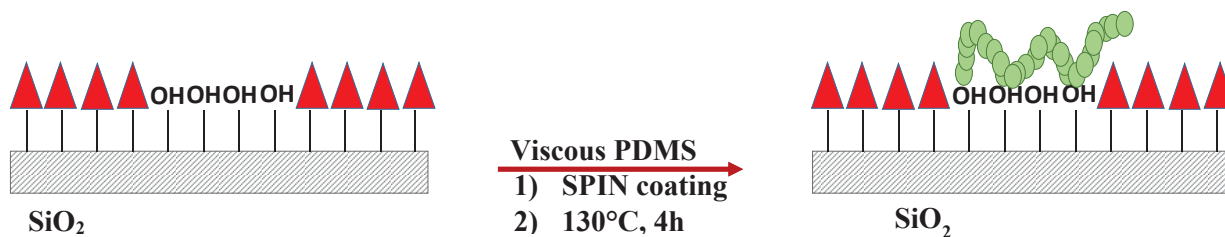


Figure 2. 4 Schematic outline of the procedure for grafting PDMS on the MTS/Si-OH patterned surface.

II-1.6-Adsorption of PDMS on activated Si-wafer

In our method, we spin-coated a 1% solution of PDMS (Hydroxyl terminated) in heptane to cover up the hydroxylated Si-wafer. To ensure the PDMS adsorption, the wafer was kept at a temperature of 130 °C for 6 hours. During such incubation, the PDMS molecules were adsorbed progressively more and more strongly by gradually bringing more segments per chain to the substrate where these segments could form hydrogen bonds with the hydroxyl groups of the substrate. This reaction finally leads to irreversible adsorption of the chains. The surfaces were then washed in a heptane bath for 2 hour to eliminate all the unadsorbed PDMS chains. Heptane being volatile at room temperature easily dried up from the PDMS adsorbed Si-wafer. Ellipsometric measurements showed that the dry thickness of the PDMS monolayer ($M_w = 139$ kg/mol) is in the range of 9-12 nm.

II-1.7-Self-assembled monolayer on activated Si-wafer

Self-assembled monolayers (SAMs) are thin films with a thickness of a single molecular layer. Silicon sample was prepared without stamp patterning, it was placed in the mixture of MTCS and toluene for 10 min. Then it was rinsed with toluene followed by 30 minutes of ultrasonic treatment in toluene, ultrasound is an efficient method for particle and aggregate removal by high frequency sound waves. Using this procedure an uniform and homogenous surface of self-assembled monolayers of methyl groups of 0.5 nm thickness were formed on silicon wafer specimen.

II-2-Experimental device: Design and construction of a Mini micro-contact printer (M μ CP)

In this thesis, we developed a small device to perform micro-contact printing. The apparatus was constructed to be small, easy to use and which requires very little manual handling. Further, the mini micro-contact printer allows for the easy, fast and simple micro patterning of several functionalities on the surface with a resolution ranging from 8 to 500 μ m.

Chapter 2 Wetting and Adhesion Investigations of patterned surfaces

The mini micro-contact printing device is a home built apparatus inspired from the micro-contact printer built by Okano et al [122]. Fig.2.5 presents a three dimensional graphic of the components of the mini micro-contact printer, where we can discern the presence of a stage on which the PDMS stamp is applied directly on the device.

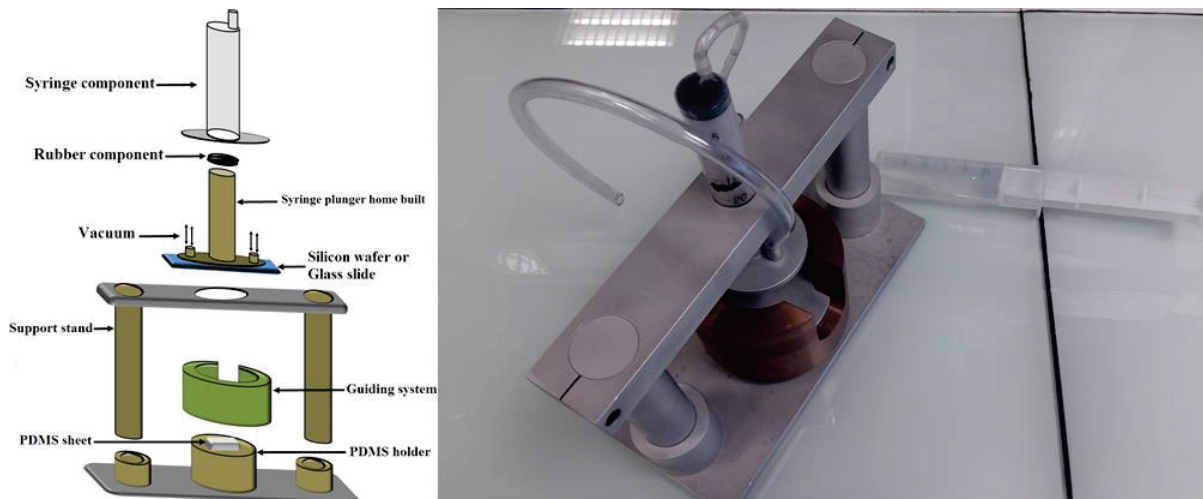


Figure 2. 5 A mini microcontact printer device. (a) Three-Dimensional Computer graphic of the components of the M μ CP. (b) Photograph of the M μ CP

A guiding system was placed to pilot the vertical movement during printing and assure the homogeneity of the patterns and a plunger with two holes related to a vacuum system holding the samples to the plunger. Furthermore, to move the plunger we use a simple hydraulic system where the fluid pumped through the syringes is water, which makes the preservation of the apparatus easier.

II-2.1-Dewetting of Thin Polymer Film

In this work, we used the dewetting as a fast and simple technique to characterize the patterns introduced on the surfaces (Fig.2.6). Thus, in the sample before annealing, Patterned MTCS was invisible underneath the PS film, due to the MTCS layer thickness, which was approximately a few angstroms. As soon as the film was annealed above T_g , PS began to dewet via nucleated holes at random locations on the MTS grid. In the first stages of annealing, roughly circular holes grew on the MTS zone until their diameter matched the width of the MTCS zone. In later stages of dewetting, the holes led to an ordered circular or linear shaped pattern of PS, it selectively dewetted the hydrophobic regions terminating in methyl groups, mirroring the underlying MTCS pattern after about 60 seconds from dewetting.

Chapter 2 Wetting and Adhesion Investigations of patterned surfaces

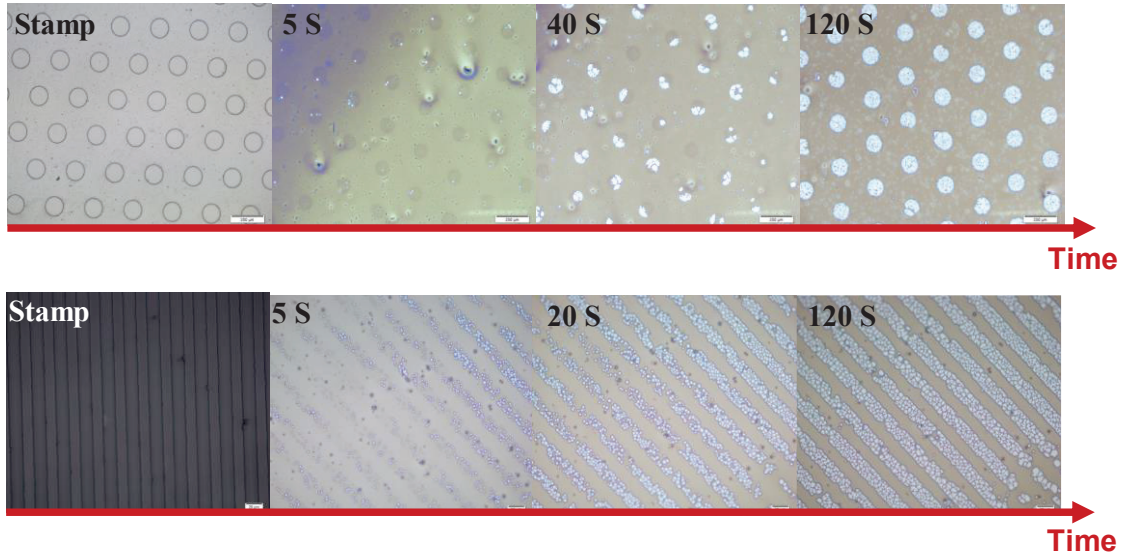


Figure 2. 6 Optical micrographs showing a typical real-time dewetting of a PS film (40 ± 0.2 nm) on a Si/SiO₂ patterned substrate. (a) Circular Patches of MTCS. (b) Linear Patches of MTCS.

As noticed in Fig.2.7, the result was a homogenous dewetted film in good agreement with the features of the PDMS stamp.



Figure 2. 7 (a) Optical microscopic image of the PDMS stamps used for μ CP experiments. 21 μ m circular (b) Optical microscopic images of a 21 μ m sized pattern of a dewetted PS film on a Si/SiO₂ patterned substrate. (c) A contrasted optical microscopic images of a 21 μ m sized pattern of a dewetted PS film on a Si/SiO₂ patterned substrate.

Following this procedure, we focused on several parameters that could affect surface properties; such as stamp size, surface ratio and the chemical entities.

II-2.2-Stamp Size

Considering the different stamp sizes and shapes, the results showed minor variation before and after stamp printing. The calculation of the surface area ratio $\alpha = f_{MTS}/f_{OH}$ (defined as the hydrophobic-to hydrophilic ratio) was extracted for numeric information about size differences. At first, using the hand pressure to stamp the textures on the surface, the Fig.2.8 (a-c) showed prior to stamp printing that as pattern size increases surface ratio remains constant. On the other side after stamp printing, surface ratio was determined after dewetting experiment, as illustrated in Fig.2.8 (b-d) surface ratio increases as the pattern increases.

Chapter 2 Wetting and Adhesion Investigations of patterned surfaces

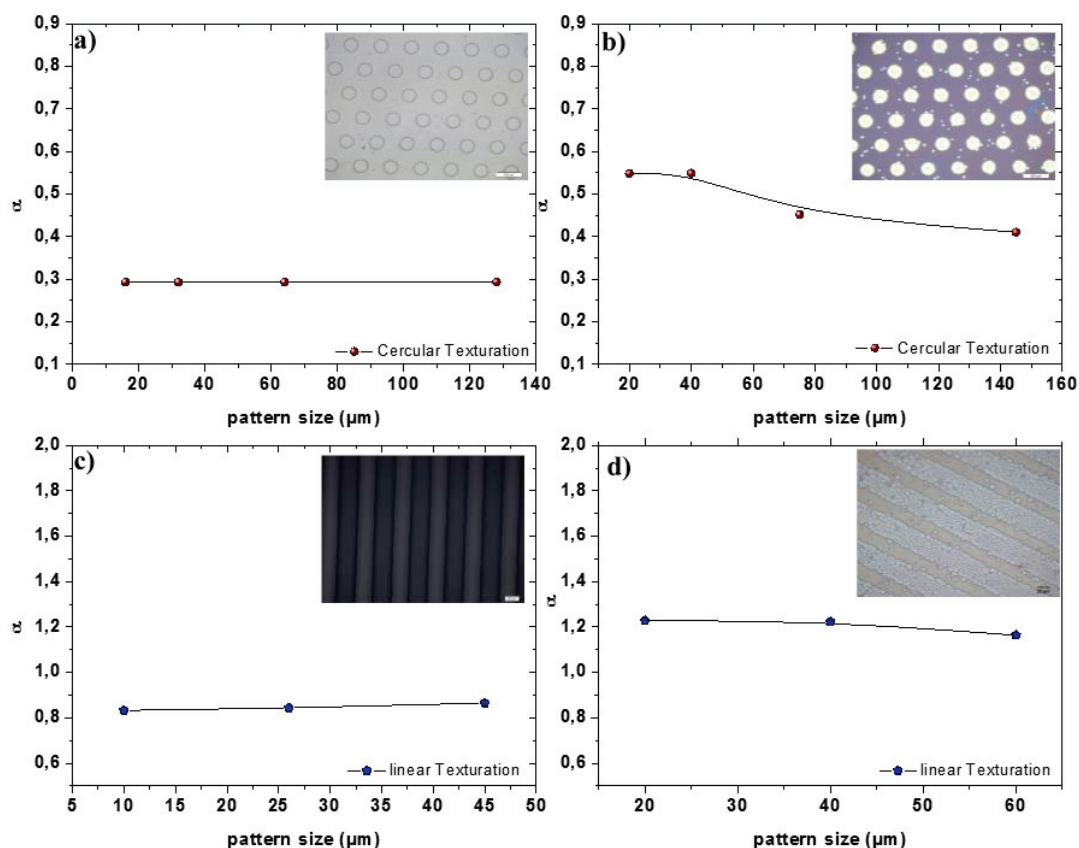


Figure 2. 8 On the left side, variation of fraction area as function of pattern size before stamp printing; **(a-c)** corresponds to an example of a selection on stamp of size 128 and 45 μm respectively circular and linear patterns that was made to measure surface. On the right side: Variation of fraction area as function of pattern size after stamp printing; **(b-d)** corresponds to an example of a selection on patterned surface with stamps of size 128 and 45 μm that was made to measure surface ratio.

Size variation as enlargement and irregularities on printed stamp could be due to uneven pressure exerted during printing, or unevenness of the stamp itself, to reduce the effect of having larger features, a more uniformly printing pressure should be adjusted, and the evenness of the stamp ensured by better control of its thickness. Diffusion is a problem with micro-contact printing, causing the features to be larger in the print than the features on the stamps. In order to make the patterns smaller, the diffusion of silane should be reduced. This could be done by regulation of printing times and the pressure exerted. For that, we used the new $M\mu\text{Cp}$ device to regulate the pressure and the printing time. Hence, Fig.2.9 (a-c) shows that micro-contact printing using the $M\mu\text{Cp}$ device provided us with similar patterns and constant surface area ratio as the PDMS stamp.

Chapter 2 Wetting and Adhesion Investigations of patterned surfaces

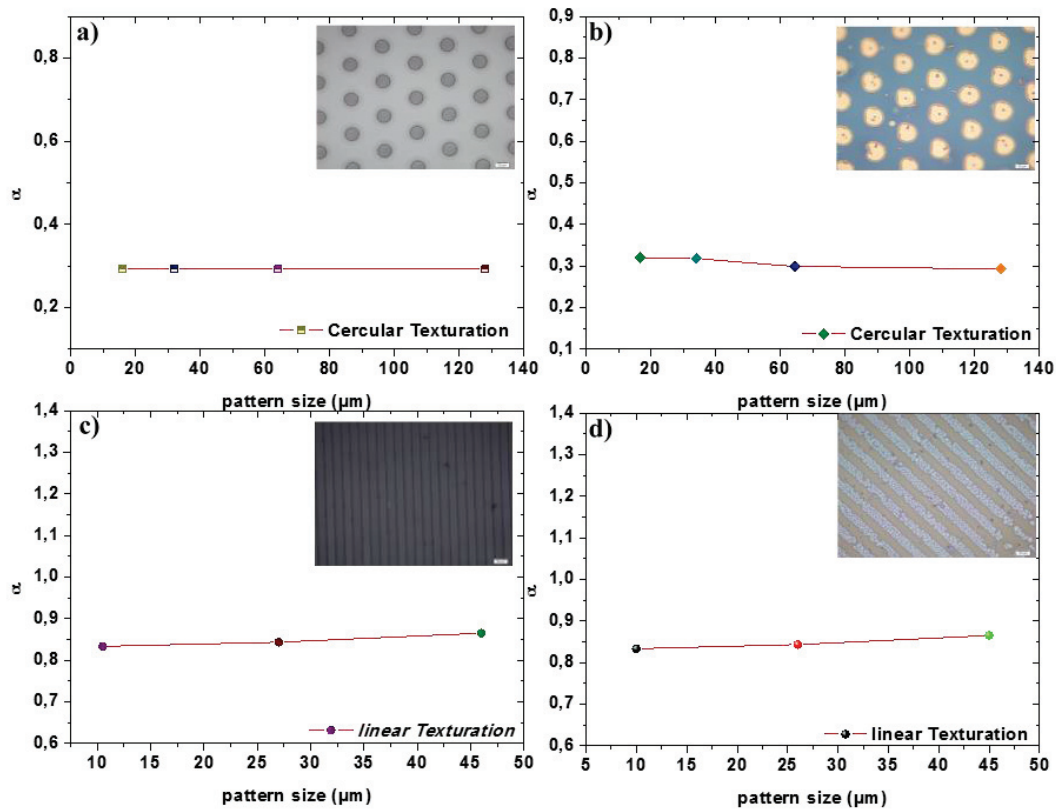


Figure 2. 9 Variation of fraction area α as function of pattern size before and after stamp printing.

As illustrated in (Fig.2.9), the ratio α remain constant following the pattern size, this means that we are texturing the surface in a complete agreement with the features of the stamps.

II-3-Experimental device: Design and construction of a JKR

Machine

The adhesion experiments are based on a protocol developed by Johnson, Kendall and Roberts (JKR). In JKR experiments, the contact area between a compliant PDMS deposited at the end of a flexible glass lever (the silicone elastomer naturally adheres to the glass) and a flat substrate is measured as a function of force during compression (approaching two surfaces) and decompression (separating two surfaces).

Chapter 2 Wetting and Adhesion Investigations of patterned surfaces

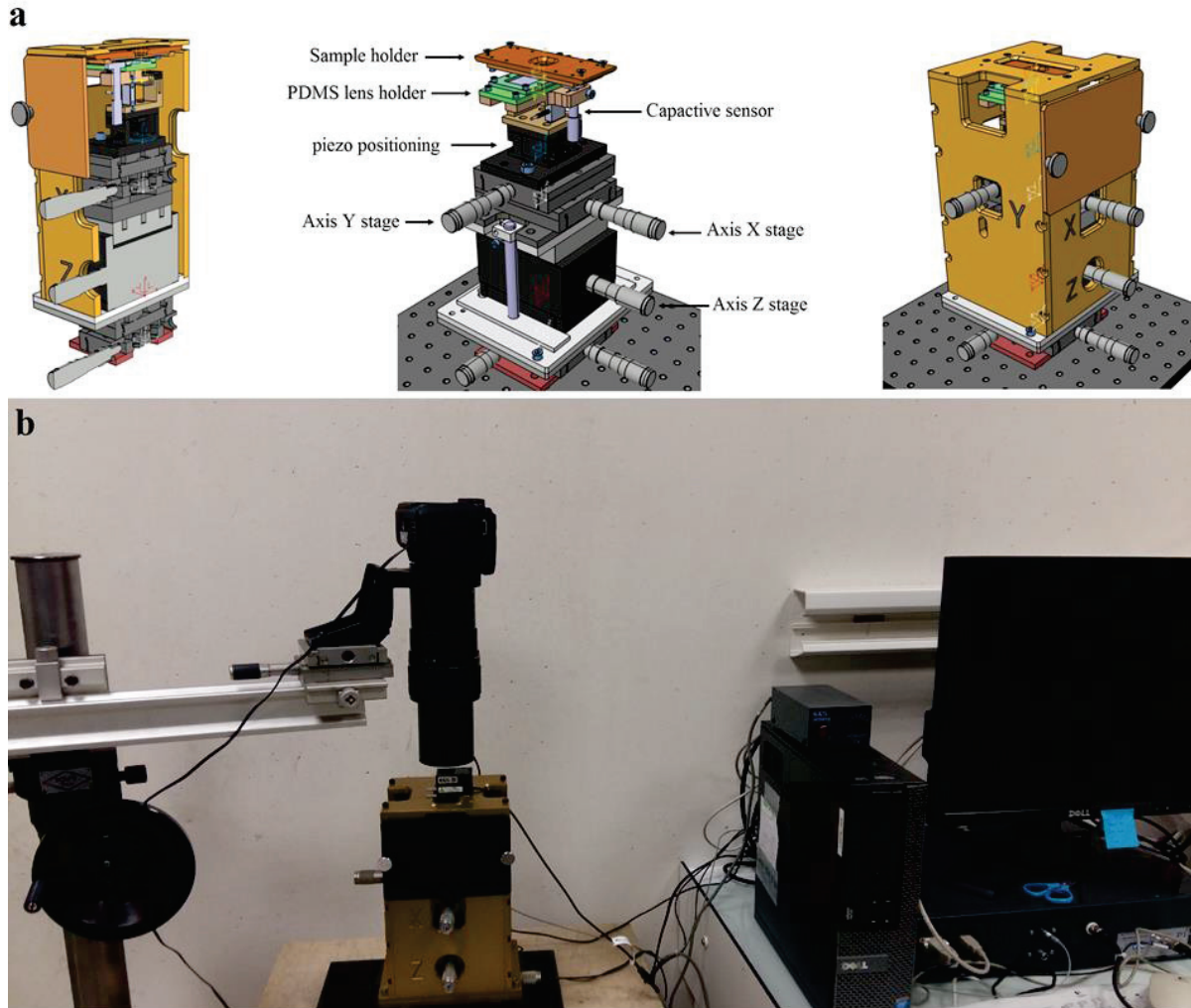


Figure 2. 10 (a) Three-Dimensional Computer graphic of the components of the JKR machine. **(b)** Photograph the JKR device.

An apparatus home-built in collaboration between LTDS/IMP was used. The apparatus is depicted schematically in Fig.2.10. A PDMS lens was attached to a microscope slide where it was secured to a translation stage and was moved down using a Newport micrometer operated with a piezoelectric drive (PI piezo positioning) until before the contact with the sample surface. The JKR machine was attached to a translation stage (Newport) and secured to an optical table (supported by the compressed air to minimize vibration). Thus, images of the contact area were taken in order to measure the contact area by an EOS 700D canon cameras, the Force applied and the pressing-in coefficient were measured in the same time. The objective is a standard 5X, MPE-65mm Canon objective. The camera was mounted on a Newport AD-100 translation stage through a post. The stage was held in place by a special heavy optical post. The analog output from the D700 camera was captured with a parallel USB port and recorded by a computer for later analysis. The Canon program was set for highest quality grey images at a resolution of 2592×1728 pixels. A typical micrographs of the contact spot is shown in Fig.2.11. The scale for every magnification or tube length was calibrated prior to data analysis. All the images were analyzed with LabVIEW Software Program. For the analysis, the contact radius, a , was calculated

Chapter 2 Wetting and Adhesion Investigations of patterned surfaces

either by using the total area of the contact spot which was obtained from the images assuming a circular area or by using an average diameter which was measured from the number of the pixels on the images. The two calculations were compared for the same image to ensure an accurate value of the radius. This analysis was repeated for every image that corresponds to a specific force. The force, F was recorded using a force sensor and the movement δ , was measured by a **E-852.10** signal conditioner electronics with PISeca™ capacitive sensor probes with a sub-nanometer position resolution, a bandwidths up to 10 kHz and output voltage range from -10 to 10 V. The readout from the capacitive sensor was recorded using the main-JKR LabVIEW Software Program. Furthermore, using several micrographs of the different lenses, the radii of curvature, R , of each lens were determined prior to contact using.



Figure 2. 11 A Photograph of a JKR measurement on a normal glass slide

II-3.1-Brief outline of the classical JKR test

The mechanics of the contact between two adhering bodies was described by Johnson, Kendall and Roberts in 1971 [12], giving rise to the so-called JKR adhesion test. This test has been widely used since then [123-125] as it provides a precise and relatively simple way to evaluate adhesion on local scales. We consider a sphere of radius R , with a Young's modulus E and a Poisson's ratio ν , placed in contact with a flat rigid surface. When a Force F is applied, a contact area of radius a is created and the deformation of the sphere in the center of the contact area is δ (δ is called the penetration depth).

In the absence of interfacial forces, F , δ , and a are given by the classical Hertz relations [126]:

$$F_H = \frac{K a^3}{R} \quad (3.2)$$

$$\delta_H = \frac{a^2}{R} \quad (3.3)$$

where K is an elastic constant defined by $K = 4E/3(1 - \nu)^2$.

In the presence of interfacial forces, the JKR predictions are [123-125]:

$$\delta = \frac{a^3}{R} + \frac{2F}{3aK} \quad (3.4)$$

$$G = \frac{(F - F_H)^2}{6\pi R F_H}. \quad (3.5)$$

Chapter 2 Wetting and Adhesion Investigations of patterned surfaces

where G is the strain energy release rate. At equilibrium, Griffith's relation [5] gives $G = W$, with W the thermodynamic work of adhesion. Equation (3.8) expresses the main idea of the JKR theory: due to the interfacial forces, the load required to create a given contact area is smaller than that predicted by Hertz. To this change in Force, at fixed a , is associated a change in δ . This effective unloading, a consequence of the interfacial forces, can be thought of as the unloading of a flat punch of radius a , under the force F , for which $\delta = 2F/3aK$.

These relations can be rewritten as

$$\delta = \frac{a^2}{R} - \sqrt{\frac{8\pi G a}{3K}} \quad (3.6)$$

$$F = \frac{Ka^3}{R} - \sqrt{6\pi K G a^3} \quad (3.7)$$

A JKR test is usually performed in three steps: firstly, the lens is placed into contact with the substrate and a compressive force is gradually applied. Between each force increment, the system is allowed to reach quasi-equilibrium. This compression step allows one to determine the stiffness K and the thermodynamic work of adhesion W of the system, as for an advancing contact, G reduces to W in equation 3.9:

$$\delta = \frac{a^2}{R} - \sqrt{\frac{8\pi W a}{3K}} \quad (3.7)$$

$$F = \frac{Ka^3}{R} - \sqrt{6\pi K W a^3} \quad (3.8)$$

Finally, the contact is broken by pulling the lens away. This can be achieved in several decompression steps: small pulling displacements are successively applied. After each displacement, the contact area recedes. During each of these relaxations of the contact area, the adhesion energy G can be obtained as a function of the advancing fracture velocity, from the continuous measurement of F and a , using equation (3.7). The adhesion test, strictly speaking, reduces to a decompression step. In fact, as both the compression and the decompression steps are described by the same equation (equation (3.9)) when the JKR analysis holds. We chose to work on the compression step alone for the mechanical modeling of the experiments on the thin layer systems: during this compression step, $G = W$, which, if W is known, makes easier the comparison between a model and the experimental results. All the JKR experiments were performed in an uncontrolled lab environment. Typical measurements were executed by shifting the position in 20 steps of $\sim 4 \mu\text{m}$ of 20 s intervals to a maximum position of $80 \mu\text{m}$ and then decreasing

Chapter 2 Wetting and Adhesion Investigations of patterned surfaces

the position in a similar fashion until pull off. The shift of the position was controlled by a (PI piezo positioning) piezoelectric drive. An image, penetration and force value were recorded at each step. After the images are analyzed as described above, the pseudo-contact radius ($A_n = a^{3/2}/\sqrt{6\pi R}$) was plotted as a function of the pseudo-force ($F_n = F/\sqrt{6\pi a^3}$) or from which the adhesion energy W_0 , Strain energy release G and the stiffness K , value was extracted (Fig.2.12)., $a_0^3 = 6\pi WR^2/K$ is the radius at zero load and $F_{pull-off} = -3\pi WR/2 = -3\pi R\gamma_{sv}$ is the pull-off force. Where, by definition, the reversible work of adhesion, W , is related to the surface energy, γ_{sv} , of the solids by $W = 2\gamma_{sv}$

$$\frac{a^{3/2}}{R} = \frac{1}{K} \frac{F}{a^{3/2}} + \sqrt{\frac{6\pi W_0}{K}} \quad (3.9)$$

$$\frac{F}{\sqrt{6\pi a^3}} = K \frac{a^{3/2}}{\sqrt{6\pi R}} - \sqrt{W_0 K} \quad F_n = \frac{F}{\sqrt{6\pi a^3}} \quad \text{and} \quad A_n = \frac{a^{3/2}}{\sqrt{6\pi R}} \quad (3.10)$$

$$F_n = K A_n - \sqrt{G K} \quad (3.11)$$

The slope of this fit gives K from the slope and the intercept gives W_0 and G from $\sqrt{W_0 K}$ using the predetermined K for both compression and decompression. Where K is the stiffness defined by $K = 4E/3$ and E is the Young's modulus defined by $E = 3K/4$

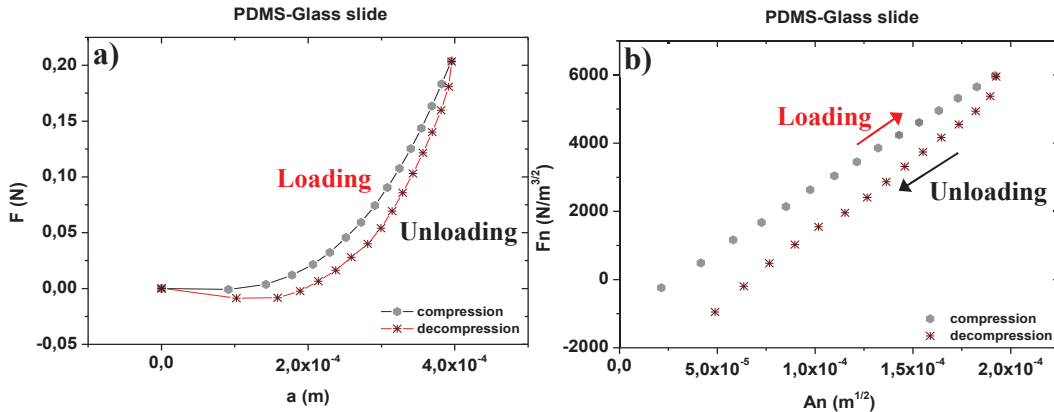


Figure 2. 12 Experimental data for a compression/decompression cycle on a glass slide. **(a)** The contact radius (a) versus the pseudo-force (F). **(b)** The pseudo-contact radius ($A_n = a^{3/2}/\sqrt{6\pi R}$) versus the pseudo-force ($F_n = F/\sqrt{6\pi a^3}$).

II-4-AFM device PEAKFORCE QNM

The atomic force microscope (AFM), invented in the early 1980's [127, 128], is now widely considered to be the instrument of choice for analyzing surfaces at the Nano- or, in some cases, atomic scale. This is mainly due to the ability of the technique to measure forces and distances at a very high resolution, and to explore non-destructively different surfaces in air or vacuum with minimal sample preparation.

Chapter 2 Wetting and Adhesion Investigations of patterned surfaces

In addition to characterizing topography, mechanical property measurements can be made by AFM-based semi-quantitative scanning techniques (i.e. force modulation [129] and tapping-mode phase imaging [130]) or by more time-consuming atomic force microscopy (i.e. force-distance curves [131]). In our case, all AFM measurements were performed using the PeakForce QNM mode with a Dimension Icon AFM from Bruker AXS . This mode was applied to measure surface topography and to quantify the various mechanical properties of the specimens. PeakForce QNM is an extension of the pulsed-force mode [132], with an improved force resolution of 10-10 N, which allows one to map adhesion, elastic modulus, deformation, or dissipation simultaneously at line rates of approximately 1 Hz. In the PeakForce QNM mode, force-separation curves are measured and analyzed pixel-wise. The maximum force (peak force) is controlled precisely each time the tip touches the surface. The elastic modulus of the sample was extracted by the Derjaguin-Muller-Toporov (DMT) model [13], which was proposed for force distance measurements that involve relatively weak adhesion forces and small tip-radii, and hence applies for the experimental conditions of this study. By definition, the DMT model fits the equation 2.13

$$F_{tip} - F_{adh} = \frac{4}{3} E^* \sqrt{R(d - d_0)^3} \quad (3.12)$$

to force-versus-separation data obtained when the tip is retracted from the surface after the approach (Fig.3.13).

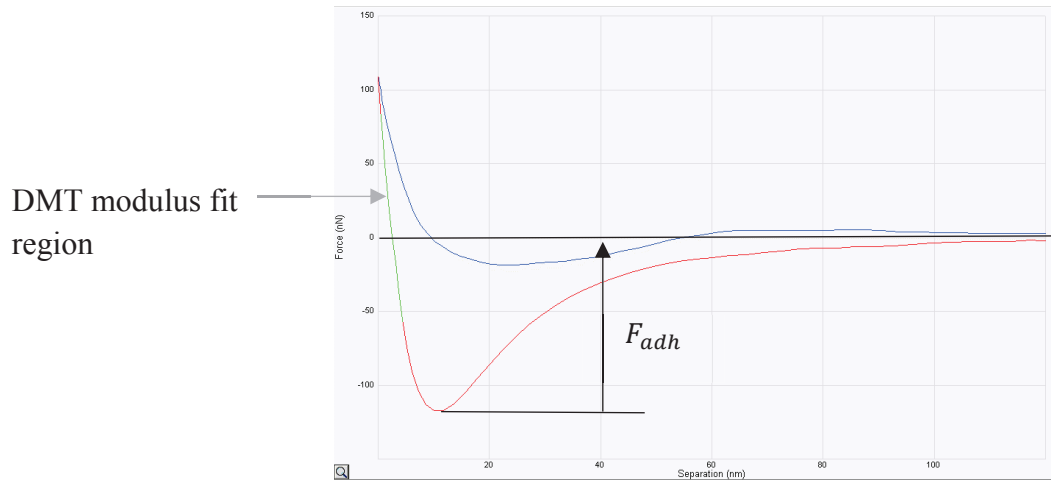


Figure 2. 13 Force versus Separation plot

This equation describes the relationship between the difference in the applied load and the adhesion force, $(F_{tip} - F_{adh})$, and the sample separation, $(d - d_0)$. Furthermore, R is the radius of the tip and E^* is the reduced modulus given by the formula:

$$E^* = \left(\frac{1 - \nu_s^2}{E_s} + \frac{1 - \nu_t^2}{E_t} \right)^{-1} \quad (3.13)$$

Chapter 2 Wetting and Adhesion Investigations of patterned surfaces

Where ν_s and ν_t are the sample's and tip's Poisson ratios and E_s and E_t the elastic moduli of the sample and tip, respectively. This technique covers a broad range of elastic moduli between 700 kPa and 70 GPa [133]. Nonetheless, quantitative measurements require calibration, either with a reference sample (relative method) or by measuring the cantilever tip radius and its spring constant (absolute method) [133]. Several additional mechanical properties can be obtained. The adhesion force at each contact point can be extracted from the vertical difference of the minimum force during retraction and the zero force in a force-distance plot. The deformation of the sample is assigned to the horizontal difference between the “peak force” tip-sample separation and the tip-sample separation corresponding to the onset of the overall repulsive force during an approach. A detailed description of the data quantification can be found elsewhere [134].

III-Results and discussion

III-1-Patterns effect on the wetting behavior

The contact angle was measured by the sessile drop technique and the surface free energy was evaluated from the static contact angle of 2 μ L water and methylene iodide droplets on the basis of the Owen's method [135] Fig.2.14. The Owens equation (3.14) was obtained from the extended Fowkes equation (3.15) the Young equation (3.16) and Dupré equation;

$$\gamma_{sl} = \gamma_{sv} + \gamma_{lv} - 2(\gamma_{sv}^d \gamma_{lv}^d)^{1/2} - 2(\gamma_{sv}^p \gamma_{lv}^p)^{1/2} \quad (3.14)$$

$$\gamma_{sv} = \gamma_{sl} + \gamma_{lv} \cos \theta \quad (3.15)$$

$$W_{sl} = \gamma_{lv}(1 + \cos \theta) = 2(\gamma_{sv} \gamma_{lv})^{1/2} \quad (3.16)$$

$$1 + \cos \theta = 2 \left[\frac{2(\gamma_{sv}^d \gamma_{lv}^d)^{1/2}}{\gamma_{lv}} + \frac{2(\gamma_{sv}^p \gamma_{lv}^p)^{1/2}}{\gamma_{lv}} \right] \quad (3.17)$$

where γ_{sv} , γ_{lv} , and γ_{sl} are the surface free energy of the solid, the surface free energy of the liquid, and the interfacial free energy between the solid and the liquid, respectively. The superscripts **d** and **p** refer to the dispersive force and polar force components.

Chapter 2 Wetting and Adhesion Investigations of patterned surfaces

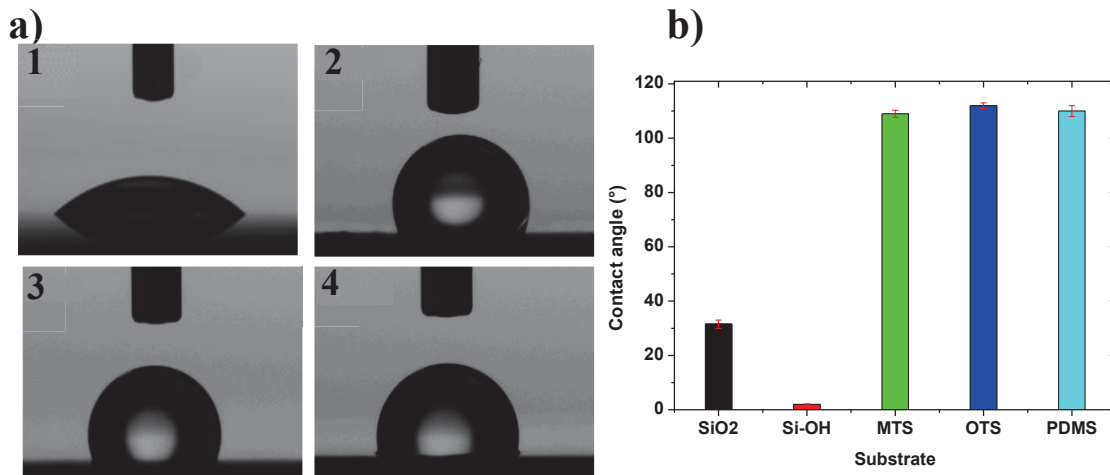


Figure 2. 14 (a) The left side shows several water contact angle measurements on substrate before and after treatment; (1) Silicon wafer, (2) Silicon grafted with adsorbed PDMS, (3) Silicon with self-assembled monolayer OTS, and (4) Silicon with self-assembled monolayer MTS. **(b)** The right side illustrate, water contact angle variation versus surface treatment.

III-1.1- Wettability of smooth Substrates

Comparing patterned and flat homogenous samples, the hydrophilic surface (silanol activated substrate) is observed to take on hydrophobic properties when patterned. This indicates a contribution of an increased surface area and the creation of a heterogeneous interface. Furthermore, the spreading ability of the droplet on the patterned surface was monitored, where it appears that the microstructures inhibit spreading over an extended time. Using the surface energy along with contact angle obtained experimentally, we are able to determine the spreading coefficient of water on the flat homogenous surface.

$$S = \gamma_{lv}(\cos \theta - 1) \quad (3.18)$$

Substrate	θ_e°	$\gamma_{sv_{tot}}(mJ/m^2)$	$S (mJ/m^2)$	$W_0(mJ/m^2)$
SiO ₂	31,5	65,8	-10,61	133,39
Si-OH	< 2	78,1	-0,044	145,55
MTS	109	24,7	-95,44	50,94
OTS	112	22,4	-98,97	45,028
PDMS	110	24,1	-96,62	47,37

Table 2 Wetting Behavior of a Water Droplet on non-patterned Surfaces

Where the negative value of S indicates the partial wetting state of the surface as shown in Tab 2.

Considering now the case of a patterned substrate with a periodic textures made of two different materials (hydrophobic layer MTS and hydrophilic layer OH). This system was used as an approach for studying the influence of the surface texturing on the wetting behavior of the surface. Several system

Chapter 2 Wetting and Adhesion Investigations of patterned surfaces

has also been studied experimentally, precisely in the context of contact angles and Cassie's empirical law [21]. This law mentions that the contact angle θ of a macroscopic drop placed on a planar heterogeneous substrate satisfies

$$\cos \theta = \sum_i f_i \cos \theta_i \quad (3.19)$$

where θ_i is the contact angle of a droplet on a (pure) material of type i , and f_i is the fractional area of the substrate made of that material. In our case, we applied the Cassie model to illustrate the dynamic of the contact angle.

$$\cos \theta = f_{MTS} \cos \theta_{MTS} + f_{OH} \cos \theta_{OH} \quad (3.20)$$

Where we can calculate f_{MTS} and $f_{OH} = 1 - f_{MTS}$ for the 2D hexagonal (circular pattern) system using these dimensions (the ratio of circular pattern area to the unit cell area $\frac{\pi D^2}{2\sqrt{3}L^2}$ where D is the pattern diameter and, L , is the centre to centre spacing) and in the case of the linear pattern $f_{MTS} = \frac{D}{L}$ (Fig.2.15).

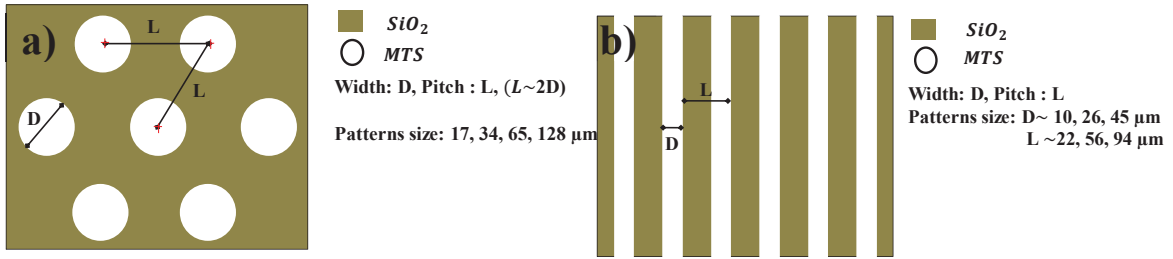


Figure 2. 15 (a) Schematic of a circular patterned surface of MTS/Si-OH. **(b)** Schematic of a linear patterned surface of MTS/Si-OH. Notations D and L denote the patterns size and pitch.

To investigate whether the wettability of patterned surface is governed by a distinct mechanism, we introduce the hydrophobic-to hydrophilic ratio, defined as a dimensionless parameter α given by equation 3.21:

$$\alpha = \frac{f_{MTS}}{f_{OH}} \quad (3.21)$$

Where $W_{CH_3} = D$ and $W_{OH} = L - D$ are the hydrophobic and hydrophilic area widths respectively. In our experiments the ratio α varies between 0.29 and 1.2, where $\alpha < 1$ and $\alpha > 1$ correspond to more hydrophilic (circular pattern) or hydrophobic surfaces (linear pattern), respectively.

Chapter 2 Wetting and Adhesion Investigations of patterned surfaces

III-1.2-Circular micro-structured Substrates (MTS/Si-OH)

At first, an smooth patterned surface with cylindrical patterns (MTS/Si-OH) is assumed, along with a complete contact between the liquid and solid. In this situation, we applied the Cassie model to understand the dynamic of the contact angle.

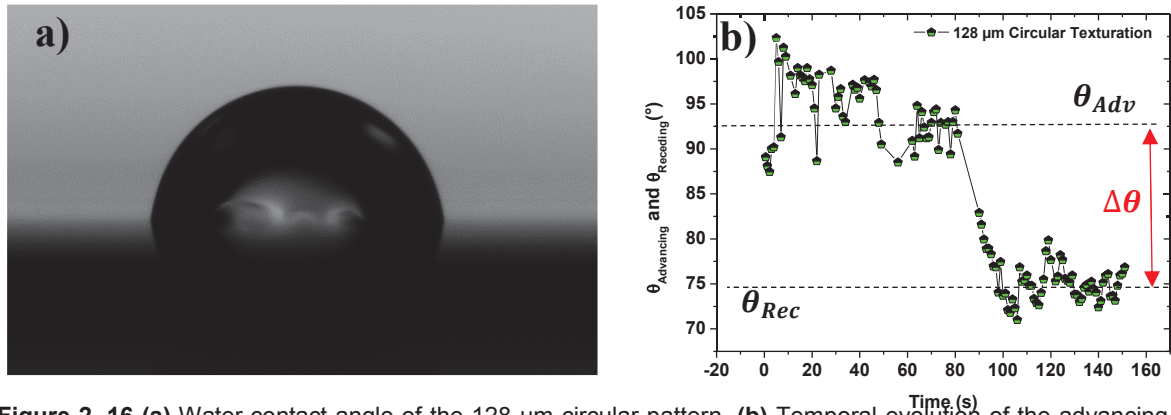


Figure 2. 16 (a) Water contact angle of the 128 μm circular pattern. **(b)** Temporal evolution of the advancing and receding contact angles for water drops of varying drop base diameter (1-6 mm).

Hence, we measured simultaneously the equilibrium contact angle both parallel θ° of 2 μL water drops for the patterned surfaces. The contact angle is the averaged value measured for at least five droplets deposited on different regions on the substrate and the error is their standard deviation. Furthermore, to understand more about the influence of the patterns sizes on the wettability response of the patterned substrates, the contact angle hysteresis was measured. The advancing and receding contact angles for liquid drops (deionized water) of varying drop base diameter (1-6 mm) are measured (Fig.2.16).

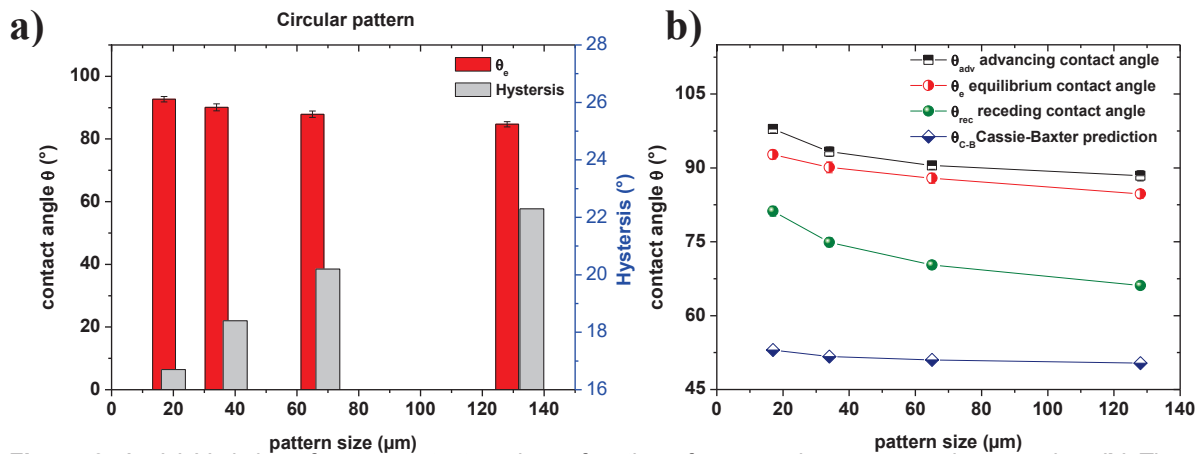


Figure 2. 17 (a) Variation of water contact angle as function of pattern size versus real stamp size. **(b)** The evolution of the equilibrium contact angle, hysteresis and Cassie Baxter predicted value as function of the pattern, size.

Fig.2.17 (a) shows the evolution of the water contact angle as function of the pattern size. A negligible decrease of the contact angle due to the change of the area fraction after pattern printing. Additionally, a regular decrease of the hysteresis with the pattern size was observed. This change can be anchored to

Chapter 2 Wetting and Adhesion Investigations of patterned surfaces

the increase of the homogeneity of the printed surface with the decrease of pattern size. Therefore, as reported in Fig 2.15 (b) the contact angles on the cylindrical patterns were higher ($30^\circ - 35^\circ$) than those the theoretical prediction calculated through the Cassie-Baxter equation and the asymmetry is more pronounced in the case of the more hydrophilic surfaces [24]. The discrepancies between the experiments and typical equilibrium approaches can be probably attributed to the unaccounted role of contact line distortion on real heterogeneous surfaces. In fact, the influence of asperity of the patterned surface on wetting can be neglected due to the low height difference between the MTS and Si-OH zone, confirming then the predominance of the surface chemistry on the wetting behavior. This asymmetry can be illustrated by considering the advancing and the receding contact angle behavior. In fact, following the contact angle hysteresis, we know that contact line pinning occurs because there is an energy barrier for the drop to move onto a hydrophobic area, while the contact line jumps when it reaches a new hydrophilic region. Therefore, it's expected to observe stick behavior when the contact line reaches un-wetted hydrophobic parts of the surface. Then, slip when it moves across partially covered hydrophobic portions, and jumps as the contact line reaches the hydrophilic areas. This is indeed mentioned in the lattice studies of using Boltzmann simulations [119].

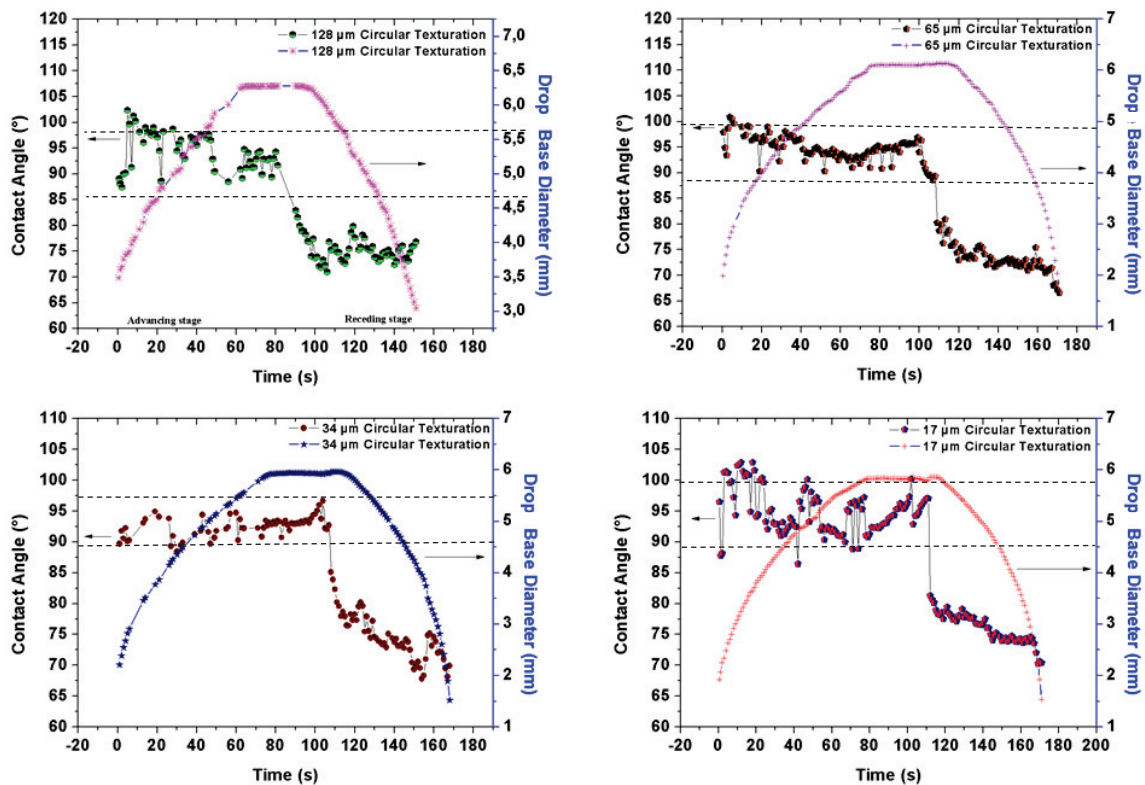


Figure 2. 18 Temporal evolution of the contact angle and the drop base diameter for an advancing and receding stage experiments on circular patterned surfaces.

Contact angle and drop base diameter for the circular patterned surfaces are illustrated in Fig.2.18 for four different sizes of patterns (17, 34, 65, 128 μm). There is clear stick–slip behavior to the baseline

Chapter 2 Wetting and Adhesion Investigations of patterned surfaces

evolution and simultaneous stick–slip behavior for the contact angle. Here it is clear that there are two phenomena-taking place alternately; an advancing phase followed by a pinning phase, with the highest contact angle being associated with pinning and depinning at the feature. In fact, the oscillations are large, even for small patterns. The Stick–slip effect was observed in all cases over the range of the water droplets studied for the different circular patterned surfaces. The stick–slip or pinning–depinning behaviour may be associated to a competition of the unbalanced Young force and the anchoring force of the defect. Hence, when the unbalanced Young force overcomes the pinning force of the defect, the contact line slips. This implies a threshold value of the force to overcome this pinning barrier. Furthermore, during the receding stage, the contact angles displace some evidence of stick–slip behavior for these surfaces but it is less clear and less reproducible. This may be also explained by the possible diffusion of the MTS molecules to the SiOH regions during the printing process. This behavior may induces a significant change in the real surface area ratio α .

III-1.3-Wettability of MTS/Si-OH patterned system

Let's consider now the linear patterns (MTS/Si-OH), the contact angle as measured for a liquid with the three phase contact line parallel to the strips should be equal to the theoretical value predictable by the Cassie equation 3.21. The analysis of the system becomes more complicated for strips of larger dimension, several microns and more. The total free energy of the system may depend on the position of the three-phase contact line (i.e., at which strip type, hydrophilic or hydrophobic, and at what distance from the boundary between the hydrophobic and hydrophilic strips). Under these circumstances several different contact angles are possible (including the thermodynamic equilibrium contact angle, which the Cassie equation predicts) [120, 136].

Chapter 2 Wetting and Adhesion Investigations of patterned surfaces

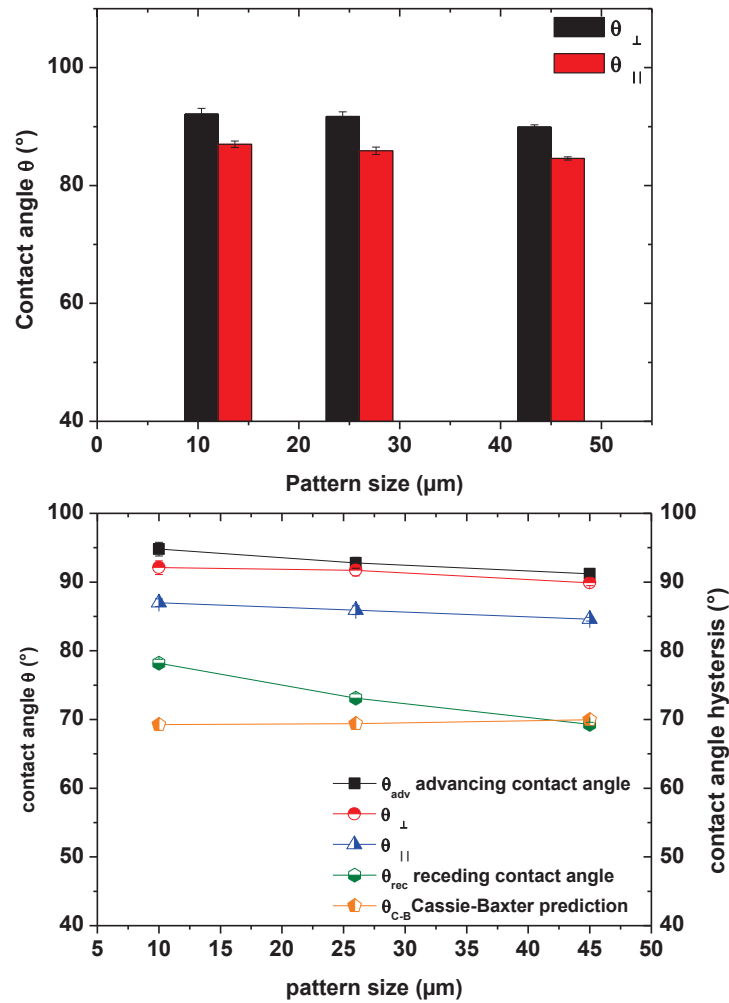


Figure 2. 19 Variation of water contact angle hysteresis versus real stamp size. (a) Circular patches. (b) Linear patches.

As reported in Fig.2.19 (a), we measured simultaneously the equilibrium contact angle both parallel $\theta_{\parallel}^{\circ}$ and perpendicular θ_{\perp}° to the stripes of 2 μL water drops for the linear patterns. The contact angle evaluation is the mean of the values measured for at least 5 independent droplets deposited on different positions on the surface and the error is their standard deviation. In fact, due to the same fractional area of the printed pattern, a similar contact angle was observed. In fact, these results were compared with contact angle values predicted by the Cassie equation. The static contact angles with contact lines situated orthogonal or parallel to the line were found to be higher ($15^{\circ} - 20^{\circ}$) than the values predicted by the Cassie equation [120, 136] Fig.2.19 (b). Furthermore, to understand more about the impact of the hydrophobicity on the wettability properties of the surface, the contact angle hysteresis was performed. The advancing and receding contact angles for liquid drops (deionized water) of varying drop base diameter (1-6 mm) are measured.

Chapter 2 Wetting and Adhesion Investigations of patterned surfaces

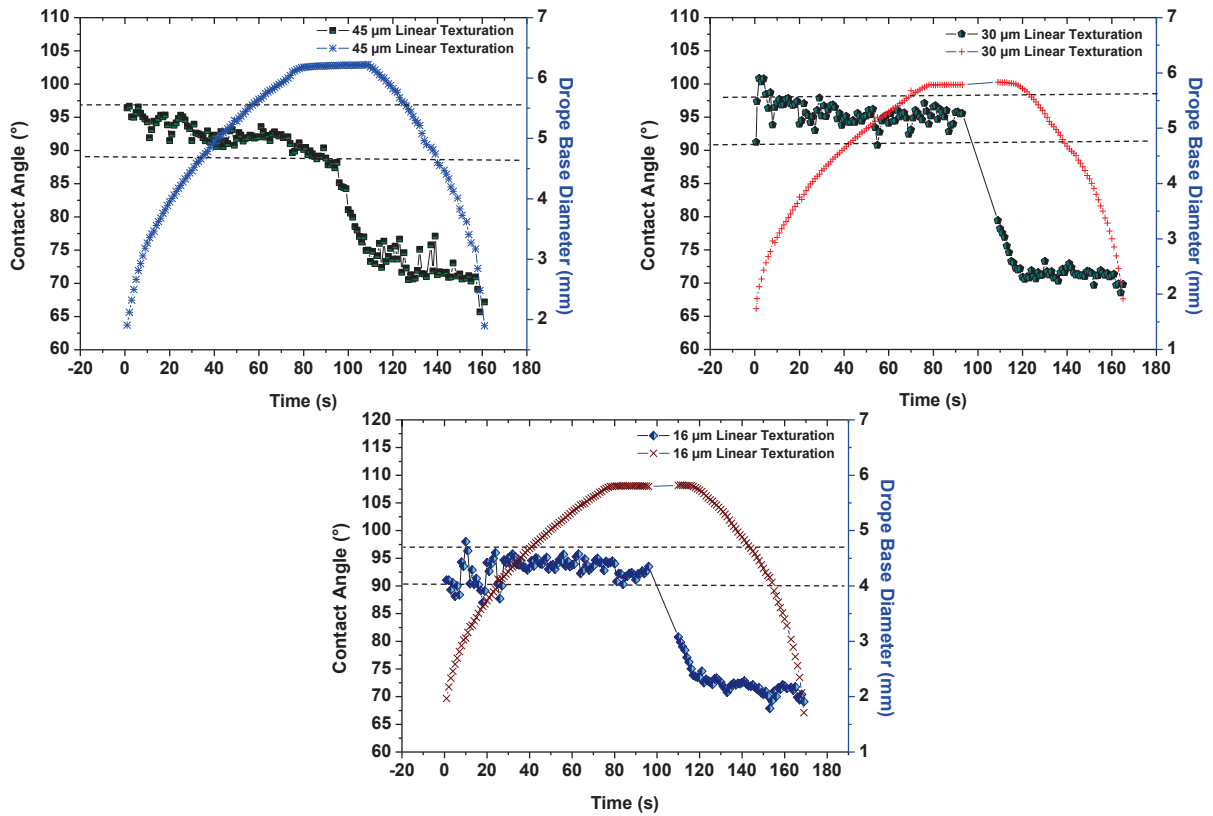


Figure 2. 20 Temporal evolution of the contact angle and the drop base diameter for an advancing and receding stage experiments on linear patterned surfaces.

Fig.2.20 shows the temporal evolution of the contact angle θ_A and θ_R and the drop base diameter for three different sizes of linear patterns (10, 26, 45 μm). Moreover, there appears to be only a small fluctuation to the baseline evolution and the measured contact angle for the 10 μm and the same behavior is observed for the contact angle. This implies that the defects are acting to introduce another wetting phenomenon, associated with intermittent pinning and depinning at the defect, and the observations are a result of the combined advance and of the pinning. For the larger patterns sizes, a clear step-like behaviour to the baseline evolution and simultaneous stick–slip behaviour for the contact angle. As explained above. The pinning–depinning behaviour may be explained by the struggle between the unbalanced Young force and the anchoring force of the defect.

Drelich et al.[137] have proposed that the line tension (τ) as a cause of the anisotropy of the contact angle. The line tension (τ), that is, the excess free energy of a solid-liquid-vapor system per unit length of the contact line, is described using a “modified Young equation” (3.22).

$$\gamma_{sv} - \gamma_{sl} = \gamma_{lv} \cos \theta + \frac{\tau}{r} \quad (3.22)$$

Equation 3.23 relates the variation of the apparent contact angle (τ) to the contact line radius (r) and shows that the wetting phenomena strongly depend on the droplet size. Drelich et al. suggested assuming

Chapter 2 Wetting and Adhesion Investigations of patterned surfaces

the value of τ to be -1×10^{-8} to $-1 \times 10^{-9} \text{ Jm}^{-1}$, a value that was believed to be reliable at the time. However, recently, Pompe et al.[138] successfully estimated the reliable τ value ($-1 \times 10^{-10} \text{ Jm}^{-1}$) by scanning probe microscopy measurements, then measuring the contact angles and curvatures of a micron-sized water droplet deposited from the aerosol phase. Their value suggests that the effect of the line tension is very negligible. Furthermore, the effects of asperity of the patterned surface on wetting are considered. In the present study, the effects of asperity of the patterned surface on wetting must be ignored because the height difference between the MTS and Si-OH areas is <6 nm. Furthermore, the surface roughness (Ra) of homogeneous and MTS/Si-OH patterned surfaces as measured by an AFM ranged from 0.5 to 0.6 nm; as such, the anisotropic wetting in the present study would only be governed by surface chemistry.

III-1.4-Anistropy wetting

Moffat et al. [139], Shanahan and Sefiane [140], demonstrates that a pinned drop (which deviates from equilibrium) increases its excess free energy up to a level where the drop “slips” to a new point on the surface where it “sticks”. Duursma et al. [141] and based on these multiple studies attributed the stick–slip behavior to the process of intermittently overcoming an energy barrier, assuming that this maximum can occur when the contact angle deviates the most from the process base angle. In our case, knowing that the surface chemistry control the wetting behavior, the assumption of using the energy barrier at the contact line as it jumping between these maxima and minima could be apply on our surfaces. In fact, under the thermodynamics equilibrium conditions, the shrinking of the free energy defines the wetting of the system. Hence, the variation in free energy can be attributed to the interactions in interfacial areas.

III-1.5- Control of Adhesion by Contact Line pinning and depinning

Let’s consider know the adhesive behavior of textured surfaces with the same fractional area of an (hydrophobic/hydrophilic) system. Fig.2.21 shows that as the patterns size decrease the work of adhesion deduced, using young equation decreases. In fact, when a polar liquid such as water contacts a surface, polar molecule in the region of the surface will rearrange or reconstruct, allow solvent penetration, and facilitate the migration of polar groups toward the water-surface interface. Therefore, the pendant hydroxyl groups grafted on the surface will be oriented and buried away from the solid-gas interface. However, because of the strong interaction with water at the solid-water interface, the

Chapter 2 Wetting and Adhesion Investigations of patterned surfaces

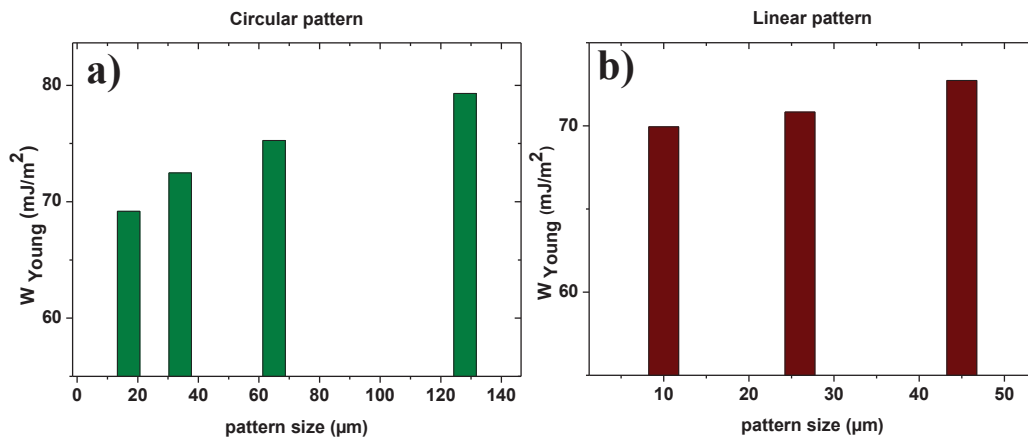


Figure 2. 21 (a) Young adhesion energy as function of the circular pattern size. (b) Young adhesion energy as function of the linear strips size for the MTS/Si-OH systems.

hydroxyl groups will cause surface reconstruction, which will result in the formation of interfacial, hydroxyl hydrogen bonds with water, increasing then the work of adhesion. In our case, where the presence of hydrophobic patterns on a hydrophilic system (MTS/Si-OH) induces a jump of the contact angle line between these two proprieties, suggest that the scaled energy barrier can be added to the work of adhesion inducing then the increase of the adhesive response. Another mechanism can be advanced: the probable contamination of the Si-OH layer by the excess MTS deposited by the stamp. Thus, this approach can explain the increase of the work of adhesion with pattern size.

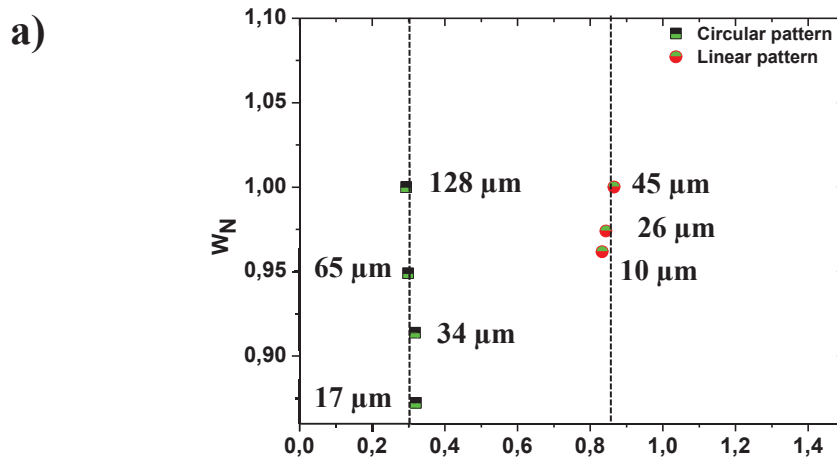


Figure 2. 22 (a) Normalized adhesion energy as function of the α parameter for the different circular and linear patterned surfaces for the MTS/Si-OH systems.

In order to identify a universal behavior, we use a normalized work of adhesion W_N , to quantify the adhesion for all the pattern surfaces as a function of pattern size. Fig.2.22 summarizes these results in terms of normalized $W_N = W_{Pattern}/W_{max}$, where the energy adhesion values are normalized by the values for the maximum thermodynamic work of adhesion displayed by the biggest patterns. The results demonstrate that the response is not universal for all the patterns and suggest that the adhesion is not a

Chapter 2 Wetting and Adhesion Investigations of patterned surfaces

consequence of the changes in the surface density, (or in our case, this area fraction α). As we observe in Fig.2.22 , that the pattern geometry and size could plays a significant role in controlling adhesion and can be used as an effective parameter in interfacial design.

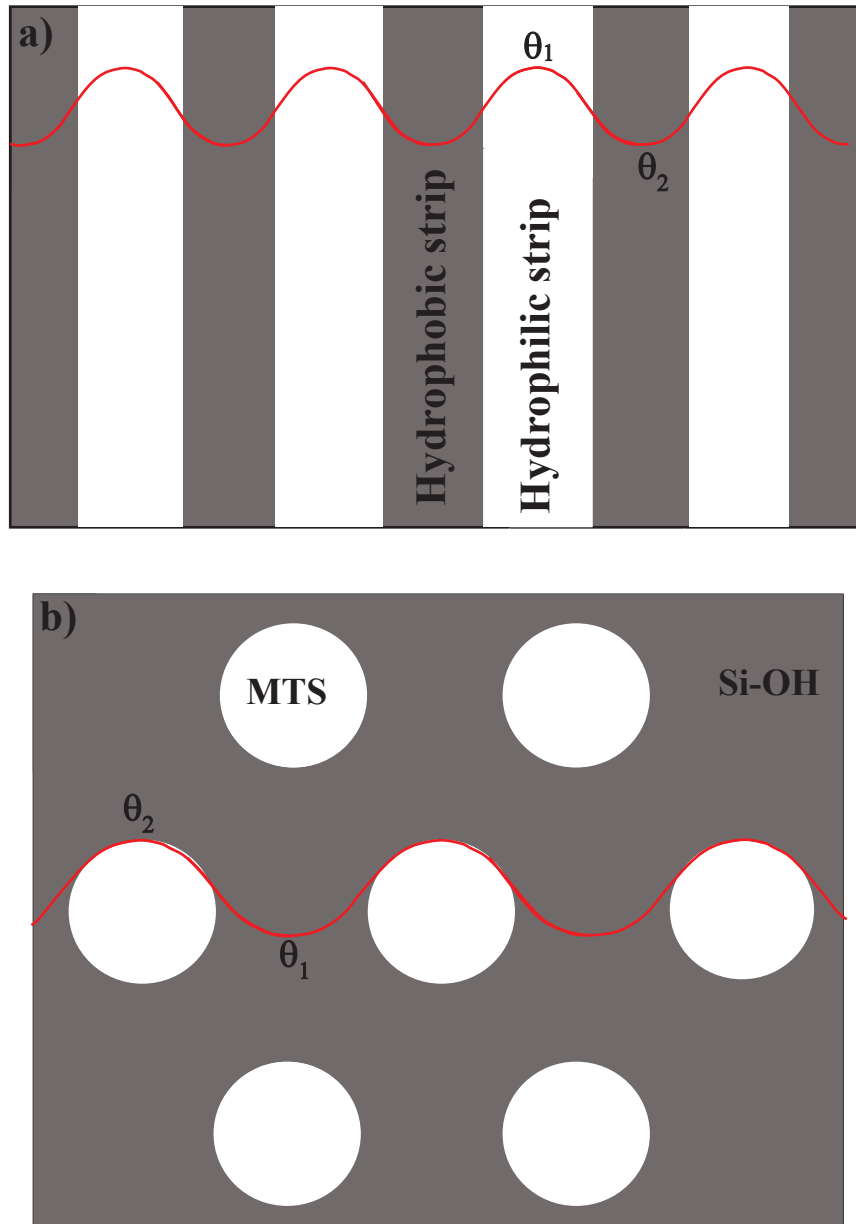


Figure 2. 23 (a-b) Illustration of the contact line pinning for the discrete circular and linear patterns of the system (MTS/Si-OH).

Hence, we suggest that the enhancement of the adhesion work is related to the lengthening of the contact line due to contact line pinning. By incorporating periodic regions of surface chemical contrast, the contact line profile increases as a function of the surface chemistry contrast and the perimeter of the pattern region. To understand this mechanism for the linear and circular patterns, we consider these surfaces as homogeneous Si-OH surfaces with the MTS species occupying discrete regions of the interface. As illustrated in Fig. 2.23, the separation process can be reported as a stick-slip behavior,

Chapter 2 Wetting and Adhesion Investigations of patterned surfaces

where the contact line defines the advancing and receding of the water contact angle. Once the advancing line front approaches the patterns, the presence of the MTS regions "pins" the contact line (Fig.2.22). This leads to the deformed, lengthened profile of the contact line, which increases the resistance for the line to propagate. As a result, additional energy must be supplied to drive the line forward. The enhancement is more significant for circular pattern compared with linear pattern, which we believe is associated with the stress concentrating geometry presented by the linear patterns. In other words, the circular geometry blunts the contact line more effectively compared to the linear patterns. Hence, a MTS circular geometry (with the same area as the linear) should provide greater efficacy in pinning the contact line compared to the linear geometry. Therefore, as the pattern, size increases a higher deformation and lengthening profile of the contact line is expected, inducing the increase of the resistance for the line to advance. As a result, additional energy is needed to drive the line forward, enhancing then the adhesive response.

III-2-Patterns effect on the adhesive behavior

In this part, the adhesion measurements on the different patterned systems (MTS/Si-OH, MTS/PDMS) for the different pattern size using a JKR machine and the PEACK Force AFM are illustrated.

III-2.1-Adhesion measurements using the JKR machine

Contact adhesion testing based on the theory of Johnson, Kendall, and Roberts (JKR) is performed to quantify the adhesion and near-surface mechanical properties of both non-patterned and patterned surfaces. It consists in squeezing the bead against the substrate by incremental steps. The full compression followed by a decompression at the same velocity. Unless otherwise stated, the results reported here deal with the compression step.

III-2.1.a- JKR Adhesion measurements on smooth Substrates

Smooth and flat PDMS, Si-OH surface, MTS and OTS grafted substrates are taken as reference substrates and characterized using a soft PDMS bead ($R \sim 9,42 \text{ mm}$) through the method described above. Fig.2.24 and Fig.2.25 shows respectively the typical result of a JKR test performed on the different smooth substrate. Using those data it's possible to measure the adhesion energy W_0 , Strain energy release G and the stiffness K . In fact, we can notice that the graphs of the compression and the decompression experiments follow the same dependence. Therefore, using a linear fit eq.(3.9) we can extract the stiffness K , the adhesion energy W_0 and Strain energy release G of the contact.

Chapter 2 Wetting and Adhesion Investigations of patterned surfaces

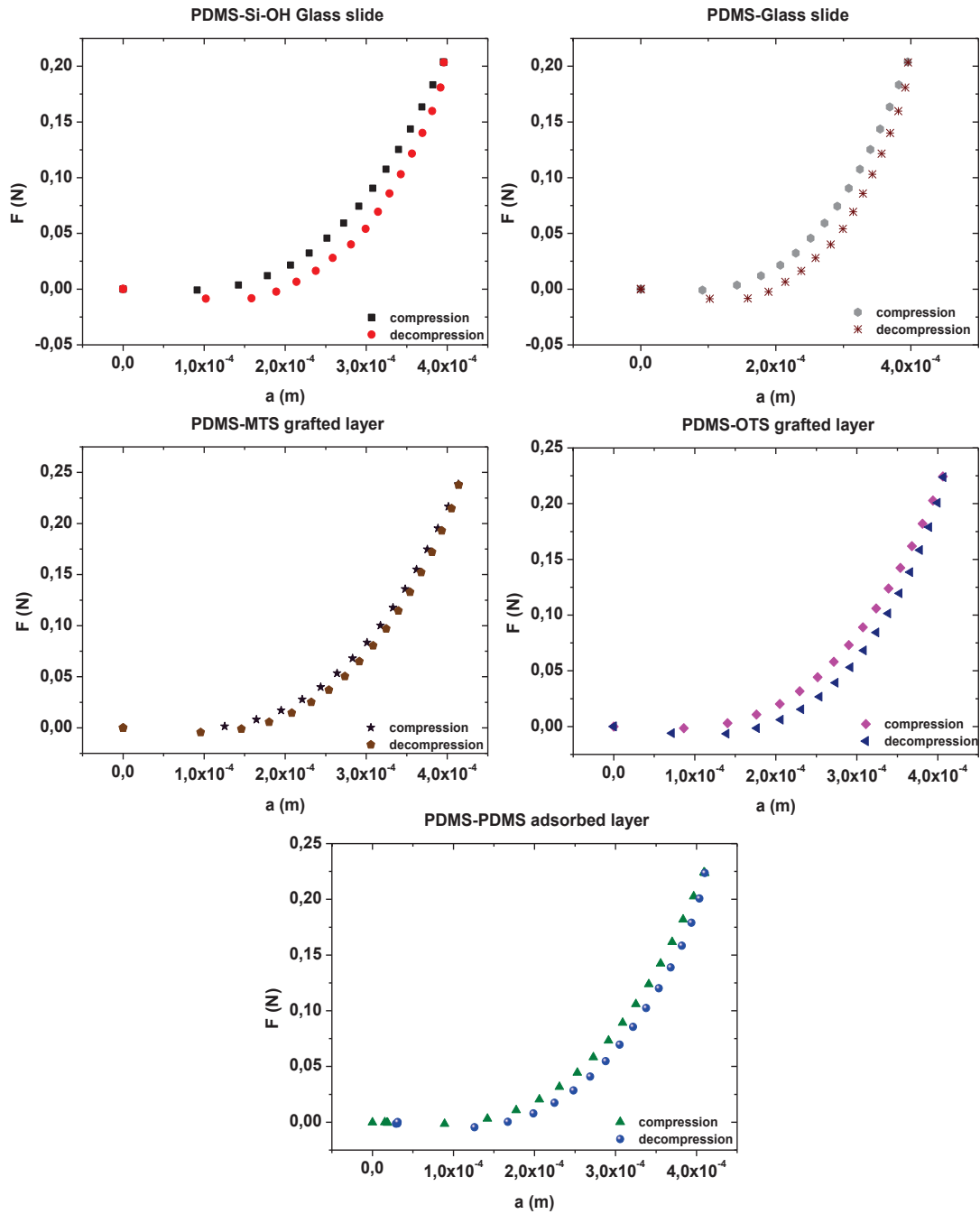


Figure 2. 24 Experimental data for a compression/decompression cycle on a several reference surfaces. Where the force (F) was plotted as a function of the contact radius (a).

Chapter 2 Wetting and Adhesion Investigations of patterned surfaces

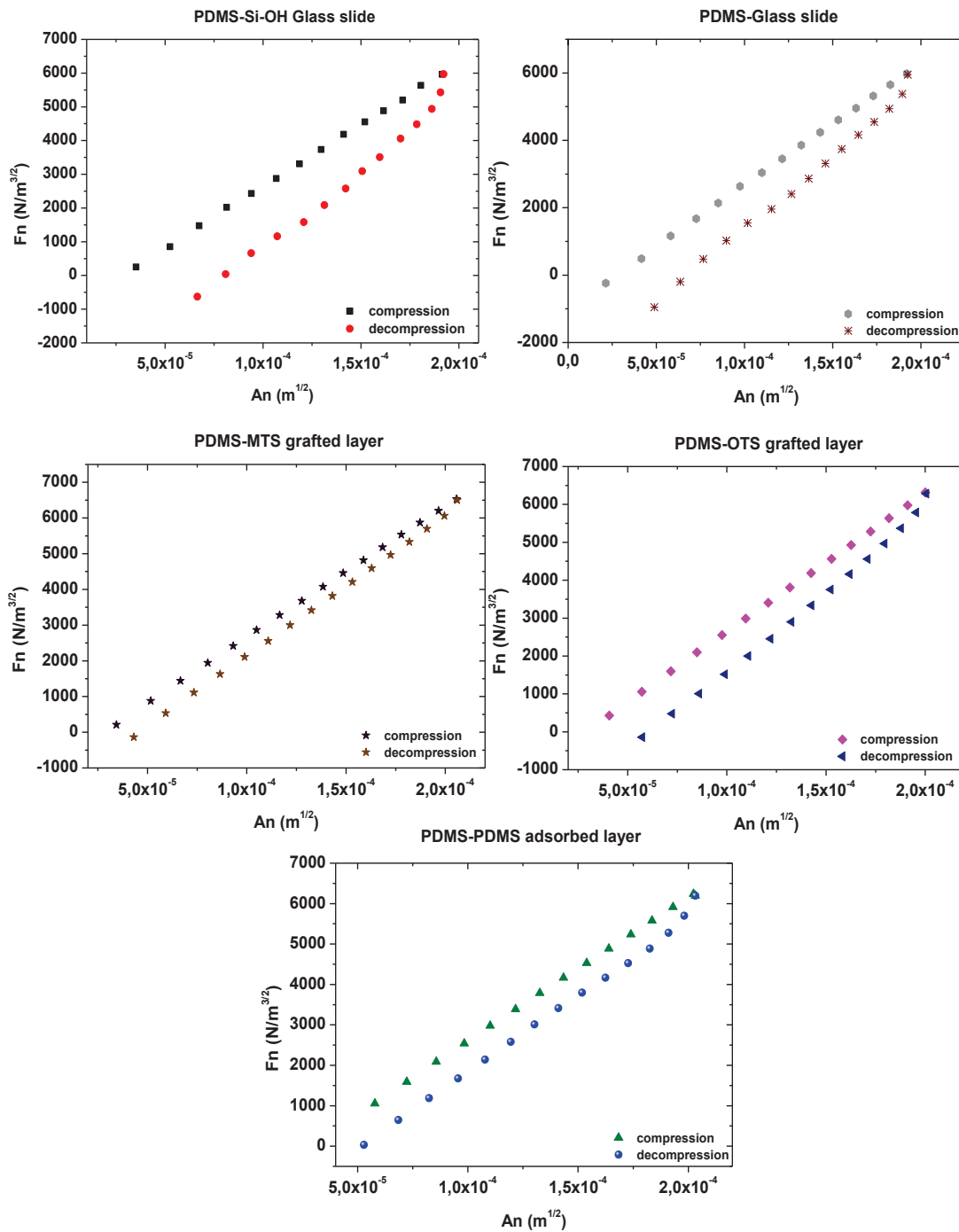


Figure 2. 25 Experimental data for a compression/decompression cycle on a several reference surfaces. Where the pseudo-force ($F_n = F/\sqrt{6\pi a^3}$) was plotted as a function of the pseudo-contact radius ($A_n = a^{3/2}/\sqrt{6\pi R}$).

Smooth PDMS surfaces lead to weak hysteresis compared with the involved adhesion energies and this value is in good agreement with previous measurements performed on the similar system [55] and is attributed to free oligomers in the bulk PDMS. Finally, contacts of higher rigidity, i.e., hard SiO_2 , Si-OH and MTS, OTS grafted layer surfaces against a PDMS bead, have been tested.

Chapter 2 Wetting and Adhesion Investigations of patterned surfaces

Substrate	K (MPa)	E (MPa)	W_0 (mJ/m ²)	G (mJ/m ²)	W_{P-o} (mJ/m ²)
SiO ₂	36,17 ± 0,29	27,12 ± 0,29	36,92 ± 4,69	293,19 ± 4,30	288,34 ± 1,31
Si-OH	37,56 ± 0,22	28,17 ± 0,22	38,01 ± 2,5	313,83 ± 3,82	304,12 ± 1,13
MTS	34,44 ± 0,18	25,83 ± 0,18	27,38 ± 3,52	84,93 ± 5,01	90,96 ± 0,92
OTS	35,31 ± 0,18	26,48 ± 0,21	28,08 ± 1,99	112,85 ± 4,87	102,94 ± 0,97
PDMS	36,84 ± 0,32	27,63 ± 0,32	33,88 ± 2,34	109,09 ± 4,96	98,67 ± 0,99

Table 3 Adhesive behavior of PDMS bead and the different non-patterned surfaces.

As reported in Tab 2 we measured K , E , W_0 , G and $W_{Pull-off}$ for the different substrates using an 9,42 mm PDMS bead. Contacts between smooth substrates are used as a reference state to study the role of a micro-structuration on the adhesion properties. Hence, the results in the Tab shows that the MTS, OTS and the PDMS substrate have almost the same adhesion energy, which it can be attributed to the same chemistry ($-CH_3$) on the interfaces. In the other hand, we can observe that, the SiO_2 and Si-OH have the highest W_0 and G and this is due to their hydrophilic behavior and their high free surface energy. To a better understanding of the adhesion behavior of the patterned surfaces, the force (F) was plotted as a function of the contact radius (a) for the non-patterned and patterned surface Fig.2.26.

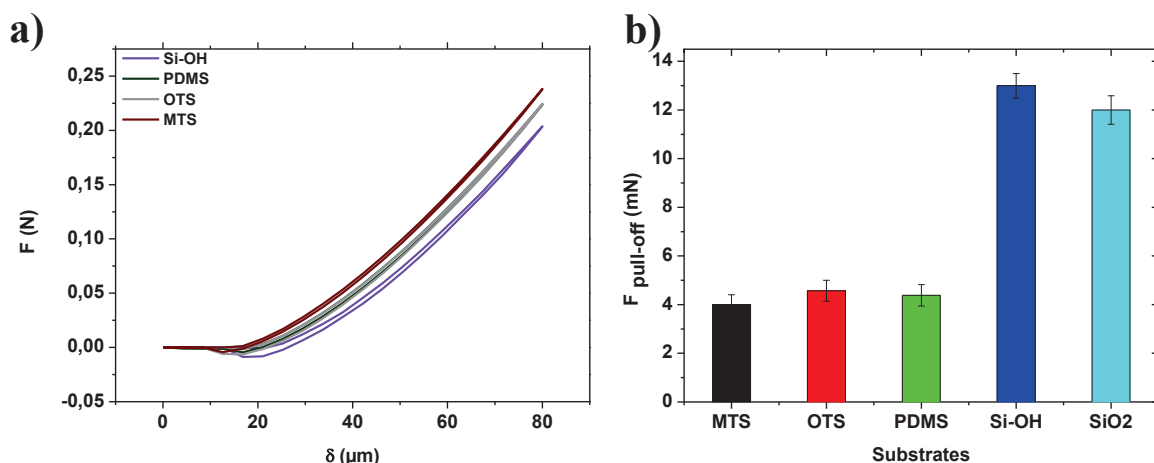


Figure 2. 26 (a) Force–displacement curves for the smooth non-patterned surfaces. (b) Pull-off Force as function as function of the smooth non-patterned systems.

Fig.2.26 (a) shows the experimentally obtained force–displacement curves for the smooth non-patterned. In a load-controlled experiment, the two surfaces will spontaneously separate once the pull-off force is reached. Following the standard convention in contact mechanics, we call the absolute value of minimum on the force curve the pull-off or adhesion force, f_c . Fig. 2.26 (b) This pull-off force

Chapter 2 Wetting and Adhesion Investigations of patterned surfaces

extracted using the last image, displacement and force recorded at the decompression step is typically defined by $F_{\text{pull-off}} = -3\pi WR/2$. In this study, we are using the pull-off force as an indicator of the evolution of the adhesive behavior following the different patterns sizes.

III-2.1.b-JKR Adhesion measurements on MTS/Si-OH linear patterned system

Fig.2.27 shows the contact area in the compression sequences. In fact, this contact area is dark and we cannot see the patterns, and is due the same refractive index between the bead and the substrates. Hence, the dark contact area can be attributed to an intimate contact between the bead and the surfaces.

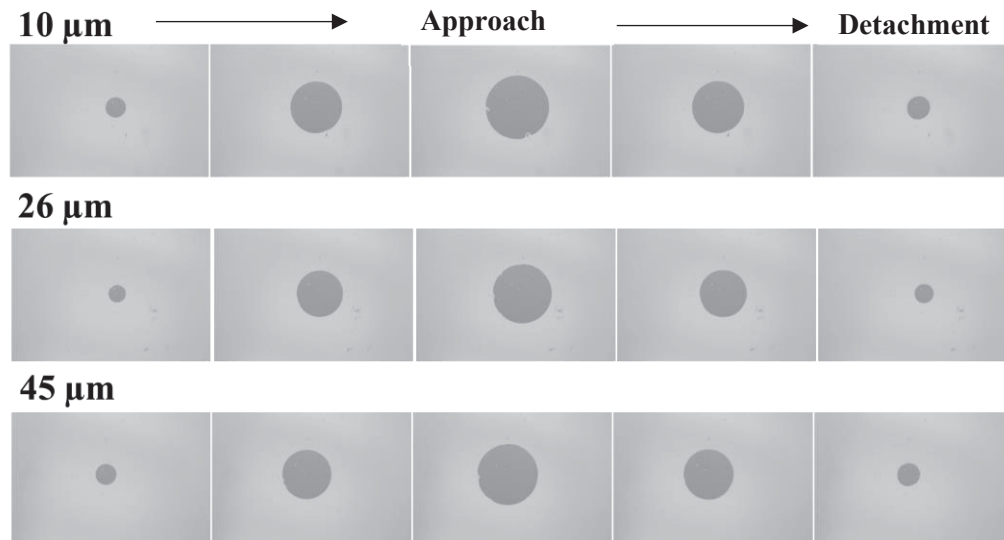


Figure 2. 27 Micrographs of the contact on substrates covered with linear strips of various patterns seize where the contact can be intimate.

Pseudo-force and Pseudo-contact radius measurements during a compression/decompression cycle are shown in Fig.2.28 for the linear micro-patterned (MTS/Si-OH) surfaces. In the case of the compression step, we find that the contact rigidity K and the Young's modules are the same as for smooth substrates whatever the size of the textures. From these curves, assuming the JKR description still holds, we determine values for K and W .

Chapter 2 Wetting and Adhesion Investigations of patterned surfaces

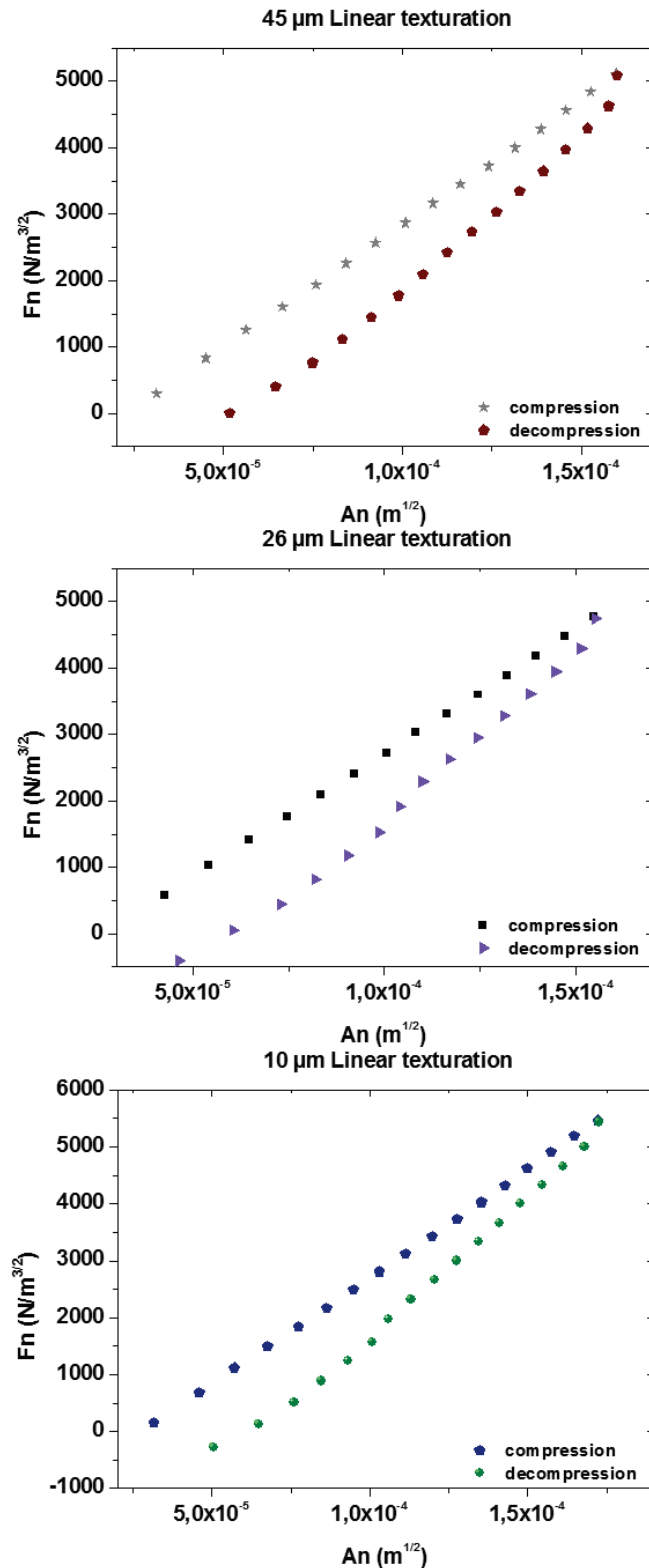


Figure 2. 28 Experimental data for a compression/decompression cycle on the(MTS/Si-OH) patterned surfaces. Where of the pseudo-force (F_n) was plotted as a function the pseudo-contact radius (A_n).

Fig.2.29 (a) shows the evolution of adhesion energy at the compression step $W = W_0$, the Strain energy release G and the adhesion energy at the pull-off as for the different pattern size. In our case, we have clearly an intimate contact between the beads and the surface.

Chapter 2 Wetting and Adhesion Investigations of patterned surfaces

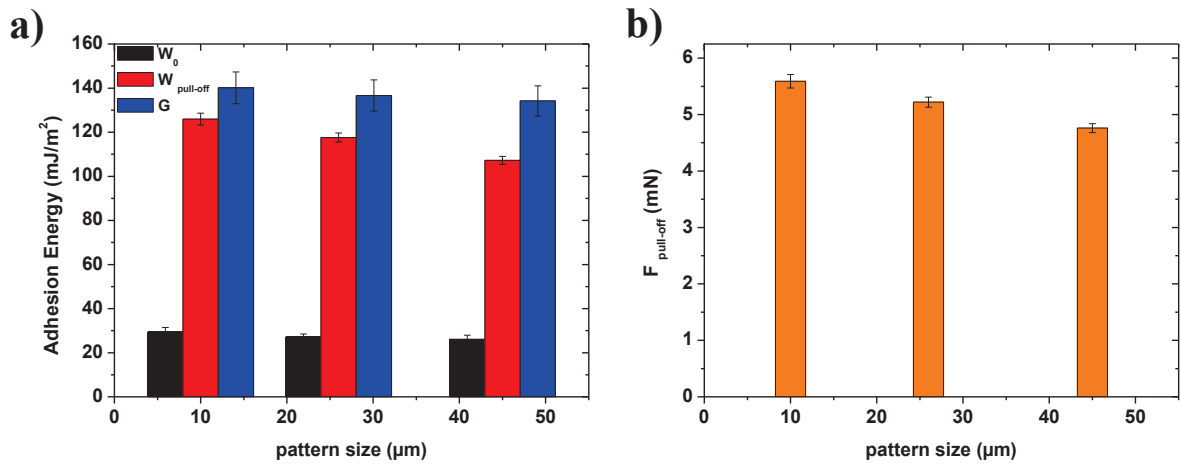


Figure 2.29 (a) Adhesion response as function of the pattern size for the MTS/Si-OH system. (b) Pull-off force as function of pattern size.

Therefore, we clearly observe that all the different patterned surfaces displays a similar adhesive response (W and G). However, the results of the force adhesion ($F_{\text{pull-off}}$) presented in Fig.2.29 (b), suggest that the adhesion energy slightly decrease linearly with the pattern size. In fact, one drawback of the micro-contact printing method used in this work was the tendency of the Si-OH layer to be contaminated by the excess MTS deposited by the stamp. Evidence of this contamination is apparent in Fig. 2.30, where MTS molecules are evident on what was supposed to be Si-OH layer substrate.

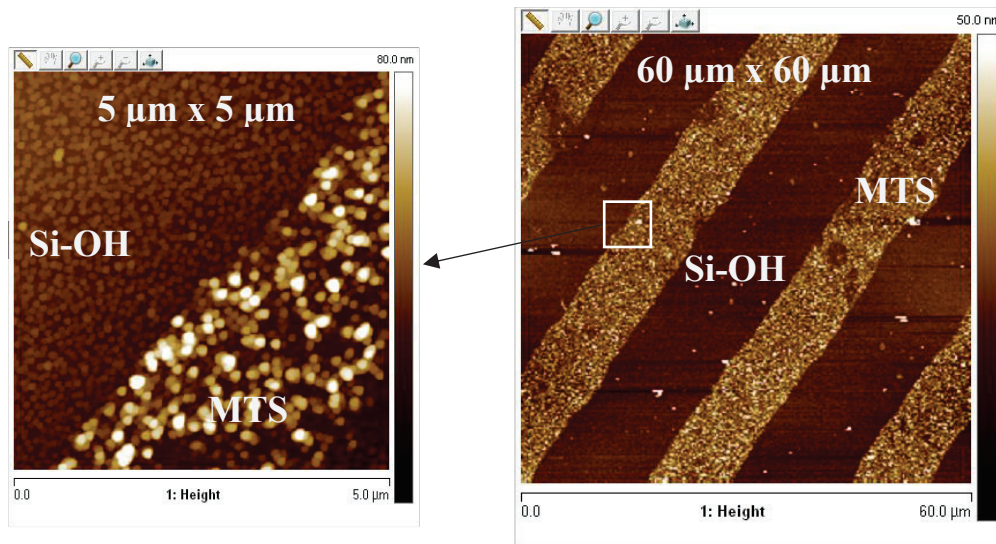


Figure 2.30 2D AFM images of the Topography ($5 \times 5 \mu\text{m}^2$, $60 \times 60 \mu\text{m}^2$) of $10 \mu\text{m}$ linear strips (MTS/Si-OH).

This contamination could explain the similar adhesive response of the different patterned substrate to the value of the work of adhesion of the non-patterned MTS substrate. These results illustrates the dependence of the adhesion behaviour to the chemistry and the relative surface fraction of the MTS domains present on the surface.

Chapter 2 Wetting and Adhesion Investigations of patterned surfaces

III-2.1.c- JKR Adhesion measurements on MTS/PDMS linear patterned system

Fig 2.31 shows the contact area in the compression sequences. In fact, this contact area is dark and we see the features of 26 and 45 μm linear patterns, which can be explained by the same refractive index between the bead and the substrates. Hence, the dark contact area can be attributed to an intimate contact between the bead and the surfaces.

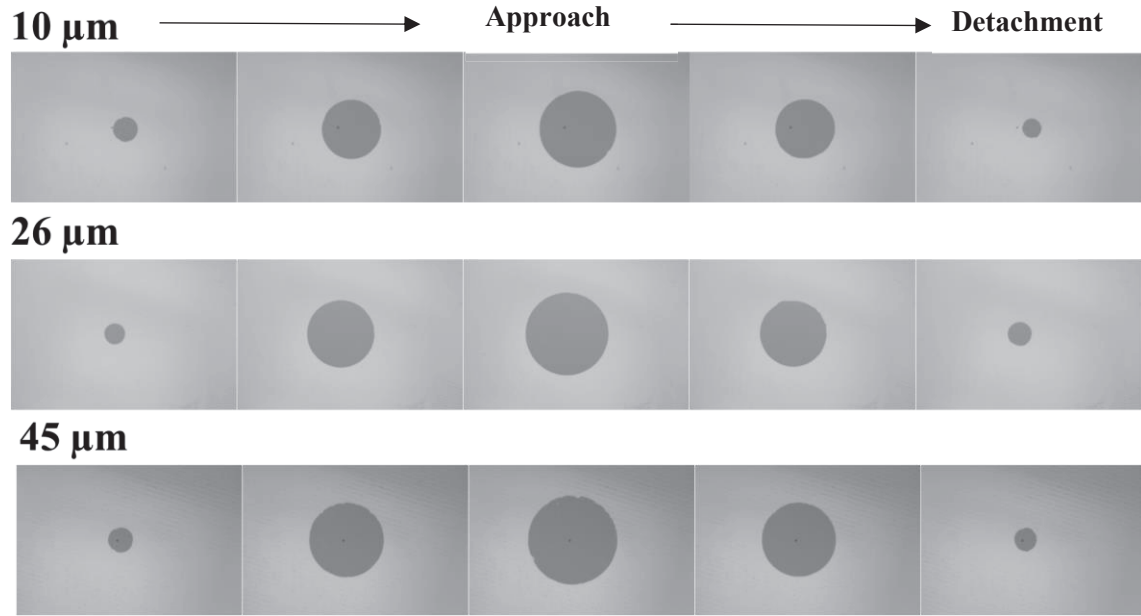


Figure 2. 31 Micrographs of the contact on substrates covered with linear strips of various patterns seize where the contact can be intimate.

Pseudo-force and Pseudo- contact radius measurements during a compression/decompression cycle are shown in Fig.2.32 for the linear micro-patterned surfaces (MTS/PDMS). In the case of the compression step, we find that the contact rigidity K and the Young's modules are the same as for smooth substrates whatever the size of the textures. In our case, the linear patterned substrates with parallel strips (MTS/PDMS), have almost the same interface chemistry (-CH₃).

The variation of adhesion energy, strain energy release and the work of adhesion at the pull-off with patterns size is illustrated in the Fig.2.33. In this case, we have an intimate contact between the beads and the surface.

Chapter 2 Wetting and Adhesion Investigations of patterned surfaces

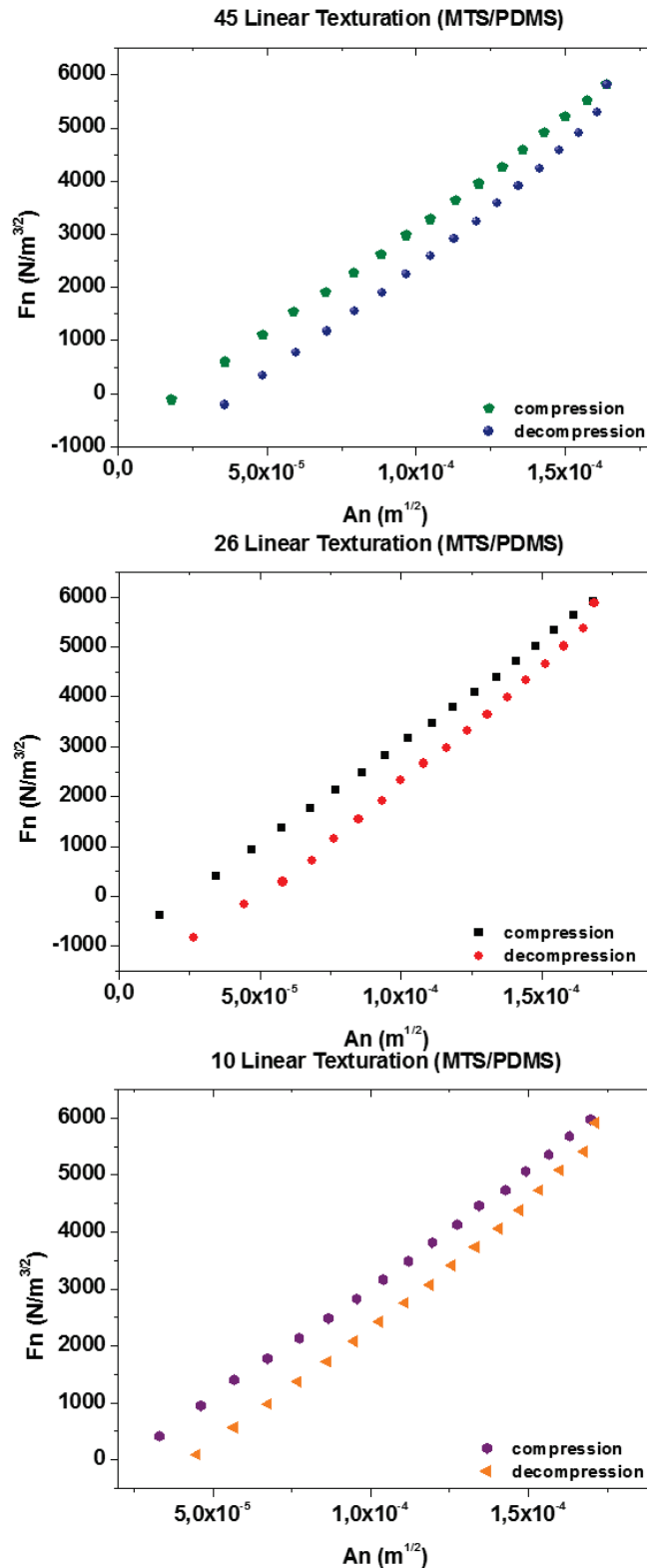


Figure 2. 32 Experimental data for a compression/decompression cycle on the(MTS/PDMS) patterned surfaces. Where the pseudo-contact radius (F_n) was plotted as a function of the pseudo-force (A_n).

Hence, we observe that the adhesion energy decreases linearly as the surface coverage of PDMS for micro-patterned surfaces Fig.2.33 (a). These results proves that the adhesion energy is greatly affected by chemistry, size and distribution of patterns. In fact, one of the possible explication to this

Chapter 2 Wetting and Adhesion Investigations of patterned surfaces

enhancement of adhesion is the viscoelastic character of the PDMS systems. The main reason behind adhesion enhancement is periodical nature of energy gain and dissipation as contacts proceeds [142].

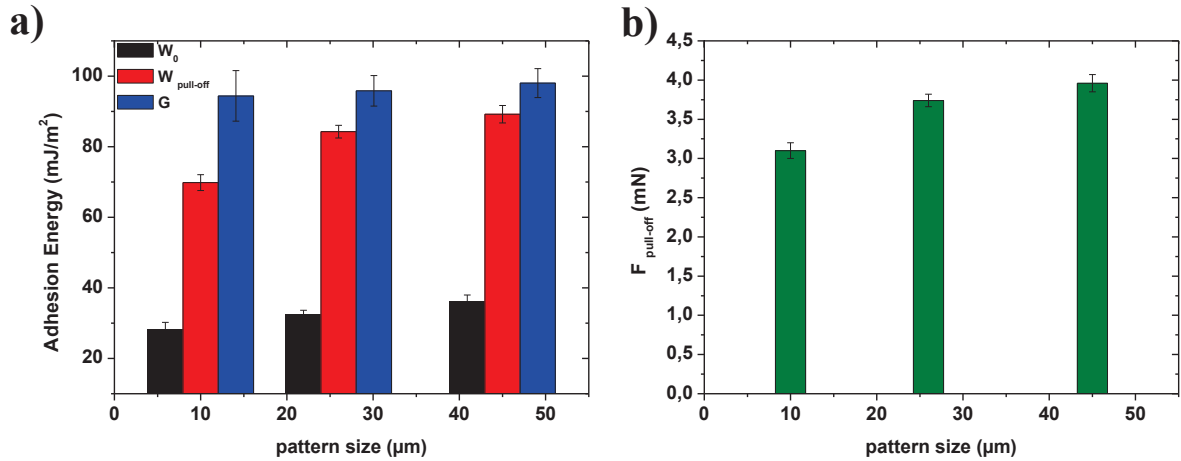


Figure 2.33 (a) Adhesion response as function of the pattern size for the MTS/Si-OH system. (b) Pull-off force as function of pattern size.

During the process of compression/decompression, excessive elastic energy dissipation could occur in the surface due to the deformation. In fact, introduction of the viscoelastic PDMS layer on top of patterned substrate enhances the dissipation of the energy in shape of viscoelastic losses inducing an increase of the adhesion.

In addition to these mechanisms, the effect of the interpenetration of the free polymer on the PDMS bead may help to increase the adhesion response. In fact, Chen et al. [143] indicate that the population of chain ends at the surfaces is the most important factor determining adhesion, and according to common views loose chain ends should preferably accumulate at the surface. Hence, we assume that in our MTS/PDMS systems the dangling chains increases with the pattern size favoring more interpenetration between the free polymer chain and the PDMS beads thus enhancing the adhesive response.

III-2.2-Adhesion measurements using the AFM PeakForce QNM

The surface morphologies of non-patterned and patterned surfaces were characterized by AFM (Bruker, AFM PeakForce QNM) with a conventional cantilever (tip curvature, 8 and 20 nm). Adhesive force (pull-off force) measurements were conducted in air at room temperature. The AFM probe used for the non-patterned measurements is a Si₃N₄ tip ($R \sim 20$ nm), and for the patterned surfaces is a Si₃N₄ tip ($R \sim 8$ nm). The adhesive force was obtained from 100 force-distance curves for each surfaces Fig.2.34.

Chapter 2 Wetting and Adhesion Investigations of patterned surfaces

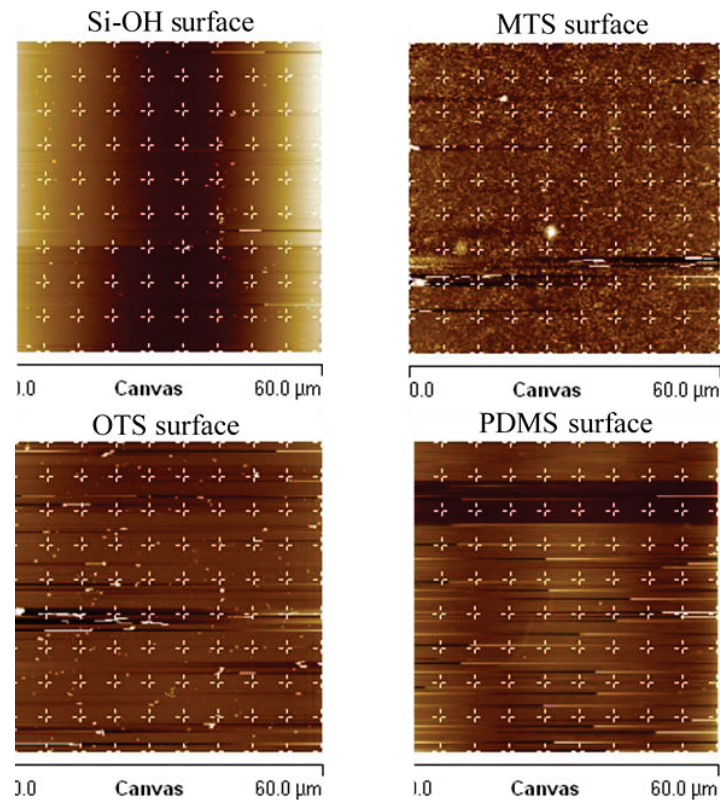


Figure 2. 34 AFM images ($60 \times 60 \mu m^2$) of the different smooth substrates.

III-2.2.a- AFM Adhesion measurements on smooth non-patterned substrates

Smooth and flat PDMS, Si-OH surface, MTS and OTS grafted substrates are taken as reference substrates and characterized using a Si_3N_4 tip ($R \sim 8$ nm) through the method described above. Fig.2.35 shows respectively the typical result of the force displacement curves performed on the different smooth substrate. Pull-off-force measurements were performed at a low applied load (5nN).

Chapter 2 Wetting and Adhesion Investigations of patterned surfaces

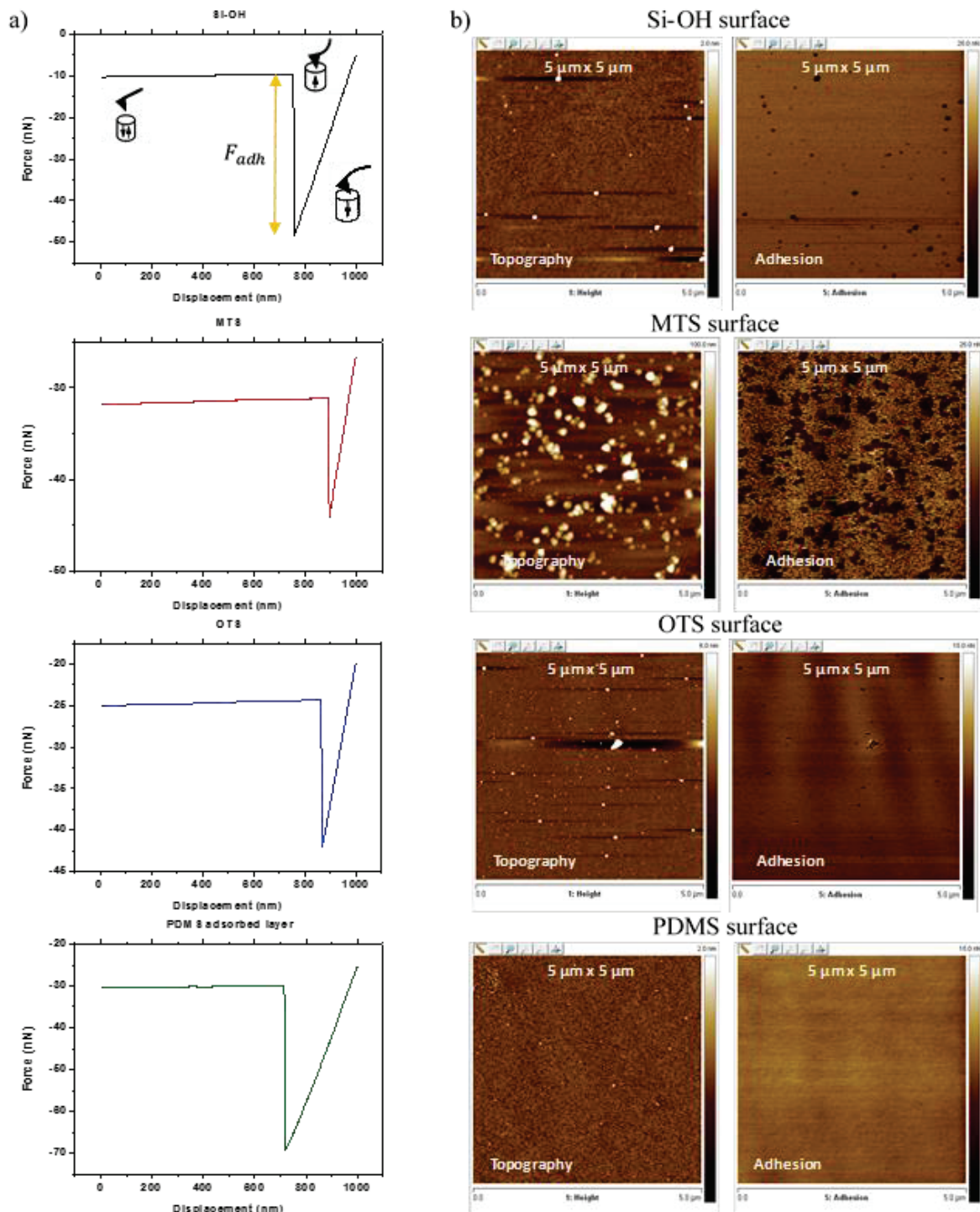


Figure 2. 35 (a) Representative force-displacement curves for the different smooth substrate. (b) 2D AFM images of the topography and the adhesion of the different smooth substrates ($5 \times 5 \mu\text{m}^2$).

In principle, the magnitude of intermolecular interactions can be assessed directly in an adhesion measurement Fig.2.35 (a). The adhesive interaction between different functional groups is determined from force-versus-sample displacement curves. In these measurements, the deflection of the cantilever is recorded during the sample approach-withdrawal cycle [144]. The observed cantilever deflection is converted into a force using the cantilever spring constant. The pull-off force determined from the jump

Chapter 2 Wetting and Adhesion Investigations of patterned surfaces

in the sample retracting trace corresponds to the adhesion between functional groups on the tip and sample surfaces. Thus, the adhesion energy can be deduced using this formula $F_{adh} = 2\pi WR$ of the Derjaguin, Muller & Toporov (DMT) theory [13], which assumes finite-range surface forces and no deformation, that is, zero contact area at the moment when bonds between functional groups on the tip and sample rupture.

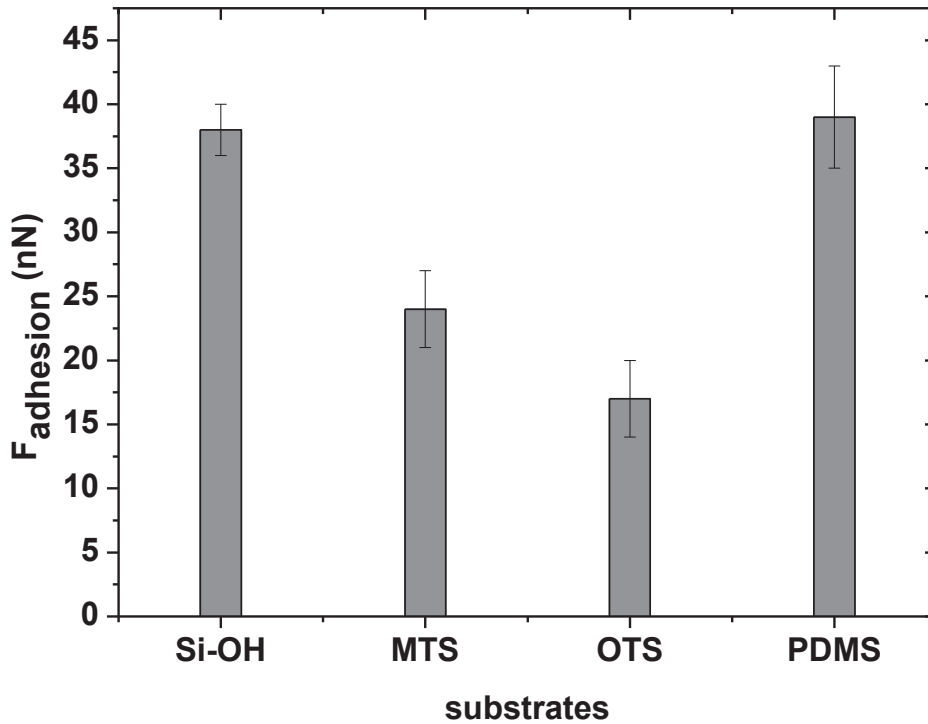


Figure 2. 36 Adhesion force of the different non-patterned substrates.

Furthermore, the intrinsic adhesive force arises due to the contribution of various attractive forces such as capillary, electrostatic, van der Waals and chemical bonding under different circumstances [145]. Amongst these forces, the capillary force that arises due to condensation of water from the environment is the strongest [145]. Hence, Fig.2.36 displays the evolution of the adhesive force as function of the different non-patterned substrates prepared through self-assembled monolayer. In the case of the Si-OH surface, capillary force dominates the inherent adhesion owing to its hydrophilic nature and thereby causes high adhesion force [146]. The higher interfacial energy of Si-OH surface therefore makes it a poor tribological material. On the contrary, SAMs and PDMS are hydrophobic in nature (water contact angles $\sim 110^\circ$) and this would greatly suppress the contribution of capillary force. Under such circumstances, where the capillary force is unlikely to dominate the adhesion force, the van der Waals forces would play a major role [147]. In fact, we can notice that, the MTS display a higher adhesion force compared to the OTS surfaces. This behaviour can be attributed to the difference in the chain length between both systems. Perry et al [148, 149] mentioned that the increase in the number of atomic

Chapter 2 Wetting and Adhesion Investigations of patterned surfaces

contacts within a unit area increases the van der Waals interaction between the AFM tip and the SAM systems. It is well known that the packing density increases with the chain length in monolayers [150]. Thus, the van der Waals interaction between the AFM tip and the molecular chains of loosely packed SAMs (monolayers with shorter chain lengths, MTS) are likely to be greater per unit area than those between the AFM tip and the molecular chains of well-packed SAMs (monolayers with longer chain lengths, OTS) [148, 149]. The van der Waals interactions therefore define the adhesion behaviour of SAMs with the AFM tip, causing an increase in adhesion with decrease in the chain length. Further, the high adhesion force of the PDMS surface compared to the SAM systems can be explained to the lubricated character of the adsorbed polymer chain at the interface. Hence, considering the length of the PDMS chains and their high mobility, the surface shows a liquid interfacial character, inducing an increasing in the interfacial adhesion.

III-2.2.b- AFM Adhesion measurements on MTS/SiOH patterned surfaces

Considering the limited imaging scale (Max $120 \times 120 \mu\text{m}^2$) of the AFM, we have chosen to work on the smallest linear patterns defined by the 10 and 26 μm patterns with two type of chemistry (MTS/Si-OH, MTS/PDMS). Fig.2.37 (a), shows the AFM images topography and adhesion ($60 \times 60 \mu\text{m}^2$) of the 10 μm patterned surface (MTS/Si-OH). Further, From these results we attribute the dark area to the Si-CH₃ layer (low adhesion) and the lighter area to the Si-OH layer (high adhesion). In fact, the greater the adhesion, the brighter the pixels in the AFM image.

Thus, the results of the evolution of the adhesive force as function of the pattern sizes was presented in Fig.2.37 (b). In the case of the adhesion measurements of the MTS/Si-OH surfaces a similar adhesive response was observed. This behavior can be anchored to the contamination of the Si-OH layer by the excess of the MTS monolayer printed by the stamp. Moreover, the magnitude of the adhesion force (5 nN) on the MTS layer extracted from the patterned substrate was greatly lower than that (22 nN) of non-patterned MTS smooth Surface. In fact, micro-contact printing did not lead to self-assembled monolayer (SAM) formation, so the silanes had a random orientation.

Chapter 2 Wetting and Adhesion Investigations of patterned surfaces

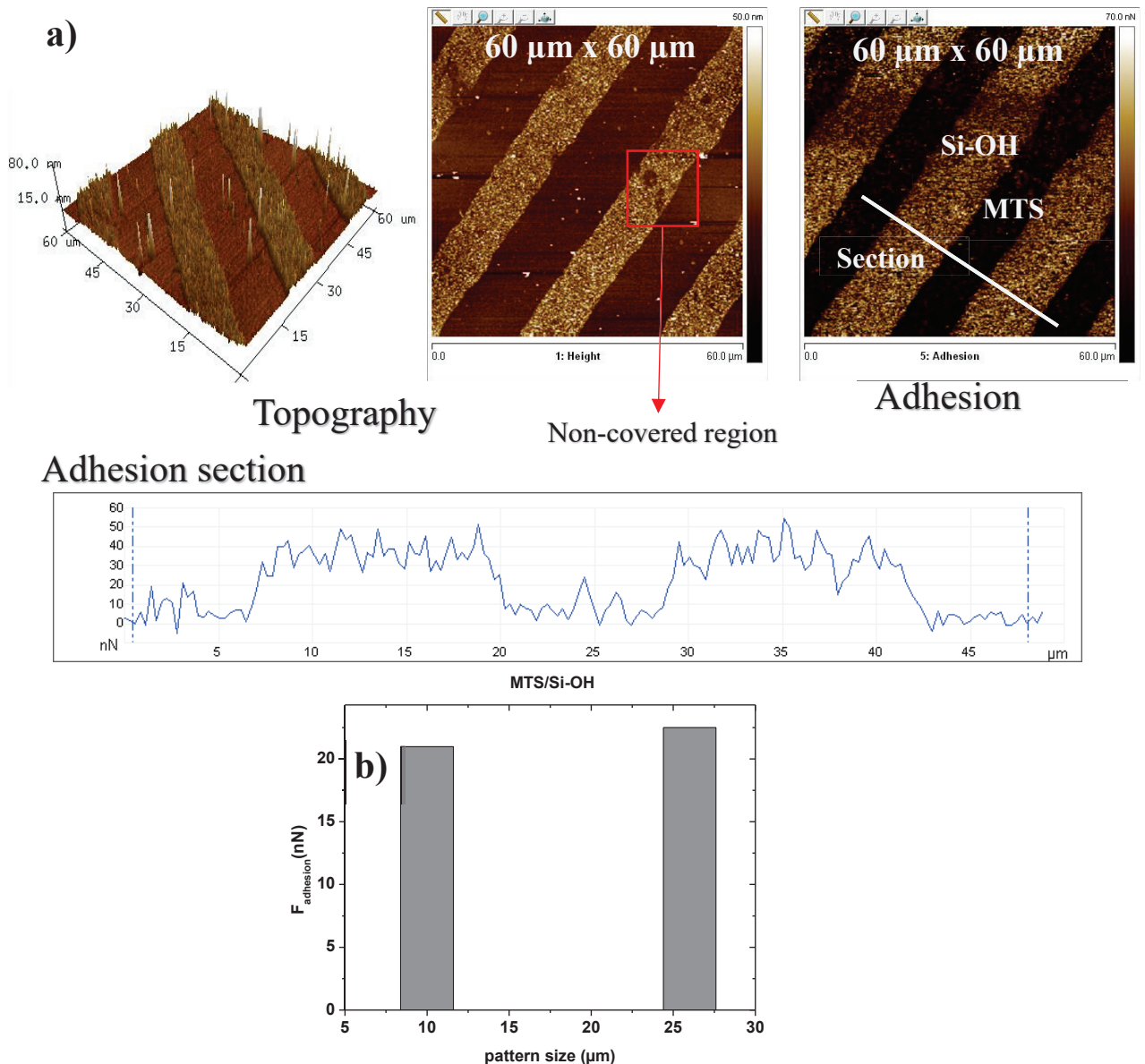


Figure 2. 37 (a) 2D and 3D AFM images of topography and adhesion ($60 \times 60 \mu\text{m}^2$) of the $10 \mu\text{m}$ patterned surface for the MTS/Si-OH system. **(b)** Adhesion force as function of pattern size for the MTS/Si-OH system.

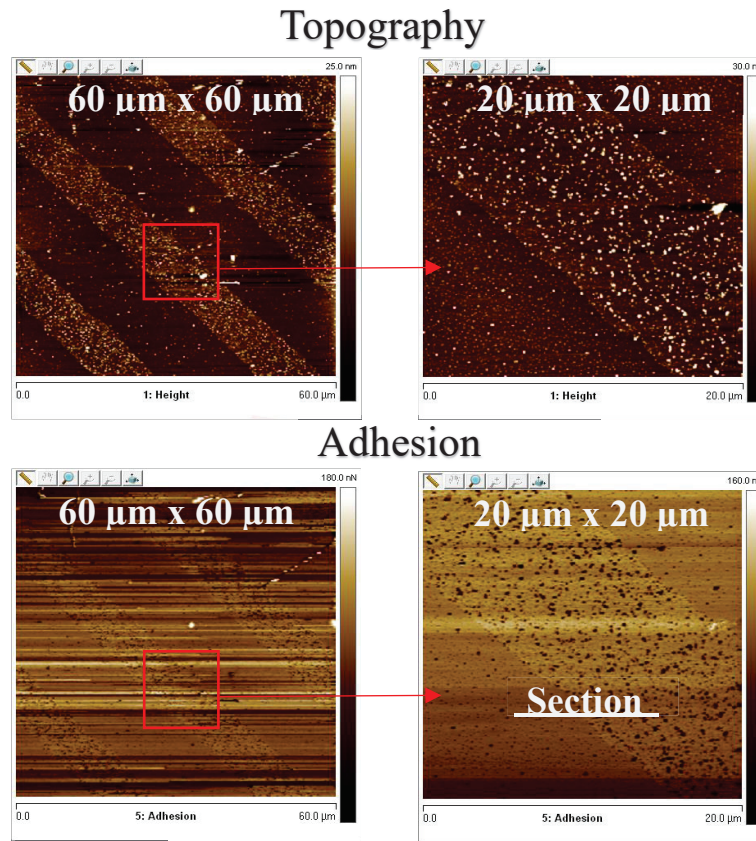
When the silanes were deposited from solution, they had time to orient themselves with their hydrolyzed groups towards the surface, whereas the micro-contact printed silanes did not have this ability. As a result, the surface chemical properties were different, and a different adhesion value was observed.

III-2.2.c- AFM Adhesion measurements on MTS/PDMS patterned surfaces

In the case of the MTS/PDMS system, Fig.2.38 (a), shows the AFM images topography and adhesion ($60 \times 60 \mu\text{m}^2, 20 \times 20 \mu\text{m}^2$) of the $10 \mu\text{m}$ patterned surface (MTS/PDMS). These results were confirmed by extracting the same magnitude of adhesion force (23 nN) on the MTS layer and (24 nN) on the PDMS layer. This behavior can be explained by a probable adsorption of some free PDMS chain on the MTS linear strips.

Chapter 2 Wetting and Adhesion Investigations of patterned surfaces

a)



Adhesion section

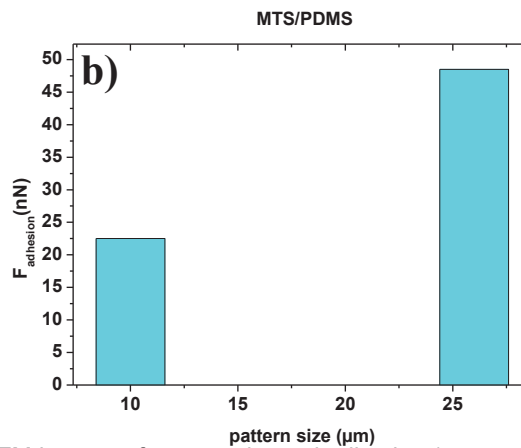
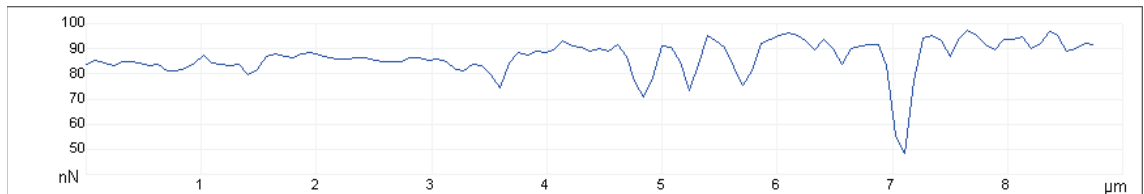


Figure 2. 38 (a) 2D and 3D AFM images of topography and adhesion ($20 \times 20 \mu\text{m}^2$, $60 \times 60 \mu\text{m}^2$) of the $10 \mu\text{m}$ patterned surface for the MTS/PDMS system. **(b)** Adhesion force as function of pattern size for the MTS/PDMS system.

In fact, micro-contact printing may lead to non-covered zones in the middle of the printed MTS layer, inducing then a possible adsorption of some PDMS molecules during the grafting process of PDMS film on the patterned substrates Fig.2.38 (a). Furthermore, a regular augmentation of the tip/interface

Chapter 2 Wetting and Adhesion Investigations of patterned surfaces

adhesion with the pattern size was clearly observed. This enhancement of the adhesive behavior with the increase of the pattern size can be attributed to an augmentation of the number of the free PDMS chain at the surface, following the increase of the PDMS area with the pattern size. Hence, an increase of the interpenetration between the free PDMS chain at the surface and the PDMS bead can be suggested.

III-2.2.d-Multiscale comparative adhesive studies

To a better understanding of the adhesive behavior for the different linear pattern, we use a normalized work of adhesion W_N , to quantify the adhesion as a function of the different strip size. Fig.2.39 and Fig 2.40 summarizes these results in terms of normalized $W_N = W_{Pattern}/W_{max}$ and $W_N = W_{Pattern}/W_{max}$ respectively for both systems (MTS/Si-OH and MTS/PDMS) where the energy adhesion values are normalized by the maximum values of thermodynamic work of adhesion displayed by the biggest patterns respectively .

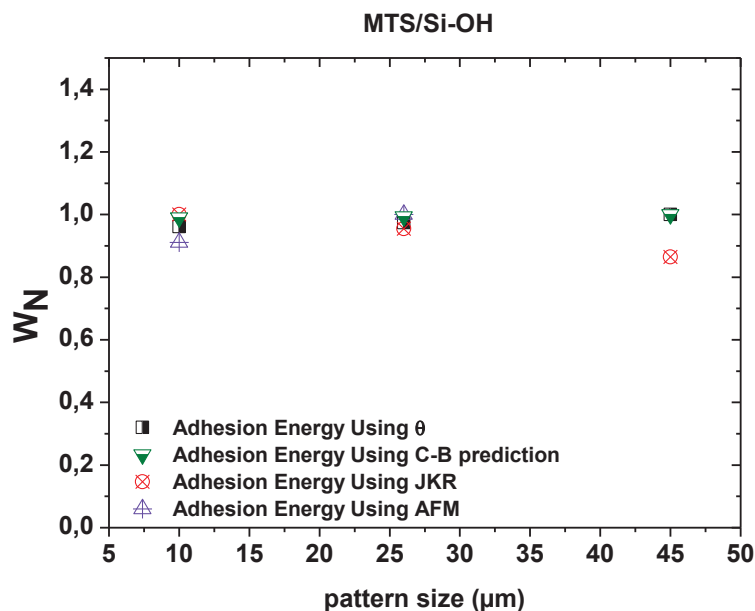


Figure 2. 39 Normalized Adhesion force as function of the pattern size for the MTS/Si-OH patterned system.

As we observe in Fig.2.39, that at macro, micro and nano scale the surface displays almost the same adhesive response suggesting that at different scales, the adhesive behaviour of MTS/Si-OH patterned surfaces was largely dependent on the chemistry and the preparation methods. These results suggest that the adhesion is not a consequence of the changes in the surface ratio, (α) Fig.2.40.

Chapter 2 Wetting and Adhesion Investigations of patterned surfaces

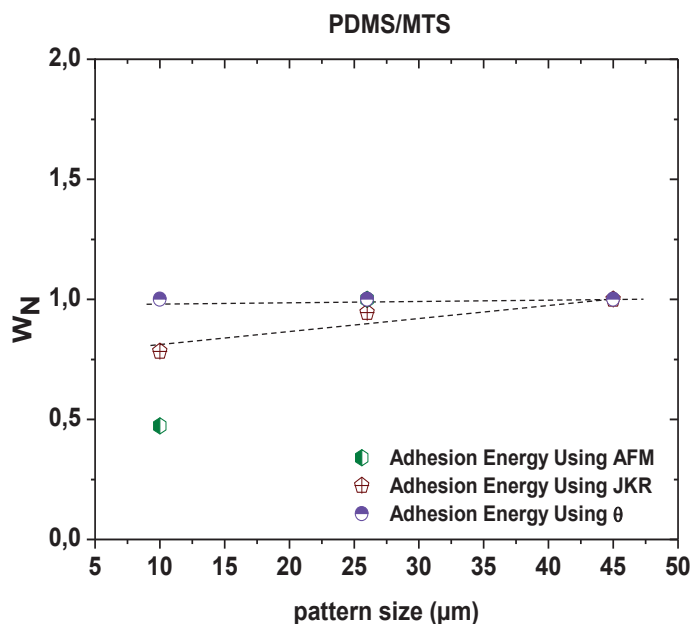


Figure 2. 40 Normalized Adhesion force as function of the pattern size for the MTS/PDMS patterned system.

However, we should note that as the pattern size decreases, the difference in the normalized work of adhesion increases. This response can be anchored to the augmentation of the impact of the contact nature (PDMS bead/Surface or Rigid Tip/Surface) on the tribological behaviour of the interface.

IV- Conclusion

Firstly, various heterogeneous silane/polymer deposition methods were explored, including micro contact printing with hand pressure and micro contact printing using the mini (μCP) machine followed by polymer grafting. For reproducible, cleanly delineated patterned surfaces, the use of micro contact printing of MTS with the mini (μCP) machine was determined to be the best method. Dewetting and AFM were used to gain additional information about the quality and chemical composition of the silane films. Lateral diffusion of micro contact printed MTS across the silicon substrate was observed.

Secondly, the pinning/depinning behaviour of the contact line of water droplet on regularly patterned surfaces (circular and linear patterns) was investigated to explain the role surface roughness plays in wettability. We observed that on the patterned surfaces the contact line motion alternates between moving (between the patterns) and a pinning/depinning phase at the pattern. This stick–slip behaviour leads to oscillation of the contact angles. It was found that the behavior of the advancing baseline and contact angle was present as the pattern sizes increases inducing a dependence of the oscillation to the pattern sizes and distributions. Hence, we suggest that the enhancement of the thermodynamic work of

Chapter 2 Wetting and Adhesion Investigations of patterned surfaces

adhesion is related to the lengthening of the contact line due to contact line pinning. In fact, by printing periodic regions of surface chemical contrast, the contact line profile increases as a function of the surface chemistry properties and the perimeter of the pattern region.

In the last part of this chapter, the adhesive properties of linear patterned surfaces of different chemistry and pattern sizes was explored using an FFM (AFM QNM Peak force) and a JKR machine homebuilt. The MTS/Si-OH patterned surfaces prepared by μ CP, showed a similar adhesive response at the macro and nanoscale. Nevertheless, these experiments shows that the adhesion response is greatly affected by the chemistry, relative fractional molecular domain and patterns sizes. Furthermore, using the results of the adhesion measurements at nano and micro-scales, we found also that the introduction of the PDMS strips on a patterned substrate induces a decrease of the adhesive response. This behavior may be attributed to the lubricated character to the adsorbed polymer chain at the interface. Thus, considering the length of the PDMS chains and their high mobility, the surface shows a liquid interfacial character, inducing an increasing in the interfacial adhesion. A second mechanism can be advanced; the adsorption of free PDMS chain on the non- covered MTS zone. In fact, micro-contact printing may lead to non-covered zones in the middle of the printed MTS layer, inducing then a possible adsorption of some PDMS molecules during the grafting process of PDMS film on the substrate. These regions can be considered as an important aspect of the enhancement of adhesion.

In summary, at macro, micro and nanoscales our patterned surfaces exhibited a similar adhesive response suggesting that at different scales, the adhesive behaviour of MTS/Si-OH or MTS/PDMS mixed surfaces are largely dependent on the chemistry and the preparation methods. These results proves that the adhesion is not a consequence of the changes in the surface density.

Chapter 3

Frictional behavior of patterned surfaces

TABLE OF CONTENTS

<u>I-INTRODUCTION</u>	87
<u>II-EXPERIMENTAL</u>	87
<u>II-1-Friction machine</u>	88
II-1.1- Friction Force Microscopy FFM device	90
<u>III-RESULTS AND DISCUSSION</u>	91
<u>III-1- Friction measurements at Macro-Scale</u>	92
III-1.1- Friction measurements on smooth Substrates	92
III-1.2-Friction measurements on MTS/Si-OH patterned surfaces	96
III-1.3- Friction measurements on MTS/PDMS patterned surfaces	98
<u>III-2-Friction measurements using the FFM</u>	101
III-2.1- FFM Friction measurements on smooth substrates	101
III-2.2 - FFM Friction measurements on MTS/Si-OH patterned substrates	104
III-2.3- FFM Friction measurements on MTS/PDMS patterned substrates	107
<u>IV-CONCLUSION</u>	110

Chapter 3 Frictional behavior of patterned surfaces

I-Introduction

Macro- and nanotribological properties are important for many modern technologies, such as medical devices, magnetic storage devices, and micro-electromechanical systems (MEMS) [151-154]. The essentials of tribology have been studied but are still matters of conjecture because of the complexity of friction, lubrication, adhesion, wear and wetting phenomena. In contrast, the origins of tribological phenomena between two surfaces have been elucidated in recent years [155].

In the previous chapter, we evaluated the adhesive response of multiple smooth non-patterned and patterned surfaces at macro, micro and nanoscales. Therefore, we found that in the case of the smooth non-patterned surfaces, chemistry is the predominant aspect in the adhesive response of the surface. In addition to these homogenous substrates, we were interested in studying the effect of alternating hydrophobic and hydrophilic stripes with a large wettability contrast on wetting and adhesive response of mixed surfaces. Hence, we found that the adhesion is not a consequence of the changes in the surface area ratio demonstrating that structured substrates are greatly impacted by the preparation methods.

Nevertheless, we explored as well the dependence of adhesion between a polymer and a rigid tip on the composition of a hydrophobic/ hydrophilic (MTS/Si-OH) system. We found that a regular increase of the adhesive response due to the expansion of the PDMS strips on the surface could be observed. These results suggest that adhesion is greatly affected by the printed strips size and chemistry.

This chapter has first sought to explore the effect of the chemistry and the pattern size on the frictional response between a polymer and a rigid tip on the composition of the patterned substrates. Both a macro-friction test and a FFM measurement were employed to characterize the frictional response of an (hydrophobic/ hydrophilic) mixed silane (MTS/Si-OH) system and a (hydrophobic/ hydrophobic) mixed polymer and silane (MTS/PDMS) covered surfaces. Therefore, we are interested in the following questions: How does a smooth non-patterned surface with the same interfacial chemistry slide, or more generally, what is the frictional response at different scales? What is the value of the friction coefficient at such interfaces? And what are the consequences of the variation of the chemistry and pattern sizes of hydrophobic/ hydrophilic (MTS/Si-OH) system or hydrophobic/ hydrophobic (MTS/PDMS) covered surfaces on the frictional behavior at macro and nanoscales?

After a brief description of our experimental conditions, we present the experimental results, which are discussed in light of the results described in the first chapter.

II-Experimental

In this part, a brief description of the friction machine and the FFM machine are presented.

II-1-Friction machine

The friction measurements were conducted using an apparatus home-built by Scheibert et al [156]. The apparatus is depicted schematically in Fig.3.1. A PDMS lens was attached to a microscope slide where it was secured to a skate. The sample is attached with a double stick tape (pressed against the sample) where is held in place tightly with screws at the front panel. Then, an increasing normal force was imposed on the skate. The area of contact before and during sliding was imaged using a CCD camera (Flare 2M360 MCL, 8 bits, 2048×1088 square pixels at 300 frames/s (100 for sphere/plane and fingertip contacts)). The pixel size in multi-contact images were typically $25 \mu\text{m}$. A typical micrographs of the contact spot is shown in Fig.3.2. The scale for every magnification or tube length was calibrated prior to data analysis. All the images were analyzed with LabVIEW Software Program. For the analysis, the contact radius, a , was calculated either by using the total area of the contact spot which was obtained from the images assuming a circular area or by using an average diameter which was measured from the number of the pixels on the images. The two calculations were compared for the same image to ensure an accurate value of the radius. This analysis was repeated for every image that corresponds to a specific force.

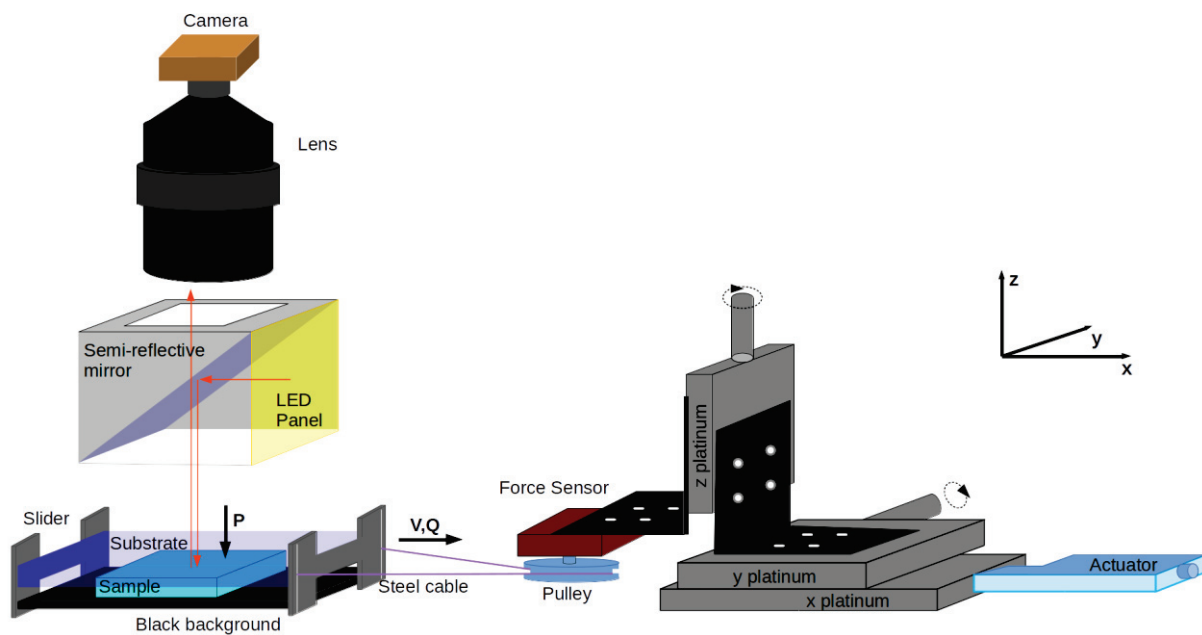


Figure 3. 1 Three-Dimensional Computer graphic of the components of the Friction machine.

The normal forces was applied through a steel wire attached to a pulley using a Newport LTA-HL motors (the pulley is attached to a force sensor as well attached to a Newport translation stage), respectively, controlled by a SMC100CC driver. The tangential force Q is measured using a stiff piezoelectric sensor (Kistler 9217A) placed close to the motor. The Q signals are digitized and recorded at a sampling rate of 3 kHz (1 kHz for sphere/plane contacts and fingertip contacts). The normal and tangential forces, P and Q , are measured with 0.1 and 1mN accuracies, respectively. For planar rough

Chapter 3 Frictional behavior of patterned surfaces

contacts, the slider is driven through a horizontal steel wire of stiffness $9700 \pm 200 \text{ N/m}$. For sphere/plane contacts, the slider is driven rigidly through the length of a cantilever beam of bending stiffness $52 \pm 1 \text{ N/m}$. The readout from the capacitive sensor was recorded using the LabVIEW Software Program. The radii of curvature, R , of each lens were determined prior to contact.

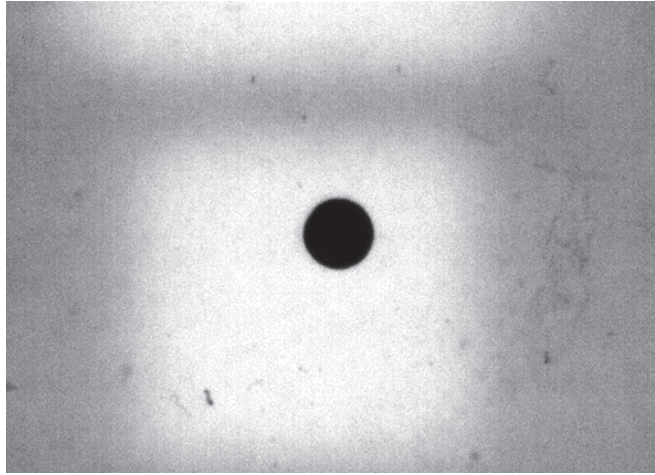


Figure 3. 2 A micrograph of a friction measurement.

The tangential force and the contact area of a PDMS smooth surface were plotted as a function of time as seen in Fig.3.3. At first, the area values is constant A_0^r , Then following the increase of the tangential force we notice an decrease of the contact area until a minimum threshold A_s^r , which can be attributed to the slip established at the interface. In our case, an 8 % of shrinking in the contact area with the augmentation of the tangential force until the maximum static friction level called F_s

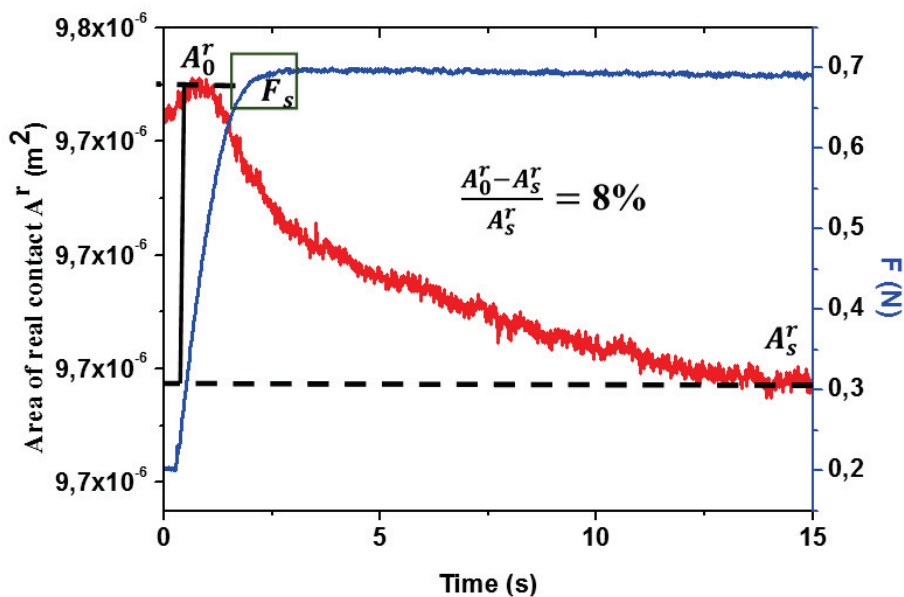


Figure 3. 3 The temporal evolution of the tangential force and the contact area of an adsorbed layer of PDMS. The load used here is $2,117 \text{ N}$ and the velocity is $0,1 \text{ mm/s}$

Chapter 3 Frictional behavior of patterned surfaces

II-1.1- Friction Force Microscopy FFM device

Friction Force Microscopy (FFM) is an interesting mode of scanning force microscopy AFM used for the measurement of the lateral forces in small sliding contacts. In fact, the original idea is to measure the local interactions with a very tipped probe for obtaining microscopic data on surfaces in lateral resolution. In FFM, the summit of a sharp tip is brought into contact with a sample surface, and the lateral forces are recorded while tip and sample slide relative to each other Fig.3.4. There are several convenience in using the FFM. First, the understanding of friction between sliding surfaces in general is a very complex problem due to multi-contact character between surfaces and the importance of lubricants and third bodies in the sliding process. By reducing one surface to a single asperity, preparing a well-defined structure of the sample surface, and controlling the normal load on the contact, the complexity of friction studies is greatly reduced and basic insights into the relevant processes can be obtained. Furthermore, the lateral resolution allows revealing several tribological contrasts caused by material differences on heterogeneous surfaces.

The experimental field of FFM has been at first explored by Mate et al. [157]. The group built a scanning force microscope where the lateral deflection of a tungsten-wire could be recorded using an optical interferometry. When the etched tip of the tungsten wire slid over a graphite surface, lateral forces exhibited a modulation with the atomic periodicity of the graphite lattice. Furthermore, an essentially linear load dependence of the lateral force could be established.

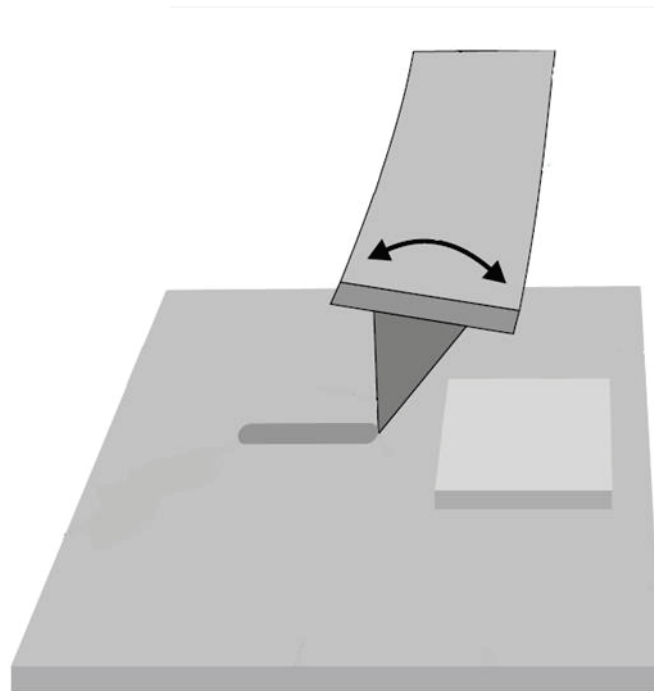


Figure 3. 4 A schematic of the experimental friction force.

In our case, all measurements were performed using the so-called friction loop: The lateral force acting on the tip is recorded for a certain distance of scanning in the direction perpendicular to the long

Chapter 3 Frictional behavior of patterned surfaces

cantilever axis and for the reverse direction. The area in the loop represents the dissipated energy, and the area divided by twice the distance is the mean lateral force. It is always very instructive to record the topography signal of forward and backward scan at the same time, as differences will reveal cross talk between normal and torsional bending of the cantilever. For our experiments where is carried out in ambient environment, the main contribution to adhesion are typically capillary forces which can be affected strongly by the humidity and on the hydrophobicity of the surface [158].

A typical example of a silicon tip scanning on a heterogeneous sample is shown in Figure 3.5 (a). In fact, we can observe a single-layer graphene (area A) deposited on a SiO₂ substrate (area B). The hysteresis loop, as shown in Figure 3.5 (b), enclosed by the forward and backward lateral signals is called a friction loop.

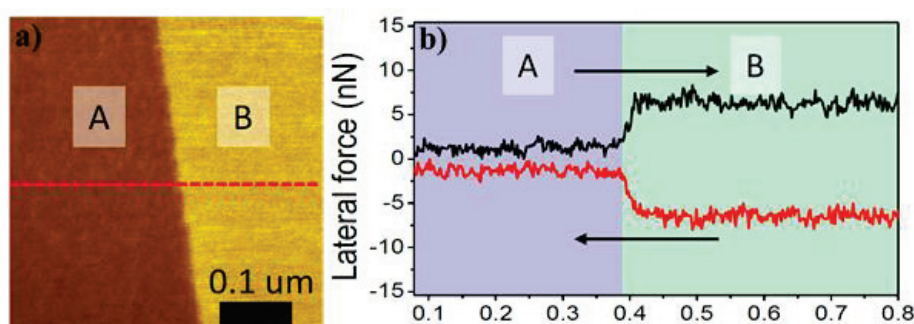


Figure 3. 5 (a) A typical friction force image from a Si tip scanned over an area consisting of two materials, graphene on A and SiO₂ on B, which exhibit distinct frictional behaviors. Lower brightness corresponds to lower friction. (b) A typical friction loop taken from the red dash line in (a). Black arrows indicate the scan direction.

The friction force is given by $F_{Friction} = \frac{F_{Trace} + F_{Retrace}}{2}$ where F_{Trace} and $F_{Retrace}$ termed as the lateral force in the forward and backward directions, simultaneously. Since the difference of the friction loop represents the friction force magnitude, we can presume that in this case the material A is exhibiting a lower friction force than material B. From such a friction loop, a many important physical parameters can be extracted. First, the mean friction force can be calculated and the maximum lateral force (the force at which slip occurs, which is the static force of friction) can also be determined. Second, when integrated over the scan distance and divided by the length scanned, one obtains the energy dissipation per unit length or unit cell of the material.

III-Results and discussion

In this part, the friction measurements on the different patterned systems (MTS/Si-OH, MTS/PDMS) are illustrated.

III-1- Friction measurements at Macro-Scale

III-1.1- Friction measurements on smooth Substrates

Different friction tests were carried out on smooth non-patterned surfaces of homogeneous stiff and compliant samples. Fig.3.6 shows optical micrographs of the contact region (darker area) between the glass slide sample and the PDMS beads. Fig.3.6 (a) shows the initial contact before the sample is sheared relative to beads – the area is nearly circular. Fig.3.6 (b) shows the contact area during sliding. We observe that the contact area decreases in size and changes to an oval shape, and the bead slides smoothly on the material.

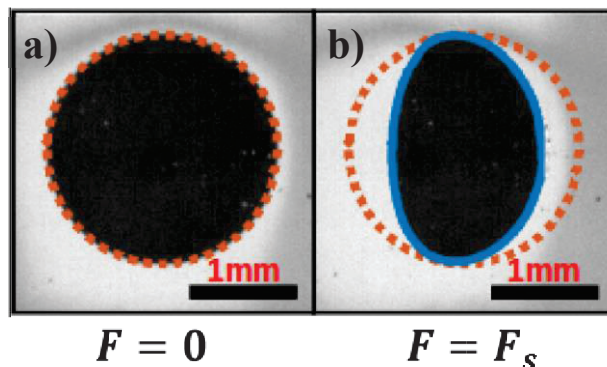


Figure 3. 6 (a) Initial contact before the sample is sheared relative to beads (the area is nearly circular $F=0$). (b) Contact area during sliding ($F=F_s$).

Chapter 3 Frictional behavior of patterned surfaces

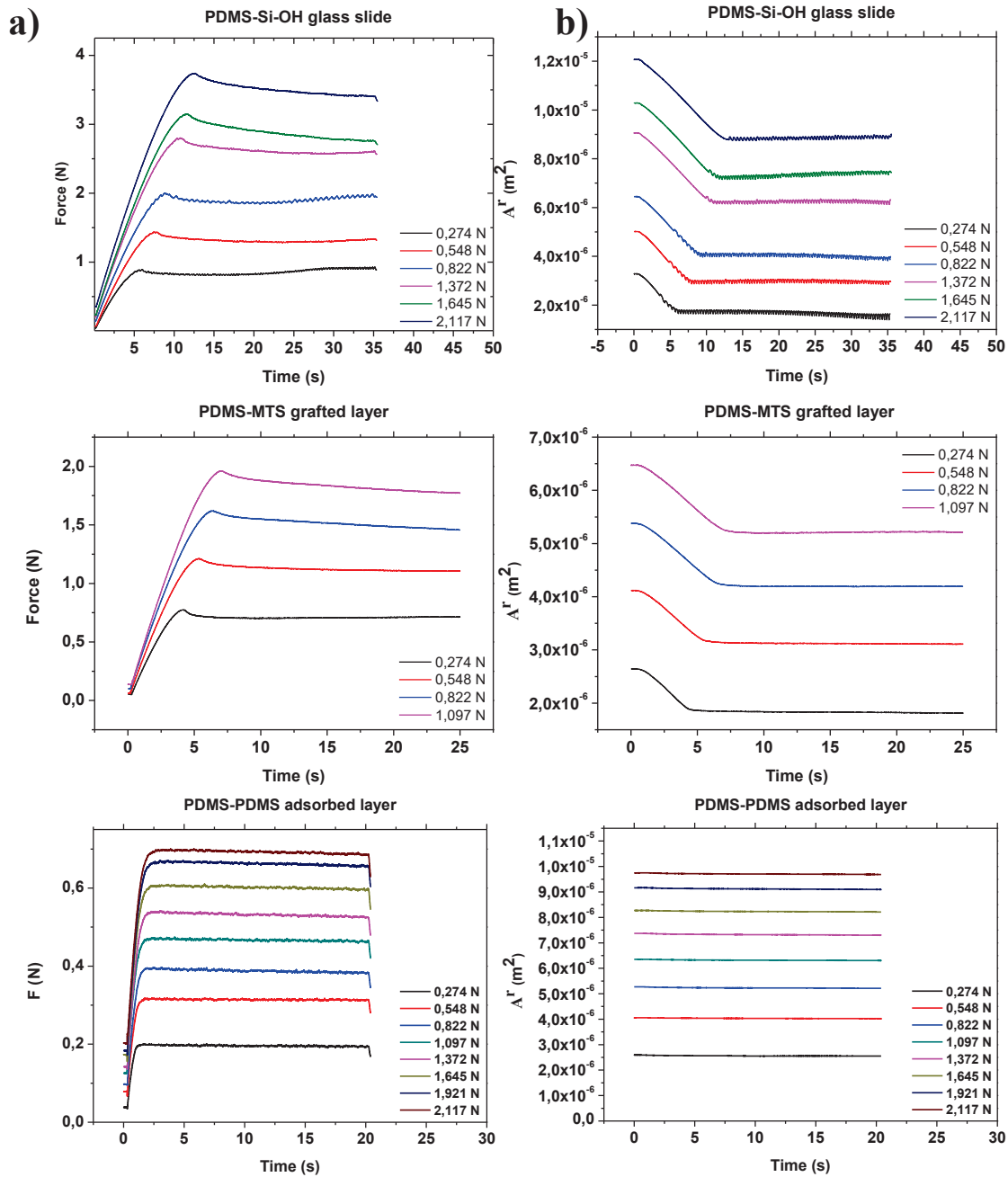


Figure 3. 7 (a-b) The temporal evolution of the lateral force and the real contact using several load for the different smooth surfaces.

Lateral sliding force was measured while applying a constant normal force (P) ranging from $0,3\text{ N}$ to $2,2\text{ N}$. The lateral velocity (v) was fixed at $0,1\text{ mm/s}$. The interfacial contact area was imaged through an inverted microscope allowing for the evaluation of changes in the contact area and the associated frictional mechanism by which the two surfaces displaced. Fig.3.7 shows respectively the typical results of a friction test performed on different smooth substrate. Where the temporal evolution of the lateral force F and the real contact area A^r are shown respectively. Following these conditions and as explained above, we can notice that those graphs display a classical behavior. In fact, the real area is measured systematically at the same time that the tangential force is recorded. We can clearly

Chapter 3 Frictional behavior of patterned surfaces

observe that as the lateral force increases the real contact area decreases which can be attributed to the slip established at the interface.

To investigate the frictional behavior, we consider a standard model for friction $F_s = \epsilon_s A_s^r$, [159] where F_s is the sliding force at the maximum static friction level, A_s^r is the real contact area at the same level and ϵ_s is the critical interfacial shear strength. In fact, we can assume that the real contact area A^r is the predominant aspect in the control of the frictional behavior of the different smooth surfaces.

Let us concentrate at first on the effect of the surface chemistry on the friction behavior. Fig.3.8 shows the real contact area as a function of the lateral forces for several normal load P for the different non-patterned substrates. A linear fit (blue line) gives the inverse of the critical shear stress

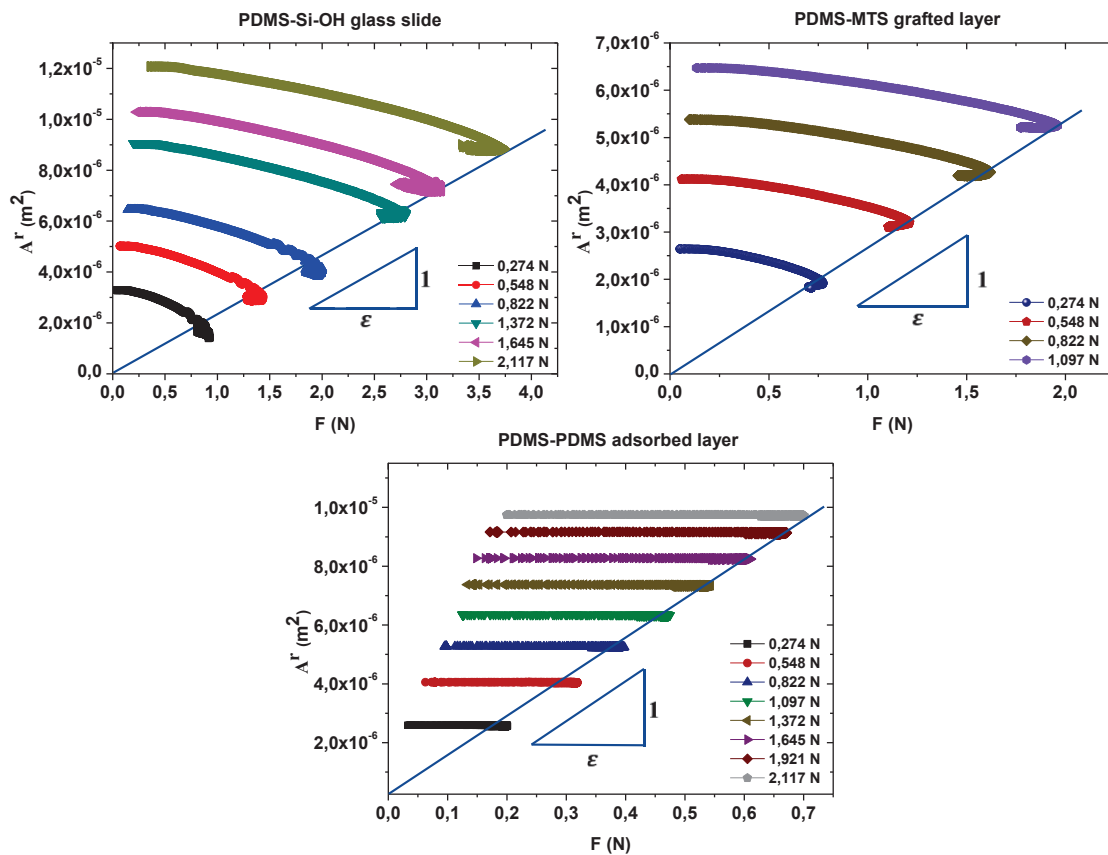


Figure 3. 8 The real contact as function of the lateral force of for the different smooth surfaces for the different smooth surfaces.

From Fig.3.9 and Fig.3.10, it could be observed respectively that all smooth systems exhibit improved friction behaviour than the uncoated silicon glass. SiO_2 substrates shows the highest friction values. At this scale, the friction is largely influenced by its wear [147, 160]. Considering the theory proposed by Bowden and Tabor [161] the real contact area clearly influences the friction under a single asperity contact $F_s = \epsilon_s A_s^r$. Thus, we can assume that any augmentation in the contact area would lead to an increase in friction force, which results at higher coefficient of friction. Further, The Si–OH surface reveals the highest friction response, which may be ascribed to the adsorbed water adhered by the hydrogen bonds [162].

Chapter 3 Frictional behavior of patterned surfaces

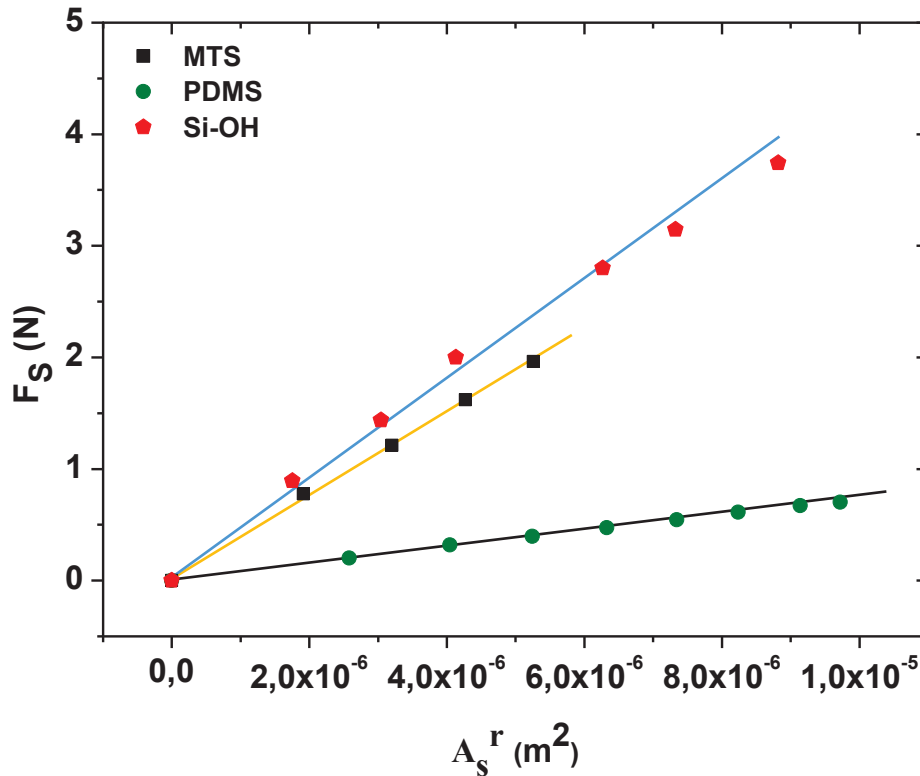


Figure 3. 9 The maximum static friction F_s versus is the real contact area A_s^r for different smooth surfaces.

Further, the contact area in the case of the MTS and the PDMS surfaces would be comparatively lower with respect to that of Si-substrate because of their lower interfacial energy. The weak polarity of tailed methyl molecule as a termination of the chain can weaken the van der Waals attractive forces. The short chain length with weak Van der Waals interaction usually results in more energy dissipating modes (chain bending and tilting, rotations, formation of gauche defects, etc.), which can be excited during frictional sliding [163]. In the case of the PDMS thin film layer, Brown et al illustrated that polymer mobility is a major factor in setting the interfacial stress and friction force at polymer surfaces [164]. Specifically, they investigated the interfacial friction forces between a polydimethylsiloxane (PDMS) network sliding against ultrathin PDMS films comprised of chains end-tethered to a polystyrene surface, and determined that while shorter, stiffer chains could penetrate the network and increase the interfacial friction force, longer chains with higher mobility showed more liquid-like interfacial qualities, lowering the interfacial shear stress [164].

Chapter 3 Frictional behavior of patterned surfaces

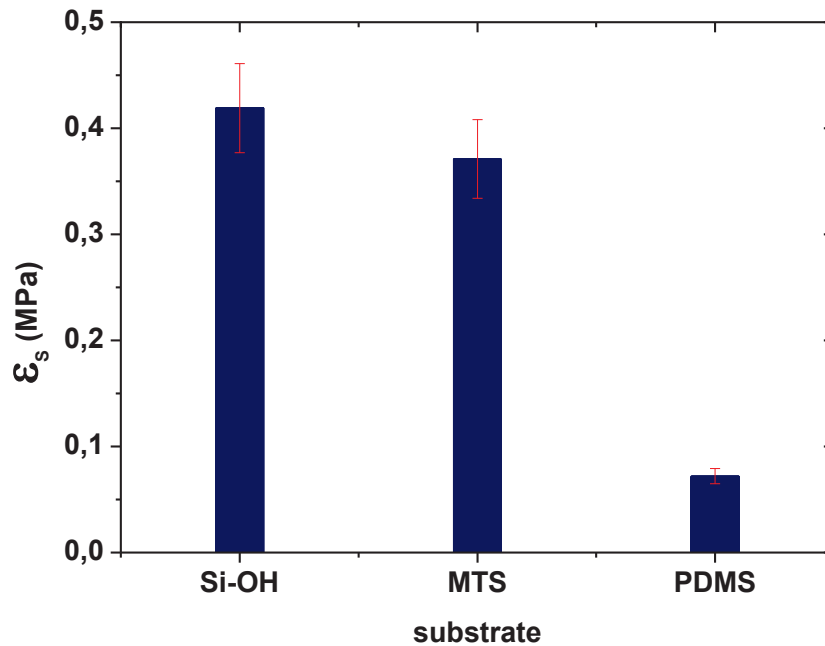


Figure 3. 10 critical shear stress of a PDMS bead for the different non-patterned surfaces

This study evidences clearly the low friction values of the PDMS surface compared to MTS substrate. Furthermore, the effect of pendent chains in PDMS networks can be greatly considered. In fact, Galliano et al [165] found that networks with larger numbers of pendent chains have lower friction stresses. The authors concluded that the dangling ends create a surface layer with low shear stress and poor cohesion. Thus by incorporating a controlled concentration of pendent chains in the micro-film systems, a lower coefficient of friction should be obtainable.

Moreover, it is worthwhile to note that though the hydrophobic nature of the SAMs allows them to perform better than the Si-OH surface, the short chain length of the MTS monolayers clearly explain the high friction value compared to the PDMS substrates.

III-1.2-Friction measurements on MTS/Si-OH patterned surfaces

Let us consider now the linear patterns (MTS/Si-OH) where a PDMS bead was moved in a parallel direction of the linear patterns of the MTS/Si-OH strips. Fig.3.11 shows temporal evolution of the lateral force and the real contact using several load and the maximum static friction F_s versus the real contact area A_s^r for the different pattern sizes. Using these graphs, a value of the critical shear stress was deduced. Hence, we can clearly notice that the introduction of MTS/Si-OH patterns on the surface induces a clear decrease of the critical shear stress values compared to smooth non-patterned samples (MTS organosilane layer and the activated silanol substrate Si-OH).

Chapter 3 Frictional behavior of patterned surfaces

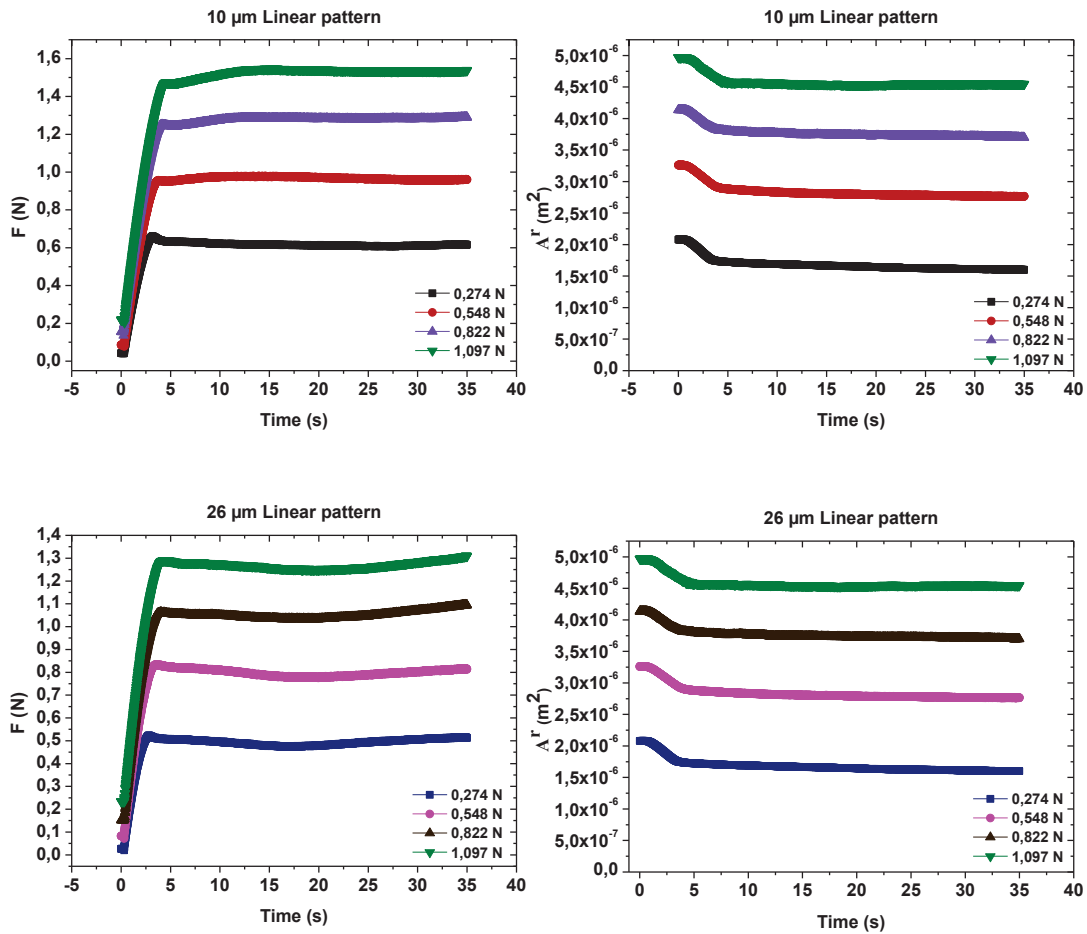


Figure 3. 11 The temporal evolution of the static friction F and the real contact area A^r for the different Patterns sizes of the MTS/Si-OH surfaces.

In the present case, it is known that methyl alkylsilane layers have stable structure and lower surface free energy compared to the hydroxyl termination (-OH). The structure of the two-component patterns may be the main factor that influences the friction coefficients.

Chapter 3 Frictional behavior of patterned surfaces

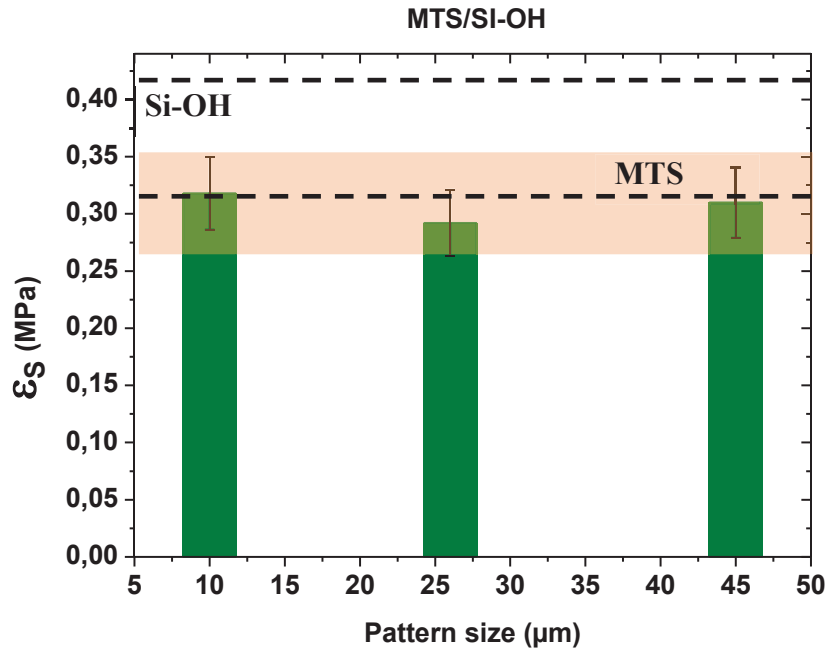


Figure 3. 12 critical shear stress of a PDMS bead for the different Patterns sizes of the MTS/Si-OH surfaces. The dashed lines represents the average values of the critical shear stress of the MTS and Si-OH smooth surfaces.

As explained in the second chapter using the Cassie–Baxter wetting model, that the obtained patterns reduces the contact of the liquid with the substrate resulting in the reduction of surface free energy. The reduction of surface free energy reduces the friction coefficient value due to the reduction of capillary forces, and consequently, changes in the adhesive component of friction. These aspects could explain the decrease of the coefficient of friction of the MTS/Si-OH covered surface, compared to the non-patterned surfaces. However, a similar frictional behavior were observed for the different patterned surfaces (Fig.3.12). In fact, a slight decrease of the coefficient of friction of the MTS/Si-OH patterns compared to the non-patterned surfaces could be observed. Hence, a negligible change on the friction behavior can be noticed as the pattern size decreases. In fact, the weak polarity of tailed methyl molecule and the short length of the methyl chain resulting possibly to a weakening of the van der Waals attractive forces. Thus, a comparable critical shear stress of both systems are observed and can explain clearly the slight change of the friction of the different patterned MTS/Si-OH substrates. This frictional response can be explained by the high loads and sliding force used in these experiments. In fact, the similar critical shear stress extracted from our sliding measurements suggests that these measurements are greatly sensitive to the mechanical proprieties as substrates stiffness and young modules compared to the chemicals layers introduced to the surface thought micro-contact printing.

III-1.3- Friction measurements on MTS/PDMS patterned surfaces

For the linear patterned substrates with parallel strips (MTS/PDMS), Fig.3.13. shows the contact area at zero load ($\sim 0N$). In fact, this contact area is dark and we see the features of the linear patterns, which

Chapter 3 Frictional behavior of patterned surfaces

can be explained by the same refractive index between the bead and the substrates.

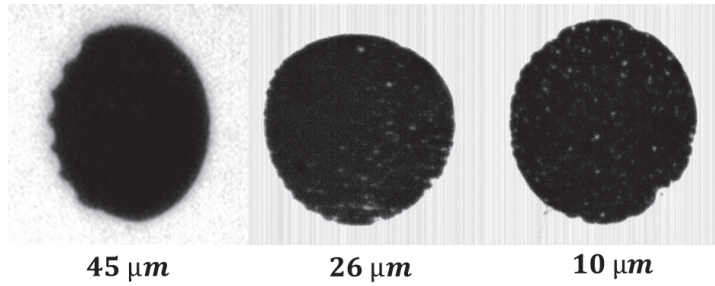


Figure 3. 13 Micrographs of the contact on substrates covered with linear strips of various patterns size for the MTS/PDMS substrates.

The temporal evolution of the lateral force and the real contact using several load and the maximum static friction F_s versus the real contact area A_s^r for the different pattern sizes are shown respectively in the Fig.3.14 and Fig.3.15.

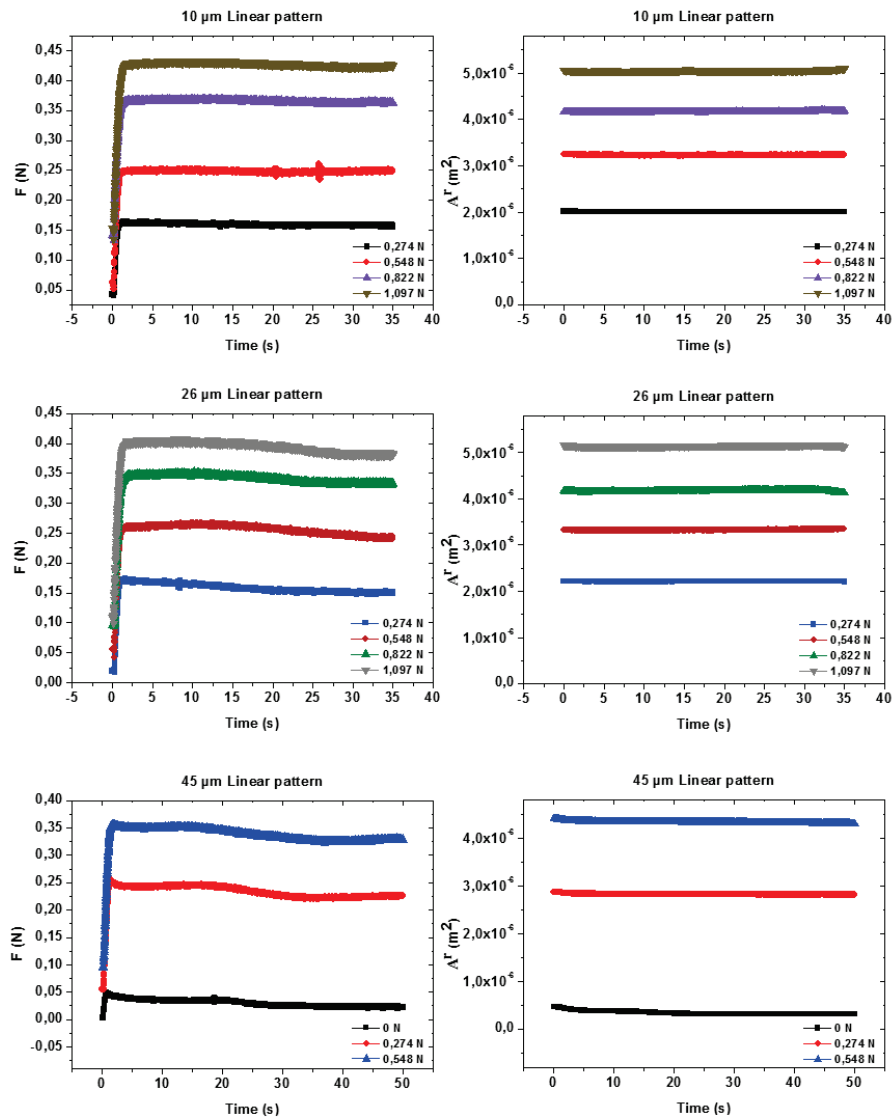


Figure 3. 14 The temporal evolution of the static friction F and the real contact area A^r for different Patterns sizes of the MTS/PDMS surfaces.

Chapter 3 Frictional behavior of patterned surfaces

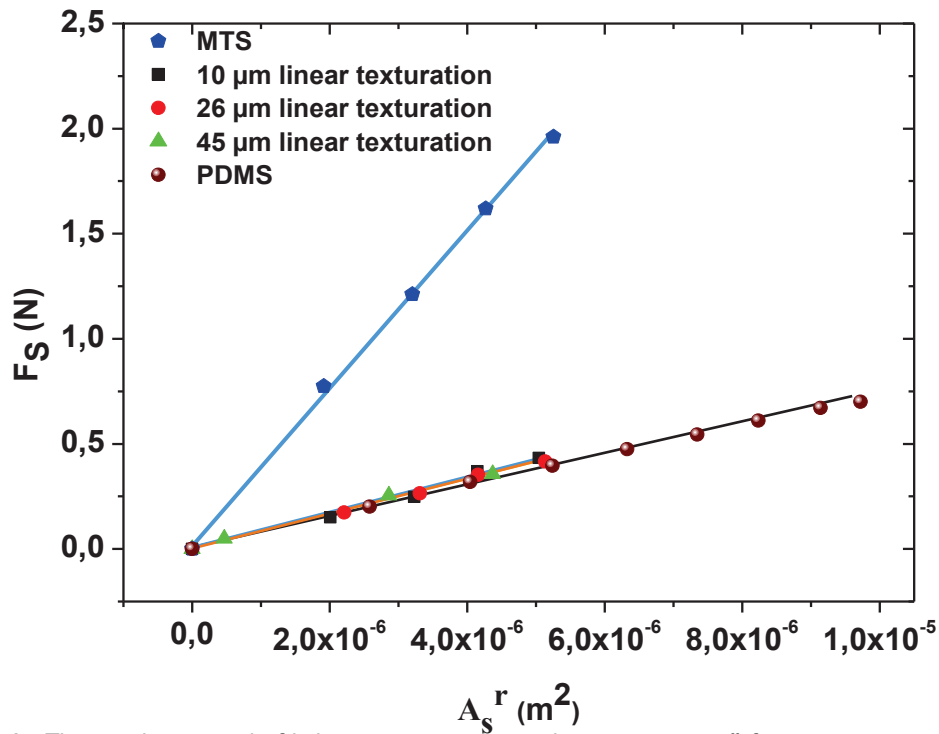


Figure 3. 15 The maximum static friction F_s versus the real contact area A_s^r for (10,26,45 μm) patterned surfaces and the MTS, Si-OH smooth surfaces.

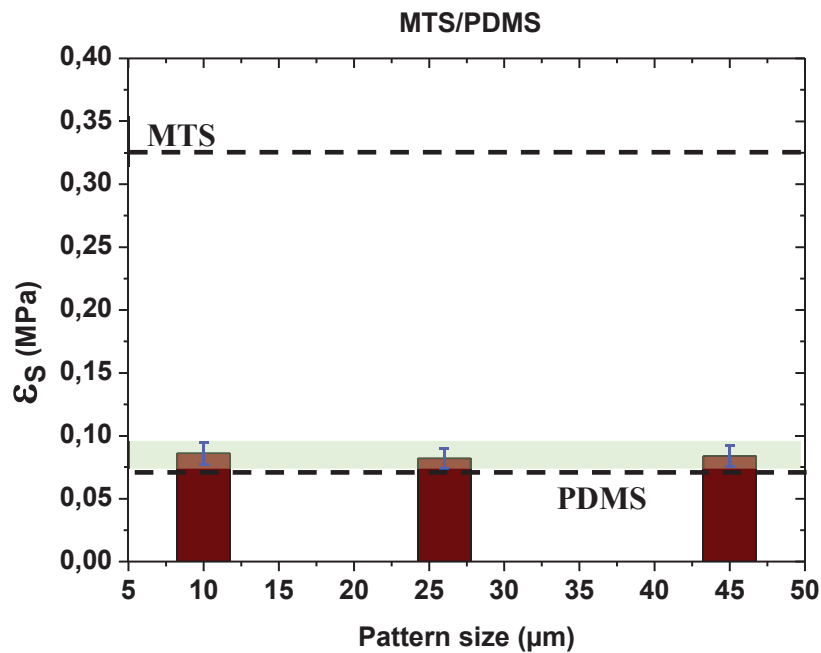


Figure 3. 16 Average critical shear stress of a PDMS bead for the different Patterns sizes of the MTS/PDMS surfaces. The dashed lines represents the average values of the critical shear stress of the MTS and PDMS smooth surfaces.

The critical shear stress values obtained for different patterned substrates are presented in the Fig.3.16. In fact, we can clearly notice that MTS/PDMS patterns increase the critical shear stress values of a 15%

Chapter 3 Frictional behavior of patterned surfaces

in comparison with the silicon surface covered by PDMS layer. Despite this augmentation the critical shear stress values stays negligible compared to the silicon surface covered with MTS layer. In the present case, our system is consisted of two layers with the same end group ($-\text{CH}_3$) but with different chain lengths. Hsu [166] shows that such surfaces provides greater opportunities for more effective protection in comparison with one-component layer since the adsorption is governed by the functional groups, the lower half of the film will be closely packed behaving like a solid. Hsu explained the frictional properties of mixed films consisted with different chain length compounds and proposed that molecules with longer chain length will have part of the molecules sticking above the shorter compounds behave like a liquid. In turn, short chain molecules can form a solid layer. Thus, a film with both liquid and solid proper-ties can be constructed. The liquid film provides damping and low friction and the solid films provide load supporting strength. Furthermore, we can consider that the mechanical proprieties of the substrates (young modules and stiffness) greatly influence our measurements of the frictional behavior, inducing then different values of the critical shear stress.

In summary, we observed that as the strip sizes increases, the frictional behavior present a negligible changes due the high influence of the substrates mechanical proprieties. Thus, the use of the friction machine does not however evidences the effect of the chemistry on the frictional response. Then, the use of low load could reduce the impact of the mechanical proprieties of the substrate. Thus as a mean to extract different information about the impact of the chemistry on the frictional behavior, we explored in the next part the frictional response of these patterned substrates using an FFM machine.

III-2-Friction measurements using the FFM

III-2.1- FFM Friction measurements on smooth substrates

The friction force was measured in Lateral Force Microscope (LFM) mode using a conventional cantilever with a Si_3N_4 tip ($R \sim 20 \text{ nm}$). Friction measurements were conducted under applied normal loads in the range of $0-50 \text{ nN}$ and at the scanning speed of $120 \mu\text{m/s}$ for the scan size of ($60 \times 60 \mu\text{m}^2$) Fig.3.17.

Chapter 3 Frictional behavior of patterned surfaces

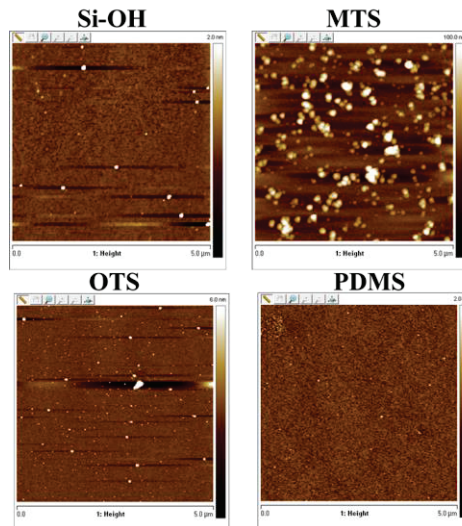


Figure 3. 17 2D AFM images of the Topography ($60 \times 60 \mu m^2$) for the different non-patterned surfaces. The different Patterns sizes of the MTS/PDMS surfaces.

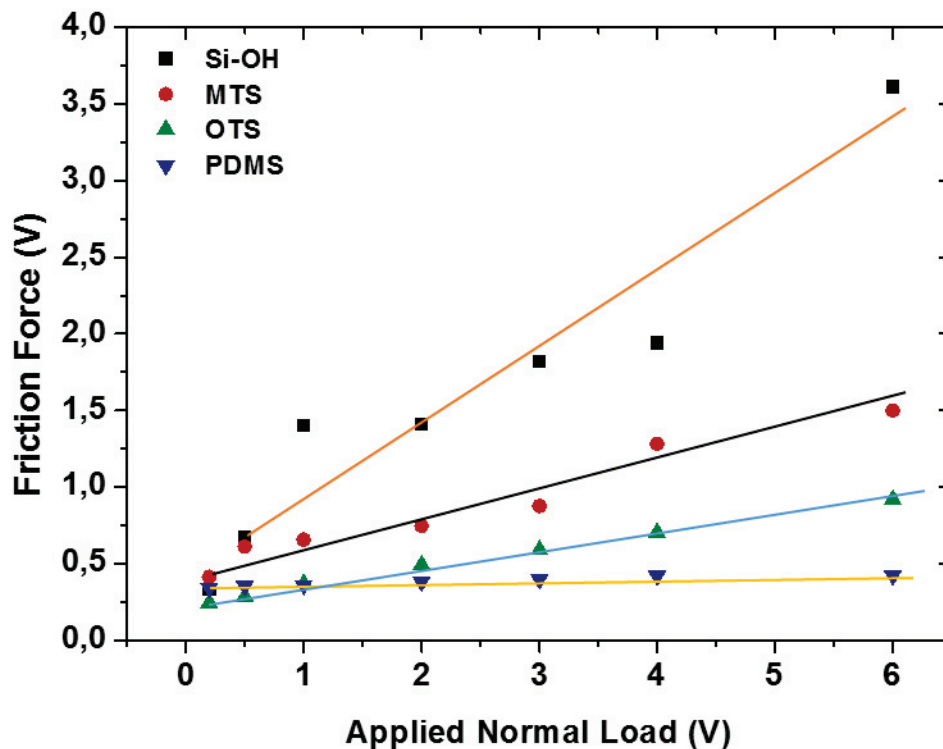


Figure 3. 18 Lateral force friction as a function for the applied normal load for the different non-patterned surfaces

Let us concentrate at first on the influence of the surface chemistry on the friction behavior. Fig.3.18 shows lateral force friction as a function for the applied normal load for the different non-patterned surfaces. We should note the these samples were prepared using the Self-assembled monolayer technic, which explains the differences in the relative friction coefficient shown bellow between these substrates and the samples prepared using the micro-contact printing approach (different grafting density non-identical homogeneity...). Thus, we can observe respectively that all smooth systems exhibit improved

Chapter 3 Frictional behavior of patterned surfaces

friction behavior than the Si-OH silicon glass. In fact, Si-OH substrates shows the highest friction values. At this scale, the friction is greatly affected by the adsorbed water adhered on the interface of the surface [162]. In fact, the high friction of those surfaces evidences clearly that solid–solid adhesion is a dominant character on the interface of the Si-substrate, which influence greatly the friction [167]. The occurrence of solid–solid adhesion in Si-surfaces is typically attributed to the high interfacial energy of those surfaces. Further, we can clearly notice that the OTS coated surface display a lower friction then the MTS grafted surface. Which it can be explained by the difference in the chain length between both systems Fig.3.19. In fact, an important feature in the monolayers that gives rise to low values of friction is their molecular chains. These chains exhibit significant freedom of swing and thereby rearrange along the sliding direction under shear stress, which eventually yields a smaller resistance during sliding resulting in lower friction values [154, 168]. Finally, the PDMS adsorbed layer present the lowest friction in comparison to the different surfaces, which can be ascribed to the lubricated character to the adsorbed polymer chain at the interface. Hence, considering the length of the PDMS chains and their high mobility, the surface shows a liquid interfacial character, inducing a lowering in the interfacial friction.

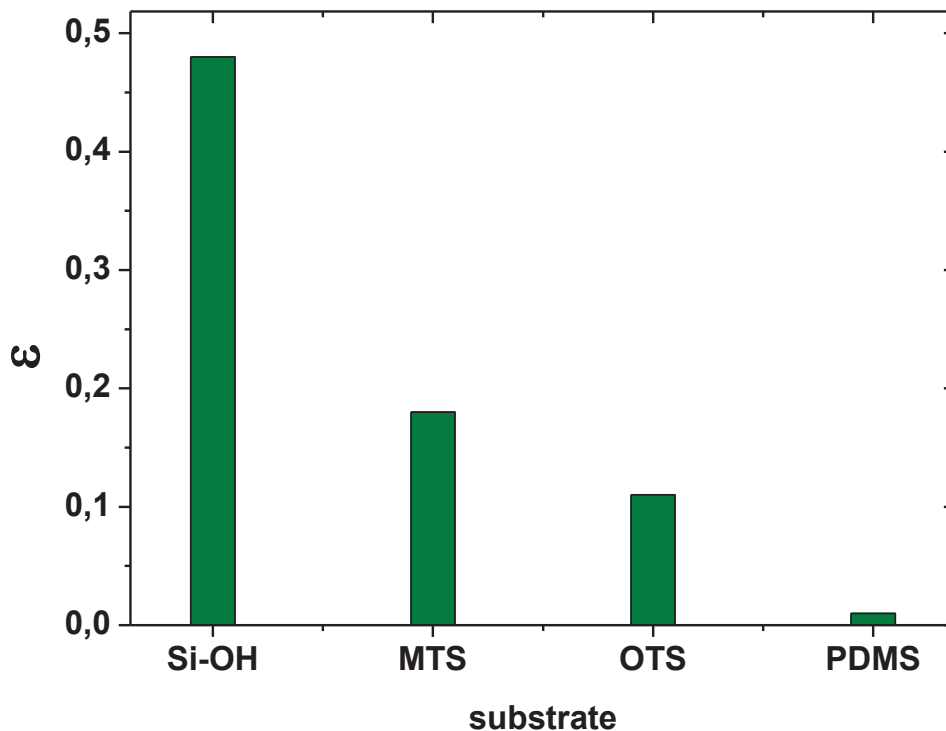


Figure 3. 19 Relative coefficient of friction for the different non-patterned surfaces

Considering the limited imaging scale (Max $120 \times 120 \mu\text{m}^2$) of the FFM, we have chosen to work on the smallest linear patterns defined by the 10 and 26 μm linear strips with different chemistry (MTS/Si-OH, MTS/PDMS).

III-2.2 - FFM Friction measurements on MTS/Si-OH patterned

substrates

Two-component, microscopically line-patterned organosilane monolayers of MTS and Si-OH were prepared by μ CP process Fig.3.20. The difference in height between the MTS and Si-OH monolayers was less than 0-5 nm. The Si_3N_4 tip was slid either parallel with or perpendicular to the direction of the line pattern of the two-component, as shown in Fig.3.21.

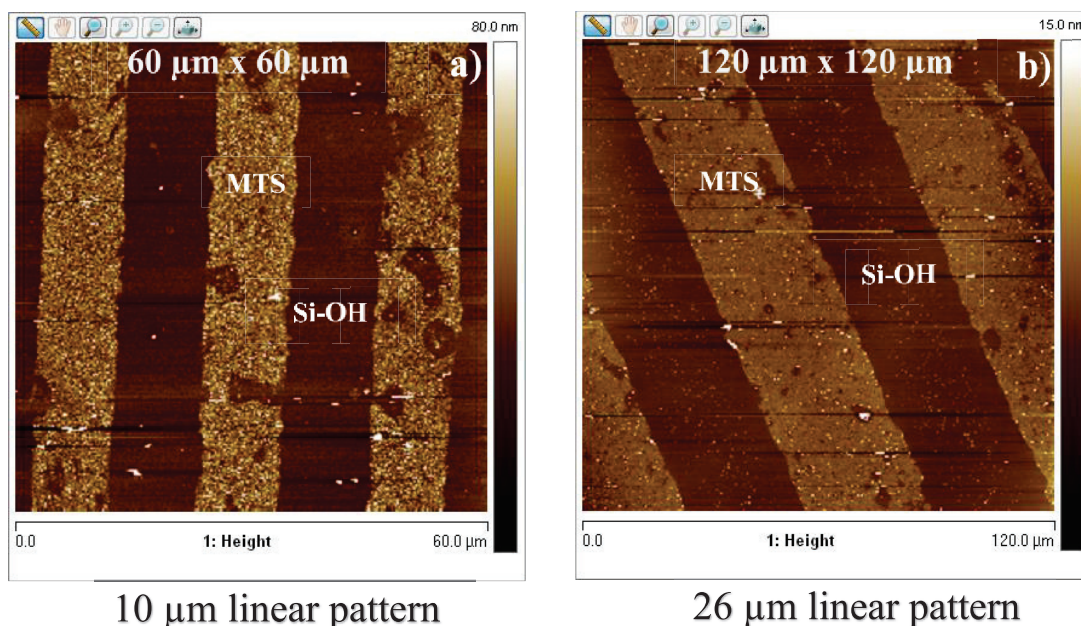
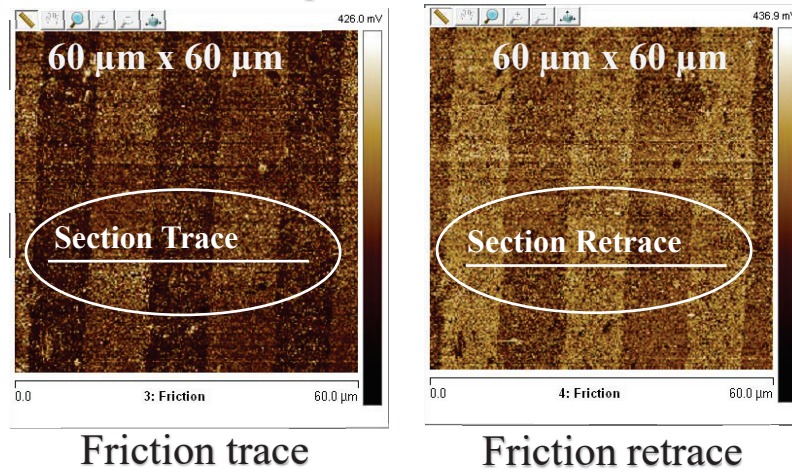


Figure 3. 20 2D AFM images of the Topography ($60 \times 60 \mu\text{m}^2$, $120 \times 120 \mu\text{m}^2$) for the different patterned surfaces (MTS/Si-OH).

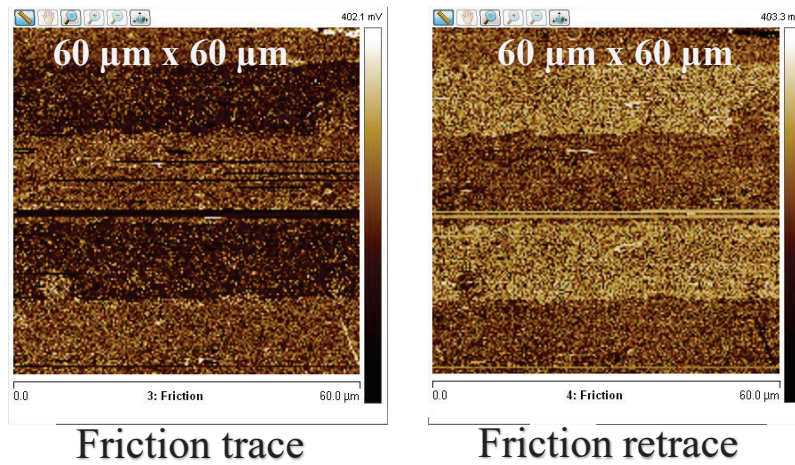
The scan rate was 120 $\mu\text{m}/\text{s}$ for a various normal load ranging from (1.5 nN up to 46 nN). As expected the measured friction force is linearly proportional to the external applied load [169]. This response is characteristic of a Coulombic behavior. Moreover, the magnitude of the friction coefficient (0.058) in perpendicular scanning was slightly lower than that (0.068) in parallel scanning. This results can be ascribed to the calculation methods of the relative friction coefficient, which takes into account the average values of each strip response Fig.3.22. Thus, in the case of parallel sliding, the contact component of the Si_3N_4 tip and monolayer surfaces was always the same; hence, there was a negligible change in frictional behavior along the strips. On the other hand, with perpendicular scanning, the contact component periodically varied as the friction tip advanced. Then, we can suggest that certain resistance can appear at the interface between the MTS and Si-OH monolayers. This result was confirmed by wetting anisotropy developed in the chapter II.

Chapter 3 Frictional behavior of patterned surfaces

a) Friction \perp to the linear pattern



b) Friction \parallel with the linear pattern



c) Friction loop \perp to the linear pattern

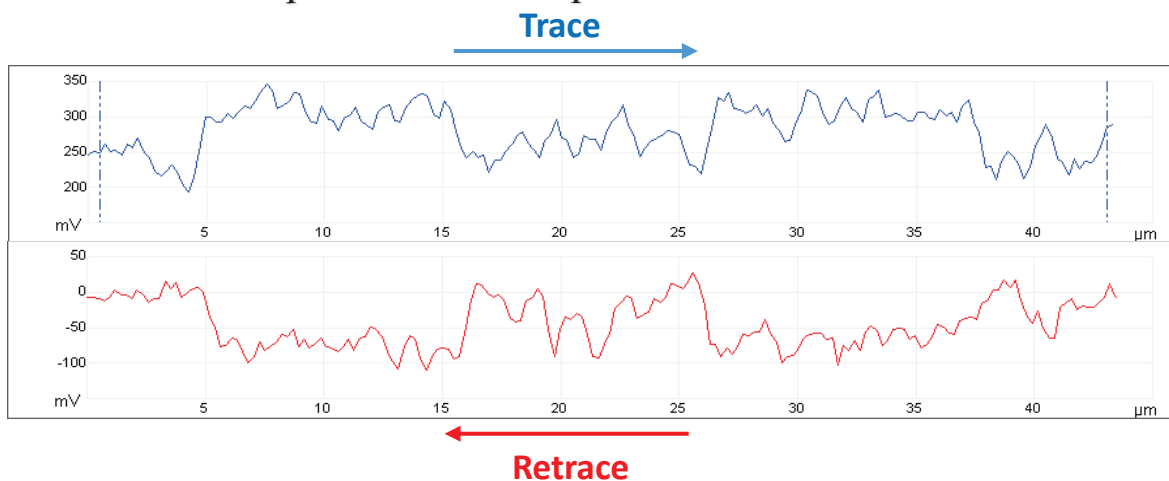


Figure 3. 21 (a-b) 2D AFM images of the Friction ($60 \times 60 \mu\text{m}^2$) of the perpendicular and parallel scanning respectively of the of Si_3N_4 tip to the 10 μm linear strips. **(c)** Friction loop of the perpendicular parallel sliding for the trace and retrace sections.

Chapter 3 Frictional behavior of patterned surfaces

We should note that the Si_3N_4 tip might be easier to move along the line direction. This was the first observation of friction force originating from the surface chemical composition of a flat surface.

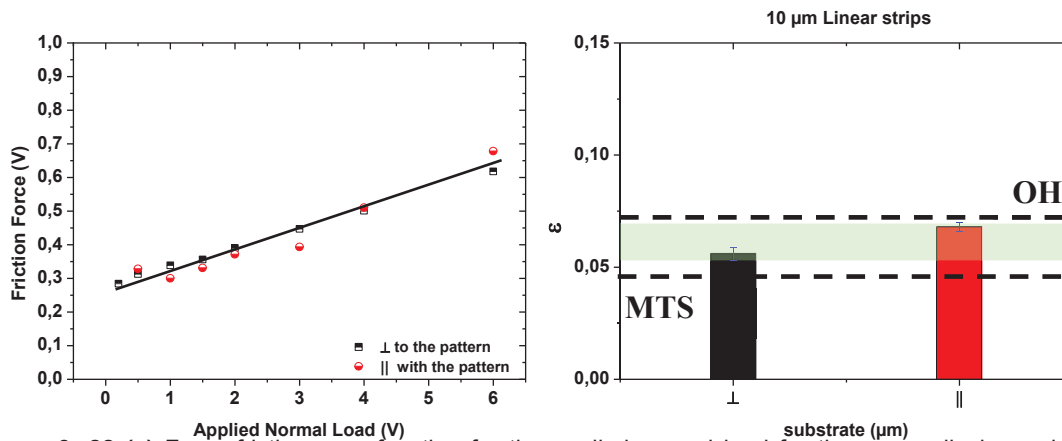


Figure 3. 22 (a) Force friction as a function for the applied normal load for the perpendicular and parallel scanning of the of Si_3N_4 tip to the 10 μm linear strips. **(b)** Relative coefficient of friction of the sliding of the Si_3N_4 tip on the different Patterns sizes of the MTS/Si-OH surfaces. The dashed lines represents the average values of the relative coefficient friction of the MTS and Si-OH smooth surfaces.

In the case of the friction measurements on the 26 μm linear pattern, we consider that the perpendicular or parallel scanning displays the same coefficient friction. Thus, in the following section only the results of the perpendicular sliding was presented Fig 3.23. Moreover, the averaged frictional response is found to be more sensitive to the chemistry and relative surface fraction of the molecular domains than to the size and distribution of patterns. This is shown by the regular increase of the tip/substrate friction on these (MTS/Si-OH)-patterned surfaces, with the surface fraction of the hydrophilic molecular species (Si-OH). Moreover, a clear difference in the values of the relative friction coefficient extracted from the results of the patterned samples (lower than the non-patterned substrates) was detected. We can attribute these differences to the higher grafting density on the non-patterned surfaces (prepared by an organosilane solution) compared to the patterned samples (prepared using μCP).

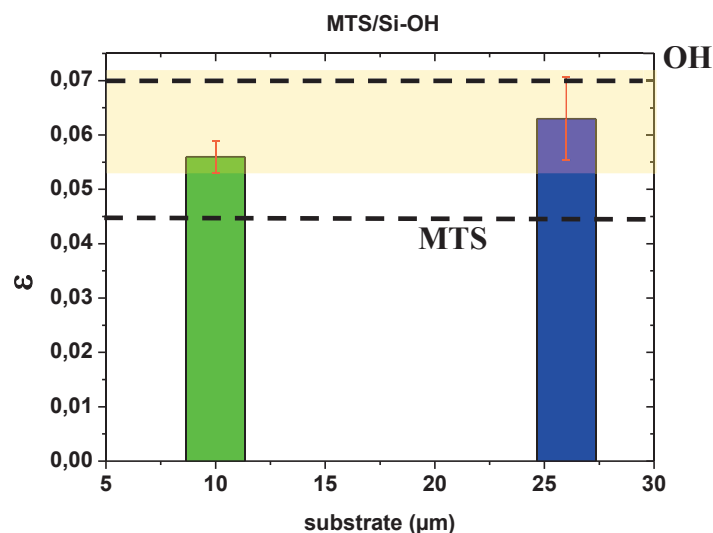


Figure 3. 23 Relative coefficient of friction of a Si_3N_4 tip for the different Patterns sizes of the MTS/Si-OH surfaces. The dashed lines represents the average values of the relative coefficient friction of the MTS and Si-OH smooth surfaces.

Chapter 3 Frictional behavior of patterned surfaces

Fig.3.23 illustrate the evolution of the relative coefficient friction as function of the pattern size. The results show that the relative coefficient friction slightly increases as the surface coverage of Si-OH for micro-patterned surfaces. The friction forces increase with the magnitude of the adhesive interaction of the SAMs and the tip. As a result, the greater the surface fraction of Si-OH in the thin film, the greater the friction response, in good agreement with the literature [170]. Lopez et al. have also prepared striped micro-patterned of methyl and hydroxyl terminated SAMs and studied correlation between friction and grafted mole fraction [170]. The friction seems to increase steadily with the mole fraction of one molecule. The dependence of friction on the chemical composition of this geometrical patterned coating can be correlated by a Cassie-type relation for heterogeneous wetting [137]: the frictional response of the patterned surface composed of two uniformly distributed components is proportional to the surface fraction of each component, $\epsilon_{\text{patterned surfaces}} = f_{\text{MTS}} \epsilon_{\text{MTS}} + f_{\text{OH}} \epsilon_{\text{OH}}$.

However, at comparable surface fraction as in our case, the relative coefficient friction is lower onto the smallest patterned surfaces. This result may traduce the coupling effects between micro-domains that lead to an average frictional response on the smallest patterned surfaces. Further investigations are required to expand the understanding of these effects on interface phenomena.

Hence, following these results, we can conclude that the introduction of a hydrophobic/ hydrophilic (MTS/Si-OH) system on a silicon surface can produce a medium frictional response. As following, what is the impact of a hydrophobic/ hydrophobic (MTS/PDMS) system on the frictional response?

III-2.3- FFM Friction measurements on MTS/PDMS patterned

substrates

For the linear patterned substrates with parallel strips (MTS/PDMS), Fig.3.24 shows the 2D AFM images of the Topography for two patterned surfaces (10, 26 μm).

Chapter 3 Frictional behavior of patterned surfaces

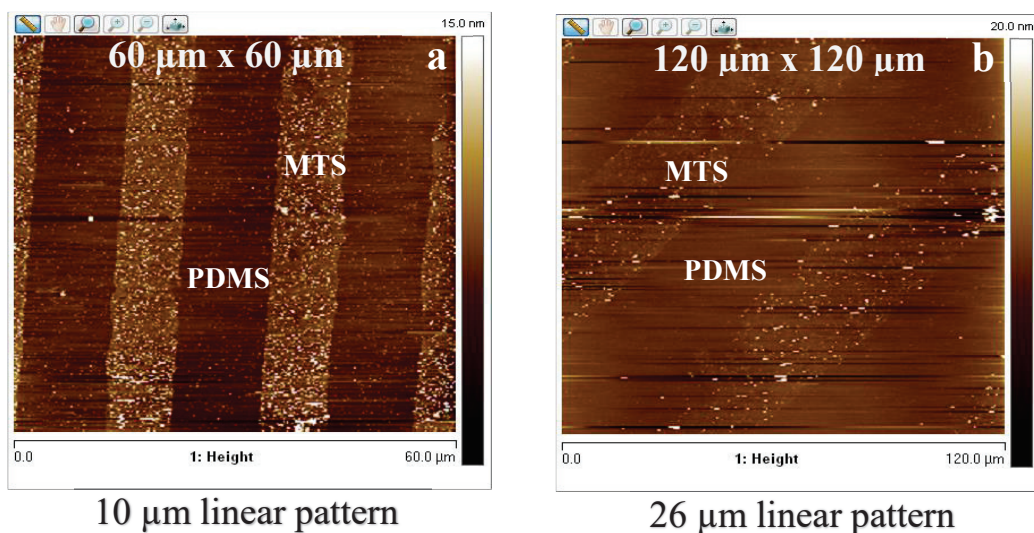


Figure 3. 24 2D AFM images of the Topography ($60 \times 60 \mu m^2$, $120 \times 120 \mu m^2$) for the different patterned surfaces (MTS/PDMS).

These images show the high sensitivity of lateral force microscopy (LFM) to the chemical contrast of the functional groups grafted onto the surface. The friction experiment consisted in scanning laterally the AFM tip under a constant velocity at $120 \mu m/s$ and constant load to get the friction pictures of the patterned surfaces and with different loads to determine their friction coefficient Fig.3.25.

Chapter 3 Frictional behavior of patterned surfaces

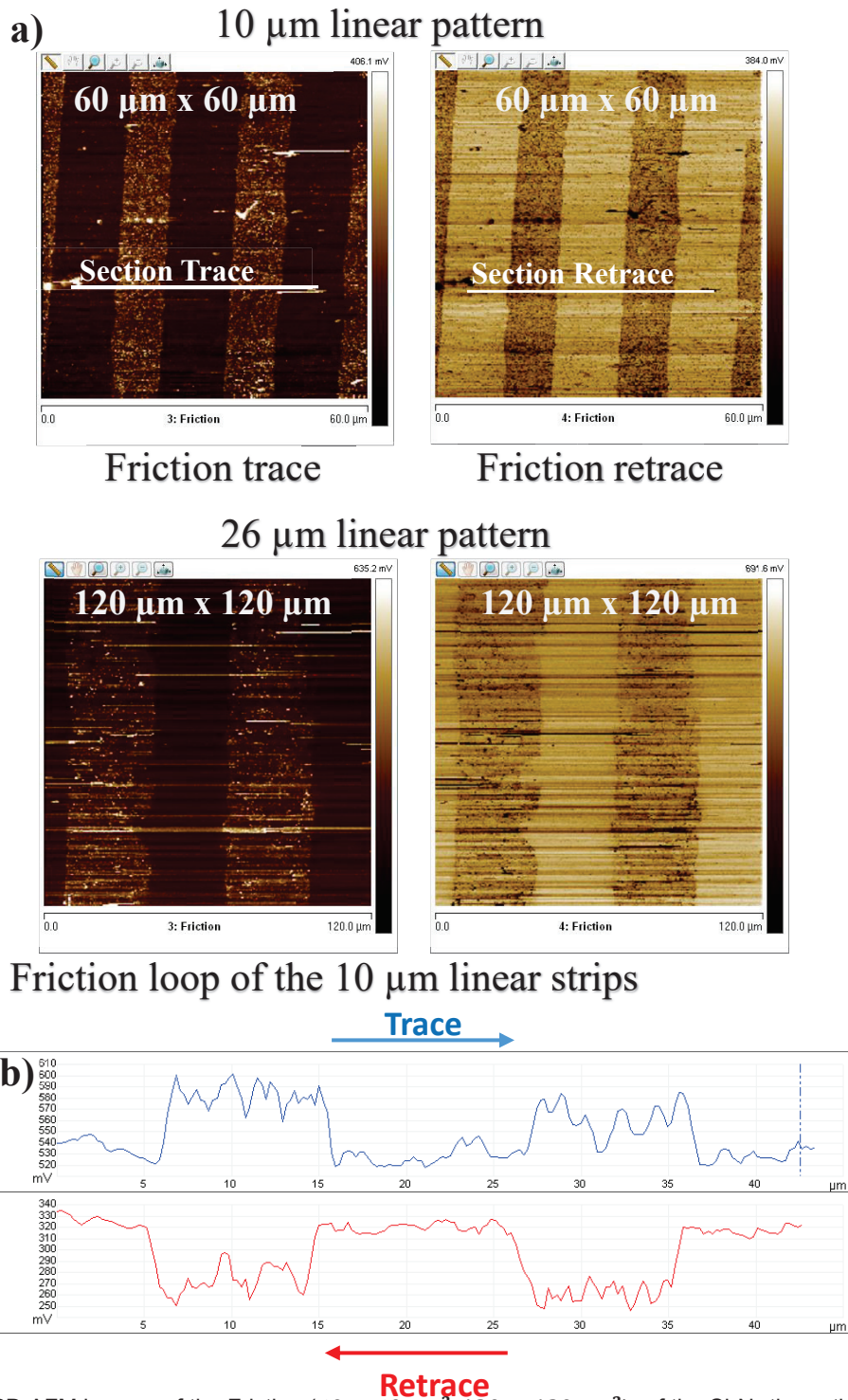


Figure 3. 25 (a) 2D AFM images of the Friction ($60 \times 60 \mu\text{m}^2$, $120 \times 120 \mu\text{m}^2$) of the Si_3N_4 tip on the 10 μm and 26 μm linear strips respectively. **(b)** Friction loop of the perpendicular parallel sliding for the trace and retrace sections of the 10 μm linear pattern.

The collected frictional response is found to be greatly influenced by the chemistry, the size and distribution of patterns. This is demonstrated by the regular augmentation of the tip/interface friction on these (MTS/PDMS) patterned surfaces. The slope of the curves is proportional to the friction coefficient and is represented in Fig.3.26.

Chapter 3 Frictional behavior of patterned surfaces

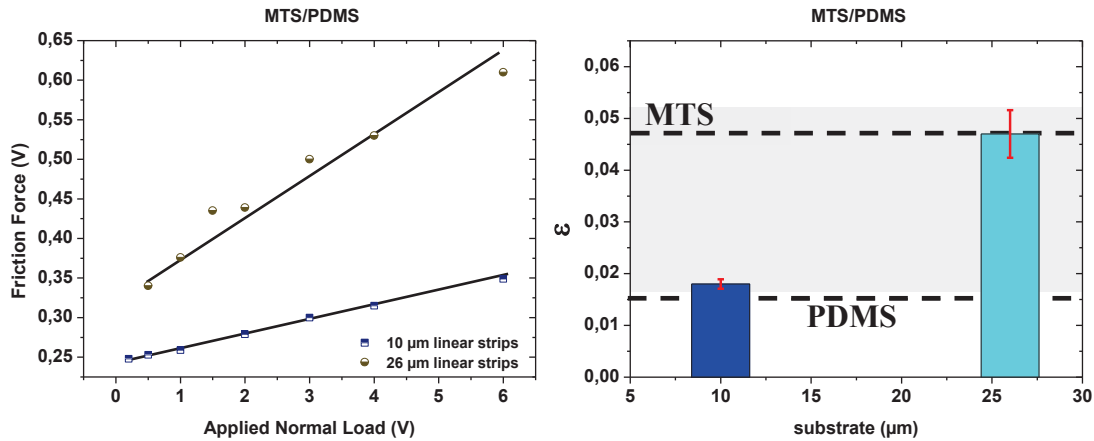


Figure 3. 26 (a) Force friction as a function for the applied normal load for to different patterned substrates. **(b)** Relative coefficient of friction of the sliding of the Si_3N_4 tip on the different Patterns sizes of the MTS/PDMS surfaces. The dashed lines represents the average values of the relative coefficient friction of the MTS and PDMS smooth surfaces.

The results show that the relative coefficient friction decreases with the expansion of the surface coverage of PDMS for micro-patterned surfaces. This frictional behavior can be attributed to the rip-off of some PDMS chain from the surfaces in the middle of the sliding experiments. In fact, as the size of the PDMS strip increases, a rise of the influence of the rip-off phenomena could be assumed. Thus, we can probably assume that the anchoring of these PDMS chain on the FFM tip greatly influence the frictional response.

A second mechanism can be advanced: the lubricated character to the adsorbed polymer chain at the interface. Hence, considering the length of the PDMS chains and their high mobility, the surface shows a liquid interfacial character, inducing a lowering in the interfacial friction. However, short chain molecules as the MTS molecules can form a solid layer increasing thus the frictional response [166]. Further, it was observed that the friction behavior of the two components substrates was consistent with their adhesion behavior. The higher the adhesion force, the higher the frictional force was [171]. In fact, the difference in the elastic modulus of these two components influenced by their mechanical nature plays a major role in defining their friction mechanisms.

IV-Conclusion

In this study, the frictional behavior of linear patterned surfaces of different chemistry and pattern sizes were investigated. Both a macro-friction test and a FFM measurement were employed to characterize the frictional response of an (hydrophobic/ hydrophilic) mixed silane (MTS/Si-OH) system and a (hydrophobic/ hydrophobic) mixed polymer and silane (MTS/PDMS) covered surfaces.

Firstly, the exploration of macro-friction dependence of a PDMS bead on a hydrophobic/hydrophilic mixed silane system, showed a similar coefficient friction independently of chemistry and sizes of the patterns printed on the surface. Furthermore, we found also that the macro-friction tests between a PDMS bead and a hydrophobic/ hydrophobic patterned system; displays a similar coefficient friction

Chapter 3 Frictional behavior of patterned surfaces

independently of chemistry and sizes of the patterns. In fact, we can clearly notice that MTS/PDMS patterns increase the critical shear stress values of a 15% in comparison with the silicon surface covered by PDMS layer. Nevertheless, despite this augmentation the critical shear stress values stays negligible compared to the silicon surface covered with MTS layer. Hence, this frictional behavior could be explained by the high loads and sliding force used in these experiments. These results, suggests that these measurements are greatly sensitive to the mechanical proprieties as substrates stiffness and young modules compared to the chemicals layers introduced to the surface, using micro-contact printing technique.

Secondly, the investigation of the frictional response at Nanoscale between a rigid tip and a MTS/Si-OH covered surface, demonstrated a negligible increases of the relative coefficient friction with the pattern sizes. In fact, these results shows that friction increases slightly with the surface coverage of Si-OH. This behavior can be explained by the rise of the magnitude of the adhesive interaction of the SAMs and the tip. As a result, the greater the surface fraction of Si-OH present on the surface, the greater the friction response can be. However, the exploration of the friction behavior of an FFM tip on MTS/PDMS patterned surfaces showed a great enhancement of the coefficient friction ($\times 2.5$) with the increase of the strip sizes. This frictional behavior can be attributed to the rip-off of some PDMS chain from the surfaces in the middle of the sliding experiments. In fact, as the size of the PDMS strip increases, a rise of the influence of the rip-off phenomena could be assumed. Thus, we can probably assume that the anchoring of these PDMS chain on the FFM tip greatly influence the frictional response.

In summary, these results shows that the relative coefficient friction is significantly influenced by the chemistry and the size of the linear patterns. Then, we can assume that the friction of patterned surfaces can be controlled and switched using a binary components of different pattern sizes.

Chapter 4

Dewetting as an investigative tool for studying the interfacial friction of patterned surfaces

TABLE OF CONTENTS

I-INTRODUCTION	113
<i>I-1-Introduction to polymer</i>	113
I-1.1-Structure of polymers.....	113
I-1.2-Dispersity of molar masses—Average molar masses	114
I-1.3-Description of a random polymer chain	114
I-1.4-Dynamic of polymer (viscoelastic polymers)	116
I-1.5-Polystyrenes	118
I-1.6-Polydimethylsiloxane.....	119
<i>I-2-Liquid jets — Rayleigh-Plateau instability</i>	119
I-2.1-Impact of viscosity.....	121
I-2.2-Droplet detachment	121
II-RESULTS AND DISCUSSION.....	122
<i>II-1-Dewetting Experiments Using a viscoelastic liquid</i>	122
II-1.1-Dewetting Dynamics.....	127
II-1.2-Regimes of the rim instability.....	129
II-1.3.a-First stage: Rim growth:.....	130
II-1.3.b-Second stage: swelling regime:	130
II-1.3.a-1-undulation:	130
II-1.3.a-2- bulging	132
II-1.3.c-Third regime: Fingering instability	133
II-1.3.d-Forth regime: Droplet detachment	135
II-1.3.d-1-Primary droplets.....	135
II-1.3.d-2-Secondary droplets.....	137
II-1.4-Thickness effect on the dewetting dynamics	137
II-1.4-1-Finger thread	142
II-1.5-Rim instability on the circular geometry	143
II-1.5.1-Impact of the geometry.....	146
<i>III-2-Dewetting Experiments Using a Newtonian Fluid on a MTS/PDMS patterned system</i>	148
III-2.1-Dewetting Dynamics.....	149
III-CONCLUSIONS.....	158

Chapter 4 Dewetting as an investigative tool for studying the interfacial friction of patterned surfaces

I-Introduction

In the previous chapter, we investigated the frictional response of multiple smooth non-patterned and patterned surfaces at macro, micro and nanoscales. Hence, we found that in the both case, mechanical proprieties, as substrate stiffness and young models are the predominant aspects in the friction response of the surface. Intriguingly, the uses of these approaches did not provide us with an explicit answer to our bewilderment concerning the influence of the chemical layer introduced on the surface using various approach (μ CP and grafting technique) on the frictional behavior. Therefore, we adopted the approach of the dewetting of thin polymer film on top of patterned surfaces, to investigate the interfacial friction response of the surface at the melt-substrate interface. In fact, dewetting experiments have been proved to be a highly sensitive tool for the determination of every significant changes at polymer/substrate interfaces [73, 76, 82, 83, 172-174].

This chapter has first sought to introduce the textured surfaces preparations and the techniques used to characterize the samples and studie the dewetting dynamics. Secondly, the study has sought to explore the impact of the solid/liquid boundary condition on the evolution of the rim instability during the course of dewetting. We studied how the sole change of the areal fraction of hydrophobic/hydrophilic (MTS/Si-OH) covered surface strongly affects the shape of the growing rim and the dynamics of the dewetting. Despite that, the characteristics of the rim instability are observed in three dimensions, this chapter concentrates on the in-plane rim instability. Furthermore, the study has sought to determine the effect of film thickness on the dewetting dynamics and the rim instabilities.

In last part of this chapter, we sought to investigate the dewetting of a PDMS film on a hydrophobic/hydrophobic (MTS/PDMS) covered surface as a mean to extract a quantitative information of the interfacial friction.

I-1-Introduction to polymer

I-1.1-Structure of polymers

The appellation polymer is quite ancient and has been used since 1866 after Berthelot mentioned that “when styrolene (styrene) is heated up to 200°C for several hours, it is converted to resinous polymer...” Is it the first synthetic polymer recognized as such? Possibly, yes. However, the concept of polymeric chain as we understand it today had to wait for the work of Staudinger [175] (Noble prize laureate in 1953) before complete acknowledgement. Polymer is a system formed by an assembly of macromolecules—that is, a system of entities with large dimension, which are obtained by the covalent linking of a huge number of constitutional repeat units, frequently called monomeric units Fig.4.1 [176]. Due to the connectivity, the units are not autonomous. However, they have certain amount of liberty that leads to several convoluted behaviors.

Chapter 4 Dewetting as an investigative tool for studying the interfacial friction of patterned surfaces

I-1.2-Dispersity of molar masses—Average malar masses

Except for certain natural polymers (enzymes) and those recently obtained by genetic engineering (perfectly defined polymers), the majority of macromolecular systems are disperse. This means that they consist of chains having different sizes (and consequently different molar masses), such a variation issuing from the odd nature of the polymerization reactions. In fact, the molar mass distribution (or molecular weight distribution) in a polymer describes the relationship between the number of moles of each polymer species (N_i) of molar mass (M_i). The number-average molar mass (\overline{M}_n) is defined as the sum (\sum_i) of the molar masses (M_i) of all the i families of species present in the system time their number fraction, that is, $N_i/\sum_i N_i$:

$$\overline{M}_n = \sum_i \frac{N_i}{\sum_i N_i} M_i = \frac{\sum_i N_i M_i}{\sum_i N_i} \quad (4.1)$$

The mass-average molar mass (\overline{M}_w) is defined as the sum (\sum_i) of the molar masses (M_i) of the i families of species present in the sample time their mass fraction, that is $N_i M_i / \sum_i N_i M_i$:

$$\overline{M}_w = \sum_i M_i \frac{N_i M_i}{\sum_i N_i M_i} = \frac{\sum_i N_i M_i^2}{\sum_i N_i M_i} \quad (4.2)$$

\overline{M}_w of a polymer is then the ratio of the second moment of the number distribution of molar masses to the corresponding first moment. According to the latter definition, longer chains have a higher statistical weight than that of shorter chains.

$$I_p = \frac{\overline{M}_w}{\overline{M}_n} \quad (4.3)$$

The dispersity index (I_p) can vary from unity for perfectly nondispersed samples (“isometric” systems) up to several tens of samples characterized by a strong dispersion in the size or molar mass of the constituting macromolecules (highly dispersed systems).

I-1.3-Description of a random polymer chain

Since its origin, polymer science has been confronted with a same duality that is the measurement of the average molar mass of macromolecules and in the same time, the determination of their size and their specific shape. The average molar mass of a sample and its dispersity (I_p) depend primarily on the experimental conditions of synthesis. As for the size and the shape of the macromolecules, they are closely controlled by the topological placement of their repetitive units (linear, branched ...) and also by the interactions that develop between each one of these units and the surrounding medium (solvent,

Chapter 4 Dewetting as an investigative tool for studying the interfacial friction of patterned surfaces

another repetitive unit, stretched or chains at rest). The arrangement of the subunits of a polymer in space is called its conformation.

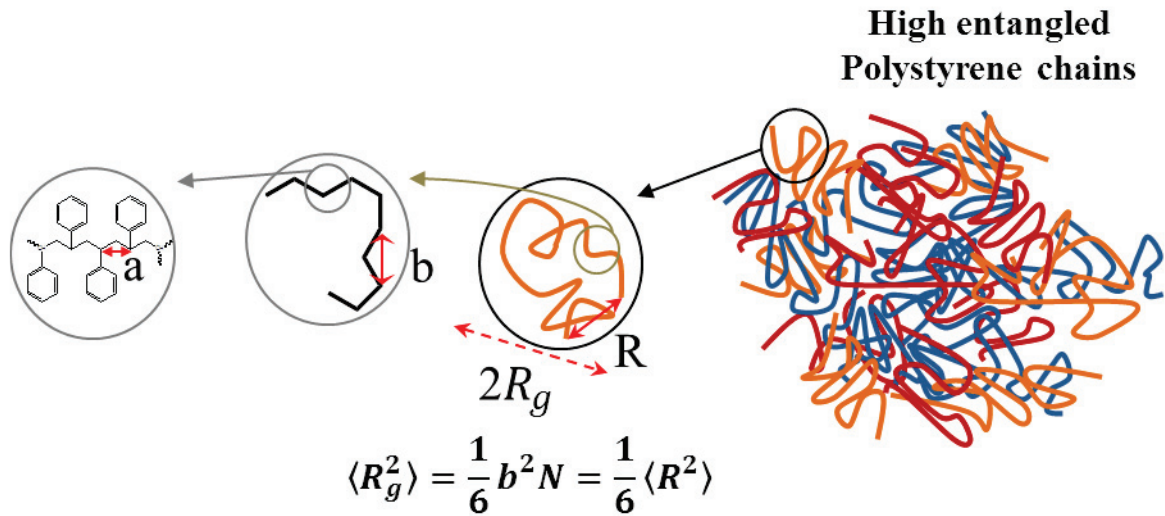


Figure 4. 1 Schematic of a polymer chain at different length scales with (*a*) is the monomer length, (*b*) is the persistence length (real chain), (*N*) is the number of segments, (*R*) is the end to end distance of a polymer chain and *R_g* is the radius of gyration.

In fact, the simplest molecular architecture corresponds to linear molecules that consist of identical monomer units linked end-to-end. For a linear polymer chain, the maximum end-to-end distance, *R*. The contour length (*L*) of a polymer chain is equal to the sum of the lengths (*a*) of all monomer segments as $L = Na$. Further, the concept of equivalent or Kuhn segments (*b*) in a chain can be embedded by introducing segments that are statistically independent. In a compilation of similar molecules, a linear polymer molecule will adopt the shape of a random coil. The global coil size can be characterized statistically by the root-mean-square end-to-end distance *R_{RMS}* which scales as the square root of the length of the molecule (*N*) or its molecular weight (*M_w*) and frequently ranges from few nanometers to tens of nanometers [177],

$$R_{RMS} \sim \sqrt{\langle R^2 \rangle} \sim aN^{1/2} \sim bN^{1/2} \quad (4.4)$$

The polymer can be characterized by a different length scales, ranging from the size of the lone monomers to the global macroscopic complicated molecules (Fig.4.1).

Another often-used measure of the chain dimension is the root-mean-square radius of gyration *R_g* (or simply radius of gyration). Its square, *R_g²*, is the second moment around the center of mass of the chain. The latter is defined as the mean square of the distance between the beads and the center of mass (Fig.4.1).

$$\langle R_g^2 \rangle = \frac{1}{6} b^2 N = \frac{1}{6} \langle R^2 \rangle \quad (4.5)$$

Chapter 4 Dewetting as an investigative tool for studying the interfacial friction of patterned surfaces

Note that (R) is defined for linear chains only, but (R_g) can be defined for any chain architecture including nonlinear chains such as branched chains. In this sense, (R_g) gives a more universal measure for the chain dimension

I-1.4-Dynamic of polymer (viscoelastic polymers)

The behaviour of materials of low relative molecular mass is generally discussed in terms of two particular types of ideal material: the elastic solid and the viscous liquid. The former has a specific shape and is deformed by external forces into a new equilibrium pattern; on removal of these forces, it reverts spontaneously to its original form. The solid stores all the energy that it from the external forces during the deformation, and this energy is available to restore the original shape when the forces are removed. On the other hand, a viscous liquid has no definite shape and flows irreversibly under the action of external forces. In fact, no material is perfectly elastic in the sense of rigorously obeying Hooke's law. Polymers, particularly when above their glass transition temperature, are surely not. For these macromolecular materials, there is an element of flow in their response to an applied stress, and the extent of this flow varies with time. Such behavior, which combines both liquid-like and solid-like features, is termed as viscoelasticity. The characteristic time between the solid-like and the liquid-like behaviour is the relaxation time (τ). The relationship between the viscosity (η), the elastic modulus (G) and the relaxation time (τ) is given by: $\eta \sim G\tau$. In fact, the approximate response of a viscoelastic material is schematically illustrated on Fig.4.2. Strain rate ($\dot{\epsilon}$) decreases with time in the creep zone (creep is the time-dependent change in strain following a step change in stress) until eventually reaching a steady state. In the recovery zone, the viscoelastic fluid recoils, finally reaching an equilibrium at a some small total relative to the strain at unloading [178].

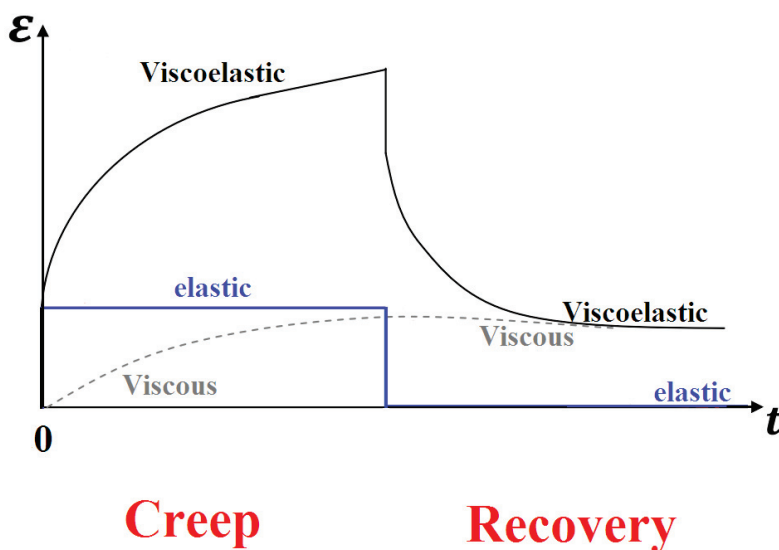


Figure 4. 2 Schematic creep and recovery of a polymeric system under a constant stress at time zero.

Chapter 4 Dewetting as an investigative tool for studying the interfacial friction of patterned surfaces

In a concentrated polymer solution, a melt or a solid polymer the molecular chains cannot pass through one another, a constraint that forcefully confines each chain within a tube [179]. The middle line of this tube characterizes the global path of the chain in space, and has been called by Edwards the primitive chain (Fig.4.3). Each chain 'identify' its environment as a tube because, although all the other chains are moving, there are so many entanglements that at any one time the tube is well defined. De Gennes [180] has illustrated the feasible motions of a polymer chain confined to a tube as snake-like, and has termed the phenomenon 'reptation'. He considered two different forms of motion. First, the comparatively short-term wriggling motions that correspond to the migration of a molecular kink along the chain, for which the longest relaxation time is proportional to the square of the molecular mass. Second, there is the much longer time associated with the movement of the chain as a whole through the polymer. This motion corresponds to a global migration of the Centre of gravity of the chain, and has a characteristic time proportional to the cube of the molecular mass.

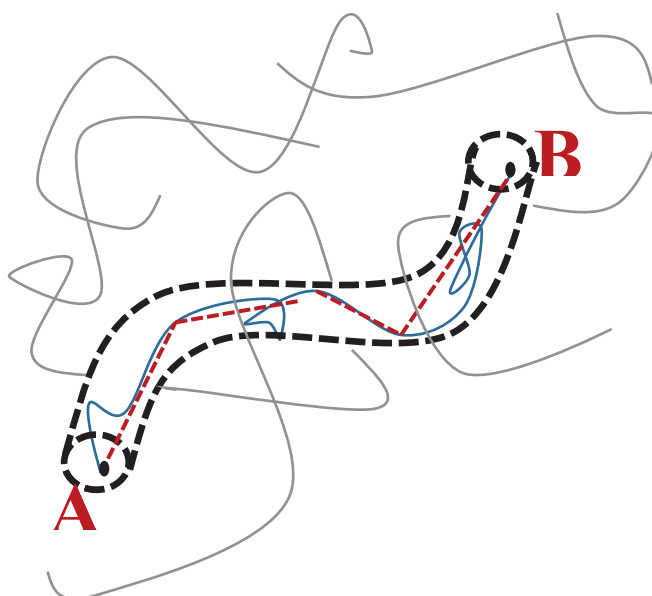


Figure 4. 3 Schematic of chain segment AB in dens rubber. The blue chain is undergoing reptation inside the tube while other green chains. The redline shows the primitive path.

Doi and Edwards [181] have continued the work of de Gennes, and have derived mathematical expressions for features such as the stress relaxation that occurs after a large strain. Their interpretation for the physical situation is schematically depicted in Fig 4.4 in which the hatched area indicates the deformed part of the tube.

Chapter 4 Dewetting as an investigative tool for studying the interfacial friction of patterned surfaces

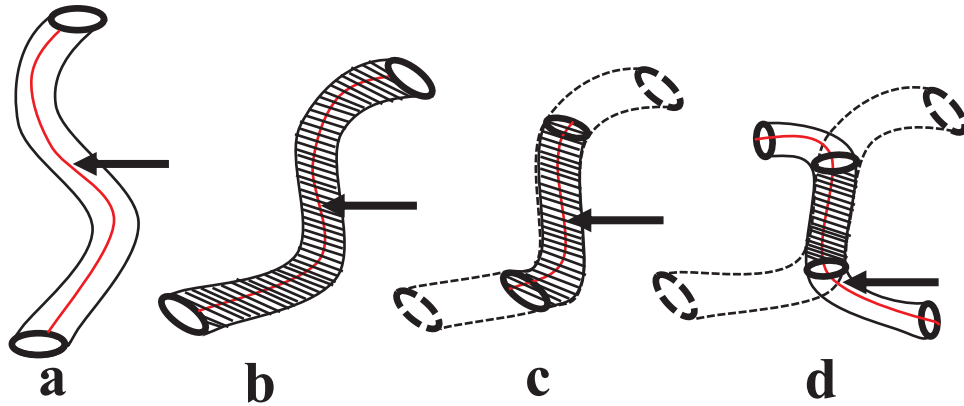


Figure 4. 4 Explanation of the stress relaxation after a large step strain. (a) Before deformations the conformation on the primitive chain is in equilibrium ($t=0$). (b) Immediately after deformation, the primitive chain is in the affinely deformed conformation ($t=+0$). (c) After time τ_e the primitive chain contracts along the tube and recovers the equilibrium contour length ($t=\tau_e$). (d) After the time τ_d , the primitive chain leaves the deformed tube by reptation ($t=\tau_d$). The oblique lines indicate the deformed part of the tube.

In fact, this τ_d is called the disengagement or reptation time and is the terminal relaxation time. The diffusion coefficient of the Rouse-like chain within the tube (not entangled) can be written:

$$D_{tube} = \frac{K_B T}{\zeta N} \quad (4.6)$$

(ζ is the monomeric friction factor).

The chain will completely leave the tube after a time $\tau_d = \langle L^2 \rangle / D_{Tube}$, where $\langle L \rangle$ is the length of the tube which is also the contour length of the chain, $L = Nb$. This is also the length of the primitive path of the chain where the potential energy of each monomer is at the minimum. In fact, here the tube itself sustain random-walk, which can be thought as random walk of entanglement strands or monomer. Hence, the reptation time can be written:

$$\tau_d = \frac{\langle L^2 \rangle}{D_{Tube}} = \tau_e \left[\frac{N}{N_e} \right]^3 \quad (4.7)$$

Where, τ_e is the Rouse time of the entanglement strand containing N_e monomers.

I-1.5-Polystyrenes

Polystyrene (as a model flexible polymer) have an important interest in the studies of ultrathin films. Polystyrene (abbreviated as PS) is a polymer made from the aromatic monomer styrene, a phenyl containing aromatic hydrocarbon. Polymers are made of chains consisting of many monomer units. Polystyrene is made (usually) by radical polymerization, from the monomer styrene Fig.4.5. The glass transition temperature for bulk PS is about **105 °C**. The surface tension is approximately **40 mN/m** at **20 – 25 °C**. Other important parameters are density = **1.05 g/cm³** and refractive index = **1.59** at ambient temperature. Kuhn statistical segment has a value of **b = 0.68 nm** and a monomer molecular

Chapter 4 Dewetting as an investigative tool for studying the interfacial friction of patterned surfaces

weight of **104 g/mol** [182]. Polystyrene samples used in this study were obtained from Polymer Source, Inc. Polystyrenes with the following molecular weight was employed: $M_w = 137 \text{ kg/mol}$ with a polydispersity index = 1.05. Toluene ($\geq 99.9\%$) was used to dissolve them.

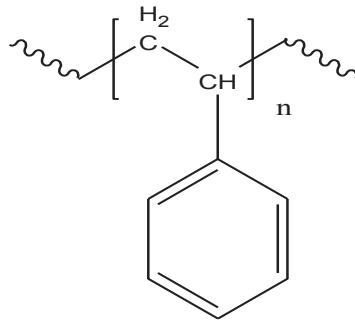


Figure 4. 5 Chemical formula of styrene monomer.

I-1.6-Polydimethylsiloxane

Polydimethylsiloxane (PDMS) belongs to a group of polymeric organosilicon compounds that are commonly referred to as silicones Fig.4.6. PDMS is the most widely used silicon based organic polymer, and is particularly known for its rheological properties. For our purpose of dewetting a PDMS thin layer, we prepared PDMS/MTS patterned silicon wafers, where PDMS acts as a non-wettable liquid underlayer enabling slippage and serve as a reproducible substrate. Dewetting dynamics is partially determined by the dissipation of the capillary energy due to the friction at the PDMS-PDMS interface [173]. PDMS are formed of a siloxane (Si-O-Si) backbone with attached methyl groups (cf. Figure 4.6). This gives rise to an apolar and hydrophobic character. The glass transition temperature (T_g) is $-125 \text{ }^\circ\text{C}$. Surface tension is ca. **21 mN/m** and refractive index = **1.46** at ambient temperature [181]. We mainly used 139 kg/mol Hydroxyl terminated PDMS (DMS-S51, 0.02% -OH, viscosity = 75000-115000 cSt.).

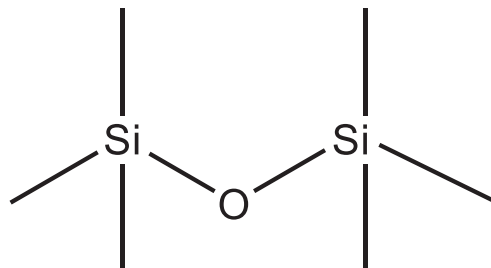


Figure 4. 6 Chemical formula of two dimethylsiloxane units.

I-2-Liquid jets — Rayleigh-Plateau instability

Break up of a liquid jet in droplets is an ordinary event that everybody is used to experience. A familiar example of it is a thin stream of water flowing steadily from a faucet, which breaks up into droplets at its lower end was illustrated in Fig.4.7 (a). This common physical occurrence is driven by surface

Chapter 4 Dewetting as an investigative tool for studying the interfacial friction of patterned surfaces

tension of the liquid, which tends to minimize the interface area between immiscible fluids. Because of this, the cylindrical shape is not a stable position of equilibrium, and under some circumstances, little perturbations drive the jet to its rupture - a phenomenon known as Plateau-Rayleigh instability.

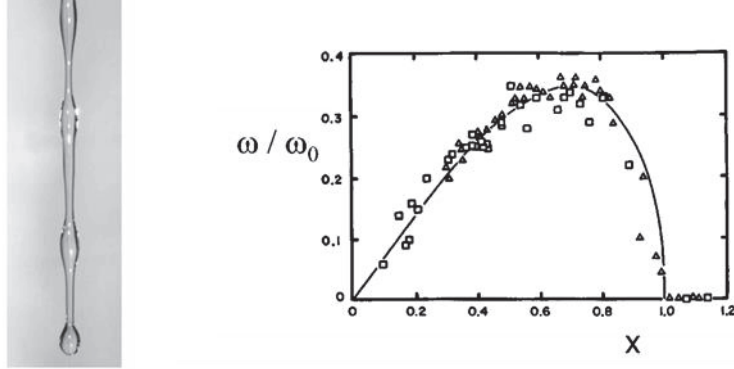


Figure 4. 7 (a) Water jet falling from a faucet **(b)** Dimensionless growth rate of sinusoidal perturbations on a cylinder as a function of the dimensionless wave number kh_0 . The solid line represents Rayleigh's theory for inviscid flow.

The cylinder is rendered unstable by capillarity induced by a reduction of the surface energy $\Delta E = E_S - E_0$, calculated as the difference between the energy of the initial state (E_0) and the final stage (E_S) in equation 4.8 [183, 184].

$$\Delta E = \frac{A^2}{4R} E_0 (q^2 R^2 - 1) \text{ with } E_0 = \gamma 2\pi\lambda \quad (4.8)$$

The perturbation of amplitude A and wave vector $q = 2\pi/\lambda$ develops when the energy of the liquid cylinder, of initial radius R , is reduced. This condition is verified when $q^2 R^2 < 1$, which is equivalent to write that each distance between droplets λ follows

$$\lambda > 2\pi R$$

Experimentally, first qualitative observations of the decay of a liquid jet took place as early as the beginning of the 19th century [185, 186]. In 1873, Plateau [187] found experimentally that a falling jet of water breaks up into droplets if it is vertically perturbed with a disturbance of wavelength greater than about 2π times its radius. He observed that the instability was related to the capacity of the perturbation of reducing the area of the jet, eventually identifying the role of surface tension for break up. However, he found that the most destabilizing wavelength was $\lambda_{opt} = 8.76h_0$, much larger than 2π . Some decades later, Rayleigh showed theoretically that a jet breaks up if it is perturbed with a wavelength that exceeds its circumference. He understood that the fact that $\lambda_{opt} > 2\pi$ was related to the dynamics [188, 189]. Based on the linear stability analysis, Rayleigh obtained the dispersion relation whose simplified form is given in equation for a perturbation $A = A_0 e^{-iwt}$, with A_0 constant and w the growth rate of the perturbation.

Chapter 4 Dewetting as an investigative tool for studying the interfacial friction of patterned surfaces

$$\omega^2 = -\omega_0^2(kh_0)[1 - (kh_0)^2] \quad \text{with} \quad \omega_0 = \sqrt{\frac{\gamma}{\rho h_0^3}} \quad (4.9)$$

The complete form includes another term based on the Bessel function and its derivative [184, 190]. Its representation in Fig.4.7 (b) reveals a maximum dimensionless growth rate ω/ω_0 achieved for a reduced wavenumber $q_{max}/h_0 \approx 0.696$. At q_{max} , the time dependance of the amplitude of the perturbation is the fastest with a time constant of τ_{max} .

$$\tau_{max} \approx \frac{3}{\omega_0} \quad (4.10)$$

The theoretical value of the wavelength disturbance for this mode reads is $\lambda_m = 9,02 h_0$, very close to the observation inferred by Plateau.

I-2.1-Impact of viscosity

Another parameter to take into account when the motion of liquids is involved is viscosity η . Even if previous results show that preconditions for the rise of the instability are independent of η , the dynamics of the deformation are affected by changes in viscous forces in the fluid. The importance of the viscosity on the propagation of the wave is determined by the penetration length δ , which is a comparison of the kinematic viscosity with the growth rate, set by the Ohnesorge number Oh measuring the relative importance of viscosity $\eta = \nu\rho$ with ν the kinematic viscosity [184].

$$\delta = \sqrt{\frac{\eta}{\omega\rho}} \quad Oh = \nu \sqrt{\frac{\rho}{h_0\gamma}} \quad (4.11)$$

At large Ohnesorge number, the perturbation undergoes a viscous slowing. The growth rate of the instability decreases as the inverse of viscosity [188, 191].

$$\omega = \frac{\gamma}{2h_0\eta} \quad (4.11)$$

I-2.2-Droplet detachment

Breakup between consecutive droplets sets the beginning of non-linear dynamics of the stability analysis reviewed in [192]. At non-negligible viscosity, the lowering of the timescale of the wave growing the fastest induces a thinning of the middle part into a flat region, a secondary thread. The pinching point sets close to the drop due to high Laplace pressure in this region at length l_v and time scales t_v whose dependence in viscosity is given via the kinematic viscosity ν in equation [193]. As an example, a water jet would reach 10^{-6} cm in 10^{-10} s before breakup whereas the transition jet to drop would occur after 0.6 s for a length of 2.8 cm in the case of glycerol [194].

Chapter 4 Dewetting as an investigative tool for studying the interfacial friction of patterned surfaces

$$\ell_v \sim \nu^2 \frac{\rho}{\gamma}, \quad t_v = \nu^3 \frac{\rho^2}{\gamma^2} \quad (4.12)$$

with ν the kinematic viscosity $\nu = \frac{\eta}{\rho}$

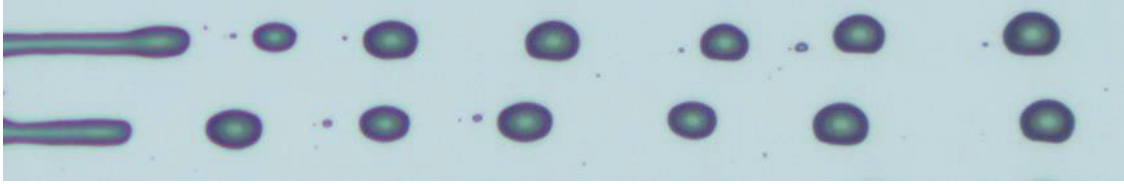


Figure 4. 8 Optical micrograph of a supported liquid cylinder decaying into droplets via the Rayleigh-Plateau instability. This is an example of our dewetting experiments of a PS film on a textured surfaces.

Before contraction, the newly created thin liquid thread destabilizes with a secondary instability into droplets, much smaller than initial ones, commonly termed satellite drops. From the length scale introduced in the previous equation, it seems obvious that the latter stage is preferentially observed for viscous fluids as depicted in Fig. 4.8. The pattern reveals an inhomogeneity in the distribution of secondary droplets which is due to the contraction of the thin thread towards its center.

II-Results and discussion

The samples fabrication used in this part are described in the second chapter section II-1

II-1-Dewetting Experiments Using a viscoelastic liquid

A thin polymer film is casted on top of a surface textured by printing linear textures of silane molecules (*MTS*). Several thicknesses of polystyrene films of molecular weight $Mw = 137 \text{ kg/mol}$ is annealed at $180 \text{ }^\circ\text{C}$.

Chapter 4 Dewetting as an investigative tool for studying the interfacial friction of patterned surfaces

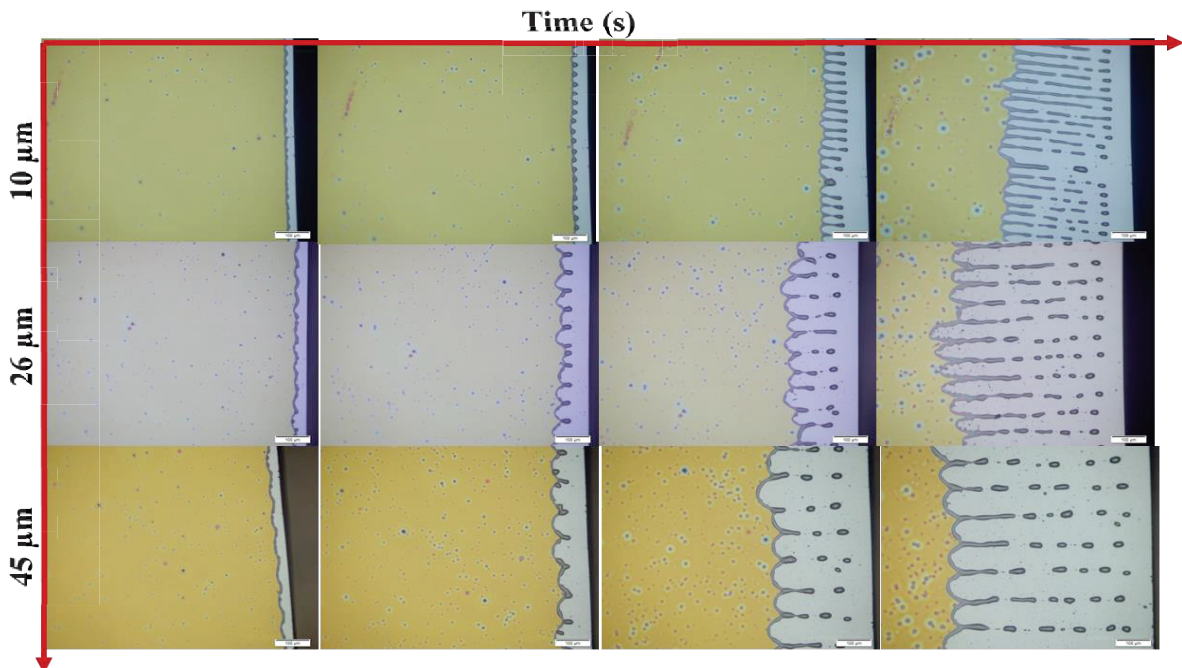


Figure 4. 9 Optical micrograph ($842 \mu\text{m} \times 660 \mu\text{m}$) of the dewetting dynamic of a 195 nm thick PS (137k) performed at 180°C for different patterned substrates.

Thus, by breaking the sample, we created a three-phase contact line between the substrate, the film and the surrounding environment. Consequently, the thin polystyrene (PS) films annealed while optical micrographs were recorded in situ Fig.4.9. The system is metastable under these conditions; the retraction of the liquid film occurs at the three-phase contact line. Dewetting is therefore immediate when the sample is placed at the desired annealing temperature. We should note that in these experiments we used a high PS thicknesses ($>195 \text{ nm}$) preventing the undesired influence of holes creation at the surface of the film. Moreover, we used a high annealing temperature (180°C) to avoid any disfavoring effect of the residual stress on the dewetting dynamic, asserting the viscous regime of our system. Hence, it is a possible to record respectively the dewetted distance $d_{Average}$ and the rim width $W_{Average}$ of the rim by optical micrographs of the dewetting dynamic in time Fig.4.10. It should be noted that from these parameters, an velocity dewetting $V_{Average}$ was obtained by taking the differences; $V = [d(t_i) - d(t_{i-1})]/(t_i - t_{i-1})$.

Consequently, using this in situ measured parameter, we could easily investigate the changes in interfacial properties in the course of the experiment, demonstrating the simplicity and the efficacy of dewetting experiments as an approach for the characterization of static and kinetic properties of polymer-polymer interfaces.

Chapter 4 Dewetting as an investigative tool for studying the interfacial friction of patterned surfaces

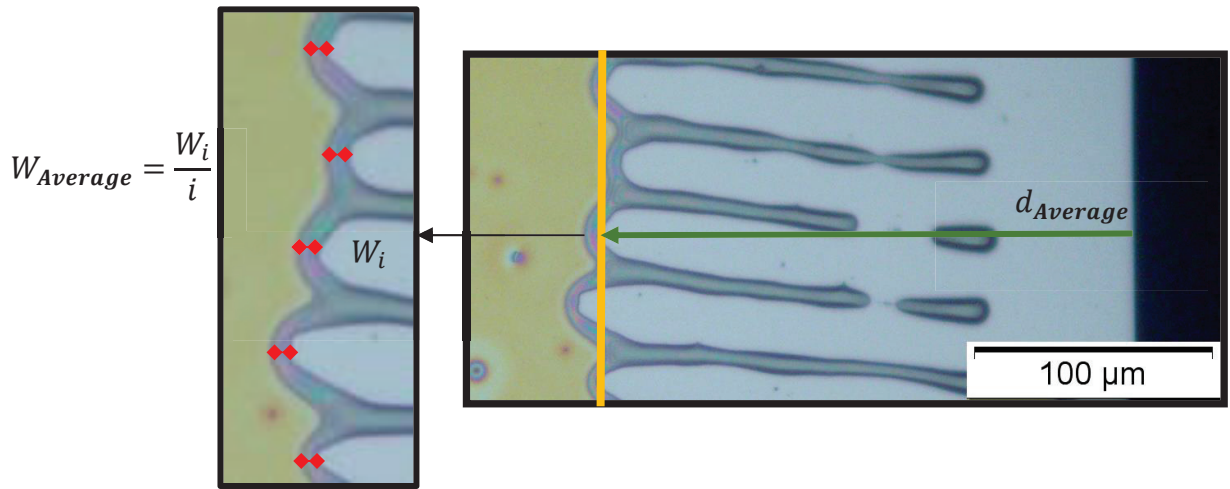


Figure 4. 10 Optical micrograph of the dewetting dynamic defining the averaged dewetting distance $d_{Average}$ and the rim width $W_{Average}$.

In Figure 4.11, we show the temporal evolution of the dewetting distance $d_{Average}$ and the averaged dewetting velocity $V_{Average}$ of a thin (195 nm PS139k) film on three patterned systems of linear strips (MTS/Si-OH) with varying sizes (10, 26, 45 μm). The first observation is that smaller patterns substrate (10 μm) dewetted faster compared to the larger patterns suggesting a dependence of the dewetting dynamics with the pattern sizes. However, we observe clearly that the growth of the straight three-phase contact line cannot be represented by a simple power law behavior. Then, based on our observations, it seems necessary to distinguish different regimes of the dewetting process. The same behavior can clearly be observed following the evolution of the rim width $W_{Average}$ with time. Fig.4.11 illustrate the non-linear behavior of the rim width proving the existence of multiples regimes of the dewetting process.

Chapter 4 Dewetting as an investigative tool for studying the interfacial friction of patterned surfaces

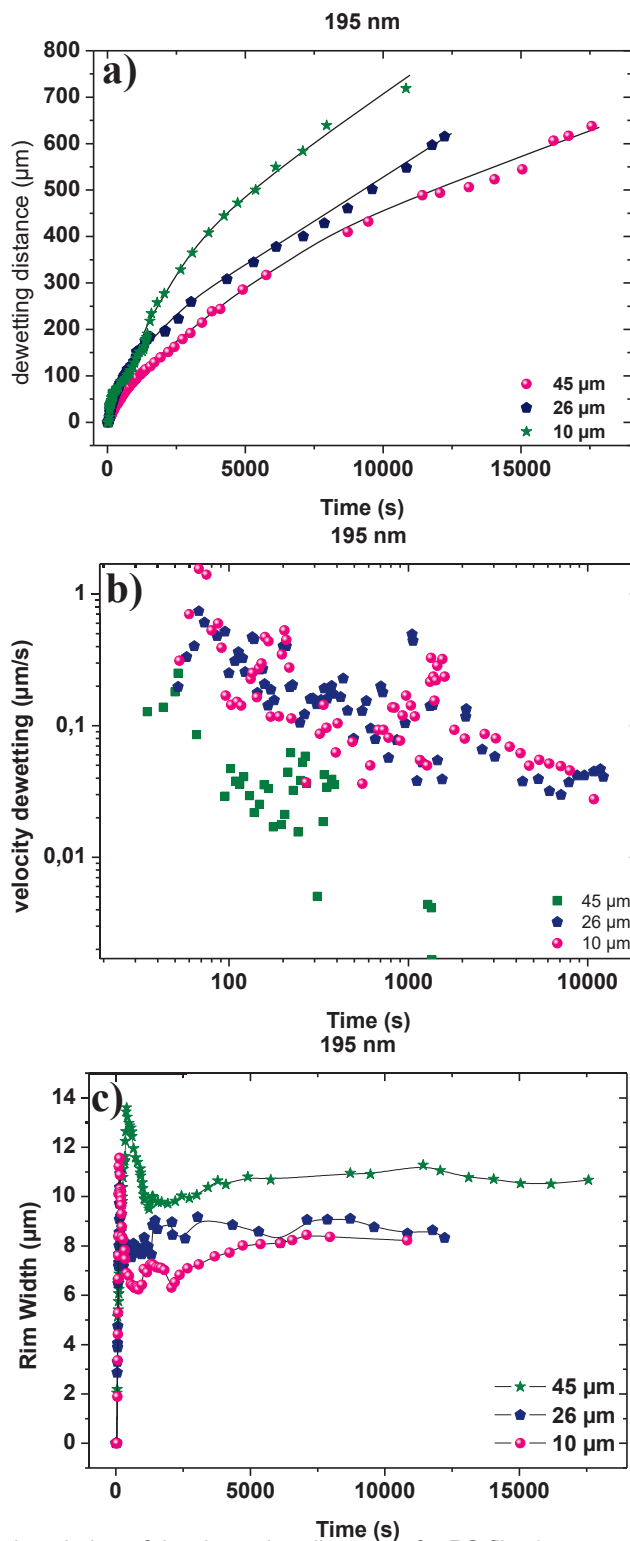


Figure 4. 11 (a) Temporal evolution of the dewetting distance of a PS film (195 nm $M_w = 139\,000$ g/mol) on top of a MTS/Si-OH patterned substrates (10, 26 and 45 μm). (b) Velocity dewetting as a function of time for the same conditions as described in (a). The lines are guideline for eyes. (c) Temporal evolution of the rim width.

Hence, we defined four different regimes as the following: an initial stage of the straight three-phase contact line formation and building-up of the rim, a second illustrated by a global undulation of the

Chapter 4 Dewetting as an investigative tool for studying the interfacial friction of patterned surfaces

ridge. Then, a third where the swelling of the rim can be observed and finally, a fourth stage where a successive droplet detachment of the liquid at the three-phase contact line occurring.

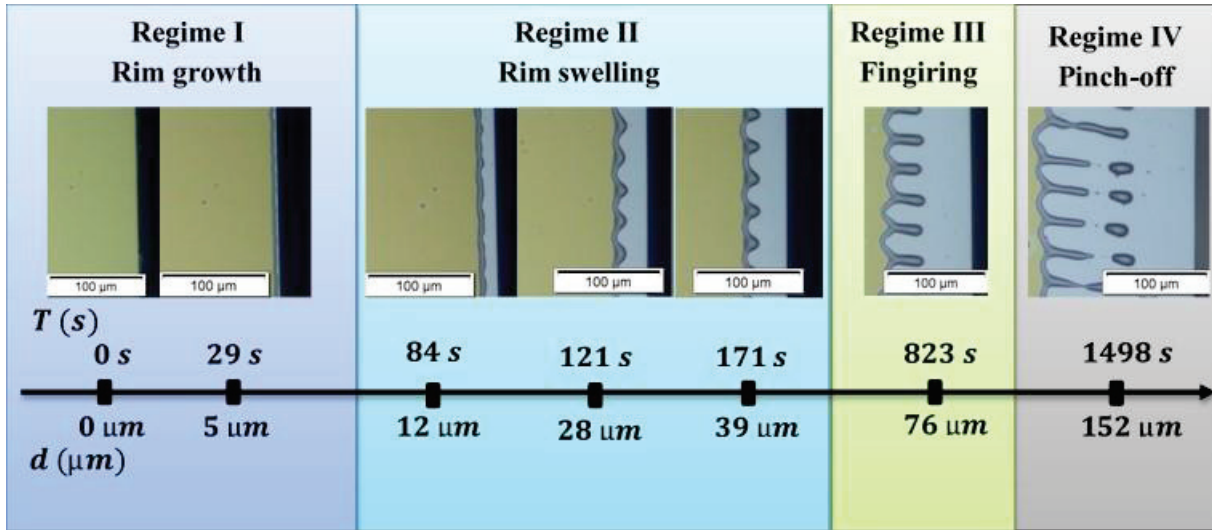


Figure 4. 12 Optical micrograph of the dewetting dynamic of a 195 nm thick PS (137k) on top of a 10 μm MTS/Si-OH patterned substrates illustrating the different regimes of the dewetting experiments.

Fig.4.12 depicts the edge of a receding thin film moving from right to left with its position given by the dewetted distance d at time t as indicated by the straight arrow. Pushed at the solid/liquid/air interface, the polymer agglomerates to form a rim rounded by the Laplace pressure, homogeneously distributed along the edge to form a ridge, the dark grey zone observed in optical micrographs. Knowing the surface tension is unable to affect the formation of the rim, we can assume that in this regime, the viscous dissipation is approximately equal to interfacial dissipation due to friction during the formation of the rim, suggesting a high interfacial friction. As the dewetting process advance, the rim in the form of “semi-cylinder” shows significant undulations along its length as the rim width increases and the velocity dewetting decreases, suggesting a swelling of the rim. It was shown in [195, 196] that the combination of slippage and surface tension in the mature-rim regime can lead to an oscillatory profile. As dewetting on the patterned surfaces proceeded, a highly undulated aspect of the rim can be clearly observed. This undulation is more important at the side in contact to the substrate, ‘dry’ side, whereas the side plunging into the film, ‘wet’ side, remains almost straight. Furthermore, the bulges increases until they protrude from the ridge and form fingers, where a slow decrease of the rim width and the velocity dewetting can be clearly related to these phenomena. This mechanism induces a decrease in the interfacial friction between the polymer melt and the micro-textures (printed on the surface) leading these fingers to breaking into droplets. As the droplets formed, we observe that the dewetting velocity and the friction remain constant and the rim width begin slowly to stabilize reaching the stage of the “mature rim” regime. We can therefore anticipate that for a viscoelastic fluid, the rheological properties of the fluid will have no significant consequences on the dewetting velocity, which clearly was proved by the constant values of the velocity dewetting at this stage.

Chapter 4 Dewetting as an investigative tool for studying the interfacial friction of patterned surfaces

In order to quantify the evolution of the retracting front on the textured surface, we recorded the local variation of the moving three-phase contact line. We differentiate the dynamics of the ridge recorded at a thick region of the ridge, termed (Tip), to the thinnest region adjacent to the tip, termed finger Fig.4.13. We present the local variation of the dynamics of dewetting and investigate the impact of friction at the solid/liquid interface on the influence of the dewetting rates.

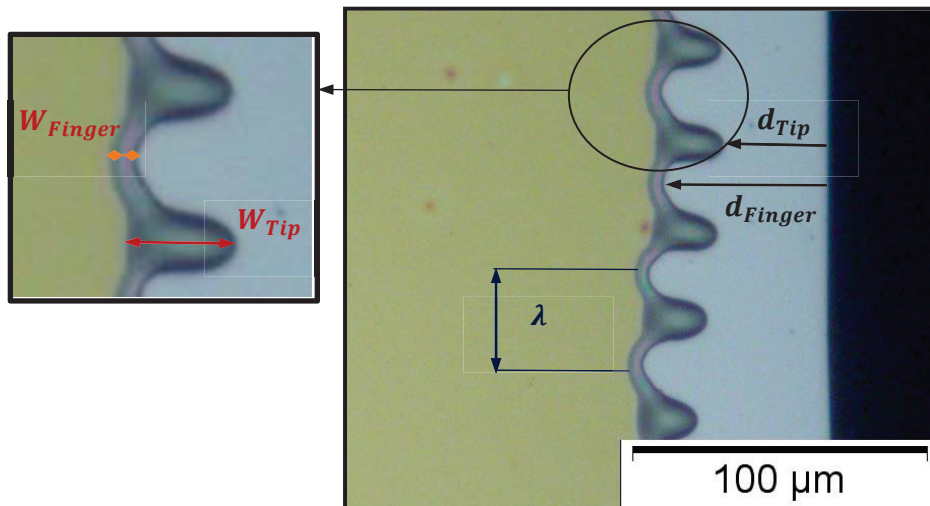


Figure 4. 13 Optical micrograph of the dewetting dynamic defining the different parameter used in this section.

II-1.1-Dewetting Dynamics

Let's consider the smallest pattern $10 \mu\text{m}$ at first, the temporal evolution of the dewetted distance d and the velocity dewetting V was reported in Fig.4.14, with the definition of dewetting distance measured at the tip displayed in the inset. It should be noted that from the local dewetting distance d and the rim width W measured in those experiments, a local velocity dewetting V was obtained by taking the differences ; $V = [d(t_i) - d(t_{i-1})]/(t_i - t_{i-1})$. As explained above three different regimes of the dewetting process were suggested. We should note the in typical dewetting experiments and due to the higher surface tension of the PS film compared to the MTS substrates a retraction of the liquid film can occur easily at the three-phase contact line. Inversely, in the case of the SI-OH substrates, the PS film cannot dewet due to his lower surface tension compared the hydrophilic surface. Then, despite this great differences in the surface tension between the (MTS/SI-OH) linear strips and the PS film and knowing that the surface tension is ineffective during the formation of the rim, a constant dewetting velocity V defined by a fast growth of d was observed up to 62 s independently on which position along the ridge the measurement is performed.

Chapter 4 Dewetting as an investigative tool for studying the interfacial friction of patterned surfaces

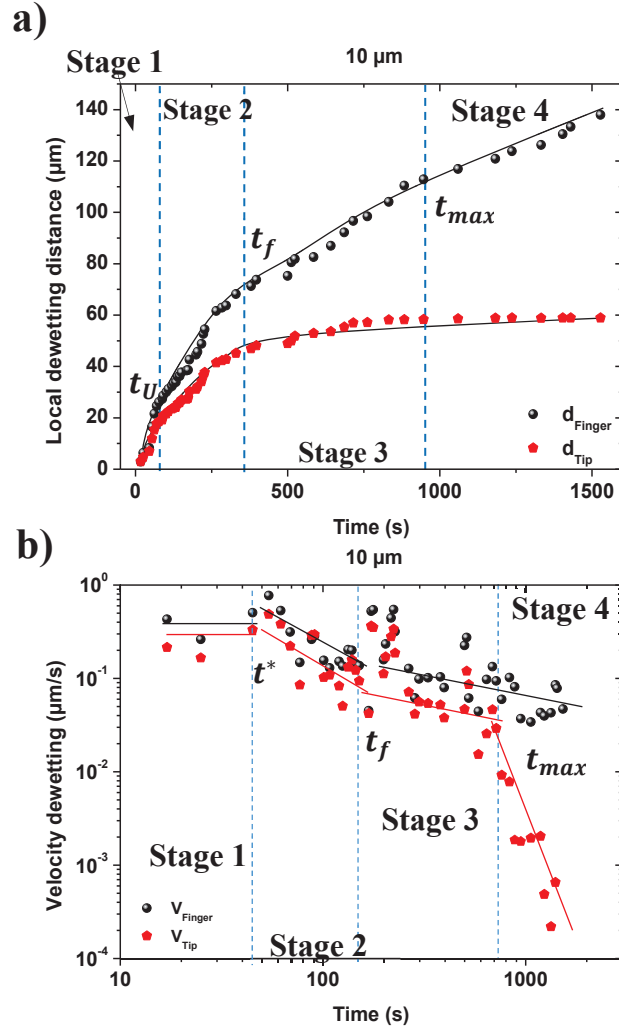


Figure 4. 14 (a) Temporal evolution of the dewetting distance (d) of the “Tip” and “Finger” rim regions of a $195\text{ nm PS}(137k)$ thick film dewetted on top of a $10\text{ }\mu\text{m}$ MTS/Si-OH patterned substrates. (b) Temporal evolution of the dewetting velocity (V) on double logarithmic scales.

This time, denoted t_U , corresponds to a distance of $d_U \sim 19\text{ }\mu\text{m}$ which marks the beginning of the undulation then the swelling of the rim as shown in Fig.4.14. We can anchor this constant behavior of the dewetting velocity to the viscoelastic PS trend to act as a simple liquid inducing the rise of an asymmetric rim. Beyond d_U , different growth rates but slower compared to the first stage are clearly observed between the two regions of the rim ridge. Moreover we can observe that $V_{tip}(t)$ and $V_{finger}(t)$ decreases slowly until 227 s . This specific time, termed t_f , correlated to the fingering instabilities and noted by the distance $d_f \sim 42\text{ }\mu\text{m}$. Above d_f , a slower decrease rates are clearly observed: $d_{finger}(t)$ decrease almost linearly but slowly, whereas $V_{tip}(t)$ slows down reaching a plateau. The ending point registered at peak ($t_{max} = 949\text{ s}$) represents the maximal distance ($d_{max} \sim 52\text{ }\mu\text{m}$) traveled by the finger before the droplets instability appears. In this regime, the viscous dissipation is negligible compared with the dissipation due to friction, and consequently leading to the mature rim situation. Thus, a high rate of the decrease of $V_{tip}(t)$ was clearly observed, announcing then the droplet detachment instability.

Chapter 4 Dewetting as an investigative tool for studying the interfacial friction of patterned surfaces

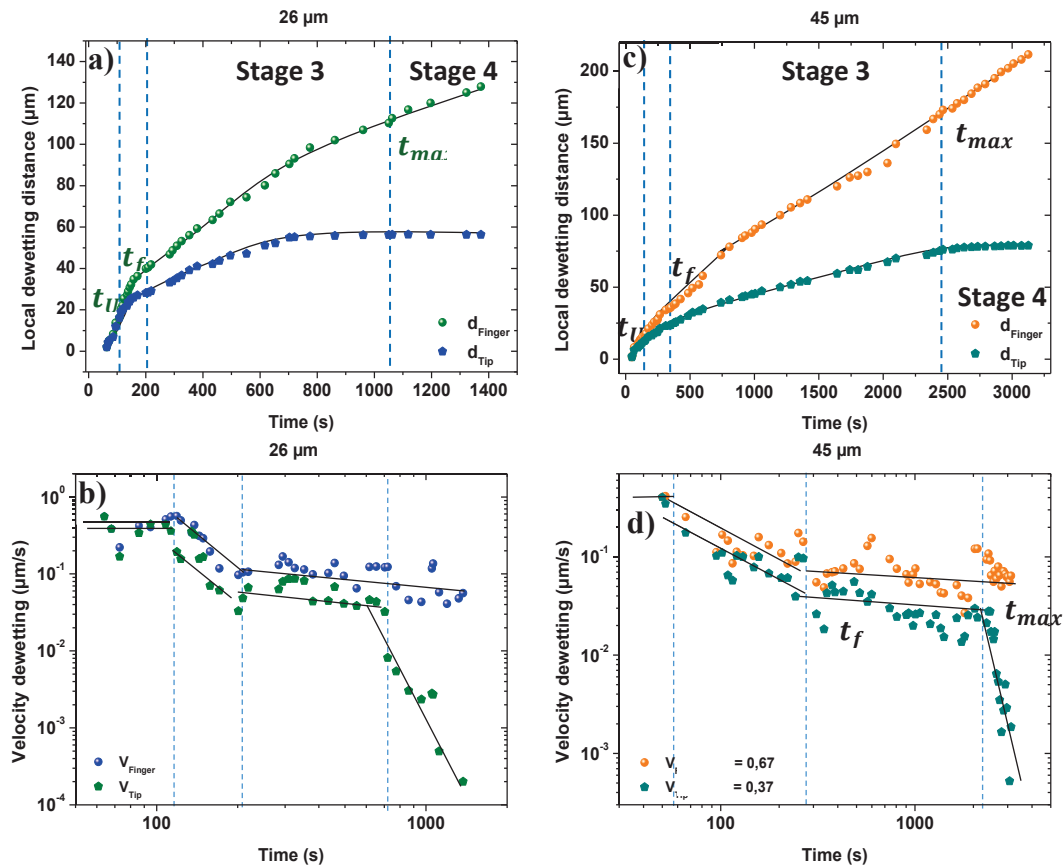


Figure 4. 15 (a-c) Temporal evolution of the dewetting distance (d) of the “Tip” and “Finger” rim regions of a **195 nm PS(137k)** thick film dewetted on top of **26 and 45 μm** MTS/Si-OH patterned substrates. **(b-d)** Temporal evolution of the dewetting velocity (V) on double logarithmic scales of **26 and 45 μm** .

Let's consider now the largest patterns **26 μm** and **45 μm** linear strips. Fig.4.15 shows respectively the temporal evolution of the dewetted distance d and the velocity dewetting V the two regions of the ridge. As discussed above we can clearly discern four different regime for all the samples used in the dewetting experiments. However, some differences can be noticed as the dewetting proceeds. In the case of the rim growth, undulation and swelling regimes, all the patterned samples displays an uniform behavior and almost the same t_U and t_f . This behavior can be explained using the ineffectiveness of the surface tension on the dewetting dynamics at the formation of the rim. As dewetting experiments proceeded, a shift of the apparition of the droplet instability (t_{max}) with the increase of the patterns sizes is observed. In fact, with the increase of sizes of the linear strips (MTS/SI-OH), we assume that the interface contact between Polymer/patterns undergoes an expansion inducing a delaying in the maturation of the rim. As consequence, the retraction of the film arise in a regime where friction at the solid/liquid interface is almost the same for all patterned samples. However, a shift of the droplet detachment regime was assumed inducing an increase of the interfacial friction with the increase of the patterns sizes.

II-1.2-Regimes of the rim instability

Chapter 4 Dewetting as an investigative tool for studying the interfacial friction of patterned surfaces

The changes in the dewetting dynamics noticed in Fig. 4.12 are divided into four regimes defined in this part to provide a quantitative comparison between the different patterned systems. Fig.4.16 and Fig.4.17 displays respectively the temporal evolution of various parameters such as local rim width (\mathbf{t}) and the wavelength $\lambda(\mathbf{t})$ defined as the finger to finger distance measured along the ridge (y-axis) between subsequent thicker regions Fig.4.13.

II-1.3.a-First stage: Rim growth:

Fig.4.16 shows the temporal evolution of the rim width measured between the three phase contact line and the wet side of the ridge at the thin and thick regions defined as W_{tip} and W_{finger} . Thus, we can clearly notice an increase of the rim width up to a limit threshold defined as the maximum width of the swelled rim in the tip region. We can attribute to this threshold a term \mathbf{t}^* defined as the specific time where this phenomena occurs.

Prior to \mathbf{t}^* , parallel to the growth of the rim width, a high constant velocity can be clearly observed on both regions Fig.4.14 (b). Moreover, the increase of the rim width strongly correlates with the high constant recorded on the different patterned system.

II-1.3.b-Second stage: swelling regime:

II-1.3.a-1-undulation:

Parallel to the increase of the rim width a growth of the wavelength $\lambda(\mathbf{t})$, defined in Fig. 4.17 as the lateral distance between successive peaks λ_i averaged between \mathbf{t} bulges over the largest possible length can be noted. Numerous wavelengths compete until the optimal wavelength λ_{max} increases with the fastest growing rate. Thus, the growth of the front and the amplification of the undulation are synchronous concerning the rim instability.

The evolution of the wavelength compared at equivalent distance traveled from the contact line in Fig. 4.18 shows, in contrast to the previous situation, a similar growth trend to \mathbf{d} . The spatial evolution of the wavelength $\lambda(\mathbf{d})$ depends on the volume of material accumulated in the rim only. Therefore, the wavelength continues to grow along the dewetting distances until an abrupt slowing down of $\lambda(\mathbf{t})$ reaching a plateau value of λ_{max} . This value corresponds to the transition from bulges to fingers. We should note that the λ_{max} increase proportionally to the increase of the linear strips patterned on the substrate.. Beyond \mathbf{t}^* , in one hand, a high grows rate of the W_{tip} is observed. In the other hand, a slow decrease of the W_{finger} can clearly be noticed. We can attribute this behavior to the rim swelling and the change of the polymer flow along the ridge from the finger to tip region.

Chapter 4 Dewetting as an investigative tool for studying the interfacial friction of patterned surfaces

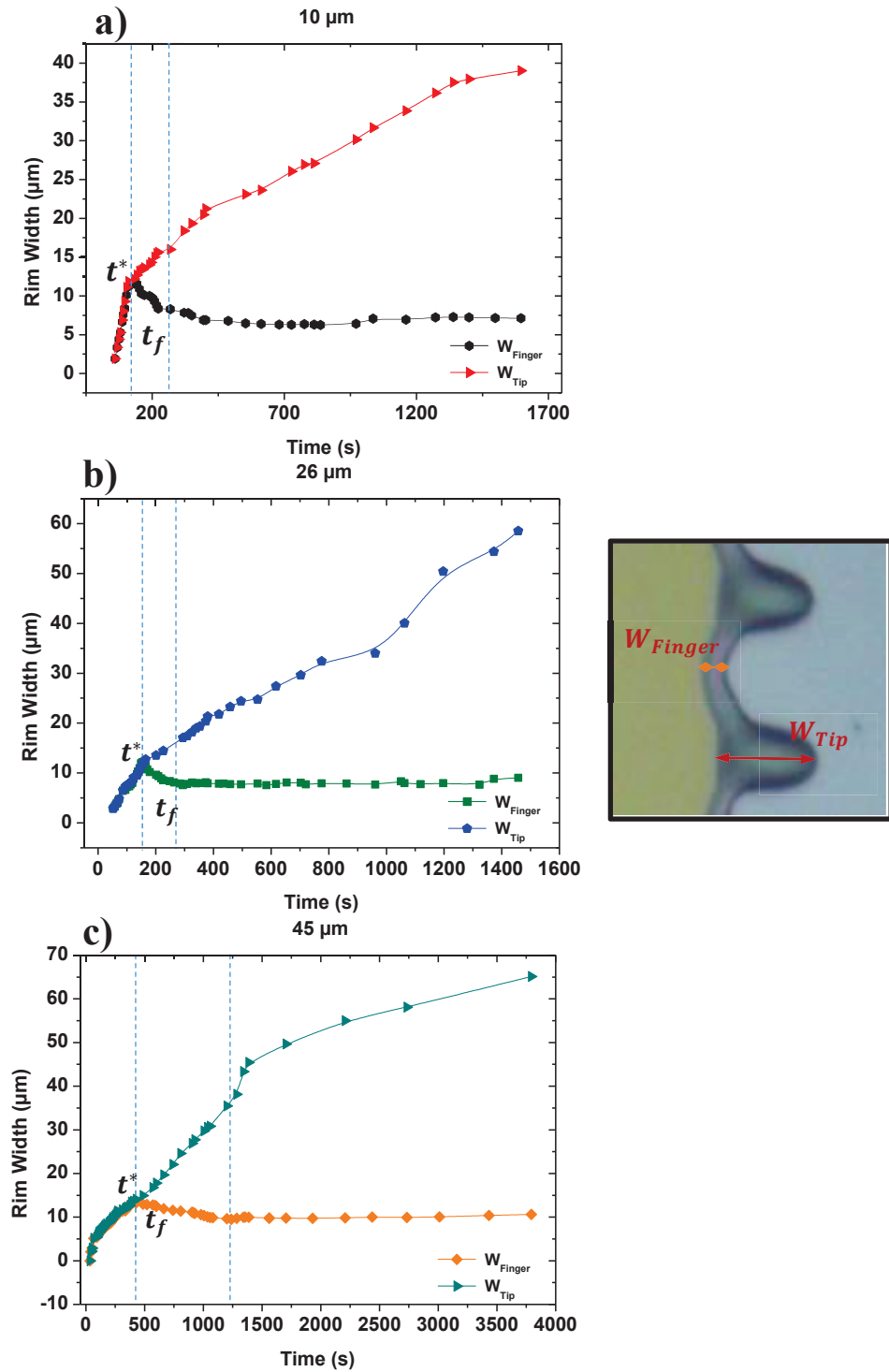


Figure 4. 16 (a-c) Temporal evolution of the rim width (W) of thicker (Tip) and thinner (Finger) rim regions of a $195\text{ nm PS}(137k)$ film on top of a $10, 26\ \mu\text{m}$ and $46\ \mu\text{m}$ MTS/Si-OH patterned substrates respectively. Dewetting experiments performed at $180\text{ }^\circ\text{C}$.

Chapter 4 Dewetting as an investigative tool for studying the interfacial friction of patterned surfaces

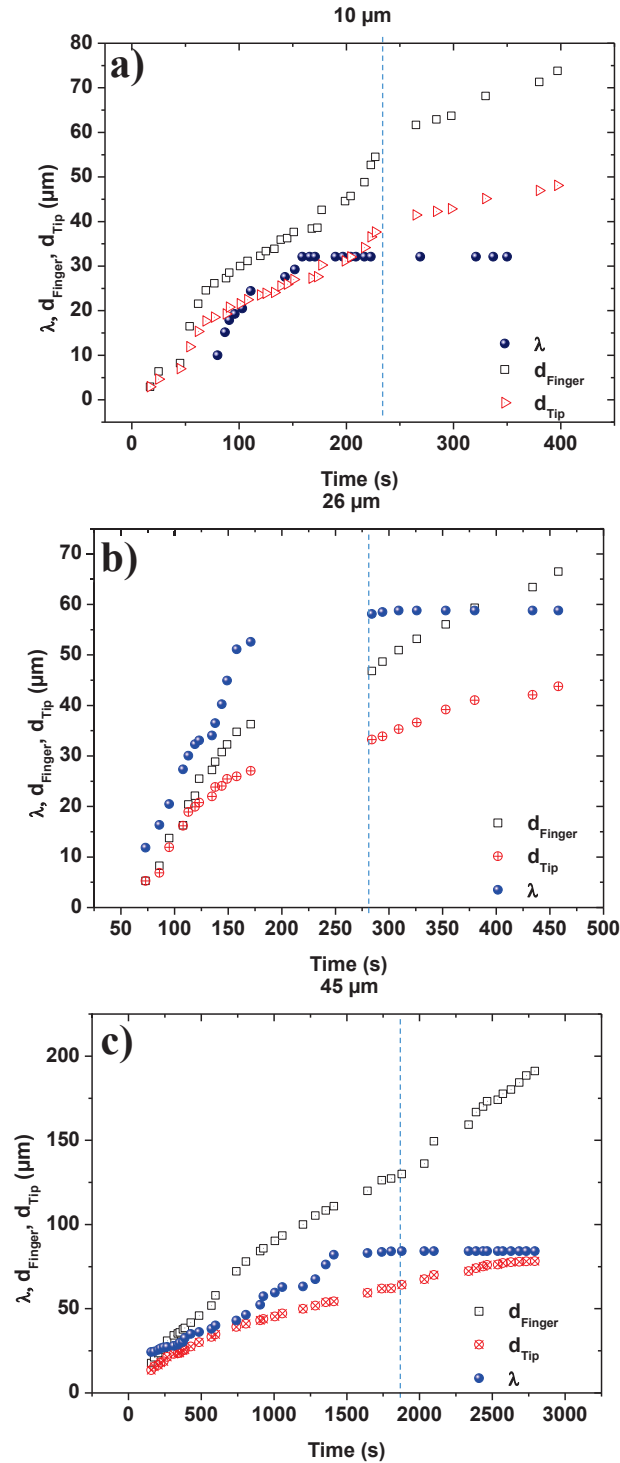


Figure 4. 17 (a-c) Temporal evolution of the wavelength $\lambda(t)$ presented for the different patterned surfaces. $\lambda(t)$ is defined as the length between successive thicker regions with the part at early stage following the solid curve. The system is a 195 nm thick $PS(137k)$. Dewetting experiments performed at 180°C .

II-1.3.a-2- bulging

The value of W_{max} at the thin region being reached for $t > t^*$, implies a discontinuity of polymer flow along the ridge. The volume of polymer accumulated on the tip of the ridge v_A is only the volume

Chapter 4 Dewetting as an investigative tool for studying the interfacial friction of patterned surfaces

collected from the advancing of the three-phase contact line in the film reduced by the volume flowing tangential to the contact line v_F towards thicker regions. Moreover, it should be noted that the liquid accumulated on the tip region is essentially due to the presence of the OH linear patterns. In fact as explained above that the PS film cannot dewet on this specific zone due to his higher surface tension compared to the hydrophobic layer. Thus, no additional material comes laterally from the collapsing of nearby bulges. Fig. 4.14 (b), illustrate the evolution of dewetting velocity with time following $V \sim (t)^{-1/2}$ at this stage. This behavior can be attributed to the viscoelastic behavior of the fluid. More precisely, in this regime the liquid behaves like an elastic solid inducing a decrease of the velocity recorded at both regions for $t > t^*$ indicates that the uptake of material equilibrates with the flow of material towards the thick region. The latter induces a thickening of the rim at the tip zone.

In fact, as discussed above we suggested that the change of the interfacial friction start with the shift of the apparition of the droplet instability (t_{max}) following the increase of the patterns sizes. However, the evolution of the local rim width proves that this change may occur earlier, precisely at the threshold of the swelling regime. We can clearly observe that with the increase of the size of strips a shift in the occurring time from a regime $t^* < t_f$ to another regime where $t^* > t_f$. Additionally, assuming that the interface contact between Polymer/patterns undergoes an expansion with the patterns size. An increase of the volume collected on the front of the rim suggest an augmentation of bulges number and sizes which induces an expansion of the time needed to the rim width to reach the maximum threshold of swelling and to relocate these bulges from the rim front (thin region) to the thicker zone leading to the fingering instabilities.

II-1.3.c-Third regime: Fingering instability

A sudden increase of the growth dynamics of $W_{tip}(t)$ can be noted on Fig. 4.17 at t_f . This increase is normally correlated to the decrease of $V_{tip}(t)$. The new regime sets the onset of fingering. At this regime, the velocity $V(t)$ of the moving front evolves as $V \sim (t)^{-1/3}$ Fig. 4.14 (b). Thereafter, we can assume that the “mature rim” regime is reached suggesting that the viscous dissipation is negligible compared with the interfacial dissipation due to friction, and, consequently, an increase of the interfacial friction can occur.

Therefore, as the swelling further protrudes from the rim, the three-phase contact line on either side of the bulge becomes normal to the dewetting direction ($t > t_f$). Further, we can observe an increase of the periodicity and the number of bulges with the increase of the strips sizes. This aspect, induce a relocation of the collapsed bulges on the front of dewetting to the sides forming then the features of fingers. Beyond t_f , the cross section at the back of the swelled rim thins, a neck is formed. At this stage, we assume that the Laplace pressure in this region could changes. Thus, a force similar to the spreading coefficient is applied at the back side of the bulge which, coupled to the dewetting velocity V_{finger} which is clearly larger then V_{tip} , initiates the finger instabilities. The finger whose shape is

Chapter 4 Dewetting as an investigative tool for studying the interfacial friction of patterned surfaces

roughly similar to a supported semi-cylinder grows until the droplet pinches-off at t_{max} . Focusing on high molecular weight polymers, Gabriele et al. [197] defined the onset of instability as the transition where fingering starts. The latter process initiated after disentanglement of polymer chains. This statement contradicts previous observations showing no finger, but the instability growing on the rim via the presence of successive wider and narrower regions of rim at the moving front. In our situation, the small molecular weight of polymers and the high temperature we used are such as the viscoelastic effects are absent. Combining the last two remarks with results obtained with our experiments, we can first conclude that the rim instability develops before fingering starts, of bulges or onset of fingering. Second, our setup strongly indicates that the main factor inducing fingering is slippage. Moreover, we should note that the acceleration of the rim instability in our case is clearly governed by the presence of different chemical domains (Hydrophobic /Hydrophilic) at the surface. In fact, the wetting and non-wetting aspect of the patterned substrates impact greatly the frictional response of the dewetted polystyrene film. Thus, the presence of the hydrophilic patterns on the surface could be the main causes of the slowing down or even the complete standby of the sliding of this film, which favorites greatly the rim instability. Furthermore, according to de Gennes' reptation model, slip length b scales with the size of the polymer as $b \propto N^3$, with N the number of monomers [198]. The transition from bulge to finger appears at a stage where the balance between dissipative forces and driving forces varies locally. In fact, at the start of dewetting, a high energy is needed to debuts the film sliding constructing then the rim. As the dewetting process, an increase of the rim width induces then an augmentation of the interfacial friction. This behavior could be attributed to the no-sliding effect provoked by the presence of the hydrophilic patterns on the surface. Therefore, in our case, this response is a result of a competition between slip and no slip behavior induced by the introduction of an (Hydrophobic /Hydrophilic) system on the surface. Hence, for strongly slippery systems, the contribution of the rim width W on the velocity leads to a gradient of velocity along the ridge (Fig.4.18). In fact, following this behavior, we consider the presence of the two types of dissipation mechanism on the interface of the patterned layer. The first being purely viscous and the second being friction at the solid/liquid interface, this two mechanism can be combined to explain why the dewetting velocity is fastest on the smallest patterns compared to the biggest patterns the ($45 \mu m$) linear strips.

Chapter 4 Dewetting as an investigative tool for studying the interfacial friction of patterned surfaces

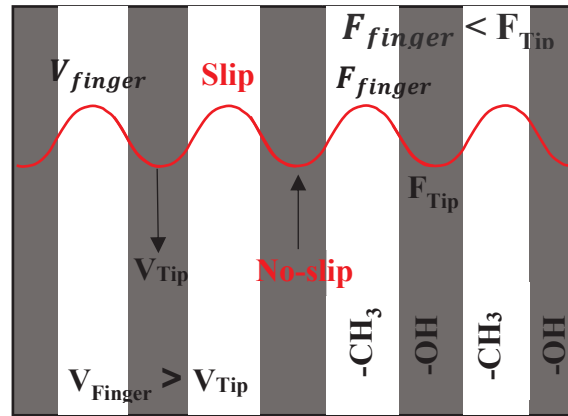


Figure 4. 18 Schematic of the competition between slip and no slip behavior induced by the introduction of (-CH₃/-OH) system on the surface. Where the velocity dewetting at the finger region is faster compared to V at the tip zone and the friction of the -OH layer is higher compared to the -CH₃ zone

II-1.3.d-Forth regime: Droplet detachment

At the release of the bulge from the finger, a force driven by the Laplace pressure is applied to the newly formed contact line to round the droplet which creates a fast decrease of the dewetting velocity at the thick region at (t_{max}). The process of droplet detachment occurs when friction energy at the solid/liquid interface is higher than the kinetic energy and the cohesive energy, which keeps the swelled part of the rim connected to the ridge. The Mechanism of the formation of a finger depicted in Fig. 4.19 (a) evidences a long neck arising after the swelling regime from the decreases of the dewetting velocity like $V \sim (t)^{-1}$ Fig. 4.14 (a). The bridge linking the projected liquid to the dewetting front, well known for viscous fluids in the field of liquid jets [184, 192], breaks up following a length scale ℓ_v and time scale t_v given by [193]. The time scale of droplet breakup in the rim instability is strongly embedded to the dynamics of displacement of the moving front and will therefore not be considered in the following. The length ℓ_v evolves with the square of viscosity, the predominant parameter in equation e. We noted in above that the pinch-off regime is reached at ($d_{max_{10\ \mu m}} = 52\ \mu m$, $d_{max_{26\ \mu m}} = 57\ \mu m$ and $d_{max_{45\ \mu m}} = 79\ \mu m$) for dewetting temperatures at $180\ ^\circ C$ which reveals the predominance of slippage and especially the contact area of the solid/liquid interface in the breakup process. In fact, at droplet detachment, the driving force equilibrates dissipative forces F_V and F_S respectively due to viscous friction within the liquid and friction of the liquid molecules at the solid/liquid interface, slippage, against the driving force. After the breakup, the presence of a finger at pinch-off, initiates several distinct patterns via the formation of the primary and secondary droplet. The latter must not be mixed up with a satellite drop, which is observed under certain conditions. We compare in this part the distinct types of droplet obtained for the different systems with the knowledge obtained in the field of physics of liquid jet [192] in order to explain the final patterns illustrated on Fig.4.19 (a)

II-1.3.d-1-Primary droplets

Chapter 4 Dewetting as an investigative tool for studying the interfacial friction of patterned surfaces

Great differences of the primary droplets was found between the different patterned systems, respectively Typical droplet diameter and lateral distance between each drop are presented in Fig.4.19 (b). We can clearly notice a dependence of the size and shape of droplets with the linear strips sizes . In fact, with the increases of the patterns size, the droplet detached from the ridge undergoes a significant deformation despite their final ellipsoidal shapes. This observation corroborates previous results on the value of the maximal distance traveled by thicker parts before breakup d_{max} , discussed above. This distance represents the volume of liquid collected in the course of dewetting. Moreover, the distance between droplets is also interconnected to d_{max} and in our case; it depends on the shape and the size of the patterned layer. We should also note that the alignment of the primary droplets asserts from the good quality of the dewetting experiments. However, we can observe also that as the thickness of the polystyrene film casted on the patterned substrates increase, the side effects such as pinning or other inhomogeneities (highly deformed drop) increase as well. Which lead to irregularities in the rise of the undulated ridge involves a premature pinch-off.

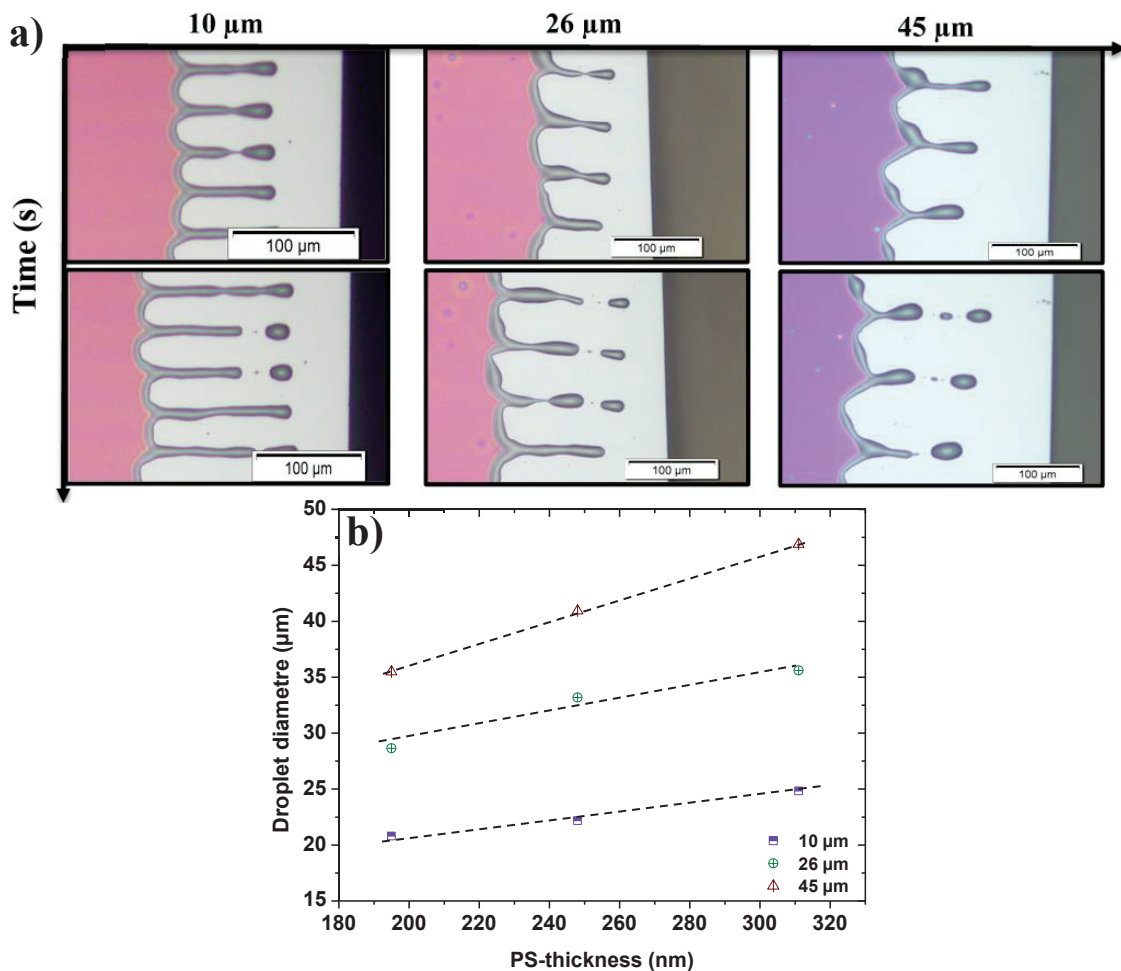


Figure 4. 19 (a) Optical micrograph of the droplet detachment instabilities of a 248 nm thick PS (137k) on top of a different patterned substrates. **(b)** Primary droplets diameters as function of the varying PS thicknesses for the different textured systems.

Chapter 4 Dewetting as an investigative tool for studying the interfacial friction of patterned surfaces

II-1.3.d-2-Secondary droplets

The size of the secondary droplet observed on optical micrographs of Fig. 4.20 is slightly smaller as the primary droplet. To understand the difference between the two droplets, We used the knowledge achieved in the hydrodynamics of liquid jets to understand the origin of this secondary droplet [184, 192]. The thread of polymer is strongly stretched. The pinched region, termed peak, of length ℓ_{peak} has no solution using the usual hydrodynamics description after breakup. The tip recedes into the detached thread at a velocity proportional to $t^{-1/2}$. The high retracting velocity initiates a rim near the newly established contact line. This velocity competes with the dewetting velocity of the retracting front. The newly elongated line formed with a smaller droplet rapidly detaches from the moving tip or finger as previously described. Right after pinch-off, the dewetting velocity at the tip V_{tip} is much slower than the velocity at the thinner region in case a finger is formed (slippery system). The finger further grows and V_{tip} slows down until the droplet rapidly detaches. The width of the neck of the different system is much smaller than the finger and no accumulation of liquid in the peak is expected since the V_{tip} reached the no-slip boundary case. Consequently, slippage affects the final pattern via the presence of fingers in the timescale of dewetting influencing the shape the droplet after the pinch-off. Thus, a deformation of the droplet can be anticipated.

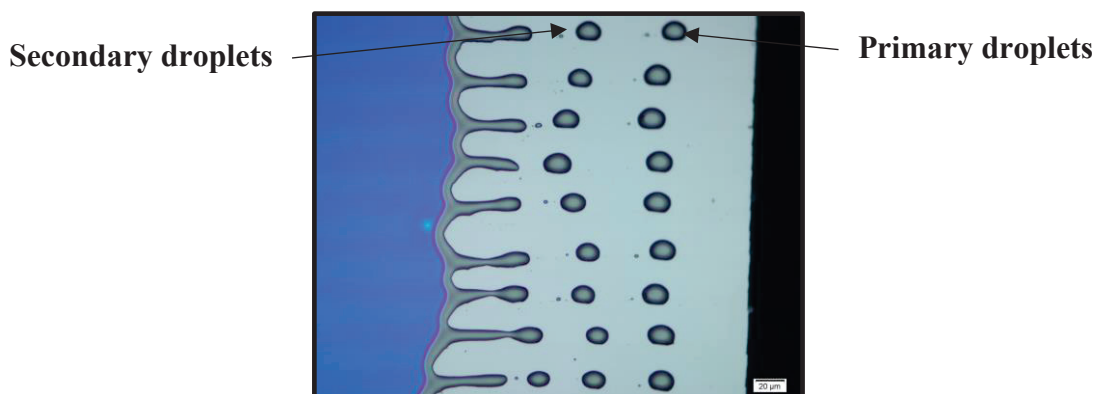


Figure 4. 20 Optical micrographs of the droplet detachment instabilities of a 311 nm thick PS (137k) on top of a different patterned substrates illustrating the primary and secondary droplets.

II-1.4-Thickness effect on the dewetting dynamics

Let's concentrate on the effect of the polystyrene thickness on the dewetting dynamics. The aim of this experiment is to highlight the impact of the capillary forces and rime width on the interfacial friction response. Therefore, in this part we will be interested on the dewetting of several thicknesses of polystyrene film ranging from (195 nm up to 311 nm) on a silicon substrate textured by 45 μm printing linear textures of MTS molecules at 180 $^{\circ}\text{C}$. Thus, using this method we can measure respectively the dewetted distance $d_{Average}$ and the rim width $W_{Average}$ of the ridge by optical micrographs of the dewetting dynamic in time Fig.4.22. It should be noted that from these parameters, an averaged velocity

Chapter 4 Dewetting as an investigative tool for studying the interfacial friction of patterned surfaces

dewetting $V_{Average}$ was obtained by taking the differences ; $V = [d(t_i) - d(t_{i-1})]/(t_i - t_{i-1})$

Fig.4.21.

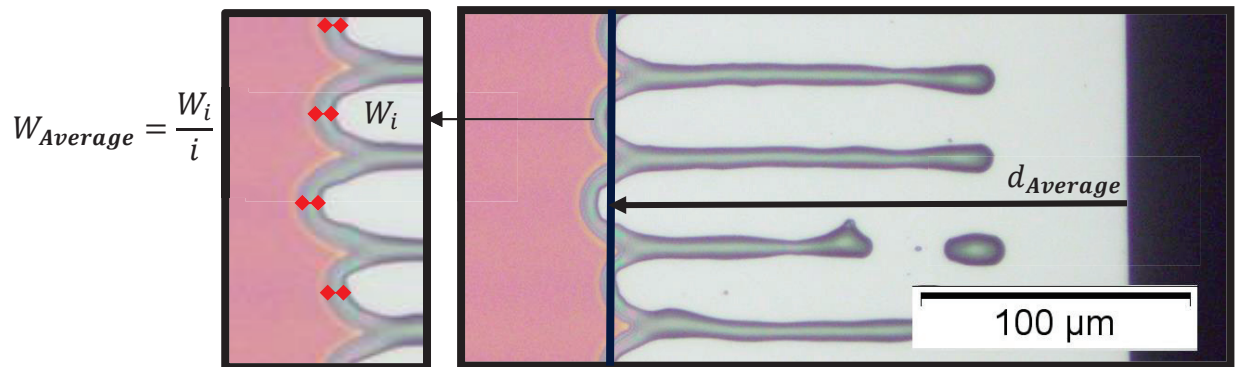


Figure 4. 21 Optical micrograph of the dewetting dynamic defining the averaged dewetting distance $d_{Average}$ and the rim width $W_{Average}$.

Chapter 4 Dewetting as an investigative tool for studying the interfacial friction of patterned surfaces

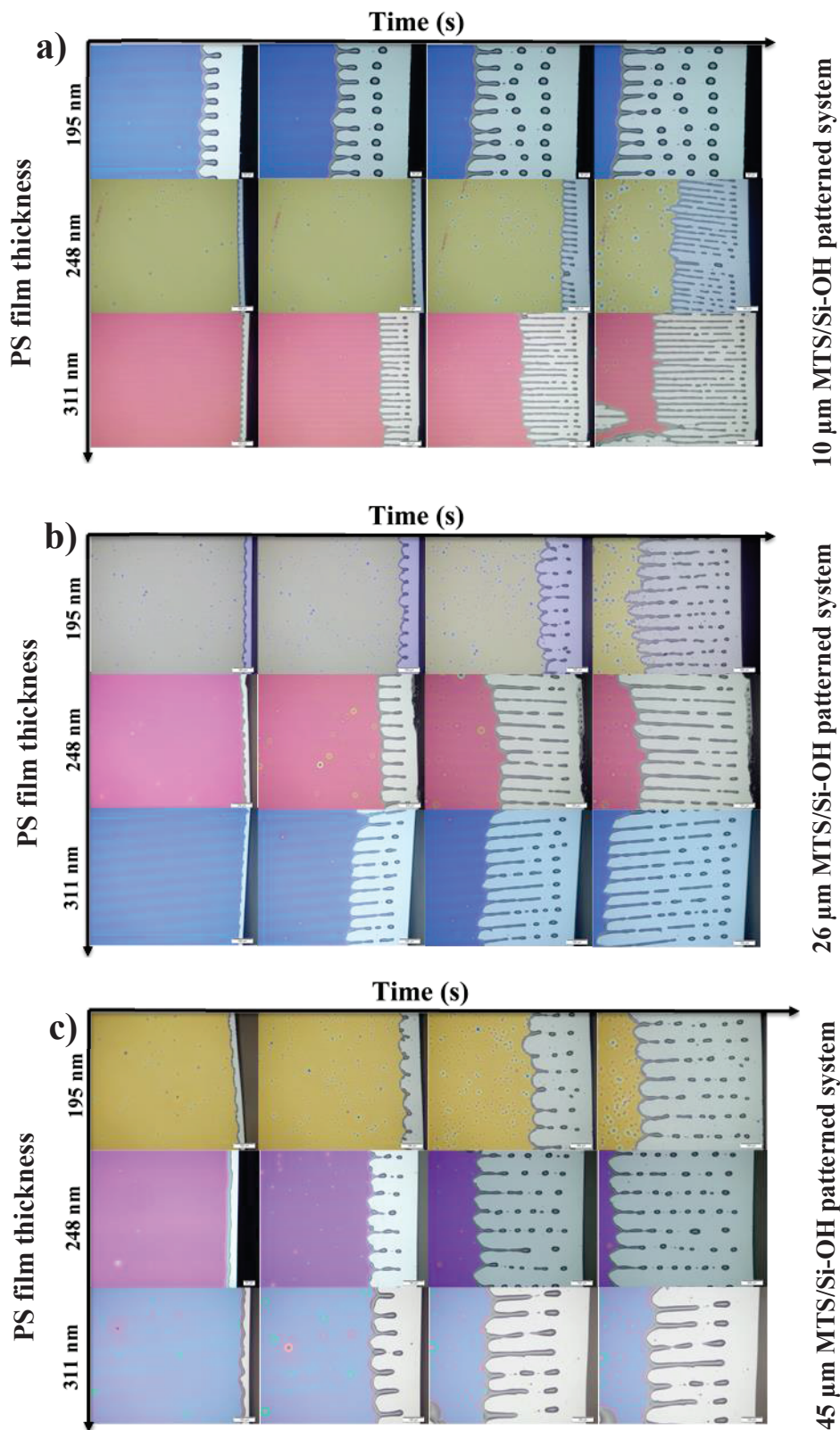


Figure 4. 22 Optical micrograph of the dewetting dynamic of a 195, 248 and 311 nm PS (137k) performed at 180 °C for different patterned substrates. ($842 \mu\text{m} \times 660 \mu\text{m}$ and $336 \mu\text{m} \times 263 \mu\text{m}$)

Chapter 4 Dewetting as an investigative tool for studying the interfacial friction of patterned surfaces

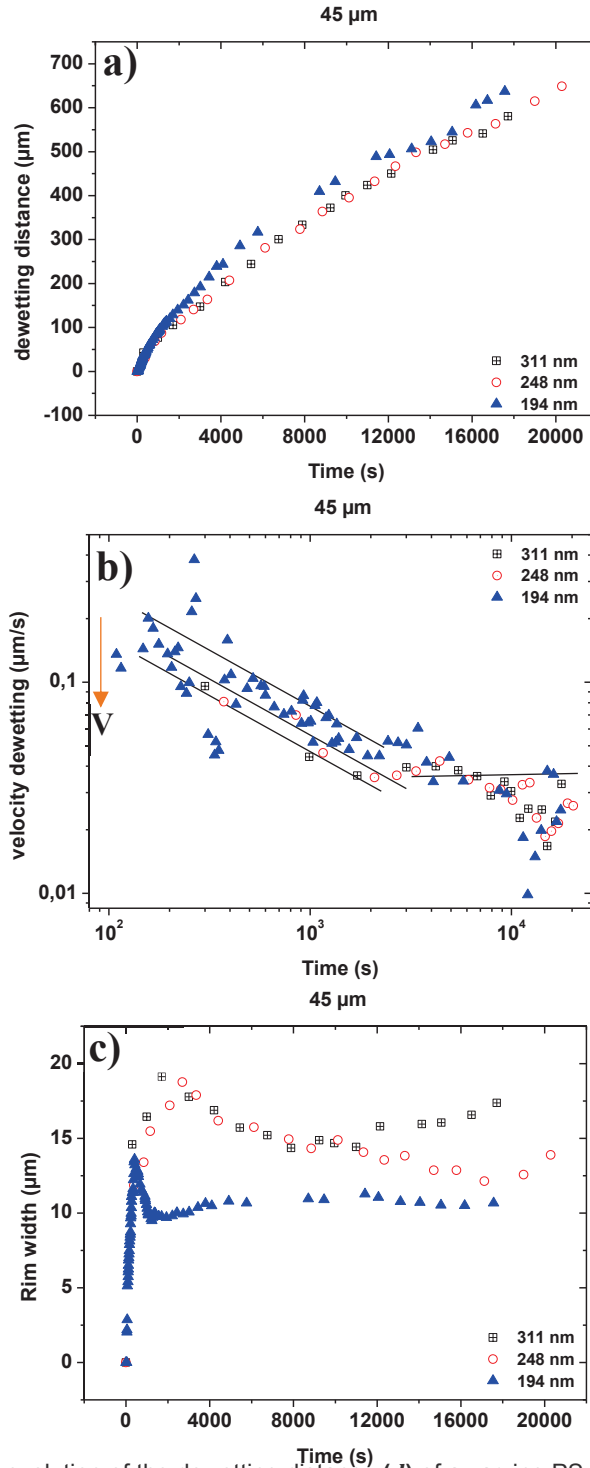


Figure 4. 23 (a) Temporal evolution of the dewetting distance (d) of a varying PS film ranging from 195 nm up to 311 nm on top of a 45 μm MTS/Si-OH patterned substrate. (b) Temporal evolution of the velocity dewetting (V) of a varying PS film ranging from 195 nm up to 311 nm on top of a 45 μm MTS/Si-OH patterned substrate. (c) Temporal evolution of the rim width (W) of a varying PS film ranging from 195 nm up to 311 nm on top of a 45 μm MTS/Si-OH patterned substrates.

Fig.4.23 shows respectively the temporal evolution of the dewetting distance, the rim width growth and the dewetting velocity. Hence, we observe clearly the non-linear behavior of the dewetting distance d , the rim width W and the velocity dewetting V . Thus, the results from films of different thicknesses clearly illustrated that thinner film dewetted faster. In fact, in this situation, we can assume that with

Chapter 4 Dewetting as an investigative tool for studying the interfacial friction of patterned surfaces

same size of patterns used in our system that the capillary force should sustain a decrease with the increase of the PS thickness, inducing then a decrease of the dewetting velocity. This was confirmed by the results extracted from Fig.4.23. Therefore, the pattern obtained for each film thickness is clearly comparable to the pattern described above, implies that the rim instability passes through all three regimes, undulation, bulging and fingering before a droplet detaches the ridge. The analogy with previous results obtained on the different patterned systems suggests that dewetting occurs under slippery conditions. These results proves the dependence of the dewetting experiments with the Ps film thickness.

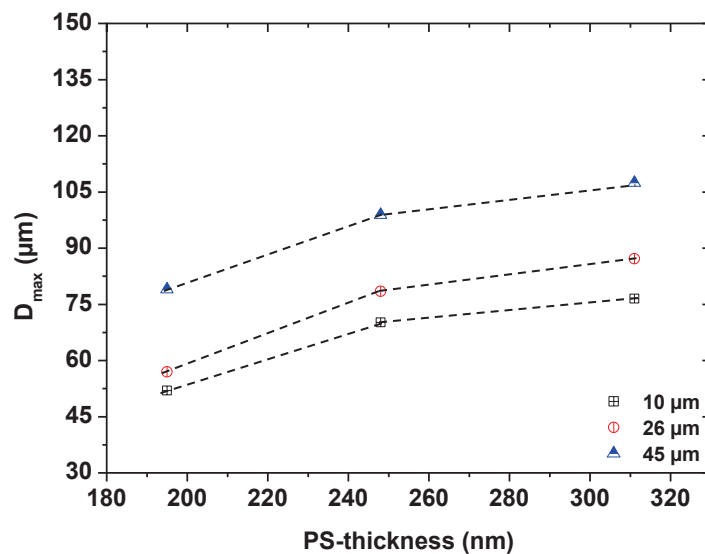


Figure 4. 24 The growth of the maximum dewetting distance (d_{max}) at the hydrophilic zone of the different patterned systems as function of the PS film.

According to results obtained above, the characteristic distance setting the transition between all three regimes and the maximal distance d_{max} recorded at peak before the droplet pinches-off are slightly affected by changes in dewetting dynamics. In fact, we can notice an increase of the W_{max} value following the increase of the film thickness suggesting an increase of the interfacial friction shifting more the apparition of the maximal swelling phenomena inducing a delay in the droplet instabilities. Let's now concentrate on the distance d_{max} traveled by the thicker part of the ridge before the droplet is released. We observe that d_{max} slightly increases when the initial film thickness h passes from 195 up to 311 nm. The increase of d_{max} with film thickness on the patterned surfaces gives evidence that the impact of slippage on the rim instability reduces with the decrease of the strips sizes Fig.4.24.

In the case of the fingering regime, precisely right before the system enters the pinch-off regime, Fig.4.26 evidences a decrease of the finger length L_f as the patterns size is reduced. At the same time, we can notice also that as the PS/thickness increase, the finger length L_f before the droplet detachment increases. The rise of the finger length, in plane length measured perpendicular to the dewetting front

Chapter 4 Dewetting as an investigative tool for studying the interfacial friction of patterned surfaces

from the backside of the droplet to the apex of the finger before it merges into the ridge and decays into the film.

II-1.4-1-Finger thread

Besides times and distances, it seems important to compare the ratio between the diameter of the droplet and the width of the neck. Following the Fig.4.25, we can notice that with the increase of polystyrene thickness, the diameter of the droplet and the distance between them increase as well. In any case, a thread of polymer links the detaching droplet to the moving front. This thread, well known in the field of decaying liquid jets with polymeric fluids, is always present at the pinch-off regime. In fact, a finger of length increasing with viscosity builds up on the patterned systems from the local gradient of the dewetting velocity, varying following $(t)^{-1}$. The width of the finger is approximately as large as the width of the rim at the hydrophilic region. The amount of material accumulated in the ridge in the region where fingering builds up is therefore much larger than in

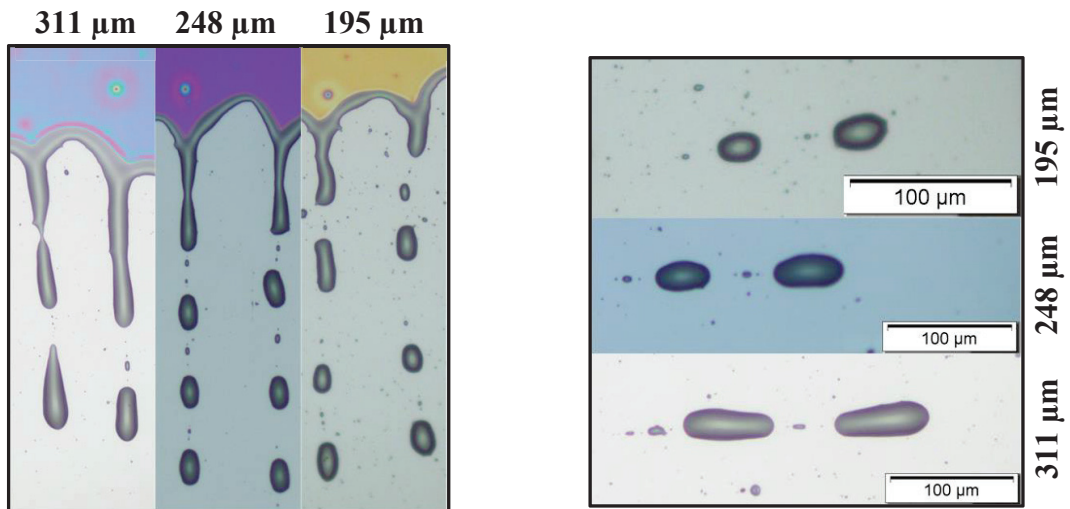


Figure 4. 25 Droplets diameter and distance between droplets as function of the varying PS thicknesses for the different textured systems.

the region the furthest away from the finger. Moreover, we can anticipate an increase of the width of the finger with the increase of the film thickness. Additionally, an increase of the distance between consecutive droplets and a decrease of the droplet diameter is suggested. This is indeed confirmed in Fig.4.26, which proves the dependence of the three regimes to the film thicknesses.

Chapter 4 Dewetting as an investigative tool for studying the interfacial friction of patterned surfaces

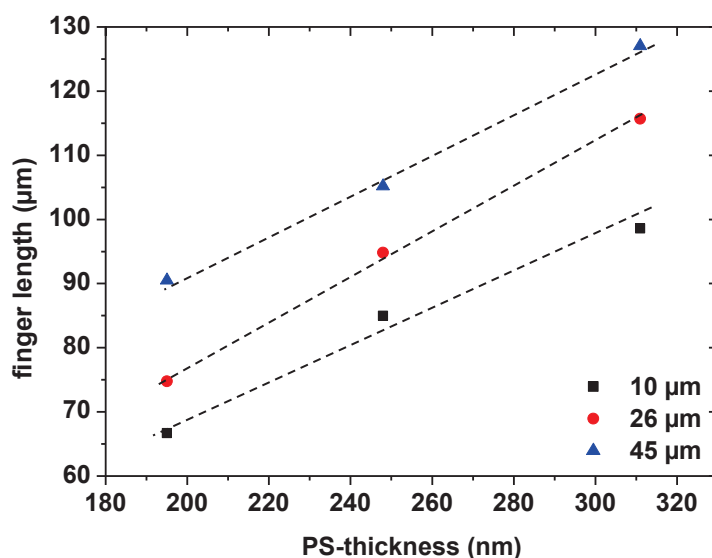


Figure 4. 26 Finger length as function of the varying PS thicknesses for the different textured systems.

II-1.5-Rim instability on the circular geometry

Up to now, the circular geometry of a dewetting hole was left aside to concentrate on the rectilinear geometry of a straight front, much easier to study the rim instability and draw comparisons with the Rayleigh-Plateau instability well known in the physics of liquid jets. In this purpose, the production of holes in the area of interest was avoided since it might hinder the rim instability. A hole growing in the vicinity of the moving front creates a premature merging of rims forming a semi-cylinder. The ideal conditions used for the experiments involves a low density of nucleation sites which enables a hole growth unperturbed from any nearby rims. The rim instability is studied for the latter situation in a first part. Now the question rises whether the geometry affects the rim instability?

Chapter 4 Dewetting as an investigative tool for studying the interfacial friction of patterned surfaces

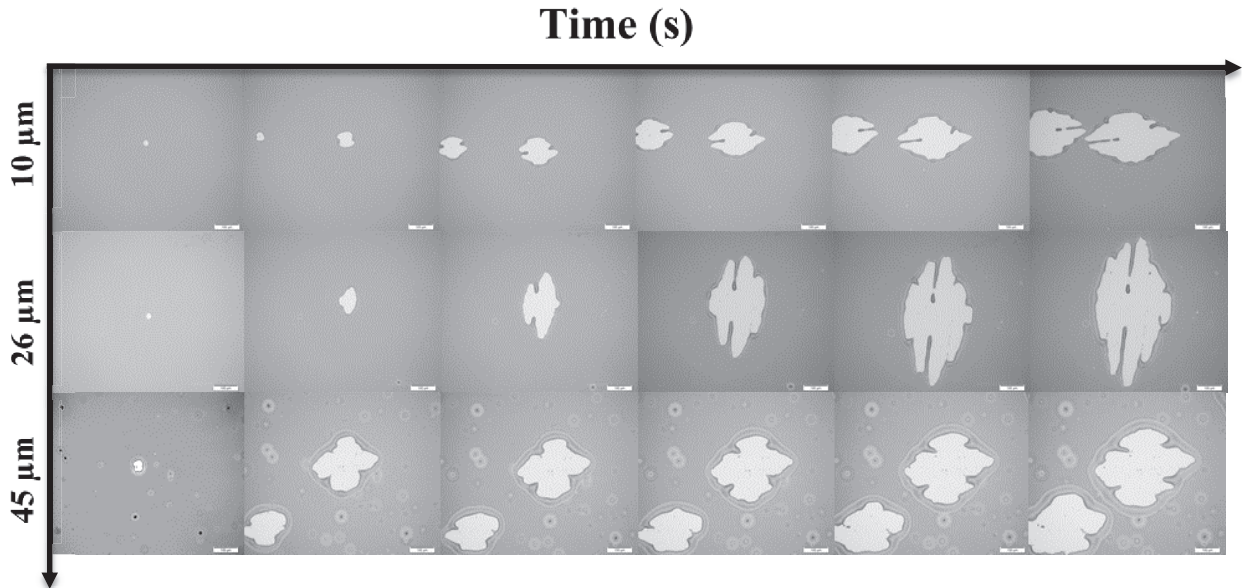


Figure 4. 27 Optical micrograph ($842 \mu\text{m} \times 660 \mu\text{m}$) of the dewetting dynamic of a 248 nm thick PS (137k) performed at 180°C for different patterned substrates.

Fig.4.27 depicts the dewetting scenario of a hole retracting from a Si-wafer patterned with (10, 26, 45 μm) linear strips of (MTS/Si-OH). The 248 nm thick polystyrene film of molecular weight $M_w = 137 \text{ kg}\cdot\text{mol}^{-1}$ is annealed at 180°C while optical images are recorded in situ. Under these circumstances, holes nucleate from the metastable system [49, 199], dry patches represented by the white zone, the polymer melt retracting from the substrate in Fig. 4.27, are initiated around a nucleus and form a disk of growing area with time. The polymer accumulates at the perimeter of the hole into a rim, dark grey zone, of increasing size as the radius of the hole grows as $R(t)$. The film, light grey, remains unperturbed until the wet side of the rim approaches. We attribute R_{finger} to the thin region precisely the finger shape formed parallel to the strips, R_{tip} to the thicker region and we define R as the averaged value of both R_{finger} and R_{tip} Fig.4.28.

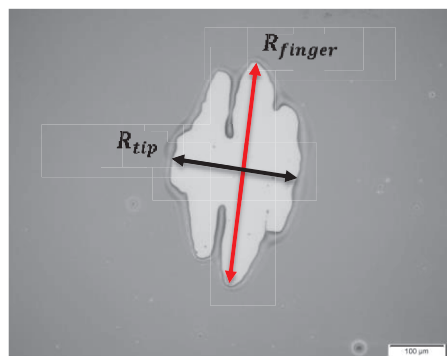


Figure 4. 28 Optical micrograph ($842 \mu\text{m} \times 660 \mu\text{m}$) of the dewetting dynamic defining the different parameter used in this part.

Chapter 4 Dewetting as an investigative tool for studying the interfacial friction of patterned surfaces

Fig.4.29 shows the temporal evolution of the hole radius R for the different patterned substrates. Hence, we observe clearly the non-linear behavior of the hole radius R . Thus, these results evidences the faster displacement of the three-phase contact line with the decreases of the strips sizes. Additionally, we observe that the rim turns rapidly into fingers on 10 μm patterns before the droplet detaches from the rim (wet side) to the four regimes previously described for straight fronts.

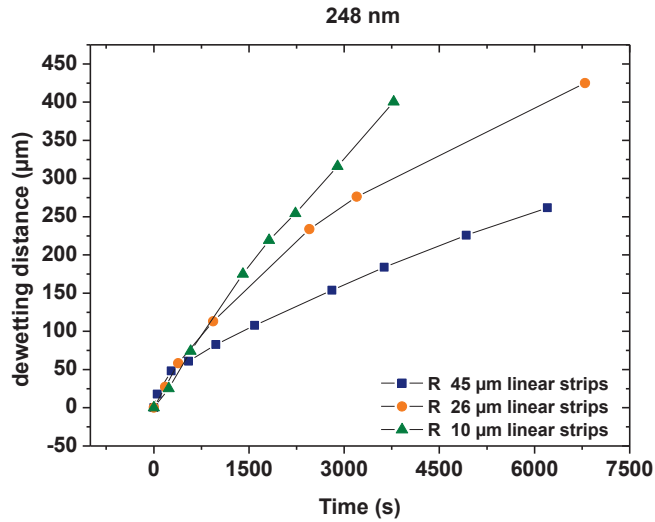


Figure 4. 29 Temporal evolution of the hole radius (R) of the different patterned systems.

It should be noted that in the chapter III, we didn't find a significant differences between the friction on perpendicular or parallel position to the linear strips using the FFM and the friction machine.

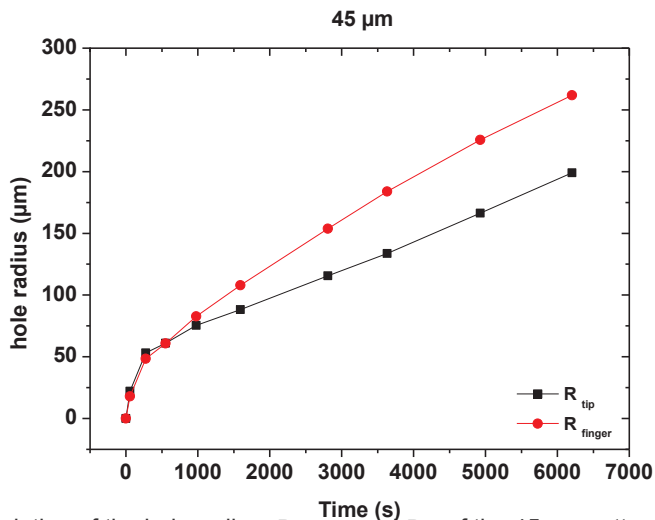


Figure 4. 30 Temporal evolution of the hole radius R_{finger} and R_{tip} of the 45 μm patterned system.

However using the dewetting technic, we proved that the film sliding in parallel fashion to the patterns, it is clearly faster and easier in comparison to the perpendicular position Fig.4.30. This behavior evidences the difference in friction between the two positions and ascertain the efficacy of the dewetting approach compared to other technics used in this study.

Chapter 4 Dewetting as an investigative tool for studying the interfacial friction of patterned surfaces

Let's consider the $26 \mu\text{m}$ linear strips. At first, we observe a spatial growth of the perimeter of the hole homogeneously distributed around the ridge despite the presence of alternatively thicker and thinner regions growing with $R(t)$ in Fig.4.31. The latter is only hypothesized in this part based on extrapolations of results obtained for straight fronts due to restrictions of the technique used, optical microscopy, for these experiments. Therefore, it is only possible to give a rough approximation of the transition from the first regime until the fingering regime, which features a deviation of the three-phase contact line from thicker to thinner zones, evidenced at $t_s < 387 \text{ s}$. We can clearly see the onset of fingering occurring around $t_f \sim 2000 \text{ s}$ and droplet detachment around $t_{max} \sim 6100 \text{ s}$. If we now compare this maximal dewetted distance for straight fronts d_{max} and holes R_{max} , we find a larger distance traveled by the three phase contact line for the circular geometry since $d_{max} = 98,92 \mu\text{m}$ and since $R_{max} = 213,23 \mu\text{m}$. Consequently, the same rim width in both situations is obtained for $R = 2d$ a trend that is confirmed by experiments.

II-1.5.1-Impact of the geometry

The evolution of the three phase contact line is depicted in Fig.4.32 for the dewetting hole R , and the straight front, open squares d . A shift of t_0 standing for the time required for hole nucleation and the creation of the three phase contact line was applied to the dynamics of hole R in order to obtain $R(t_0) = d(t_0) = 0$.

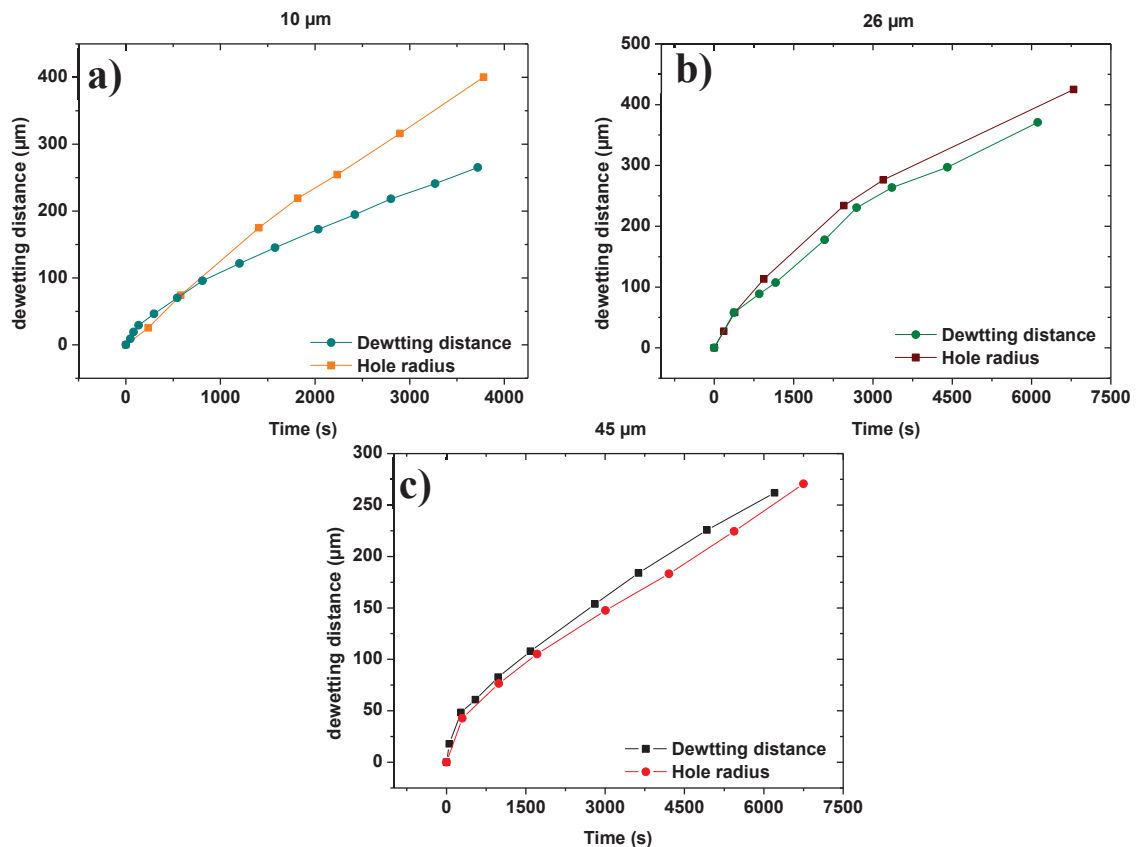


Figure 4. 31 A comparison of the temporal evolution of the dewetting distance (d) and the hole radius (R) for the different patterned systems.

Chapter 4 Dewetting as an investigative tool for studying the interfacial friction of patterned surfaces

Fig. 4.27 evidences a faster motion of the three-phase contact line for holes than for straight fronts. Although this difference might be interpreted at early stage as part of the error, R clearly deviates from d . Using the same system for both types of geometry limits the number of parameters varying for the experiments; the viscosity, the surface tension, the film thickness and the rim height are the same for both cases. Since the driving force is also identical in both cases, it is necessary to find an explanation from dissipation mechanisms and/or the geometry..

In the dynamical situation, a qualitative analysis of the rim instability developing along the ridge of a straight front or a hole leads to the same conclusions, which are, among the most important, the presence of four regimes for the different systems. The morphology of a single bulge is also much alike. A quantitative analysis, however, evidence discrepancies mostly concerning a temporal and spatial change of transitions. The most significant being an early distance of droplet detachment for straight fronts compare to holes which is explained by a faster spatial growth rate of the rim width for straight fronts. In summary, we defined that the dewetting process can be divided into a four regimes (rim growth, undulation and rim swelling, fingering and finally pinch-off instabilities) varying with slippage. We observed that as polymer accumulates in the rim at the three-phase contact line, a Rayleigh-Plateau type instability takes place at the liquid/air interface.

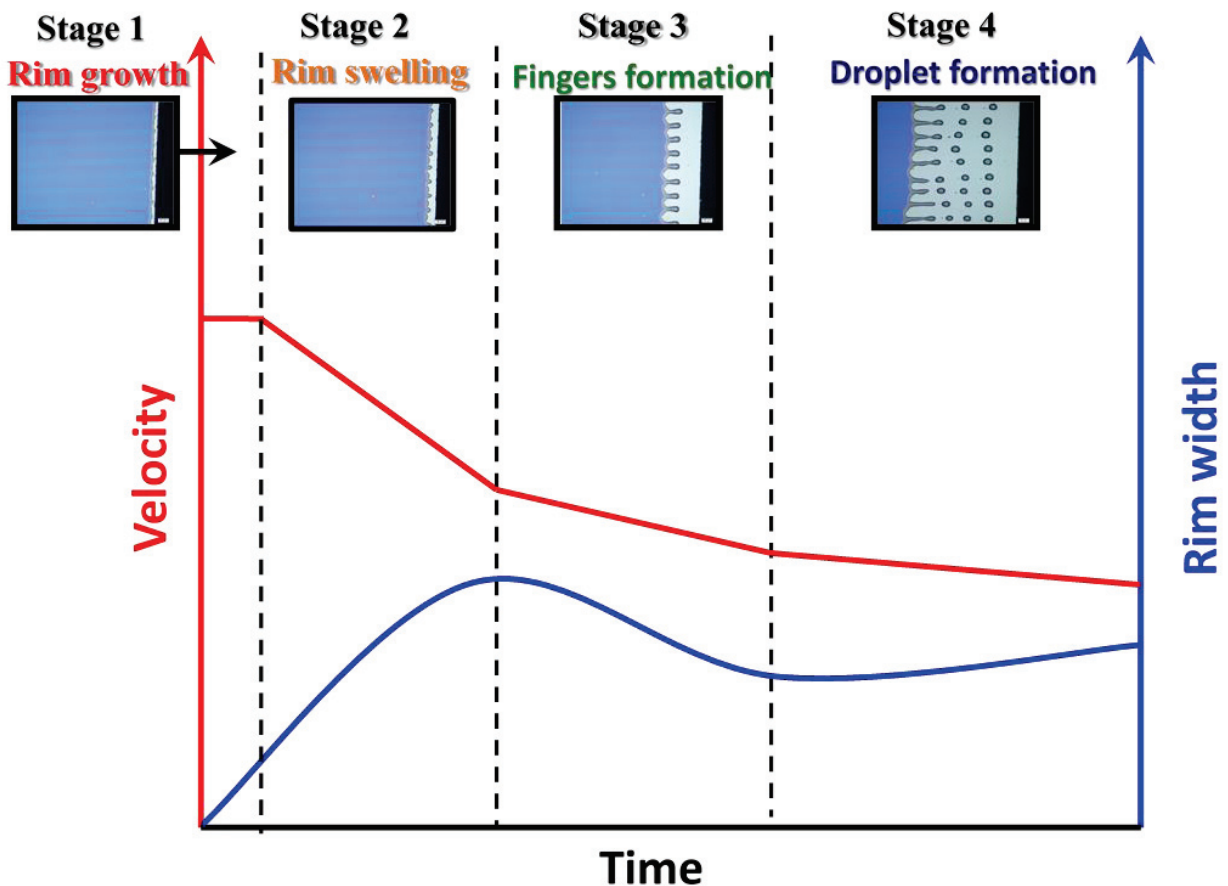


Figure 4. 32 Schematic of the dewetting dynamic of a 311 nm thick PS (137k) on top of a 10 μm MTS/Si-OH patterned substrates illustrating the different regimes of the dewetting experiments, defined by the relation between dewetting velocity and rim width.

Chapter 4 Dewetting as an investigative tool for studying the interfacial friction of patterned surfaces

From the start of the dewetting process until the droplet detachment instabilities, slippage or friction was considered the most important aspect defining the dewetting dynamics. In fact, a clear connection between the slippage (velocity dewetting) and the rim instability was established Fig 4.32. This aspect relates the transition between the different dewetting stages to the variation of the rim shape and slippage. However, the dewetting of the polystyrene film used in this work presented a qualitative analysis of the frictional response of a polymer melt sliding on (hydrophobic/ hydrophilic) patterned system. Hence, how we can obtain a quantitative information about the interfacial changes along a dewetting experiment?

Therefore, using a PDMS film for dewetting experiments on (hydrophobic/hydrophobic) patterned surfaces will allow us to extract in situ and in real time the contact angle and the slippage length at the melt-polymer interface. Then, this autohophobic dewetting will present us the opportunity to extract a quantitative information of the interfacial friction.

Based on the theoretically predicted relations between velocity, energy dissipation, capillary driving force, viscosity and film thickness, we have access to an interpretation of the changes in interfacial properties in the course of the experiment, impossible for any other technique of such simplicity. Thus, we demonstrate that dewetting experiments represent a valuable tool for the characterization of static and kinetic properties of polymer-polymer interfaces.

III-2-Dewetting Experiments Using a Newtonian Fluid on a MTS/PDMS patterned system

In this part, dewetting of a 500 nm of thin PDMS polymer film on top of MTS/PDMS system was studied. In fact, a silicon substrate was textured by printing linear strips of silane molecules (*MTS*) then grafted by a monolayer of adsorbed PDMS is compared to a silicon substrates coated with 10 nm monolayer adsorbed PDMS layers. In fact, the changes in the chemical nature of the surface, properties of polymer surfaces can also affect the entropy of the polymer chains. If polymers were grafted or adsorbed to a solid surface, these molecules may loose some of their configurational states, which means a lower entropy This may lead to autophobic behavior [172-174], i.e., the free molecules dewetted the adsorbed PDMS layer. Moreover, by breaking the sample, we created a three-phase contact line between the substrate, the film and the surrounding environment. Consequently, the thin PDMS films annealed at 150 °C while optical micrographs were recorded in situ Fig.4.33. Furthermore, it is a possible to record respectively the dewetted distance d and the rim width W of the rim by optical micrographs of the dewetting rim in time. It should be noted that from these parameters, a velocity dewetting V was obtained by taking the differences ; $V = [d(t_i) - d(t_{i-1})]/(t_i - t_{i-1})$ Fig.4.34.

Chapter 4 Dewetting as an investigative tool for studying the interfacial friction of patterned surfaces

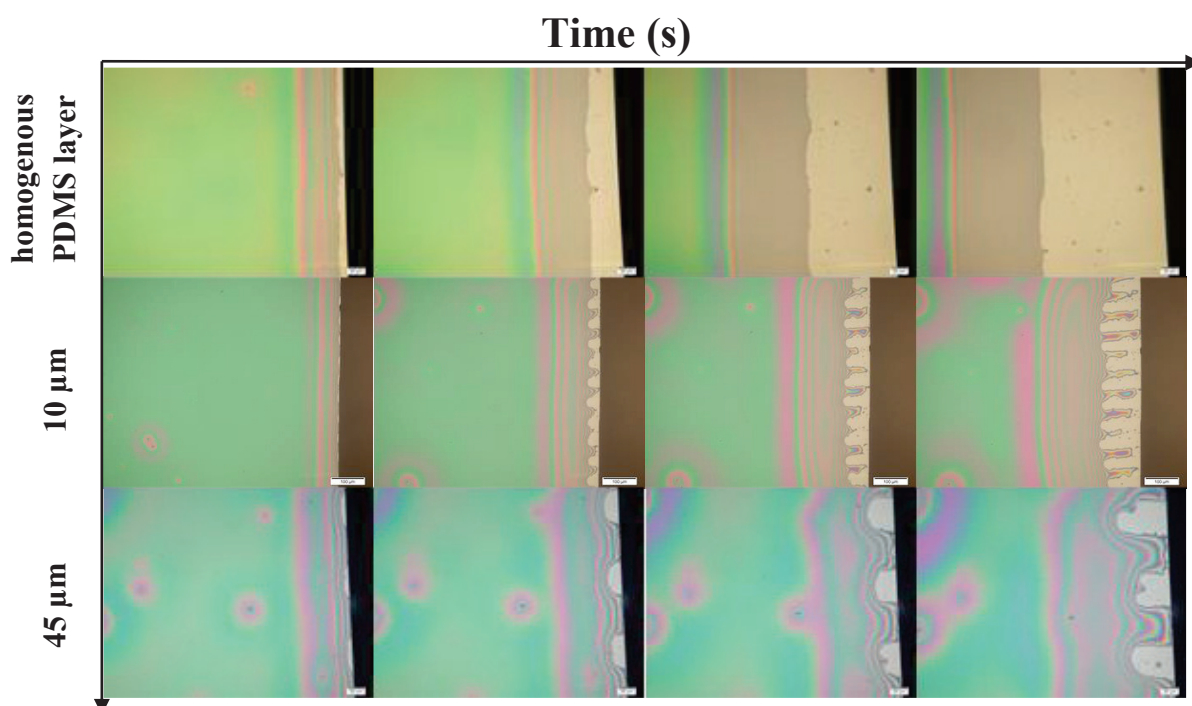


Figure 4. 33 Optical micrograph ($842 \mu\text{m} \times 660 \mu\text{m}$) of the dewetting dynamic of a 500 nm thick PDMS (139k) performed at 150°C on top of a homogenous PDMS absorbed layer and of a $10 \mu\text{m}$ MTS/PDMS patterned surface. ($336 \mu\text{m} \times 263 \mu\text{m}$) micrograph correspond the $45 \mu\text{m}$ patterned substrates MTS/PDMS

III-2.1-Dewetting Dynamics

Fig.4.35 and Fig.4.36 shows respectively the temporal evolution of the dewetting distance and the rim width growth. Hence, we observe clearly the non-linear behavior of the dewetting distance d and rim width W .

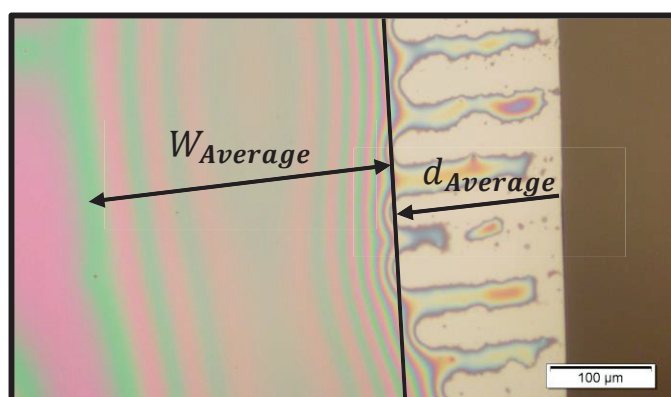


Figure 4. 34 Optical micrograph of the dewetting dynamic defining the averaged dewetting distance $d_{Average}$ and the rim width $W_{Average}$.

Chapter 4 Dewetting as an investigative tool for studying the interfacial friction of patterned surfaces

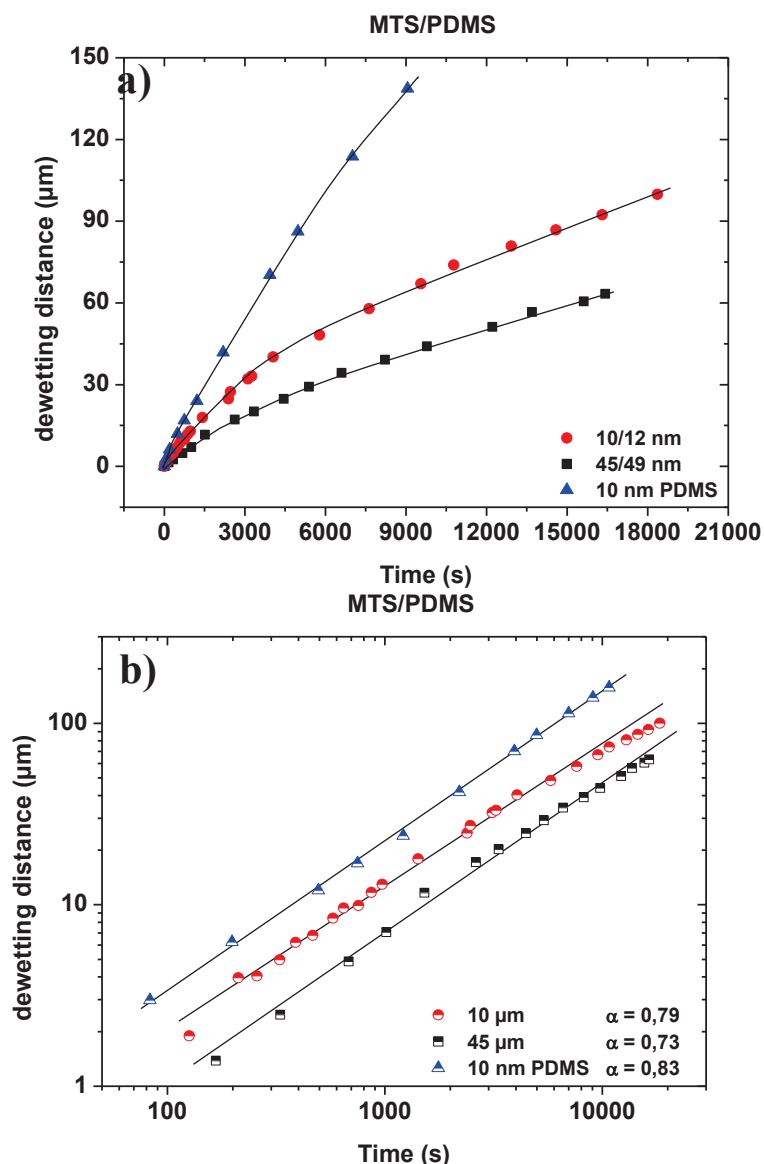


Figure 4. 35 (a) Temporal evolution of the dewetting distance (d) of a PDMS film ($500 \text{ nm } M_w = 139\,000 \text{ g/mol}$) on top of a homogenous PDMS absorbed layer and of a 10, 45 μm MTS/PDMS patterned system at 150°C . **(b)** Dewetted distance (d) as a function of time on double logarithmic scales for the same conditions as described in **(a)**.

Thus, the results clearly illustrated that PDMS monolayer dewetted faster compared to the mixed substrate (MTS/PDMS) proving that introducing MTS molecules on the surface increase the interfacial friction. In fact, for a PDMS mono layer we can assume that the surface is perfectly recovered with the PDMS layer inducing then a fast dewetting, which mean low interfacial friction. However, in the case of the MTS patterned substrate, a low grafting density could induces a massive adsorption of the PDMS film on the non-covered zone (as explained in the chapter III). This phenomenon could easily slow the sliding of the PDMS film and increase the frictional response of the surface. Hence, as the MTS pattern size increase an augmentation of the friction response could be presumed.

Chapter 4 Dewetting as an investigative tool for studying the interfacial friction of patterned surfaces

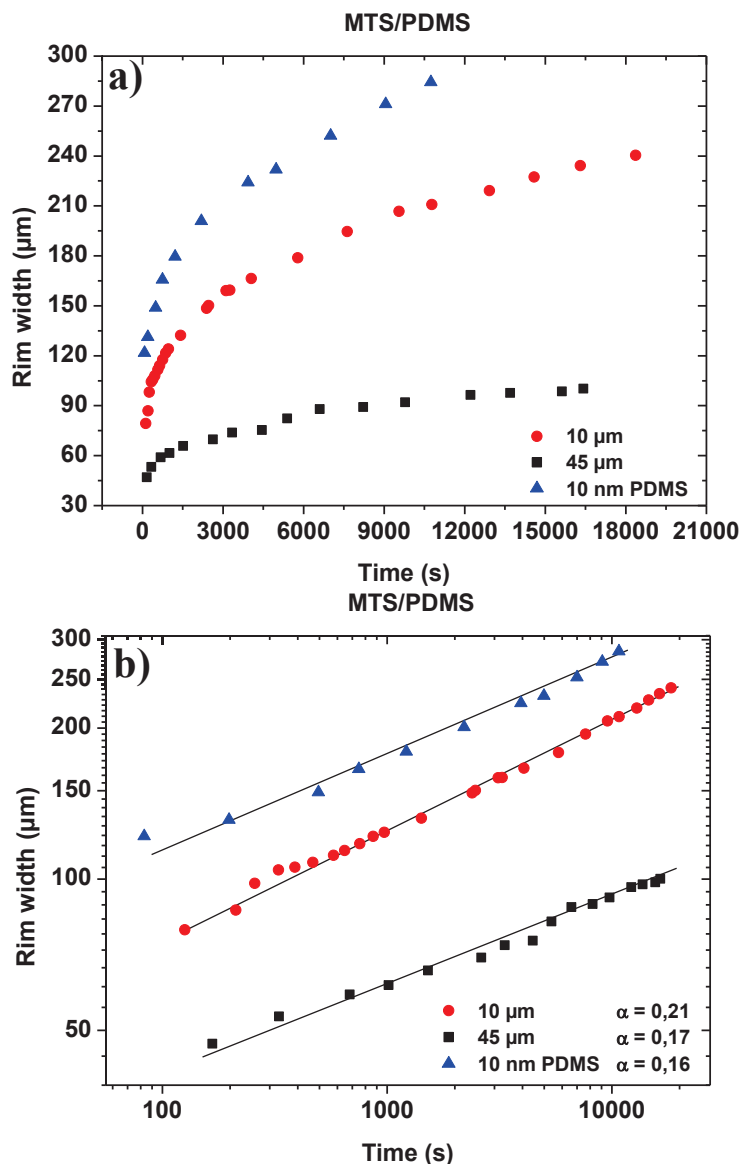


Figure 4. 36 (a) Temporal evolution of the rim width (W) of a PDMS film ($500 \text{ nm } M_w = 139\,000 \text{ g/mol}$) on top of a homogenous PDMS absorbed layer and of a 10, 45 μm MTS/PDMS patterned system. The temperature was 150°C . (b) Rim width (W) as a function of time on double logarithmic scales for the same conditions as described in (a).

The increase of the dewetting distance with the augmentation of patterns sizes could be attributed to the increase of the autophobicity with the increase of the periodicity between the linear strips MTS and PDMS. As dewetting proceeded, we should note that the in one hand, the PDMS dewetts on the PDMS strips of the substrate. In the other hand, a no slip behavior could be observed on the MTS part of the linear patterns. In fact, following the sliding of the PDMS on the film we can clearly notice an anchoring of the PDMS film on the MTS strips Fig.4.37. We can attribute this phenomenon to the attachment of the free polymer chain on the non-covered zone (OH molecules) due to the low grafting density of the printed MTS layer. In fact, an important feature in the monolayers that gives rise to low values of friction is their molecular chains. These chains exhibit significant freedom of swing and thereby rearrange along the sliding direction, which eventually yields a smaller resistance during sliding resulting in lower

Chapter 4 Dewetting as an investigative tool for studying the interfacial friction of patterned surfaces

friction values [154, 168]. Furthermore, Brown et al [164] studied the interfacial friction forces between a polydimethylsiloxane (PDMS) network sliding against ultrathin PDMS films comprised of chains end-tethered to a polystyrene surface. They determined that while shorter, stiffer chains could penetrate the network and increase the interfacial friction force, longer chains with higher mobility showed more liquid-like interfacial qualities, lowering the interfacial shear stress [164].

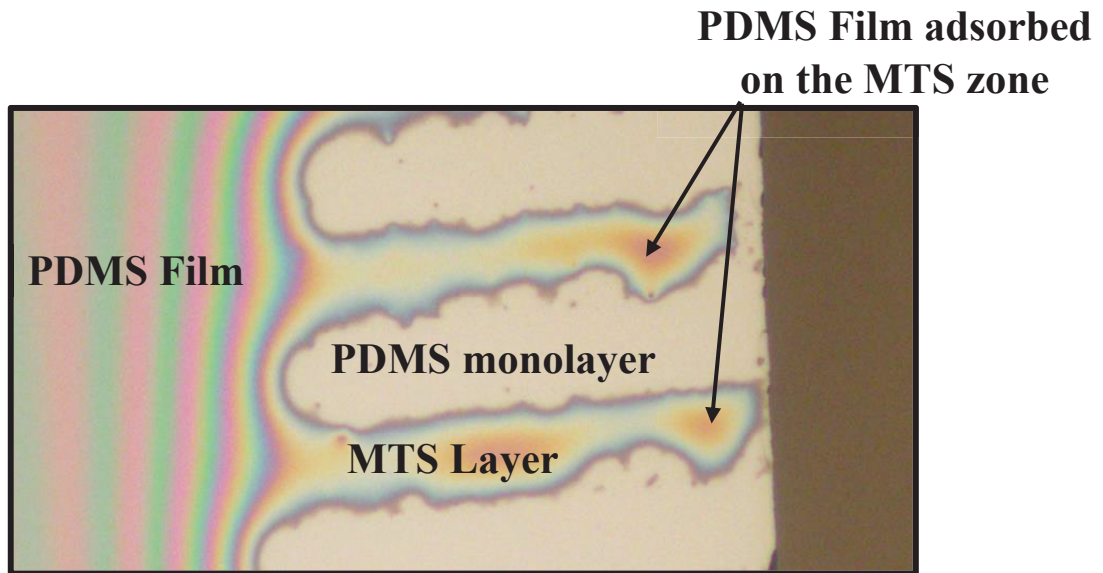


Figure 4. 37 Optical micrograph of the autophobic dewetting dynamic illustrating the anchoring phenomena of the PDMS film on the MTYS patterned layer.

Following the experimental condition used in these measures, we can observe that At $t = 0$ s motion at the three phase contact line starts and evolves as an algebraic power law $D \propto t^\alpha$. Fitting the data points for $d(t) = A(t - t_0)^\alpha$ to a power-law gave an exponent of α , varying between **0,73** and **0,83** which is considered in the range of the value of the no-slip boundary condition $\alpha = 1$ and the the plug-flow situation $\alpha = 2/3$. As observed in the Fig.4.34 that slippage, clearly exhibit a dependence behavior of the patterns size. In our case, the dewetting velocity decreases with the increase the linear strips. The dewetting velocity follow a power law of $-1/3$, indicating a semi-ideal behavior [173, 174, 200]. Hence, interfacial friction increases with the MTS pattern sizes and dewetting proceeds more slowly in larger strips.

Chapter 4 Dewetting as an investigative tool for studying the interfacial friction of patterned surfaces

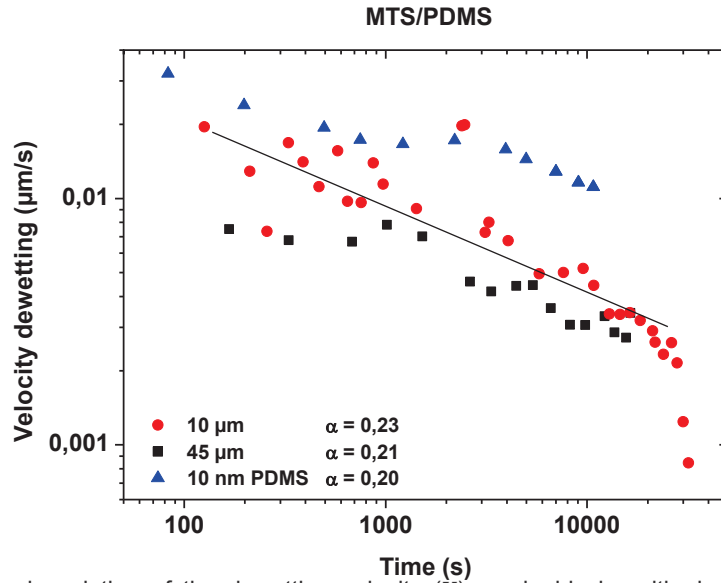


Figure 4. 38 Temporal evolution of the dewetting velocity (V) on double logarithmic scales for the same conditions as described in the legend of **Fig.4.30.a**.

Based on theoretical consideration, measuring the dewetted distance and the width of the rim simultaneously allowed us to determine the contact angle in situ and in real time based on the assumption of mass conservation. In fact, following a typical dewetting experiment, the driving capillary forces (uncompensated Young force) are balanced by viscous forces (forces per unit length of the three-phase contact line) : $F_{Young} = F_{visc}$.

$$\theta(t) = \frac{d(t)h(t)}{CW^2(t)} \quad (4.13)$$

Typical results are presented in Fig.4.39. Two regimes are always observed on the contact angle θ , there is an increase of its value at shorter time while at longer time the value is almost constant. In this situation, a similar contact angle was observed for the smaller pattern 10 μm and the homogenous non-patterned PDMS adsorbed layer. However, a higher contact angle was noticed on the largest MTS pattern 45 μm suggesting the dependence of the contact angle to the anchoring of the PDMS film on the MTS zone of the surface. We should note that the PDMS film used for these experiments is a 500 nm thick PDMS film, which explain the large value of the rim width and the small value of the contact angle. In fact, When a PDMS polymer layer is leaded in contact with a polymer of linear chains, these diffusing free chains will try to penetrate into the network.

Chapter 4 Dewetting as an investigative tool for studying the interfacial friction of patterned surfaces

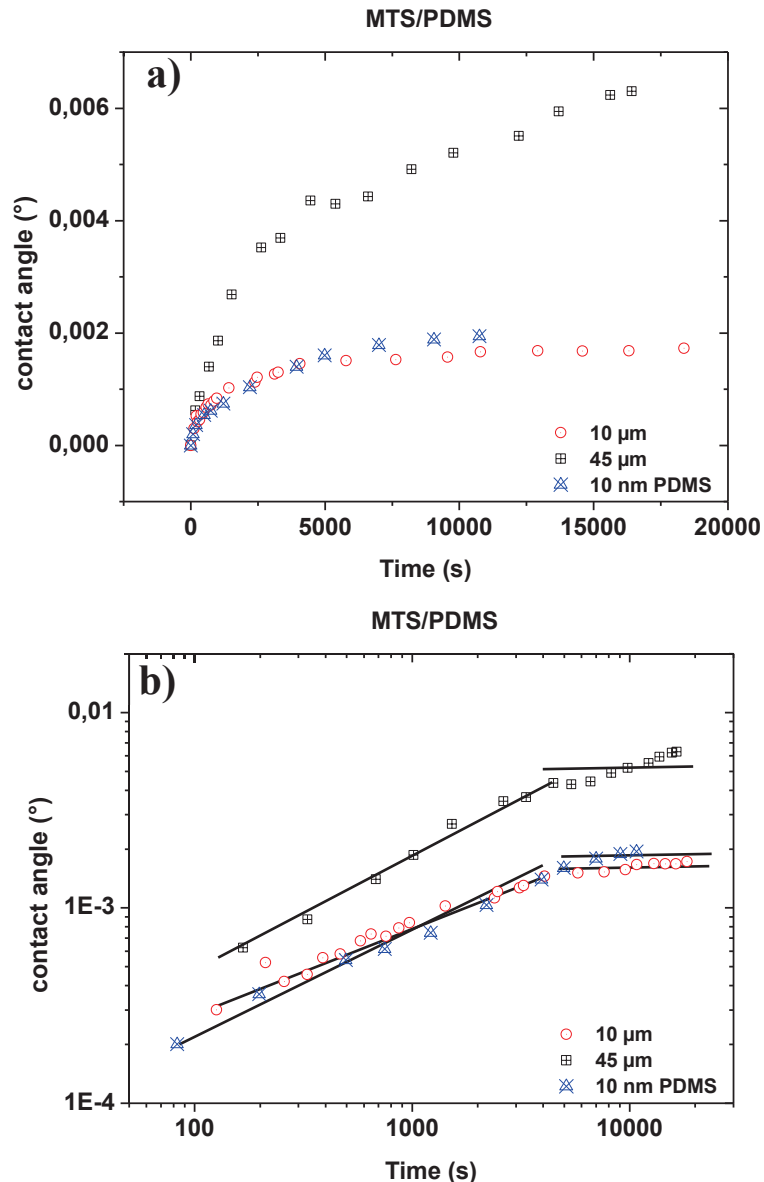


Figure 4. 39 (a) Temporal evolution of the contact angle (θ) as determined from eq 4.13. (b) Temporal evolution of the contact angle (θ) on double logarithmic scales. The straight lines are guideline for eyes.

The corresponding elastic constraints are, however, rather disfavoring this interpenetration and hence the diffusing chains will experience a repulsion. Such behaviour can result an autophobic behavior which may be described in a quantitative form by the value of the contact angle and the slippage length. Then, the increase of the contact angle with the augmentation of the pattern size can be explained by the increase of the interfacial contact between the two layers suggesting an increase of the elastic constraints in the bulk. This behaviour induces then, the anchoring of the PDMS film on the MTS layer and the interpenetration of the free polymer chain on the PDMS layer. Similarly, knowing that viscous forces balance the driving capillary we can also obtain the value of the slippage length b and its temporal evolution using:

Chapter 4 Dewetting as an investigative tool for studying the interfacial friction of patterned surfaces

$$b(t_i) = \frac{3\eta V(t_i) W(t_i)}{0,5\gamma \theta^2(t_i)} \quad (4.14)$$

In the case of a slipping film, the energy is dissipated over the moving part of the film characterized by the width W of the rim collecting the liquid from the dewetted region.

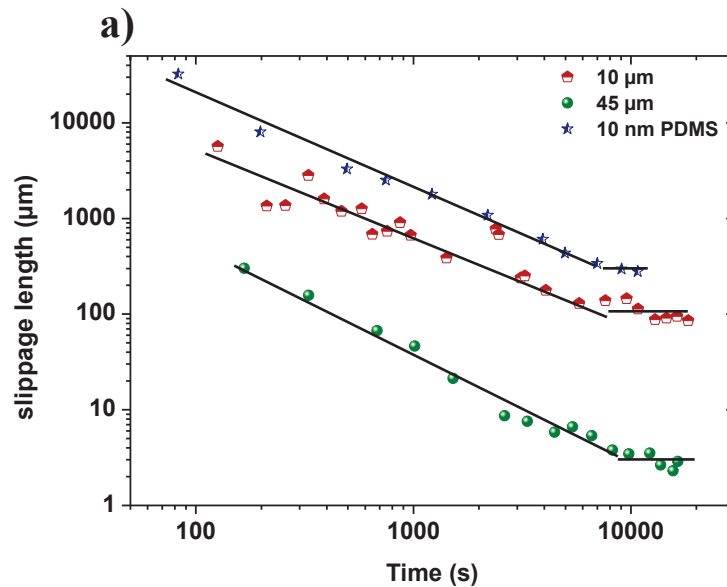


Figure 4. 40 Slippage length a function of time on double logarithmic scales. The dotted lines are guideline for eyes.

The results at 150°C are shown in Fig.4.40. Thus, we can observe that the initial value of the slippage length are clearly different for the several systems and exhibit two different regime as the contact angle. At short time, we can notice clearly a fast decrease of the b with time while at longer time the value is almost constant for the different systems (non-patterned and patterned). Furthermore, a decrease of the slippage length with the pattern size was clearly observed. These results, proves the dependence of the interfacial friction of the patterned substrates to the MTS pattern size added to the homogenous surface.

Chapter 4 Dewetting as an investigative tool for studying the interfacial friction of patterned surfaces

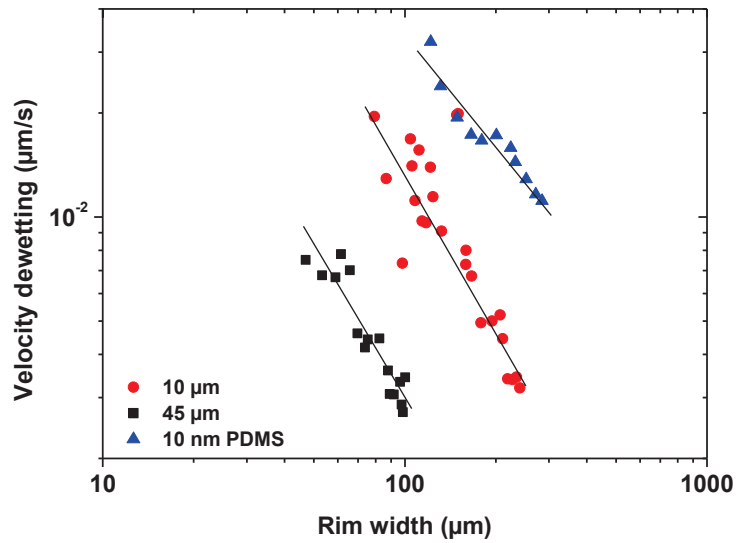


Figure 4. 41 Dewetting velocity (V) as a function of the rim width (W) of a homogenous PDMS absorbed layer and of a 10, 45 μm MTS/PDMS patterned system at 150°C. The straight lines are guideline for eyes.

According to the equation (4.13), and knowing that in the course of the dewetting experiments described in Fig.4.33 that the driving force characterized by θ increase slightly. Thus, we anticipate a decrease of the dewetting velocity V with the increase in W . This is clearly demonstrated in Fig.4.41 by plotting the dewetting velocity V as a function of the rim width W . In this case, we can clearly observe a decrease of the velocity dewetting with rim width, proving that the dissipation increases linearly with W . Such a relation between V and W implies that the whole rim slips.

Chapter 4 Dewetting as an investigative tool for studying the interfacial friction of patterned surfaces

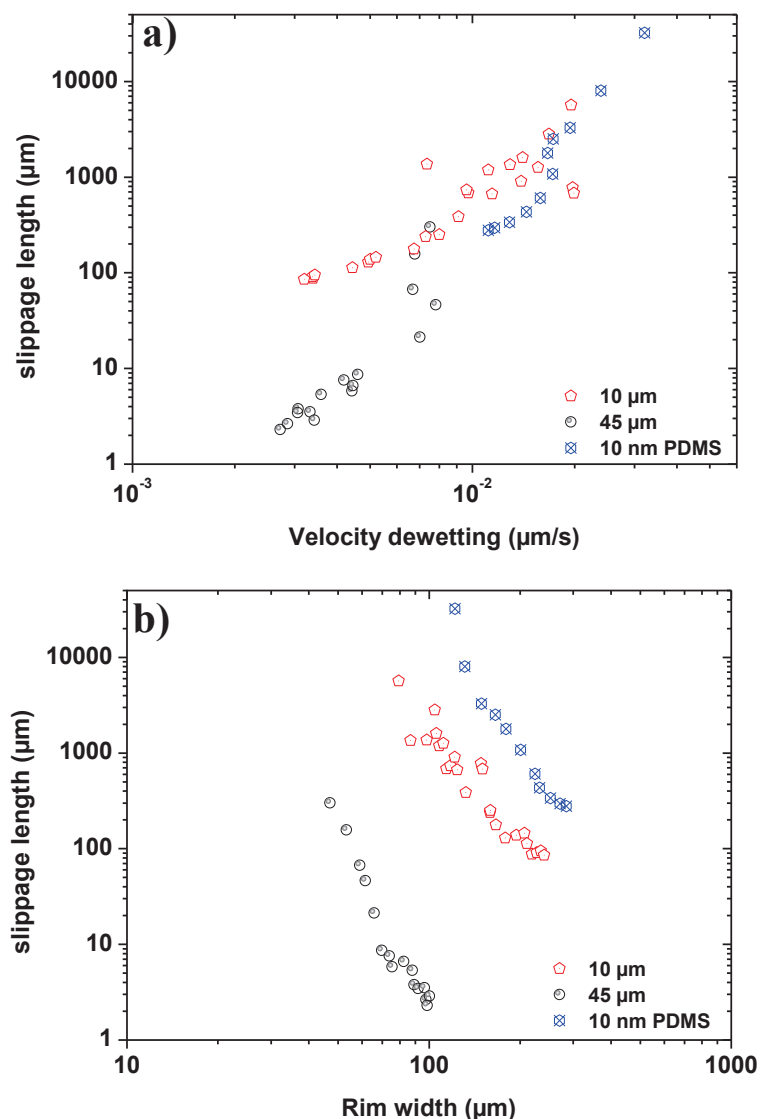


Figure 4.42 (a) Slippage length (b) as a function of dewetting velocity (V). (b) Slippage length (b), as a function of rim width (W).

Fig.4.42 shows the slippage length plotted as a function of the dewetting velocity. In fact, these results indicate the slippage length b increase with the grows of the velocity V . This behavior can be related to the adsorption of the free polymer chain on the non-covered zone (SIOH) randomly distributed on the MTS patterns Fig.4.43. Hence, due to the low grafting density, an expansion of these non-covered zone should be greatly possible with the increase of the pattern size. Thus, as expected an increase of the rim width induces a clear slowing effect of the dewetting velocity, which results to an augmentation of the rate of PDMS adsorption on the SIOH molecules and expansion of the contact zone. Then, a decrease of the slippage length can be predicted, which proves our assumption of the dependence of the friction response to the MTS layer printed on the surface. We should note that b also decrease as the rim width W increases.

Chapter 4 Dewetting as an investigative tool for studying the interfacial friction of patterned surfaces

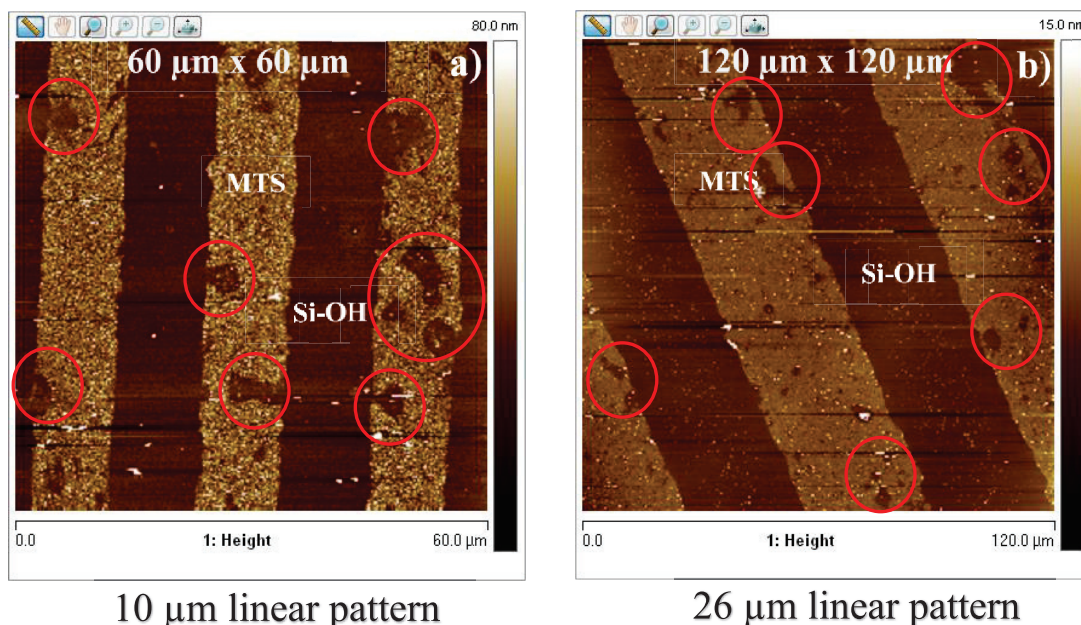


Figure 4. 43 2D AFM images of the Topography ($60 \times 60 \mu\text{m}^2$, $120 \times 120 \mu\text{m}^2$) of the several non-covered Zone for the different patterned surfaces (MTS/Si-OH).The red circle presents the non-covered zone on the MTS patterns

III-Conclusions

In summary, at first, we define that the dewetting process can be devised into a four stages (rim growth, undulation and rim swelling, fingering and finally pinch-off instabilities) varying with slippage. We observed that as polymer accumulates in the rim at the three-phase contact line, a Rayleigh-Plateau type instability takes place at the liquid/air interface. Hence, we found that this type of instabilities is clearly governed by the presence of different chemical domains (Hydrophobic /Hydrophilic) at the surface.

From the start of dewetting until the droplet detachment instabilities, the rim instability undergoes a varying shift in the apparition of the fingering and pinch-off regime with the increase of the pattern sizes. In fact, the increase of the volume collected on the front of the rim suggest an augmentation of bulges number and sizes with pattern sizes. Moreover, we can suggest that the rim instability develops before fingering starts and that the main factor inducing fingering is slippage. However, the transition from bulge to finger appears at a stage where the balance between dissipative forces and driving forces varies locally. Then, at the start of dewetting, a high energy is needed to debuts the film sliding constructing then the rim. Hence, as the dewetting process, an increase of the rim width induces then an augmentation of the interfacial friction. This behavior could be attributed to the no-sliding effect provoked by the presence of the hydrophilic patterns on the surface. Therefore, in our case, this response is a result of a competition between slip and no slip behavior induced by the introduction of an (Hydrophobic /Hydrophilic) system on the surface. Following this behavior, we consider the presence of the two types of dissipation mechanism on the interface of the patterned layer. The first being purely

Chapter 4 Dewetting as an investigative tool for studying the interfacial friction of patterned surfaces

viscous and the second being friction at the solid/liquid interface, this two mechanism can be combined to explain why the dewetting velocity increases with the pattern sizes.

Further, we observed that with the increase of the strips sizes and the thickness of the polystyrene film, the side effects such as pinning or other inhomogeneities increase as well. Which lead to irregularities in the rise of the undulated ridge involves a premature pinch-off. Hence, a decrease of the diameter of the droplets between the primary and the secondary droplet is observed. This effect induces then an increase of the ratio of both diameters with the increase of the textures sizes and the PS thicknesses. Thus, satellite drops eventually appear between the primary and a secondary droplet depending whether a thin thread is left over during the pinch-off process.

Secondly, we investigated the impact of the geometry on the dewetting process. Thus, a qualitative analysis of the rim instability rising on dewetting holes evidence an identical features compared to the straight front geometry, i.e. fingering and an asymmetrical growth of the ridge are observed on the different patterned systems. Furthermore, a quantitative analysis, however, evidence discrepancies mostly concerning a temporal and spatial change of transitions. The most significant being an early distance of droplet detachment for straight fronts compare to holes, which is explained by a faster spatial growth rate of the rim width for straight fronts.

However, the dewetting of the polystyrene film used in this work presented a qualitative analysis of the frictional response of a polymer melt sliding on (hydrophobic/ hydrophilic) patterned system. Hence, in the final part of this chapter, we studied the autophobic dewetting of a thin PDMS film (hydrophobic/hydrophobic) MTS/PDMS patterned surface as a mean to extract a quantitative information of the interfacial friction.

As dewetting proceeded, we observed that the in one hand, the PDMS dewetts on the PDMS strips of the substrate. In the other hand, a no slip behavior was be observed on the MTS part of the linear patterns. This behavior can be related to the adsorption of the free polymer chain on the non-covered zone (SIOH) randomly distributed on the MTS patterns. Hence, due to the low grafting density, an enlargement of the non-covered zone should be greatly possible with the increase of the pattern size. Thus, as expected an increase of the rim width induces a clear slowing effect of the dewetting velocity, which results to an augmentation of the rate of PDMS adsorption on the SIOH molecules and expansion of the contact zone. Then, a decrease of the slippage length can be predicted, which proves our assumption of the dependence of the friction response to the MTS layer printed on the surface.

Chapter 5

Dewetting and friction measurements on homogeneous deformable substrates

TABLE OF CONTENTS

I-INTRODUCTION	161
<i>I-1-Dewetting Dynamics</i>	161
I-1.1-Stages of dewetting	161
I-1.2-Driving forces	162
<i>I-2-Dissipation mechanisms</i>	163
I-2.1-Viscous dissipation: No-slip boundary condition	163
I-2.2-Full slippage: Friction at the solid/liquid interface	164
II-EXPERIMENTAL	165
<i>II.1-Sample Fabrication</i>	165
II.1.1-Polydimethylsiloxane monolayer	165
II.1.2-Cross-linked PDMS with varying thicknesses	165
II.1.3- Cross-linked PDMS for thicker films ($>1.8 \mu\text{m}$)	166
III-RESULTS AND DISCUSSION	166
<i>III-1-Friction measurements at macro scale</i>	166
III-1.1-Smooth Substrates	166
<i>III-2-Dewetting Experiments Using a Newtonian Fluid PDMS</i>	172
III-2.1-Dewetting Dynamics	173
III-2.3-Interfacial friction behaviour	179
IV-CONCLUSION	182

Chapter 5 Dewetting and friction measurements on homogeneous deformable substrates

I-Introduction

Interfacial phenomena are observed everywhere in our daily life [1–3]. Problems of adhesion, friction, wetting, or dewetting can be essential for the faultless performance of various applications. Intriguingly, such performance often depends on very tiny changes only. For example, the wetting behavior can be easily switched from perfect wetting to non-wetting by modifying the very surface, i.e., the last monolayer or, in some case, the end-group of the molecules at this surface.[3] Accordingly, small variations on a molecular scale can lead to dramatic effects on macroscopically observable scales.

This chapter has first sought to introduce the homogenous surfaces preparations and the techniques used to characterize the samples and studies the dewetting dynamics. In fact, we used different thicknesses of homogenous surfaces with same chemistry as a mean to investigate of the predominant aspect between the chemistry introduced on the surface and the mechanical proprieties of the substrate. Thereby, we used friction experiments and autophobic dewetting of a thin PDMS polymer as mean to extract quantitative information of the interfacial friction. In one hand, we measured in situ the contact angle and the slippage length at the melt-substrate interfaces and in the other hand, we explored the correlation between both micro and macros scales friction analysis bringing to light the impact of the mechanical proprieties of the surface on the frictional response.

I-1-Dewetting Dynamics

Let consider the case of a supported thin film partially wetting a smooth and passive surface. This case accounts for film thicknesses smaller than the capillary length $k^{-1} = \sqrt{\gamma/\rho g}$ (typically in the millimeter range for water), but larger than few nanometers, which corresponds to the metastable case discussed in the stability of supported thin films. In fact, dewetting takes place by heterogeneous nucleation of a hole, whose nuclei are defects such as dust particles, inhomogeneities on the surface. The distinctive feature of this rupture case is the random distribution of holes, a crucial issue to distinguish this process from other scenario like spinodal dewetting [74] where the dewetting that takes place by amplification of capillary waves shows a periodic distribution of sites, following the capillary wavelength [199].

In fact, one of the main aspects of experimental studies concerning the flow dynamics of thin polymer films is to obtain a comprehensive view on the molecular mechanisms of slippage and on the responsible parameters.

I-1.1-Stages of dewetting

The system attains equilibrium when a set of droplets with a Young contact angle θ_Y lie on the substrate.

The changeover from the liquid film covering the surface to the final equilibrated stage was splitted in

Chapter 5 Dewetting and friction measurements on homogeneous deformable substrates

several stages reported by Brochard-Wyart et al [200]. Each of which being limited by length scales taking into account the hole radius R and the slip length b . Brochard-Wyart et al. made a theoretical description of the different dewetting regimes [201]. First, an exponential growth of the hole radius has been anticipated right after the hole has formed : $R \propto \exp t/\tau$, where the characteristic time depends on the initial parameters, film thickness h_0 , surface tension γ and viscosity η , $\tau = h_0 \eta/\gamma$. The growth law has been experimentally characterized by Masson and Green under extreme conditions (dewetting under vacuum and with low contact angle) [202]. The absence of a hole describes this stage and last until the hole radius equals a critical radius R_c with $R_c = \sqrt{bh_0}$. However, we should note that the analysis considers viscoelastic polymers and is based on elastic dissipation for the stress release. The limit R_c might not be suitable for purely viscous films. Indeed, in the case of bursting of a soap bubble for newtonian liquids [203, 204], which is similar to dewetting of suspended films, a rim could be directly noticed. The rim appears in a second stage where the temporal evolution of the hole radius is ($R \approx \frac{|S|}{\eta} \left(\frac{b}{h_0}\right)^{0.5} t$) and the rim becomes mature above another critical hole radius $R'_c = b$.

I-1.2-Driving forces

For a Newtonian fluid, capillarity represents the main driving force for dewetting. It is related to an imbalance between the three interfacial tensions (γ_{ls} , γ_l and γ_{sv}) that meet at the contact line and are responsible for a dynamic contact angle θ_D . In contrast, when all interfacial tensions are balanced we obtain the equilibrium contact angle θ_Y (which represents the absolute minimum in free energy of the system) and the contact line will be at rest [205]. Thus, we can consider that the Driving forces of wetting and dewetting experiments are capillary forces [17]. Hence, the capillary force per unit length of the contact line is given by

$$F_{Young} = \gamma_l (\cos \theta_Y - \cos \theta_d) \quad (5.1)$$

The three phase contact line resulting from the nucleation of a hole is in motion when the dynamic contact angle θ_d formed differs from the equilibrium contact angle θ_Y . As long as $\theta_d < \theta_Y$ remains valid, the capillary force is negative and the three-phase contact line will recede; the liquid film dewets. For small contact angles, the “cos” term can be approximated by the first term of its series expansion, i.e., $\cos \theta \approx 1 - \left(\frac{1}{2}\right)\theta^2$. This then leads to:

$$F_{Young} = \frac{1}{2} \gamma_l (\theta_Y^2 - \theta_d^2) = |S| \quad (5.2)$$

We should note that no gravity acting as the initially prepared film thickness is much lower than the capillary length $h_0 \ll \kappa^{-1}$ (κ^{-1} is in the millimeter range for water). The Laplace pressure affects

Chapter 5 Dewetting and friction measurements on homogeneous deformable substrates

the rounded shape of the rim, therefore influences indirectly the dewetting dynamics (as a contribution of the friction of the S/L interface via the rim width) in the evolution of the rim width. The dewetting dynamics of velocity V of the system is balanced by the driving force $|S|$ and the sum of dissipations within the fluid and the corresponding velocities v_i , denoted by viscous friction F_v , and friction at the solid/liquid interface, denoted by F_s with s standing for slippage.

$$|S|V = F_v v_v + F_s v_s. \quad (5.3)$$

I-2-Dissipation mechanisms

I-2.1-Viscous dissipation: No-slip boundary condition

In a system whose friction forces are purely viscous, the resulting dewetting velocity $V = v_v$ is constant (eq. 5.4) [200]. Redon et al. demonstrated that viscous fluids (silicon oils or alkanes of viscosity $\eta < 60 \text{ Pa s}$) in the range of $20 - 50 \text{ }\mu\text{m}$ dewet hydrophobic substrates with a dewetting velocity proportional to θ_Y^3 [206]. The constant of proportionality $C_v(\theta_v)$ reflects the dissipation at the three-phase contact line.

$$V = C_v(\theta) \frac{|S|}{\eta t a} \propto \frac{\gamma}{H} \theta_Y^3. \quad (5.4)$$

The integration of the velocity $V = \dot{R}$ gives a linear growth of the hole radius as seen in eq. 5.5.

$$R \propto t \quad (5.5)$$

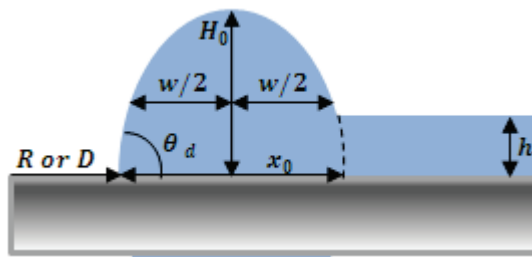


Figure 5. 1 Schematic representation of the rim forming in the middle of dewetting of a thin liquid film. Here an illustration of the rim width w , the distance x_0 for a given film thickness h and hole radius R (or dewet distance D of a straight front).

In the case of a no-slip boundary condition, the movement of the contact line with dewetting velocity V results from a balance between driving force and viscous dissipation in the ridge close to the moving contact line. Integration over the whole moving part of the fluid from its lowest thickness at the contact line having a minimum thickness of h_{min} to its thickest part with the maximum thickness of h_{max} yields the total viscous force F_{Visc} per unit length of the contact line during dewetting [17, 207]:

Chapter 5 Dewetting and friction measurements on homogeneous deformable substrates

$$F_{Young} = \frac{1}{2} \gamma_l (\theta_Y^2 - \theta_d^2) = \frac{3\eta}{\theta_d} \ln\left(\frac{h_{max}}{h_{min}}\right) = F_{Visc} \quad (5.6)$$

For dewetted distances much larger than x_0 , both ends of the rim move at approximately the same velocity. Moreover, at the rear position the equilibrium value of the contact angle is zero (rim in contact with the film of the same liquid) and thus yields:

$$F_{Young} = \frac{1}{2} \gamma_l \theta_d^2 = \frac{3\eta}{\theta_d} \ln\left(\frac{h_{max}}{h_{min}}\right) = F_{Visc} \quad (5.7)$$

Here, h_{max} and h_{min} are evaluated at the rear position.

I-2.2-Full slippage: Friction at the solid/liquid interface

Systems whose friction at the solid/liquid interface prevails show a reducing dewetting velocity with time. In the plug flow situation (large slip length b), the velocity with a slip contribution varies with b/W with W being the rim width and b representing the friction at the solid/liquid interface: $b \sim h_{min} = \eta/\xi$, ξ is the friction coefficient.

$$V = \frac{1}{3} \frac{|S| b}{\eta W} \quad \text{with} \quad W = C_s \sqrt{h_0} \sqrt{R} \quad (5.8)$$

Due to conservation of mass the rim width for a hole varies as $W \propto \sqrt{R}$, C_s is a constant of proportionality of representing the growth of W . The integration of the velocity $V = v_v$ gives a Radius growing as a power law with time, with an exponent $\alpha = 2/3$ (eq. 5.9).

$$R \propto t^{2/3} \quad (5.9)$$

Experimentally, Redon et al. observed that an increase of molecular weight together with a decrease of the initially prepared film thickness lead to dewetting dynamics following the plug flow situation [208]. We should note also that the geometry of the system doesn't affect the power law mentioned before as $W \propto \sqrt{R}$ in both cases according to [209]. Schematic views on the differences of the no-slip or slip boundary condition in the context of dewetting are given in Figure 5.2 [210].

Chapter 5 Dewetting and friction measurements on homogeneous deformable substrates

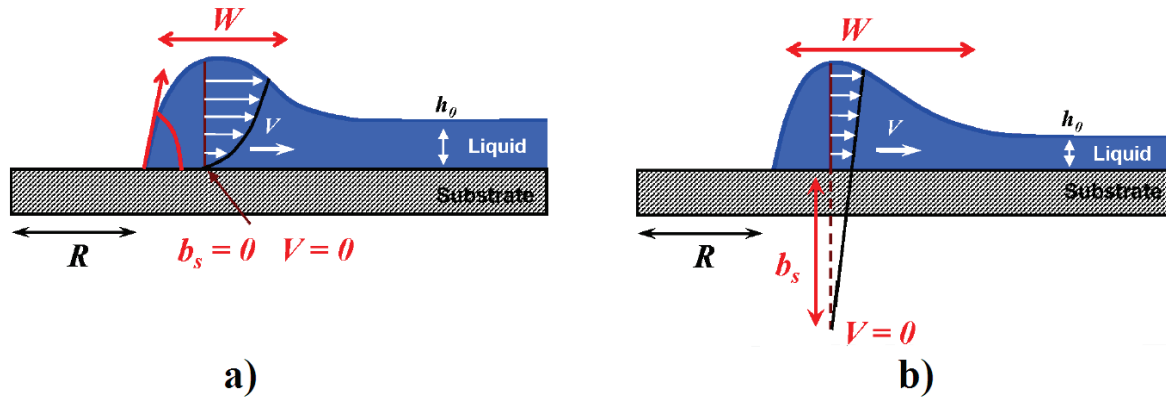


Figure 5. 2 Schematic presentation of late stages of dewetting of Newtonian fluid on a substrate with (a) a non-slip and (b) a slip boundary condition

II-Experimental

In order to better understanding the interfacial friction phenomena, we used in this part of our study, the autophobic dewetting of a PDMS film and the mechanical friction test on homogenous surfaces with different mechanical proprieties. In fact, the use of a PDMS film for dewetting experiments on the same chemical type of substrates allows in one hand, to extract in situ the contact angle and the slippage length at the melt-substrate interface. In the other hand, to highlight the correlation between both micro and macros scales and bring to light the impact of the mechanical proprieties of the surface on the frictional response.

II.1-Sample Fabrication

II.1.1-Polydimethylsiloxane monolayer

A 100mg/ml of PDMS (139 K) solution (in heptane) was passed through a micro-filter to remove any impurities. Then it was spin coated at 2000 rpm for 30 s using a spin coater onto a cleaned and oxidized microscope glass slide, the Film was cured at 130 °C for 4 h. Then each surface was rinsed in toluene for 2 h. The various substrates were then dried with N_2 . A 10 nm Polydimethylsiloxane adsorbed coated layer is obtained.

II.1.2-Cross-linked PDMS with varying thicknesses

A various concentration of Sylgard 184 PDMS elastomer is prepared by mixing the elastomer base and curing agent according to the prescribed proportion (mass ratio 10:1) in heptane). Then, passed through a micro-filter to remove any impurities. Then it was spin coated at 2000 rpm for 30 s using a spin coater onto a cleaned and oxidized silicon wafer, the Film was cured at 130 °C for 4 h. The various substrates were then dried with N_2 . Different thicknesses of a cross-linked PDMS layers ranging from 30 nm to 1,8 μm was obtained.

Chapter 5 Dewetting and friction measurements on homogeneous deformable substrates

II.1.3- Cross-linked PDMS for thicker films ($>1,8 \mu\text{m}$)

Sylgard 184 PDMS elastomer solution was prepared by mixing the elastomer base and curing agent according to the prescribed proportion (mass ratio 10:1). The mixture is then poured into a mold composed of two glass plates separated by a polytetrafluoroethylene spacer. After crosslinking at room temperature for 150 hours, one glass plate is peeled away, leaving the other with the elastic coating to be used for friction experiments. A varying thicknesses of a cross-linked PDMS layers ranging from $500 \mu\text{m}$ up to 1 cm was produced.

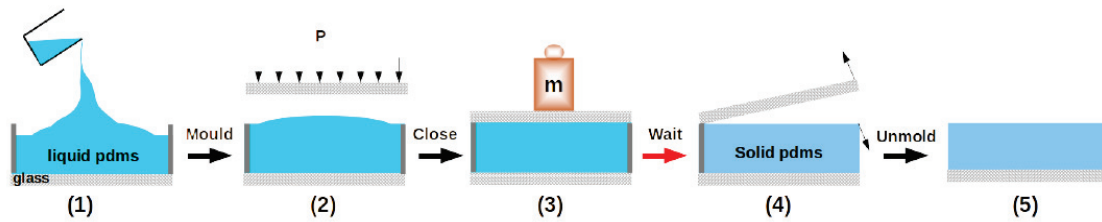


Figure 5. 3 Schematic of the fabrication processes of the thick PDMS surfaces

Furthermore, the spin-coated samples fabrication used in this part were described in the second chapter section II-2

III-Results and discussion

To a better understanding of the predominant aspect between the chemistry introduced on the surface and the mechanical proprieties of the substrate, different friction tests are carried out on smooth non-wettable silicon substrates coated with varying thicknesses of PDMS layers ranging from 11 nm - 1 cm . At macro-scale, several friction measurements were conducted using an apparatus home-built by Scheibert et al [1] described in Chapter III.

III-1-Friction measurements at macro scale

III-1.1-Smooth Substrates

Several friction measurements were carried out on varying thicknesses of homogeneous stiff and compliant samples. Hence, we clearly observed that the contact was maintained throughout over a single region for both the controls (Fig3.1 Chapter III). The different measurements were performed at the following: Lateral sliding force was measured while applying a constant normal force (P) ranging from $0,3 \text{ N}$ to $2,2 \text{ N}$ and the lateral velocity (v) was fixed at $0,1 \text{ mm/s}$. Then, the interfacial contact area was imaged through an inverted microscope allowing for the evaluation of changes in the contact area and the associated frictional mechanism by which the two surfaces displaced. Therefore, typical result

Chapter 5 Dewetting and friction measurements on homogeneous deformable substrates

of a friction test performed using several load for a smooth surface of an 11 nm adsorbed PDMS coated layer are presented in Fig.5.4. Thus, the temporal evolution of the lateral force F and the real contact area A^r are shown respectively. Following these conditions and as explained above we can notice that those graphs displays a classical behavior. In fact, the real area is measured systematically at the same time that the tangential force is recorded. We can clearly observe that the lateral force increases with the normal load P

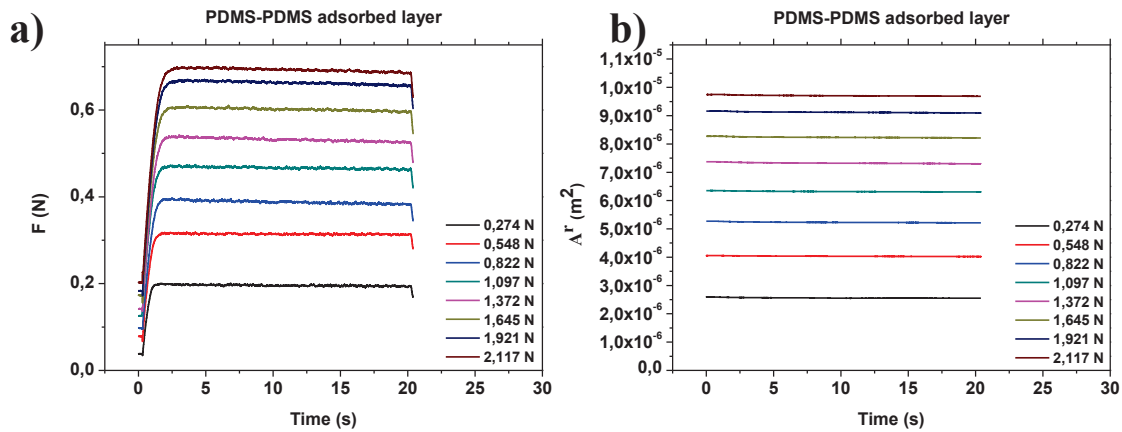


Figure 5. 4 (a-b) Temporal evolution of the lateral force and the real contact using several load for a smooth surface of an 11 nm adsorbed PDMS coated layer.

Fig.5.5 shows the real contact area as a function of the lateral forces for several normal load P surface of an 11 nm adsorbed PDMS coated layer. A linear fit (blue line) gives the inverse of the critical shear stress. To investigate the frictional behavior, we consider a standard model for friction $F_s = \epsilon_s A_s^r$, [159] where F_s is the sliding force at the maximum static friction level, A_s^r is the real contact area at the same level and ϵ_s is the critical interfacial shear strength. Then, respectively, we notice that the static friction force is directly proportional to the real contact area A^r which proves the predominant aspect of the A^r in the control of the frictional behavior Fig.5.5.

Chapter 5 Dewetting and friction measurements on homogeneous deformable substrates

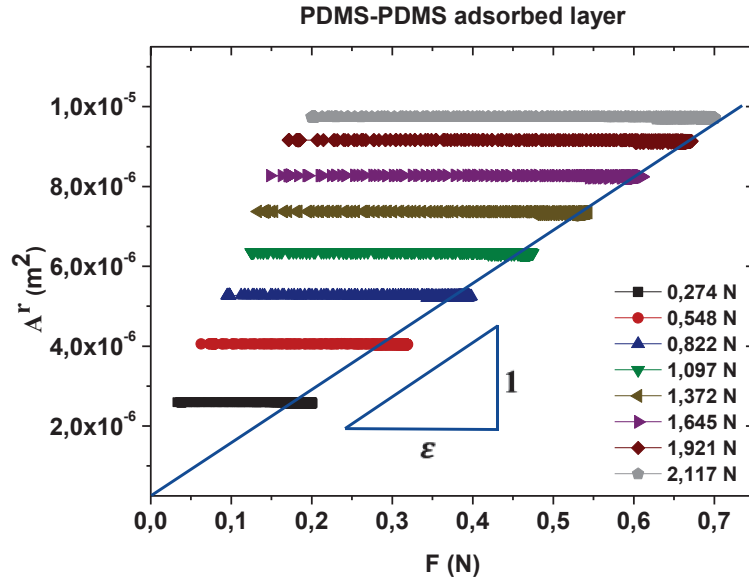


Figure 5. 5 (a-b) real contact area versus lateral force using several load for a homogenous surface of an **11 nm** adsorbed PDMS coated layer.

From Fig.5.6 (a), we can clearly observe a systematic increase of the critical shear stress with the thickness of the coated PDMS layer h . In fact, to understand this systematic evolution, the critical shear stress is plotted as function of the thickness Fig5.6 (b).

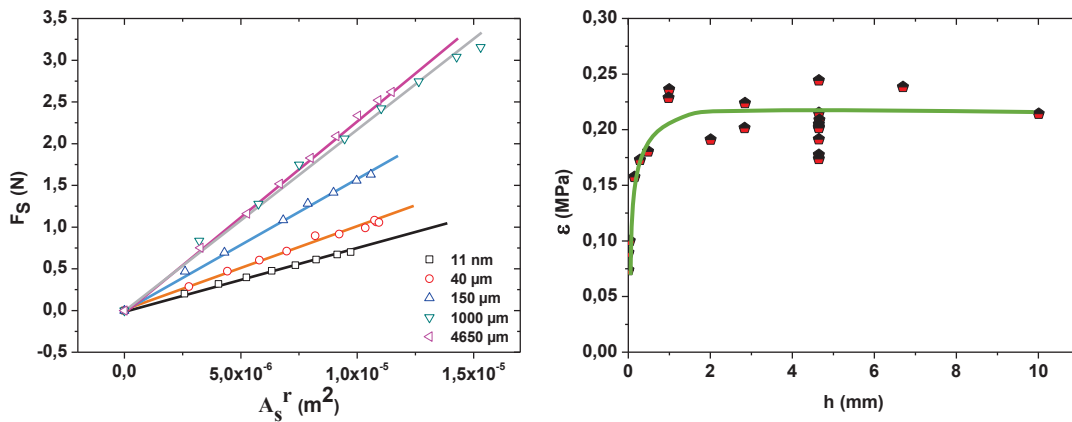


Figure 5. 6 **(a)** The maximum static friction F_s versus is the real contact area A_s^r for the different thickness of the PDMS cross-linked layer. The straight lines are the fits data using the following equation $F_s = \epsilon_s A_s^r$. **(b)** Critical shear stress ϵ_s , averaged over the whole time and load range of the experiment, as a function of coated layer thickness h . The line is a guideline for eyes.

We can notice that the results exhibit two regimes. At first, in the case of the thinner coated layer the ϵ_s displays a fast augmentation from a minimal value for $h = 11 \text{ nm}$ $\epsilon_s = 0,074 \pm 0.008 \text{ MPa}$ up to $\epsilon_s = 0,2 \text{ MPa}$ for $h = 1 \text{ mm}$. In the other hand, a constant behavior $\epsilon_s = 0,22 \text{ MPa}$ was observed in the case for the thicker coated layer.

Furthermore, to a better understanding of the predominant aspect between the chemistry introduced on the surface and the mechanical proprieties of the substrate, we followed the evolution of the young modules and the stiffness as function of the different PDMS coated layer Fig.5. Hence, these results

Chapter 5 Dewetting and friction measurements on homogeneous deformable substrates

suggests that at small thicknesses, the stiffness and the young modulus of the surface dominate the friction

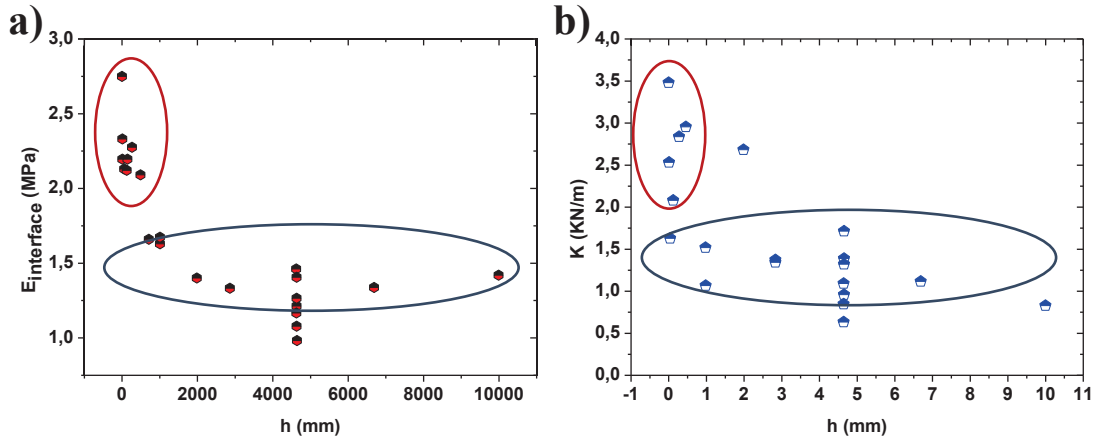


Figure 5. 7 (a) Young modulus as function of the PDMS thickness. (b) Tangential stiffness as function of the PDMS thickness.

response. In fact, as explained in the chapter two section II, we can extract the stiffness K and the young modulus E of the substrates used in this study employing the JKR modulus. We should note that using the friction machine we could easily determine these parameters following the contact between the PDMS bead and the substrates. Where K is the stiffness defined by $K = 4E/3$ and E is the Young's modulus defined by $E = 3K/4$. Therefore, following the results on Fig.5.7, we can notice that up to 1 mm thickness of the cross-linked PDMS, that K and E clearly decreases with the PDSM coated thicknesses. However, for the thicker samples, a constant value of the young modulus and the tangential stiffness were observed. These results suggest the presence of two regimes. At first, for thicknesses ranging from 0 up to 500 μm , we found that stiffness and the young modulus of the substrate dominates the friction behavior. However, the surface chemistry does not really present any influence on the frictional response. In fact, as friction test process, the increase of the normal force applied induces of an expansion of the contact zone between the PDMS bead and the thin-coated layer until meeting the solid substrate Fig.5.8. At this point, stiffness and the young modulus of the substrate dominates the friction, which explain the decrease of K and E with the cross-linked PDSM thicknesses. In the other hand, for thicker layers ($h = 500 \mu\text{m}$) we can clearly observe that independently of the thickness layer a plateau for the values of K and E is reached. This behavior suggest that the chemistry of the surface at high thickness probably influence the frictional response.

Chapter 5 Dewetting and friction measurements on homogeneous deformable substrates

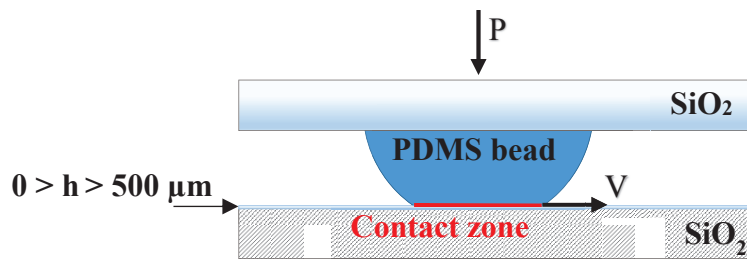


Figure 5. 8 Schematic of the friction test between a PDMS bead and a thin cross-linked PDMS layer $0 > h > 500 \mu\text{m}$

In our case, during the friction experiments, the normal force is increasingly applied; the recorded shear stress reflects both contributions of adhesive and elastic contacts. Moreover, the high frictional response observed on the thickest PDMS coated layer can be anchored to the deformation of the cross-linked layer and the creation of a depression at the border of the contact (in the direction of the sliding). In fact, this depression could be generated due to the restoration force applied by the deformed cross-linked PDMS layer Fig.5.9. This behavior results then to a more direct and efficient contact with the cross-linked network of the coated PDMS layer. The bulk network will then be principally constrained all along the friction, increasing the dissipation, precisely the bulk dissipation and the restorative force of the PDMS bulk.

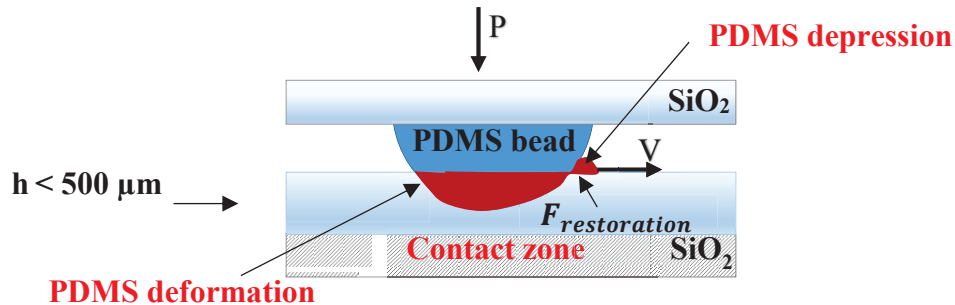


Figure 5. 9 Schematic of the friction test between a PDMS bead and a thick cross-linked PDMS layer $h < 500 \mu\text{m}$.

Therefore, the viscous behavior of the confined interfacial layer could therefore be advanced. In fact, the increase of the contact area between the hemisphere and the coated substrate with the thickness of the cross-linked PDMS can increase as well the viscoelastic deformation at the bulk. In our case, precisely in the case of soft materials which the harmony between both the interface strength and the bulk cohesion is more chaotic. These friction results demonstrates that the elastic contact maybe can sometimes compensate the great adhesive contact inducing an enhanced stress shift to the interface. These experiments shows the same behaviour as the dewetting experiments mentioned in the next section, assuming two mechanisms the effect the viscoelastic deformation of the creation of a depression at the border of the sliding direction.

Chapter 5 Dewetting and friction measurements on homogeneous deformable substrates

A second explanation can be presented [156], which can explain the dependence of the friction to the PDMS thickness using the energetic dissipation at the interface of the contact combined to volumes dissipation in the bulk given by this equation.

$$dW = dE_{Surface} + dE_{Volume} \quad (5.10)$$

Then, considering the standard model of friction $F = \epsilon A^r$ [159], where the sliding force F is proportional to the real contact area A_s^r . This relation can clearly illustrate the areal contribution to the friction termed as adhesive dissipation [165, 211, 212]. In the other hand, the volume contribution is probably related to the viscoelastic dissipation at the deformed region of the substrate [213]. For that, Fig.5.10 shows the critical shear stress as function of sliding velocity. In fact, a global increase (50%) of ϵ_s is observed when the friction speed is increased up to 100 time of the initial speed, which can be explained by an increase of the global dissipation of the system with the sliding velocity.

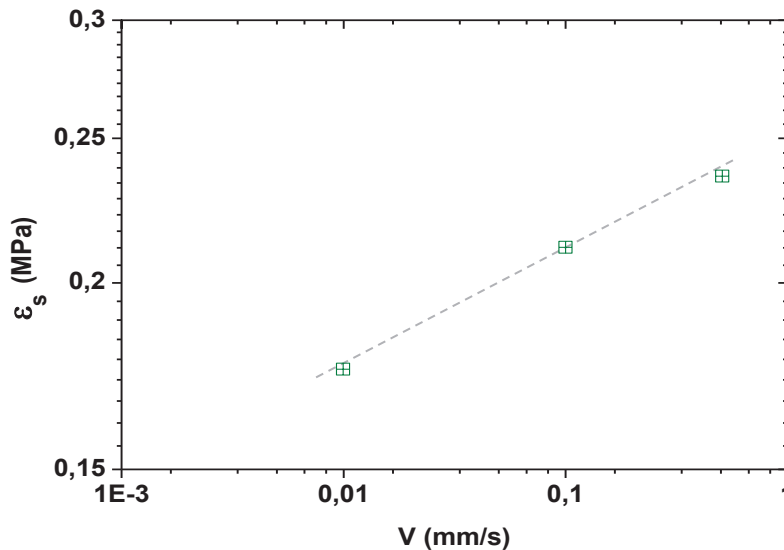


Figure 5. 10 Critical shear stress ϵ_s , as a function of the sliding velocity V for a thickness $h = 4,65 \mu m$ and a load $P = 1,1 N$. The straight line is a guideline for eyes.

Scheibert and Sahli [156] assumed that the volume dissipation is directly proportional to the volume deformation at the contact for a varying thickness regimes Fig.5.11.

Chapter 5 Dewetting and friction measurements on homogeneous deformable substrates

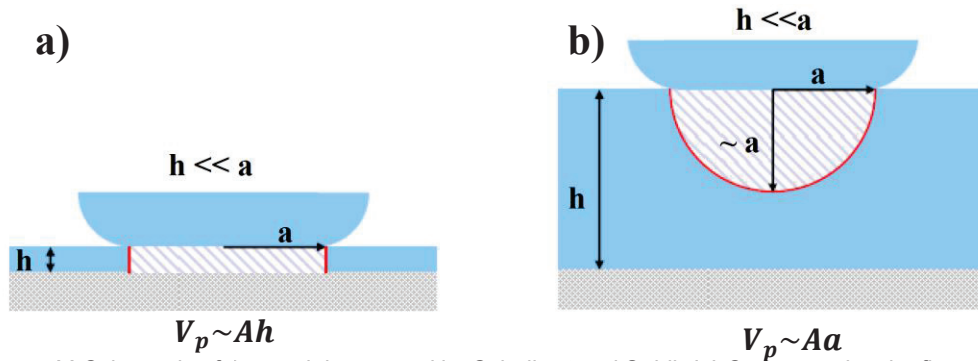


Figure 5. 11 Schematic of the model proposed by Scheibert and Sahli. (a) Correspond to the first regime thinner thickness $\frac{h}{a} < 0,25$. (b) Correspond to the second regime thicker thickness $\frac{h}{a} > 1,8$. The deformed volume V_p is presented by the grey zones.

III-2-Dewetting Experiments Using a Newtonian Fluid PDMS

Macroscopic friction experiments mentioned above, shows clearly that at small cross-linked thickness ($<500 \mu\text{m}$) an important dependence of the friction response to the coated layer thicknesses. Thus, to better understanding this phenomena, we used here the autophobic dewetting of a PDMS film on smooth non-wettable silicon substrates coated with varying thicknesses of cross-linked PDMS layers ranging from 30 nm-1,8 μm (Fig.5.12).

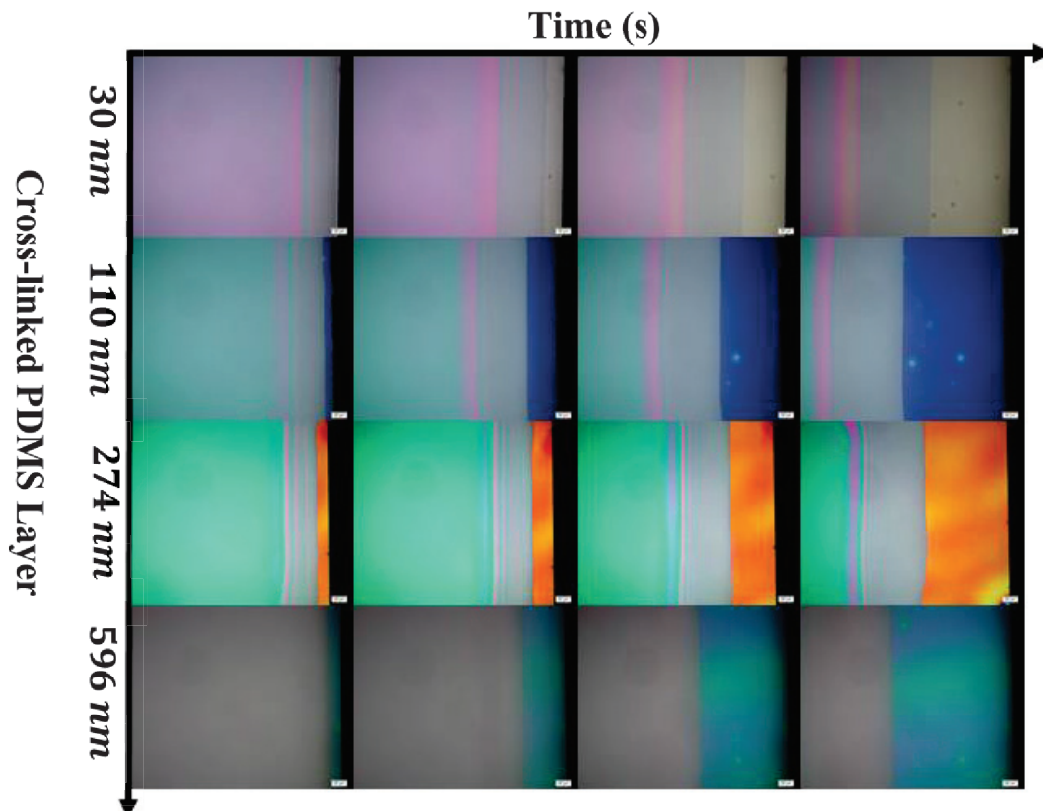


Figure 5. 12 Optical micrograph of the dewetting of a 500 nm PDMS (139k) at 150 °C for different cross-linked PDMS coated layer ($336 \mu\text{m} \times 263 \mu\text{m}$).

Chapter 5 Dewetting and friction measurements on homogeneous deformable substrates

Following these experiments, we can measure in situ and in real time, the contact angle and the slippage length at the melt-polymer interface. Thus, this approach presents a quantitative information of the interfacial friction. Based on the theoretically predicted relations between velocity, energy dissipation, capillary driving force, viscosity and film thickness, we have access to an interpretation of the changes in interfacial properties in the course of the experiment, impossible for any other technique of such simplicity.

III-2.1-Dewetting Dynamics

In this part, dewetting of a 500 nm thin PDMS polymer film on smooth non-wettable silicon substrates coated with various thicknesses of cross-linked PDMS layers ranging from 30 nm-1,8 μm was studied (Fig.5.12). In all the experiments presented here, we investigated exclusively the interfacial properties between chemically identical polymers.

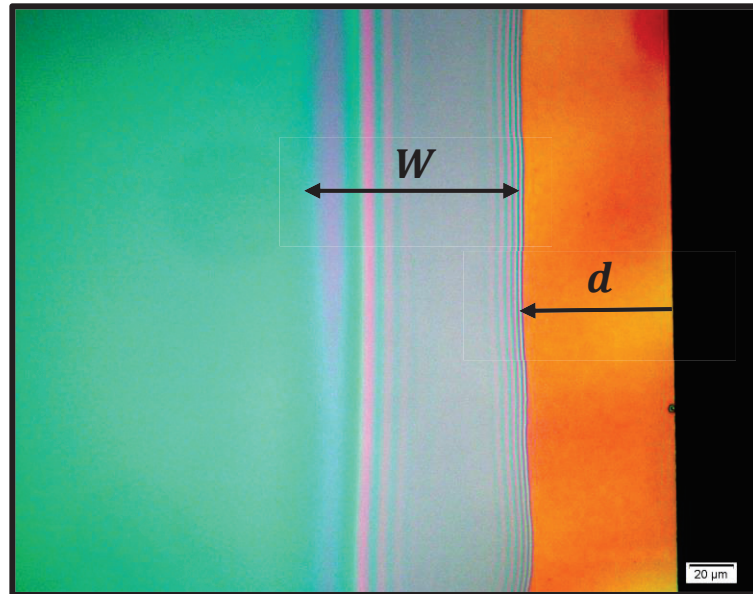


Figure 5. 13 Optical micrograph of the dewetting of a 500 nm PDMS film at 150 °C on of the 274 nm cross-linked PDMS coated layer.

There, such interfaces are characterized by the difference in conformational entropy between cross-linked layer and free polymer film. This may lead to autophobic behavior [172-174], i.e., the free molecules dewetted the cross-linked PDMS layer. Thus, by breaking the sample, we created a three-phase contact line between the substrate, the film and the surrounding environment. Consequently, the thin PDMS films annealed at 150 °C while optical micrographs were recorded in situ Fig.5.12. The system is metastable under these conditions; the retraction of the liquid film occurs at the three-phase contact line. Furthermore, it is a possible to record respectively the dewetted distance d and the rim width W of the rim by optical micrographs of the dewetting rim in time. It should be noted that from these parameters, a velocity dewetting V was obtained by taking the differences ; $V = [d(t_i) - d(t_{i-1})]/(t_i - t_{i-1})$ Fig.5.13.

Chapter 5 Dewetting and friction measurements on homogeneous deformable substrates

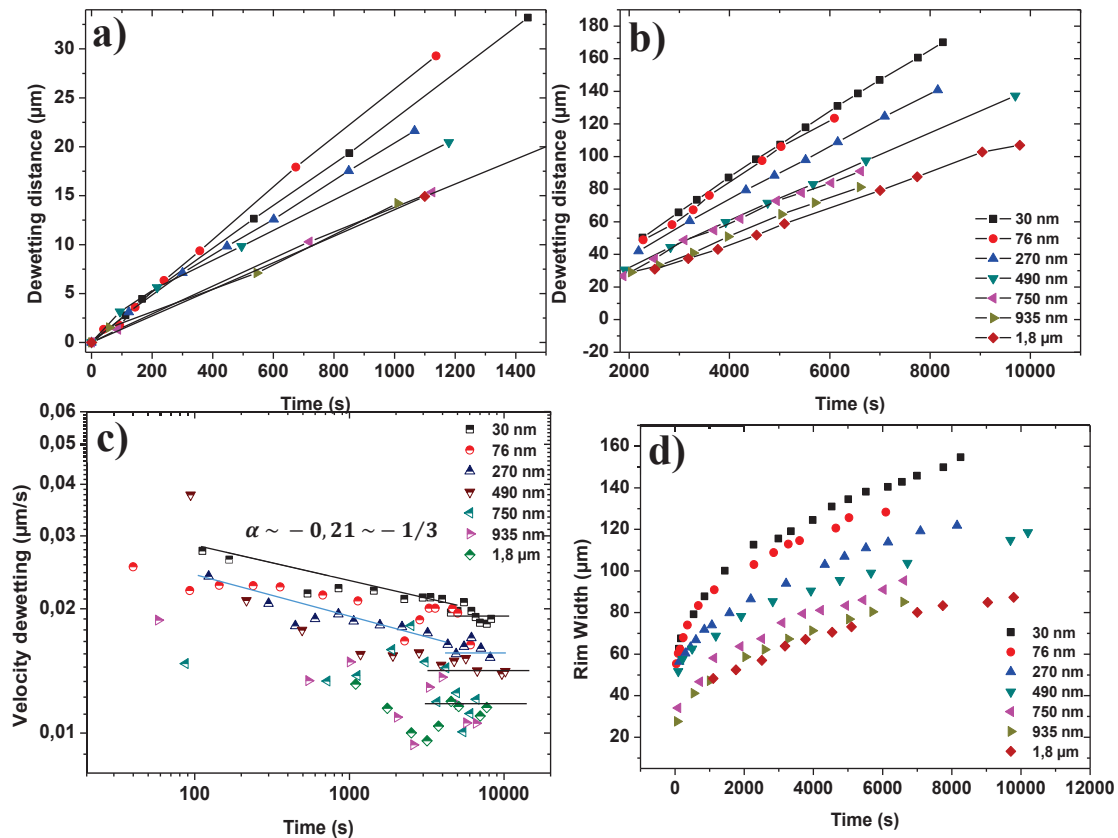


Figure 5.14 (a) Temporal evolution of the dewetting distance of a PDMS film ($500 \text{ nm } M_w = 139\,000 \text{ g/mol}$) on top of a cross-linked PDMS coated layer of a varying thickness ranging from ($30 \text{ nm up to } 1.8 \text{ }\mu\text{m}$) at 150°C . (from 0 to 1400 S) (b) Dewetted distance as a function of time from (2000 to 10000 S) . (c) Temporal evolution of the dewetting velocity on double logarithmic scales. (d) Temporal evolution of the rim width for the same conditions as Fig.5.14 (a).

Furthermore, Fig.5.14 shows respectively the temporal evolution of the dewetting distance and the rim width growth. Where, we observe clearly the non-linear behavior of the d and W . Thus, these results clearly illustrates that the thinner coated layers dewetts faster compared to the thicker cross-linked PDMS. However, following the temporal evolution of the dewetting velocity and the rim width (Fig.5.14 (c-d)) we can clearly discern the presence of two different regimes. We should note that larger rim width, for a given dewetted distance, could be attributed to the thick PDMS film (500 nm) used in the different dewetting experiment. Therefore, as the dewetting process and parallel to the increase of the rim width, we notice a clear decrease of V with the cross-linked PDMS layer thickness. In fact, in this situation, the dewetting velocity follows a power law of $-1/3$, indicating thus a semi-ideal behavior [173, 174, 200]. Furthermore, at a later stage of dewetting, an almost constant value of V and W was reached. Hence, interfacial friction increases with coated layer thickness and dewetting proceeds more slowly in thicker layers.

Based on mass conservation and the theoretical prediction, recording the temporal evolution of the dewetted distance and the rim width simultaneously allowed us to determine the value of the contact

Chapter 5 Dewetting and friction measurements on homogeneous deformable substrates

angle θ in situ and in real time and any possible variations of θ in time, without any fitting. For slipping films we get [83]:

$$\theta(t) = \frac{d(t)h(t)}{CW^2(t)} \quad (5.11)$$

Typical results are presented in Fig.5.15. Two regimes are clearly observed following the evolution of the contact angle θ , where an increase of its value at shorter time can be noticed, while at longer time the value attain a plateau, being almost similar for the different thickness of cross-linked PDMS coated layer.

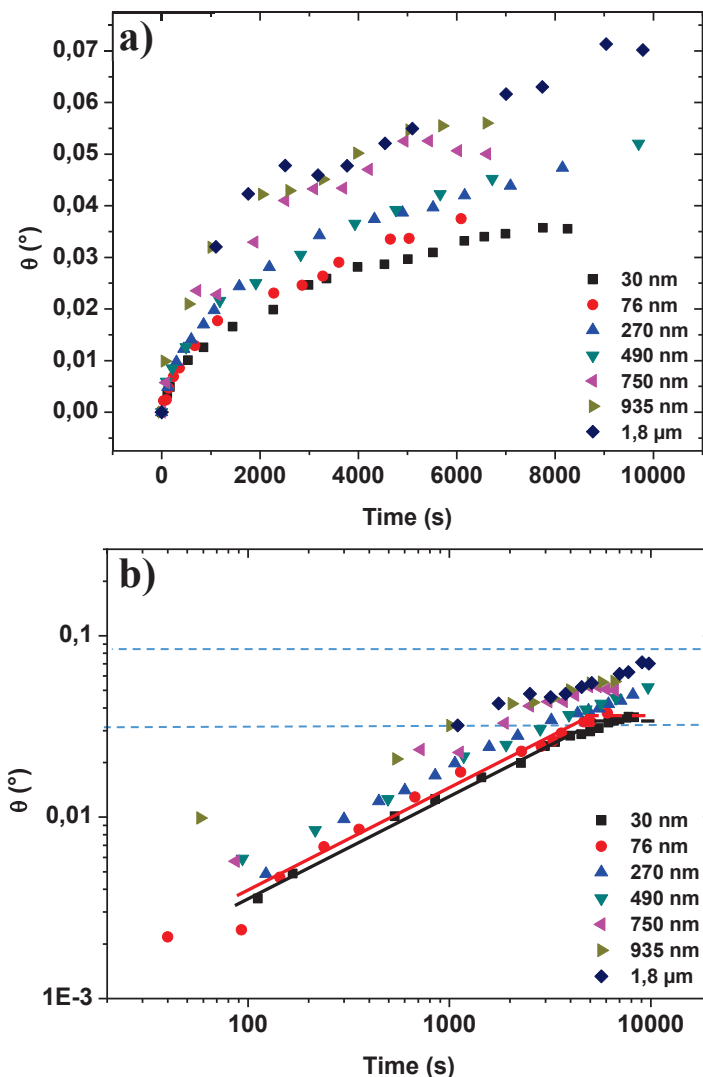


Figure 5. 15 (a) Temporal evolution of the contact angle as determined from eq 5.11 of a PDMS film (500 nm $M_w = 139\,000$ g/mol) on top of a cross-linked PDMS of a varying thickness ranging from (30 nm up to 1,8 μm) at 150°C. (b) Temporal evolution of the contact angle on double logarithmic scales. The straight lines are guideline for eyes.

Chapter 5 Dewetting and friction measurements on homogeneous deformable substrates

At the first regime, a clear difference appears for the thinner coated layers: the increase of the contact angle is slower compared to the thicker coated layers. Therefore, the variation of the contact angle θ at this stage can be attributed to the inhomogeneity and the instability of the dewetting system. Nevertheless, at later stage of dewetting an almost constant value of θ can be clearly observed. In fact, as the dewetting process the contact angle trend to stabilize despite that the macroscopic visual continues evolution of the dewetting dynamics. This aspect suggests that at this stage, the dewetting dynamics can be considered as a homogenous system. However, as we mentioned above that the PDMS film used for these experiments is thick film (500 nm) which explain the large value of the rim width and the small value of the contact angle. Then, the increase of the contact angle with the augmentation of the cross-linked PDMS layer can be explained by the increase of the interfacial contact between the two layers suggesting an increase of the elastic constraints in the bulk. In fact, while the contact angle reflects entropic properties of the interface, the presence of interfacial and viscoelastic dissipation influences the frictional behavior and thus the slippage length. The loss of entropy will assist the dewetting while at the same time the presence of the elastic deformation will disfavor the wetting process. Hence, knowing that viscous forces balance the driving capillary forces $F_D = F_V$, we can also obtain the value of the slippage length b and its temporal evolution using:

$$F_D = 0,5\gamma \theta^2(t_i) = \frac{3\eta V(t_i) W(t_i)}{b(t_i)} = F_V \quad (5.12)$$

$$b(t_i) = \frac{3\eta V(t_i) W(t_i)}{0,5\gamma \theta^2(t_i)} \quad (5.13)$$

In the case of a slipping film, the energy is dissipated over the completely moving part of the film characterized by the width W of the rim collecting the liquid from the dewetted region.

Chapter 5 Dewetting and friction measurements on homogeneous deformable substrates

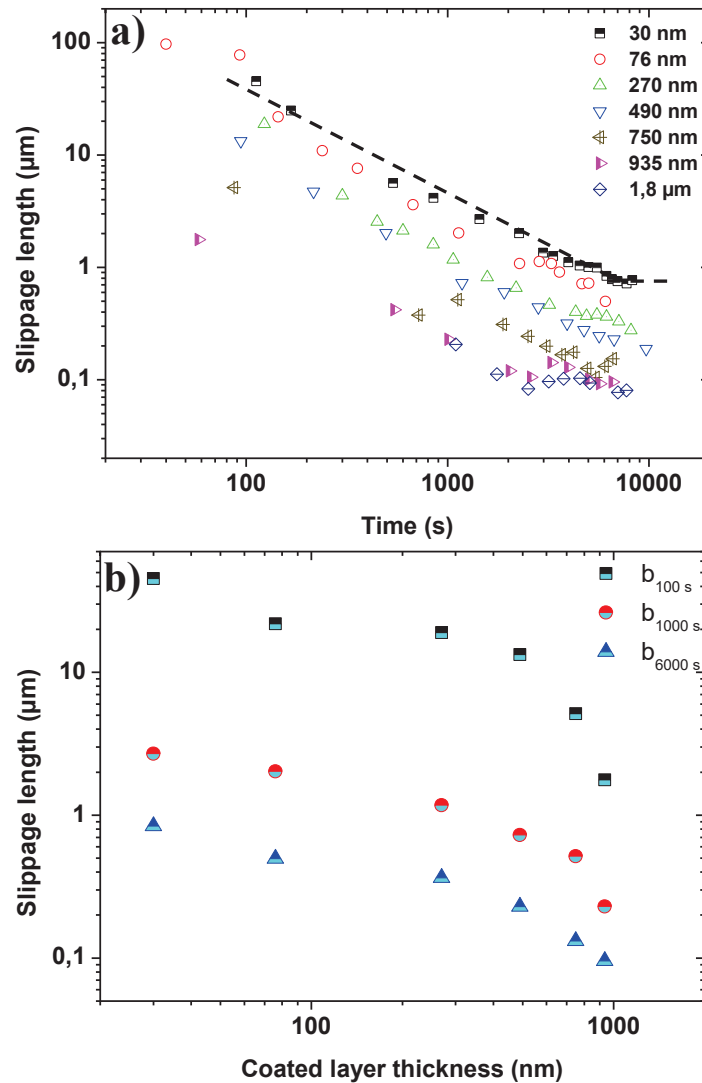


Figure 5. 16 (a) Temporal evolution of the slippage length as determined from eq 5.13 of a PDMS film ($500 \text{ nm } M_w = 139\,000 \text{ g/mol}$) on top of a cross-linked PDMS coated layer of a varying thickness ranging from ($30 \text{ nm up to } 1,8 \mu\text{m}$) at 150°C . The dotted lines are guideline for eyes. **(b)** Slippage length as determined from eq 5.13, deduced over the time range of 100 s, 1000s and 6000 s respectively, as a function of coated layer thickness on double logarithmic scales.

The results at 150°C are shown in Fig.5.16. In fact, this approach of measuring the contact angle and slippage length allows us to investigate the changes in the interface of the cross-linked PDMS layer during the experiment. Furthermore, the initial value of the slippage length are clearly different for the several systems and exhibit two different regime as the contact angle. At short time, we can notice clearly a fast decrease of b with time while at later stage the value is almost constant for the different thickness of PDMS cross-linked coated layer. We can observe also the decrease of the slippage length with the increase of the cross-linked PDMS layer. This observation prove our assumption about the dependence of the interfacial friction to the cross-linked PDMS coated layer thickness.

Chapter 5 Dewetting and friction measurements on homogeneous deformable substrates

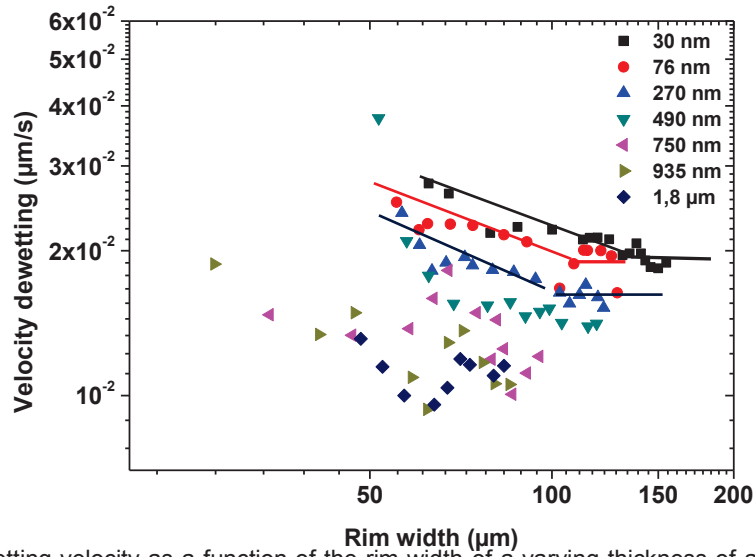


Figure 5. 17 Dewetting velocity as a function of the rim width of a varying thickness of a cross-linked PDMS layer ranging from (30 nm up to 1,8 µm) at 150°C. The straight lines are guideline for eyes.

According to the equation (5.12), $F_D = F_V$, then the viscous force F_V will increase with rim width W . Moreover, in a good approximation and knowing that in the course of the dewetting experiments described in Fig.5.14 (c) that the driving force characterized by θ increase slightly. Then we anticipate that the dewetting velocity V decreases with the increase in W . This is clearly demonstrated in Fig.5.17 by plotting the dewetting velocity V as a function of the rim width W , which proves the existence of two different regimes. At shorter time, we can clearly observe a decrease of the velocity dewetting with rim width, proving that the dissipation increases regularly with W . Such a relation between V and W implies that the whole rim slips. In the other hand, at longer time the velocity dewetting exhibit an constant behavior which can be explained by the jump from the plug flow case $\alpha = 2/3$ to the no-slip boundary situation $\alpha = 1$. It should be noted that at late time, W trend to be larger then $W = bL/\theta$ inducing the cross over from the slip situation to no-slip boundary [214]. As discussed above, while an increase in contact angle causes faster dewetting, a decrease in slippage length will lead to slower dewetting. Thus, depending on which effect dominates, one may observe a faster or slower decrease in dewetting velocity. The observed data suggests the existence of two regimes. Then, to a better understanding of the active force affecting the dewetting dynamics, we define this force as a combination of the friction dissipation, viscous dissipation and finally elastic restoration force

$$F_{dewetting} = F_{friction} + F_{Visc dis} + F_{restoration} \quad (5.14)$$

At first, for the (30 nm up to 270 nm) we can assume that the viscous dissipation and the elastic restoration force are negligible compared to the dissipation due to friction, and, consequently, the dewetting velocity is proportional to $t^{-1/3}$. Furthermore, as explained above (Fig.5.7) that K and E clearly decreases with the PDMS coated thicknesses. We can assume that at thin thicknesses, the effect

Chapter 5 Dewetting and friction measurements on homogeneous deformable substrates

of the rigidity and the young modules is the most important parameter governing the interfacial friction response. In fact, as dewetting proceeds; the increase of the rim width induces an expansion of the

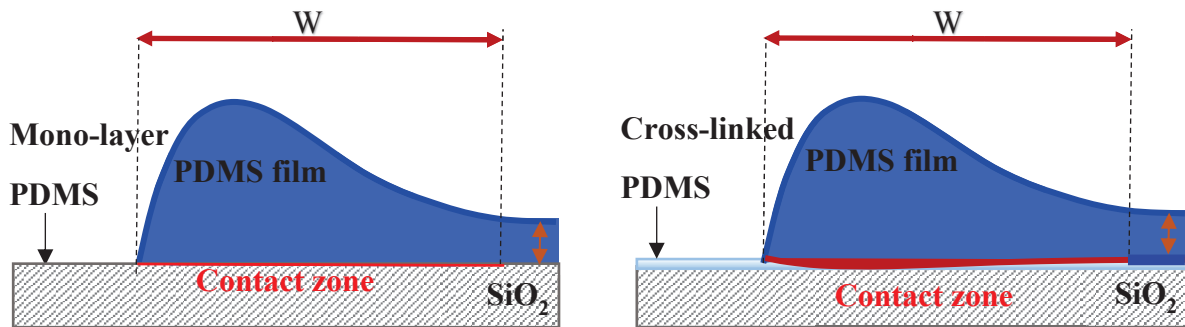


Figure 5. 18 Schematic presentation of late stages of dewetting of a PDMS film on a substrate of a cross-linked PDMS coated layer of a thin thickness (30 nm up to 270 nm).

contact zone between the PDMS film and the cross-liked layer until meeting the rigid substrate Fig.5.18. At this point, the friction dissipation dominates the interfacial friction compared to the other forces, which explain the fast decrease of the slippage length and the velocity dewetting. On the other hand, for thicker cross-linked PDMS layer (490 nm up to 1,8 μm) an increase of the contact surface between the thick PDMS film and the coated layer can be assumed. Consequently, the dewetting velocity and the slippage length slowly decreases compared to the thinner samples. Thus, the viscous dissipation is approximately equal to interfacial dissipation due to friction, proving the increase of the viscoelastic deformation of the bulk, thus enhancing the effect of the elastic restoration force Fig.5.19.

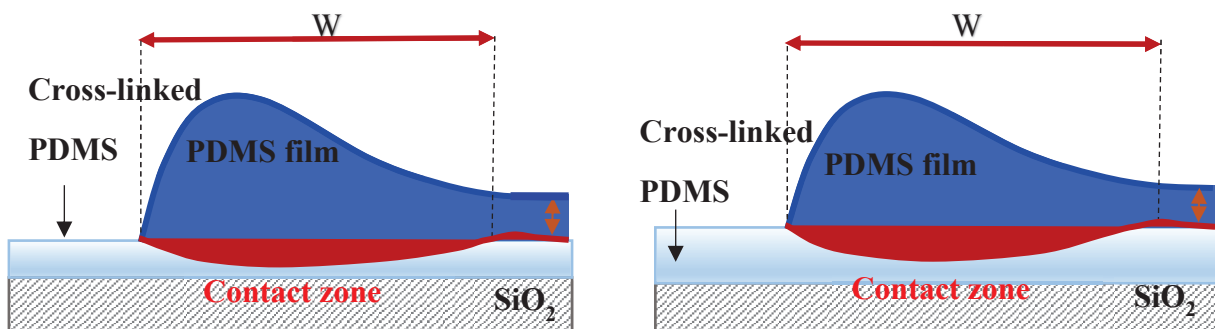


Figure 5. 19 Schematic presentation of late stages of dewetting of a PDMS film on a substrate of a cross-linked PDMS coated layer of a thin thickness (490 nm up to 1,8 μm).

Therefore, we can attribute the low slippage length observed on the thickest cross-linked PDMS layer to the deformation of the cross-linked layer and the creation of a depression at the border of the rim ridge (in the direction of the slipping). In fact, this depression could be induced by to the restoration force applied by the deformed cross-linked PDMS layer Fig.5.19.

III-2.3-Interfacial friction behaviour

Fig.5.20 shows the slippage length plotted as a fonction of the dewetting velocity. Interestingly, these results indicate that for the slow dewetting velocities (the thickest cross-linked PDMS coted layer 490

Chapter 5 Dewetting and friction measurements on homogeneous deformable substrates

nm up to 1,8 μm) of these experiments, b not influenced by the dewetting velocity. This behavior can be attributed to the bulk viscous dissipation, which is at most larger, or of the order of the interfacial

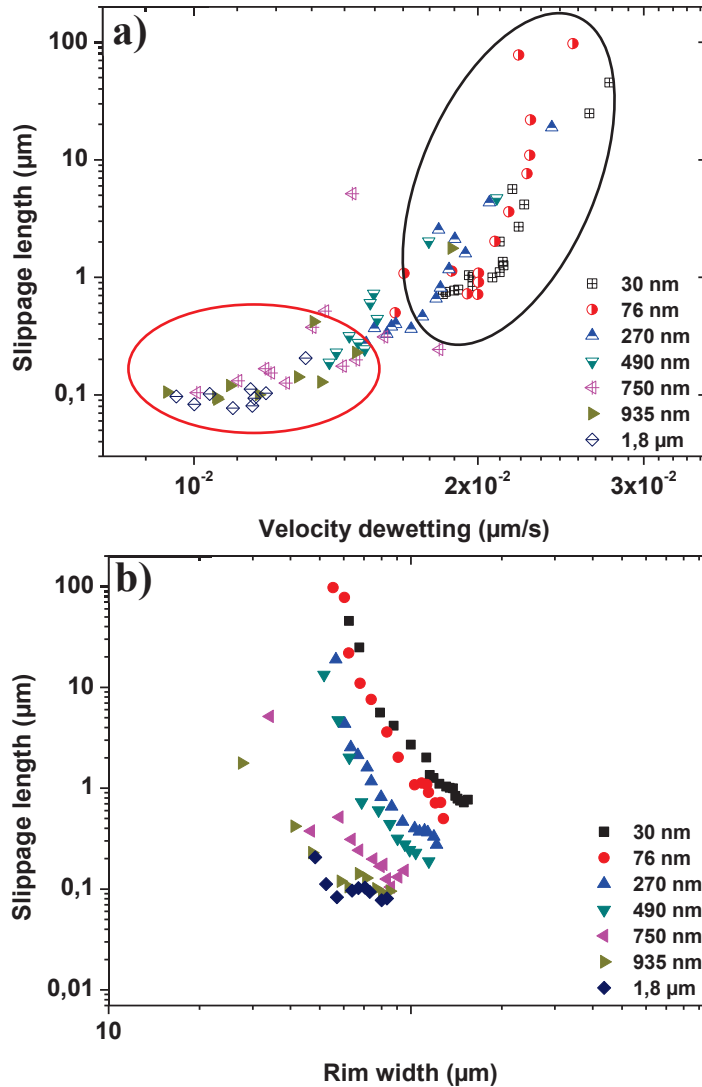


Figure 5. 20 (a) Slippage length as a function of dewetting velocity width of a varying thickness of of a cross-linked PDMS layer ranging from (30 nm up to 1,8 μm) at 150°C. (b) Slippage length (b) as a function of rim width (W) for the same conditions as 5.23. (a).

dissipation due to friction. However, for the thinnest coated layer b increase with the augmentation of the velocity V and with the decrease of the thickness of the coated layer. We should note that b also decrease as the rim width W increase. For the first regime (thin coated layer 30 nm up to 270 nm) we can explain this behavior by the ineffectiveness of the surface tension and the domination of the interfacial dissipation due to the friction of the film onto the substrate. Al Akhrass et al [215] mentioned that the increase of the elastic deformation within the bulk with the increase of the surface of contact, induces as well an increase of the friction at the interfaces.

Chapter 5 Dewetting and friction measurements on homogeneous deformable substrates

Systems whose friction at the solid/liquid interface prevails show a reducing dewetting velocity with time. In the plug flow situation (large slip length b), the velocity with a slip contribution varies with b/W with W being the rim width and b representing the friction at the solid/liquid interface: $b = \eta/\xi$, ξ is the friction coefficient (per area a^2 of a monomer)[198]. Thus, the observed values of the slippage length was quite different with the PDMS coated layer thickness and knowing that the viscosity of the dewetting PDMS film ($\eta = 90 \text{ Pa s}$) we can deduce a relative value of ξ Fig.5.21. Comparing this value to the monomeric friction coefficient $\xi_0 \approx 3,7 \cdot 10^7 \text{ Pa s/m}$ [164] indicates that as the thickness of the time of the experiment and the coated PDMS layer increases, the number of monomers at the interface contributed to friction increases as well.

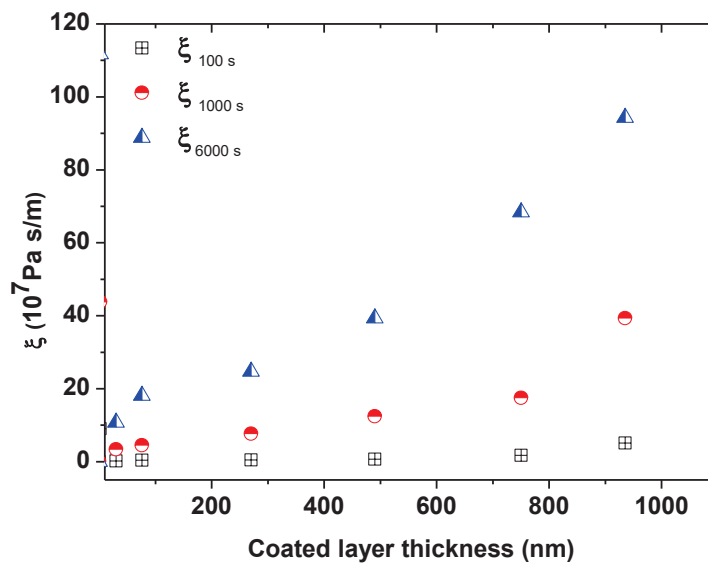


Figure 5. 21 Interfacial friction coefficient (ξ) as determined following the equation $\xi = \eta/b$ of a PDMS film (500 nm $M_w = 139\,000 \text{ g/mol}$ $\eta = 90 \text{ Pa s}$) on top of a cross-linked PDMS coated layer of a varying thickness ranging from (30 nm up to 1,8 μm) at 150°C, deduced over the time range of 100 s, 1000s and 6000 s respectively, as a function of coated layer thickness.

Hence, in the same fashion as the results of the friction experiments the viscous behavior of the confined interfacial layer can be advanced. Then, knowing that in a normal dewetting experiment, the driving capillary forces are balanced by viscous force, we can assume that the elastic deformation of the substrate influence greatly the dewetting dynamics of thin films inducing a decrease of the velocity dewetting. Considering that, and assuming that the elastic deformation is directly proportional to the interfacial contact. The increase of the thickness of the PDMS coated layer induces a jump from a regime dominated by pure interfacial friction for the thinner thickness (30 nm up to $\sim 270 \text{ nm}$) to a second regime governed by the viscoelastic dissipation and restorative forces of the PDMS bulk, for the thicker PDMS (490 nm up to $\sim 1,8 \mu\text{m}$).

Chapter 5 Dewetting and friction measurements on homogeneous deformable substrates

IV-Conclusion

Firstly, we found that friction measurements results, exhibit higher friction stress for the thicker PDMS coated layer. Hence, a systematic variation of the critical shear stress with the thickness of the cross-linked PDMS layer was found. In fact, following the variation of the stiffness and the young modulus of the substrate with cross-linked PDMS, suggests the presence of two regimes. At first, for thicknesses ranging from 0 up to 500 μm , we found that stiffness and the young modulus of the substrate dominates the friction behavior. However, the surface chemistry does not really present any influence on the frictional response. In fact, as friction test process, the increase of the normal force applied induces of an expansion of the contact zone between the PDMS bead and the thin-coated layer until meeting the solid substrate. At this point, stiffness and the young modulus of the substrate dominates the friction, which explain the decrease of K and E with the cross-linked PDMS thicknesses. In the other hand, for thicker layers ($h = 500 \mu\text{m}$) we clearly observed that independently of the thickness layer a plateau for the values of K and E is reached. In this situation, during the friction experiments, the normal force is increasingly applied. Moreover, the high frictional response observed on the thickest PDMS coated layer can be anchored to the deformation of the cross-linked layer and the creation of a depression at the border of the contact (in the direction of the sliding). In fact, this depression could be generated due to the restoration force applied by the deformed cross-linked PDMS. A second mechanism to understand this behavior was advanced. The sliding properties of free and pendant chains on one hand and elastic contact on the other hand is one of the probable explanation. However, the dependence of the friction behaviour to the thickness of the cross-linked PDMS coated layer can be also explained using the energetic dissipation at the interface of the contact and the volumes dissipation in the bulk.

Secondly, the autophobic dewetting of a PDMS film on various thicknesses of cross-linked PDMS layers ranging from 30 nm-1,8 μm was investigated. The observed data suggests the existence of two regimes. At first, for the (30 nm up to 270 nm) we can assume that the viscous dissipation and the elastic restoration force are negligible compared to the dissipation due to friction. In fact, as dewetting proceeds; the increase of the rim width induces an expansion of the contact zone between the PDMS film and the cross-linked layer until meeting the solid surface (SiO_2). Hence, in this situation, the friction dissipation dominates the interfacial friction compared to the other forces, which explain the fast decrease of the slippage length and the velocity dewetting. Thus, we can assume that at thin thicknesses, the effect of the rigidity and the young modulus is the most important parameter governing the interfacial friction response. For thicker cross-linked PDMS layer (490 nm up to 1,8 μm) an increase of the contact surface between the thick PDMS film and the coated layer can be assumed. Consequently, the dewetting velocity and the slippage length slowly decreases compared to the thinner samples. Thus, the viscous dissipation is approximately equal to interfacial dissipation due to friction, proving the increase of the viscoelastic deformation of the bulk, thus enhancing the effect of the elastic restoration force. Thus, we can attribute

Chapter 5 Dewetting and friction measurements on homogeneous deformable substrates

the high friction response observed on the thickest cross-linked PDMS layer to the deformation of bulk and the creation of a depression at the border of the rim ridge. Therefore, dewetting experiments have been proved to display a highly sensitive approach for determining the frictional response of polymer/substrate interfaces.

Finally, these experiments suggests a certain similarities between the interfacial friction between a melt/polymer interface and polymer/polymer solid interface, specially concerning the effect the viscoelastic deformation on the bulk on the friction behavior.

General Conclusion

The principle aim of this work is a multiple scale analysis of the adhesion, friction and wetting behaviors for different patterned interfaces.

In a first chapter, a bibliographic review briefly surveys the principles of adhesion and friction phenomena. The effects of surface texturing on the tribological performances were provided. Then, the fundamentals of thin liquid film and the dewetting scenario on chemically and topographically patterned surfaces were presented.

In the second chapter, various heterogeneous silane/polymer deposition methods were explored, including micro contact printing with hand pressure and micro contact printing using the mini (μ CP) machine followed by polymer grafting. Then, we studied the pinning/depinning behaviour of the contact line of water droplet on regularly patterned surfaces (circular and linear patterns) was investigated to explain the role surface chemical heterogeneity plays in wettability. We observed that on the patterned surfaces the contact line motion alternates between moving (between the patterns) and a pinning/depinning phase at the pattern. This stick–slip behaviour leads to oscillation of the contact angles. It was found that the behavior of the advancing baseline and contact angle was present as the pattern sizes increases inducing a dependence of the oscillation to the pattern sizes and distributions. Hence, we suggest that the enhancement of the thermodynamic work of adhesion is related to the lengthening of the contact line due to contact line pinning. In fact, by printing periodic regions of surface chemical contrast, the contact line profile increases as a function of the surface chemistry proprieties and the perimeter of the pattern region.

In the last part of this chapter, the adhesive properties of linear patterned surfaces of different chemistry and pattern sizes was explored using an FFM (AFM QNM Peak force) and a JKR machine homebuilt. The MTS/Si-OH patterned surfaces prepared by μ CP, showed a similar adhesive response at the macro and nanoscale. Nevertheless, these experiments show that the adhesion response is greatly affected by the chemistry, relative fractional molecular domain and patterns sizes. Furthermore, using the results of the adhesion measurements at nano and micro-scales, we found also that the introduction of the PDMS strips on a patterned substrate induces a decrease of the adhesive response. This enhancement of the adhesive behavior, can be attributed to the adsorption of free PDMS chain on the non- covered MTS zone. In fact, micro-contact printing may lead to non-covered zones in the middle of the printed MTS layer, inducing then a possible adsorption of some PDMS free polymer chain during the grafting process. These regions can be considered as an important aspect of the enhancement of adhesion.

In summary, at macro, micro and nanoscales our patterned surfaces exhibited a similar adhesive response suggesting that at different scales, the adhesive behaviour of MTS/Si-OH or MTS/PDMS

General Conclusion

mixed surfaces are largely dependent on the chemistry and the preparation methods. These results prove that the adhesion is not a consequence of the changes in the surface density.

In the third chapter, we explored the macro-friction dependence of a PDMS bead on a hydrophobic/hydrophilic mixed silane system and a hydrophobic/hydrophobic patterned system. Hence, we observe a similar frictional response independently of chemistry and sizes of the patterns printed on the surface. In fact, we can clearly notice that MTS/PDMS patterns increase the critical shear stress values of a 15% in comparison with the silicon surface covered by PDMS layer. Nevertheless, despite this augmentation the critical shear stress values stay negligible compared to the silicon surface covered with MTS layer. Hence, this frictional behavior could be explained by the high loads and sliding force used in these experiments. These results suggest that these measurements are greatly sensitive to the mechanical properties as substrate stiffness and young modules compared to the chemical layers introduced to the surface. Secondly, the investigation of the frictional response at nanoscale between a rigid tip and a MTS/Si-OH covered surface, demonstrated a negligible increase of the relative coefficient of friction with the pattern sizes. In fact, these results show that friction increases slightly with the surface coverage of Si-OH. This behavior can be explained by the rise of the magnitude of the adhesive interaction of the SAMs and the tip. As a result, the greater the surface fraction of Si-OH present on the surface, the greater the friction response can be. However, the exploration of the friction behavior of an FFM tip on MTS/PDMS patterned surfaces showed a great enhancement of the coefficient of friction ($\times 2.5$) with the increase of the strip sizes. This frictional behavior can be attributed to the rip-off of some PDMS chains from the surfaces in the middle of the sliding experiments. In fact, as the size of the PDMS strip increases, a rise in the influence of the rip-off phenomena could be assumed. Thus, we can probably assume that the anchoring of these PDMS chains on the FFM tip greatly influences the frictional response.

Intriguingly, the uses of these approaches did not provide us with an explicit answer to our bewilderment concerning the influence of the chemical layer introduced on the surface on the frictional behavior.

Therefore, in the fourth chapter, we adopted an approach of dewetting of thin polymer film on top of patterned surfaces, to investigate the interfacial friction response of the surface at the melt-substrate interfaces. In fact, dewetting experiments have been proved to be a highly sensitive tool for the determination of every significant change at polymer/substrate interfaces. As following, we found that the dewetting process can be divided into four stages (rim growth, undulation and rim swelling, fingering and finally pinch-off instabilities) varying with slippage. We observed that as polymer accumulates in the rim at the three-phase contact line, a Rayleigh-Plateau type instability takes place at the liquid/air interface. Hence, we found that this type of instabilities is clearly governed by the presence of different chemical domains (Hydrophobic /Hydrophilic) at the surface.

General Conclusion

Furthermore, from the start of dewetting until the droplet detachment instabilities, the rim instability undergoes a varying shift in the apparition of the fingering and pinch-off regime with the increase of the pattern sizes. In fact, the increase of the volume collected on the front of the rim suggest an augmentation of bulges number and sizes with pattern sizes. Moreover, we can suggest that the rim instability develops before fingering starts and that the main factor inducing fingering is slippage. However, the transition from bulge to finger appears at a stage where the balance between dissipative forces and driving forces varies locally. In fact, at the start of dewetting, a high energy is needed to debuts the film sliding constructing then the rim. Hence, as the dewetting process, an increase of the rim width induces then an augmentation of the interfacial friction. This behavior could be attributed to the no-sliding effect provoked by the presence of the hydrophilic patterns on the surface. Therefore, in our case, this response is a result of a competition between slip and no slip behavior induced by the introduction of an (Hydrophobic /Hydrophilic) system on the surface. Following this behavior, we consider the presence of the two types of dissipation mechanism on the interface of the patterned layer. The first being purely viscous and the second being friction at the solid/liquid interface, these two mechanisms can be combined to explain why the dewetting velocity increases with the pattern sizes. Further, we observed that with the increase of the strips sizes and the thickness of the polystyrene film, the side effects such as pinning or other inhomogeneities increase as well. Which lead to irregularities in the rise of the undulated ridge involves a premature pinch-off. Hence, a decrease of the diameter of the droplets between the primary and the secondary droplet is observed. This effect induces then an increase of the ratio of both diameters with the increase of the textures sizes and the PS thicknesses. Thus, satellite drops eventually appear between the primary and a secondary droplet depending whether a thin thread is left over during the pinch-off process. However, the dewetting of the polystyrene film used in this work presented a qualitative analysis of the frictional response of a polymer melt sliding on (hydrophobic/ hydrophilic) patterned system. Hence, in the final part of this chapter, we studied the autophobic dewetting of a thin PDMS film on top of an (hydrophobic/hydrophobic) MTS/PDMS patterned system. The aim of this analysis is to extract quantitative information of the interfacial friction. Then, as dewetting proceeded, we observed that the in one hand, the PDMS dewetts on the PDMS strips of the substrate. In the other hand, a no slip behavior was be observed on the MTS part of the linear patterns. This behavior can be related to the adsorbtion of the free polymer chain on the non-covered zone (SiOH) randomly distributed on the MTS patterns. Hence, due to the low grafting density, an enlargement of the non-covered zone could be greatly possible with the increase of the pattern size. Thus, as expected an increase of the rim width induces a clear slowing effect of the dewetting velocity, which results to an augmentation of the rate of PDMS adsorption on the SiOH molecules and expansion of the contact zone. Then, a decrease of the slippage length can be predicted, which proves our assumption of the dependence of the friction response to the MTS layer printed on the surface.

General Conclusion

As a mean to understand the predominant aspect between the chemistry introduced on the surface and the mechanical proprieties of the substrate. In the fifth chapter, we found that that friction measurements results, exhibit higher friction stress for the thicker PDMS coated layer. Hence, a systematic variation of the critical shear stress with the thickness of the cross-liked PDMS layer was found. In fact, following the variation of the stiffness and the young modulus of the substrate with cross-linked PDMS, suggests the presence of two regimes. At first, for thicknesses ranging from 0 up to 500 μm , we found that stiffness and the young modulus of the substrate dominates the friction behavior. However, the surface chemistry does not really present any influence on the frictional response. In fact, as friction test process, the increase of the normal force applied induces of an expansion of the contact zone between the PDMS bead and the thin-coated layer until meeting the solid substrate. At this point, stiffness and the young modulus of the substrate dominates the friction, which explain the decrease of K and E with the cross-linked PDSM thicknesses. In the other hand, for thicker layers ($h = 500 \mu\text{m}$) we clearly observed that independently of the thickness layer a plateau for the values of K and E are reached. In this situation, during the friction experiments, the normal force is increasingly applied. Moreover, the high frictional response observed on the thickest PDMS coated layer can be anchored to the deformation of the cross-linked layer and the creation of a depression at the border of the contact (in the direction of the sliding). In fact, this depression could be generated due to the restoration force applied by the deformed cross-linked PDMS. A second mechanism to understand this behavior was advanced: the energetic dissipation at the interface of the contact and the volumes dissipation in the bulk. Secondly, the autophobic dewetting of a PDMS film on various thicknesses of cross-linked PDMS layers ranging from 30 nm-1,8 μm was investigated. The observed data suggests the existence of two regimes. At first, for the (30 nm up to 270 nm) we can assume that the viscous dissipation and the elastic restoration force are negligible compared to the dissipation due to friction. In fact, as dewetting proceeds; the increase of the rim width induces an expansion of the contact zone between the PDMS film and the cross-liked layer until meeting the solid surface (SiO_2). Hence, in this situation, the friction dissipation dominates the interfacial friction compared to the other forces, which explain the fast decrease of the slippage length and the velocity dewetting. Thus, we can assume that at thin thicknesses, the effect of the rigidity and the young modules is the most important parameter governing the interfacial friction response. For thicker cross-linked PDMS layer (490 nm up to 1,8 μm) an increase of the contact surface between the thick PDMS film and the coated layer can be assumed. Consequently, the dewetting velocity and the slippage length slowly decreases compared to the thinner samples. Thus, we can assume that at this point the viscous dissipation is approximately equal to interfacial dissipation due to friction. This assumption indicates that the increase of the viscoelastic deformation of the bulk could enhance the impact of the elastic restoration force. Thus, we can attribute the high friction response observed on the thickest cross-linked PDMS layer to the deformation of bulk and the creation of a depression at the border of the rim ridge. In summary, dewetting experiments have been proved a highly sensitive technique for determining the frictional response of polymer/substrate interfaces.

Bibliography

1. Israelachvili, J.N. and *Intermolecular and Surface Forces, 3rd ed.* . Academic Press Ltd, Burlington, MA., (2011).
2. Langmuir, I., *Surface Chemistry*. Chemical Reviews, 1933. **13**(2): p. 147-191.
3. Hu, D.L., B. Chan, and J.W. Bush, *The hydrodynamics of water strider locomotion*. Nature, 2003. **424**(6949): p. 663-666.
4. Hertz, H.R., *Miscellaneous Papers: With an Introd. by Philipp Lenard. Authorised English Translation by DE Jones and GA Schott*. 1896: Macmillan.
5. Griffith, A.A., *The Phenomena of Rupture and Flow in Solids*. Philosophical Transactions of the Royal Society of London. Series A, Containing Papers of a Mathematical or Physical Character, 1921. **221**: p. 163-198.
6. Derjaguin, B., V. Muller, and Y. Toporov, *On different approaches to the contact mechanics*. Journal of Colloid and Interface Science, 1980. **73**(1): p. 293-294.
7. Derjaguin, B., V. Muller, and Y.P. Toporov, *On the role of molecular forces in contact deformations (critical remarks concerning Dr. Tabor's report)*. Journal of Colloid and Interface Science, 1978. **67**(2): p. 378-379.
8. Hughes, B. and L. White, *Analytic approximations for the elastic contact of rough spheres*. Journal of Applied Mechanics, 1980. **47**(1): p. 194-196.
9. Muller, V., V. Yushchenko, and B. Derjaguin, *On the influence of molecular forces on the deformation of an elastic sphere and its sticking to a rigid plane*. Journal of Colloid and Interface Science, 1980. **77**(1): p. 91-101.
10. Tabor, D., *Surface forces and surface interactions*. Journal of Colloid and Interface Science, 1977. **58**(1): p. 2-13.
11. Tabor, D., *On the role of molecular forces in contact deformations (Critical remarks concerning Dr. Tabor's report)*. Journal of Colloid and Interface Science, 1978. **67**(2): p. 380.
12. Johnson, K., K. Kendall, and A. Roberts. *Surface energy and the contact of elastic solids*. in *Proceedings of the Royal Society of London A: Mathematical, Physical and Engineering Sciences*. 1971. The Royal Society.
13. Derjaguin, B.V., V.M. Muller, and Y.P. Toporov, *Effect of contact deformations on the adhesion of particles*. Journal of Colloid and Interface Science, 1975. **53**(2): p. 314-326.
14. Fisher, R.A., *On the capillary forces in an ideal soil; correction of formulae given by W. B. Haines*. The Journal of Agricultural Science, 2009. **16**(3): p. 492-505.
15. Haines, W.B., *Studies in the physical properties of soils: IV. A further contribution to the theory of capillary phenomena in soil*. The Journal of Agricultural Science, 2009. **17**(2): p. 264-290.
16. Melrose, J.C., *Model calculations for capillary condensation*. AIChE Journal, 1966. **12**(5): p. 986-994.
17. De Gennes, P.-G., *Wetting: statics and dynamics*. Reviews of modern physics, 1985. **57**(3): p. 827.
18. Harkins, W.D. and H. Livingston, *Energy relations of the surfaces of solids II. Spreading pressure as related to the work of adhesion between a solid and a liquid*. The Journal of Chemical Physics, 1942. **10**(6): p. 342-356.
19. Schrader, M.E., *Young-Dupre Revisited*. Langmuir, 1995. **11**(9): p. 3585-3589.
20. Wenzel, R.N., *Resistance of solid surfaces to wetting by water*. Industrial & Engineering Chemistry, 1936. **28**(8): p. 988-994.
21. Cassie, A. and S. Baxter, *Wettability of porous surfaces*. Transactions of the Faraday society, 1944. **40**: p. 546-551.

22. Erbil, H.Y. and C.E. Cansoy, *Range of applicability of the Wenzel and Cassie–Baxter equations for superhydrophobic surfaces*. *Langmuir*, 2009. **25**(24): p. 14135-14145.
23. Marmur, A. and E. Bittoun, *When Wenzel and Cassie are right: reconciling local and global considerations*. *Langmuir*, 2009. **25**(3): p. 1277-1281.
24. McHale, G., *Cassie and Wenzel: were they really so wrong?* *Langmuir*, 2007. **23**(15): p. 8200-8205.
25. Bormashenko, E., *A variational approach to wetting of composite surfaces: is wetting of composite surfaces a one-dimensional or two-dimensional phenomenon?* *Langmuir*, 2009. **25**(18): p. 10451-10454.
26. Erbil, H.Y., *The debate on the dependence of apparent contact angles on drop contact area or three-phase contact line: A review*. *Surface Science Reports*, 2014. **69**(4): p. 325-365.
27. Johnson Jr, R.E. and R.H. Dettre, *Contact angle hysteresis. III. Study of an idealized heterogeneous surface*. *The journal of physical chemistry*, 1964. **68**(7): p. 1744-1750.
28. Schwartz, L.W. and S. Garoff, *Contact angle hysteresis on heterogeneous surfaces*. *Langmuir*, 1985. **1**(2): p. 219-230.
29. Xu, X. and X. Wang, *Analysis of wetting and contact angle hysteresis on chemically patterned surfaces*. *SIAM journal on applied mathematics*, 2011. **71**(5): p. 1753-1779.
30. Butt, H.-J. and M. Kappl, in *Surface and Interfacial Forces*. 2010, Wiley-VCH Verlag GmbH & Co. KGaA. p. 219-250.
31. Bowden, F.P. and D. Tabor, *The friction and lubrication of solids*. Vol. 1. 2001: Oxford university press.
32. Dowson, D., *History of tribology*. 1979: Addison-Wesley Longman Limited.
33. Bowden, F., A. Moore, and D. Tabor, *The ploughing and adhesion of sliding metals*. *Journal of Applied Physics*, 1943. **14**(2): p. 80-91.
34. Sutton, A.P., *Deformation mechanisms, electronic conductance and friction of metallic nanocontacts*. *Current Opinion in Solid State and Materials Science*, 1996. **1**(6): p. 827-833.
35. Bowden, F. and A. Hanwell. *The friction of clean crystal surfaces*. in *Proceedings of the Royal Society of London A: Mathematical, Physical and Engineering Sciences*. 1966. The Royal Society.
36. Lüthi, R., et al., *Friction on the atomic scale: An ultrahigh vacuum atomic force microscopy study on ionic crystals*. *Journal of Vacuum Science & Technology B*, 1996. **14**(2): p. 1280-1284.
37. Maeda, N., et al., *Adhesion and friction mechanisms of polymer-on-polymer surfaces*. *Science*, 2002. **297**(5580): p. 379-382.
38. Singh, R., et al., *Friction welding of dissimilar plastic/polymer materials with metal powder reinforcement for engineering applications*. *Composites Part B: Engineering*, 2016. **101**: p. 77-86.
39. Zeng, H., et al., *Adhesion and friction of polystyrene surfaces around T g*. *Macromolecules*, 2006. **39**(6): p. 2350-2363.
40. Brewer, N.J., B.D. Beake, and G.J. Leggett, *Friction Force Microscopy of Self-Assembled Monolayers: Influence of Adsorbate Alkyl Chain Length, Terminal Group Chemistry, and Scan Velocity*. *Langmuir*, 2001. **17**(6): p. 1970-1974.
41. Evans, D.C.B., J.F. Nye, and K.J. Cheeseman, *The Kinetic Friction of Ice*. *Proceedings of the Royal Society of London. A. Mathematical and Physical Sciences*, 1976. **347**(1651): p. 493-512.
42. Hardy, W.B., *Collected Scientific Papers of Sir William Bate Hardy*. 2015: Cambridge University Press.
43. Tomlinson, G., *CVI. A molecular theory of friction*. *The London, Edinburgh, and Dublin philosophical magazine and journal of science*, 1929. **7**(46): p. 905-939.
44. Akhmatov, A.S., *Molecular physics of boundary friction*. Vol. 2108. 1966: Israel program for scientific translations.
45. Ajaev, V.S., E.Y. Gatapova, and O.A. Kabov, *Stability and break-up of thin liquid films on patterned and structured surfaces*. *Advances in colloid and interface science*, 2016. **228**: p. 92-104.

46. Zhu, Y. and S. Granick, *Rate-Dependent Slip of Newtonian Liquid at Smooth Surfaces*. Physical Review Letters, 2001. **87**(9): p. 096105.
47. Vinogradova, O.I. and G.E. Yakubov, *Dynamic Effects on Force Measurements. 2. Lubrication and the Atomic Force Microscope*. Langmuir, 2003. **19**(4): p. 1227-1234.
48. Cho, J.-H.J., B.M. Law, and F. Rieutord, *Dipole-Dependent Slip of Newtonian Liquids at Smooth Solid Hydrophobic Surfaces*. Physical Review Letters, 2004. **92**(16): p. 166102.
49. Bäumchen, O. and K. Jacobs, *Can liquids slide? Linking stability and dynamics of thin liquid films to microscopic material properties*. Soft Matter, 2010. **6**(24): p. 6028-6035.
50. Sabzevari, S.M., et al., *Sacrificial mica substrates influence the slip boundary condition of dewetting polymer films*. Polymer, 2015. **78**: p. 202-207.
51. McGraw, J.D., et al., *Slip-mediated dewetting of polymer microdroplets*. Proceedings of the National Academy of Sciences, 2016. **113**(5): p. 1168-1173.
52. Geim, A.K., et al., *Microfabricated adhesive mimicking gecko foot-hair*. Nat Mater, 2003. **2**(7): p. 461-463.
53. Crosby, A.J., M. Hageman, and A. Duncan, *Controlling polymer adhesion with "pancakes"*. Langmuir, 2005. **21**(25): p. 11738-43.
54. Greiner, C., A. del Campo, and E. Arzt, *Adhesion of Bioinspired Micropatterned Surfaces: Effects of Pillar Radius, Aspect Ratio, and Preload*. Langmuir, 2007. **23**(7): p. 3495-3502.
55. Verneuil, E., et al., *Adhesion on microstructured surfaces*. The Journal of Adhesion, 2007. **83**(5): p. 449-472.
56. Aksak, B., M.P. Murphy, and M. Sitti, *Adhesion of biologically inspired vertical and angled polymer microfiber arrays*. Langmuir, 2007. **23**(6): p. 3322-3332.
57. Murphy, M.P., B. Aksak, and M. Sitti, *Adhesion and anisotropic friction enhancements of angled heterogeneous micro-fiber arrays with spherical and spatula tips*. Journal of Adhesion Science and Technology, 2007. **21**(12-13): p. 1281-1296.
58. Murphy, M.P., B. Aksak, and M. Sitti, *Gecko-Inspired Directional and Controllable Adhesion*. Small, 2009. **5**(2): p. 170-175.
59. Glassmaker, N.J., et al., *Biologically inspired crack trapping for enhanced adhesion*. Proc Natl Acad Sci U S A, 2007. **104**(26): p. 10786-91.
60. Kim, S., et al., *Reversible dry micro-fibrillar adhesives with thermally controllable adhesion*. Soft Matter, 2009. **5**(19): p. 3689-3693.
61. Reddy, S., E. Arzt, and A. del Campo, *Bioinspired surfaces with switchable adhesion*. Advanced materials, 2007. **19**(22): p. 3833-3837.
62. Greiner, C., E. Arzt, and A. del Campo, *Hierarchical Gecko-Like Adhesives*. Advanced Materials, 2009. **21**(4): p. 479-482.
63. Jeong, H.E., et al., *A nontransferring dry adhesive with hierarchical polymer nanohairs*. Proceedings of the National Academy of Sciences, 2009. **106**(14): p. 5639-5644.
64. Lee, J., et al., *Gecko-inspired combined lamellar and nanofibrillar array for adhesion on nonplanar surface*. Langmuir, 2009. **25**(21): p. 12449-12453.
65. Ramrus, D.A. and J.C. Berg, *Characterization and adhesion testing of mixed silane-treated surfaces*. Journal of adhesion science and technology, 2004. **18**(12): p. 1395-1414.
66. Kovalchenko, A., et al., *The effect of laser surface texturing on transitions in lubrication regimes during unidirectional sliding contact*. Tribology International, 2005. **38**(3): p. 219-225.
67. Pettersson, U. and S. Jacobson, *Influence of surface texture on boundary lubricated sliding contacts*. Tribology International, 2003. **36**(11): p. 857-864.
68. Komvopoulos, K., N. Saka, and N. Suh, *Plowing friction in dry and lubricated metal sliding*. Journal of tribology, 1986. **108**(3): p. 301-312.
69. Saka, N., H. Tian, and N.P. Suh, *Boundary lubrication of undulated metal surfaces at elevated temperatures*. Tribology Transactions, 1989. **32**(3): p. 389-395.
70. Suh, N.P. and H.-C. Sin, *The genesis of friction*. Wear, 1981. **69**(1): p. 91-114.
71. Tian, H., N. Saka, and N.P. Suh, *Boundary lubrication studies on undulated titanium surfaces*. Tribology Transactions, 1989. **32**(3): p. 289-296.

72. Mougín, K. and H. Hamidou, *Nanoscale friction of self-assembled monolayers*, in *Fundamentals of Friction and Wear on the Nanoscale*. 2015, Springer. p. 489-514.
73. Reiter, G., *Dewetting of thin polymer films*. Physical Review Letters, 1992. **68**(1): p. 75.
74. Jacobs, K., S. Herminghaus, and K.R. Mecke, *Thin liquid polymer films rupture via defects*. Langmuir, 1998. **14**(4): p. 965-969.
75. Dutcher, J.R. and A.G. Marangoni, *Soft materials: structure and dynamics*. 2004: CRC Press.
76. Reiter, G. and S. Napolitano, *Possible origin of thickness-dependent deviations from bulk properties of thin polymer films*. Journal of Polymer Science Part B: Polymer Physics, 2010. **48**(24): p. 2544-2547.
77. Tsui, O.K.C., *Polymer thin films*. Vol. 1. 2008: World Scientific.
78. Navier, C., *Mémoire sur les lois du mouvement des fluides*. Mémoires de l'Académie Royale des Sciences de l'Institut de France, 1823. **6**: p. 389-440.
79. Oron, A., S.H. Davis, and S.G. Bankoff, *Long-scale evolution of thin liquid films*. Reviews of modern physics, 1997. **69**(3): p. 931.
80. Damman, P., et al., *Relaxation of residual stress and reentanglement of polymers in spin-coated films*. Physical review letters, 2007. **99**(3): p. 036101.
81. Hamieh, M., et al., *Influence of substrate properties on the dewetting dynamics of viscoelastic polymer films*. The Journal of Adhesion, 2007. **83**(4): p. 367-381.
82. Reiter, G., *Dewetting of highly elastic thin polymer films*. Physical Review Letters, 2001. **87**(18): p. 186101.
83. Reiter, G., et al., *Dewetting as an investigative tool for studying properties of thin polymer films*. The European Physical Journal Special Topics, 2009. **166**(1): p. 165-172.
84. Reiter, G., et al., *Residual stresses in thin polymer films cause rupture and dominate early stages of dewetting*. Nature Materials, 2005. **4**(10): p. 754-758.
85. Vilmin, T. and E. Raphaël, *Dewetting of thin polymer films*. The European Physical Journal E, 2006. **21**(2): p. 161-174.
86. Ziebert, F. and E. Raphaël, *Dewetting dynamics of stressed viscoelastic thin polymer films*. Physical Review E, 2009. **79**(3): p. 031605.
87. Damman, P., N. Baudelet, and G. Reiter, *Dewetting near the glass transition: transition from a capillary force dominated to a dissipation dominated regime*. Physical review letters, 2003. **91**(21): p. 216101.
88. Al Akhrass, S., L. Vonna, and G. Reiter, *From Holes to Drops to Toroids: Conditions for the Transcription of Surface Patterns into Three-Dimensional Morphologies via Rim Instabilities in the Course of Dewetting*, in *Polymer Surfaces in Motion*. 2015, Springer. p. 23-42.
89. Kargupta, K. and A. Sharma, *Morphological self-organization by dewetting in thin films on chemically patterned substrates*. The Journal of chemical physics, 2002. **116**(7): p. 3042-3051.
90. Sehgal, A., et al., *Pattern-directed dewetting of ultrathin polymer films*. Langmuir, 2002. **18**(18): p. 7041-7048.
91. Geoghegan, M., et al., *Thin polymer films on chemically patterned, corrugated substrates*. Journal of Physics: Condensed Matter, 2005. **17**(9): p. S389.
92. Khare, K., et al., *Dewetting of liquid filaments in wedge-shaped grooves*. Langmuir, 2007. **23**(24): p. 12138-12141.
93. Volodin, P. and A. Kondyurin, *Dewetting of thin polymer film on rough substrate: II. Experiment*. Journal of Physics D: Applied Physics, 2008. **41**(6): p. 065307.
94. Higgins, A.M. and R.A. Jones, *Anisotropic spinodal dewetting as a route to self-assembly of patterned surfaces*. Nature, 2000. **404**(6777): p. 476-478.
95. Bao, L.-R., et al., *Polymer inking as a micro-and nanopatterning technique*. Journal of Vacuum Science & Technology B, 2003. **21**(6): p. 2749-2754.
96. Ferrell, N. and D. Hansford, *Fabrication of Micro-and Nanoscale Polymer Structures by Soft Lithography and Spin Dewetting*. Macromolecular rapid communications, 2007. **28**(8): p. 966-971.

97. Rockford, L., et al., *Polymers on nanoperiodic, heterogeneous surfaces*. Physical review letters, 1999. **82**(12): p. 2602.
98. Rehse, N., et al., *Stability of thin polymer films on a corrugated substrate*. The European Physical Journal E, 2001. **4**(1): p. 69-76.
99. Mukherjee, R., D. Bandyopadhyay, and A. Sharma, *Control of morphology in pattern directed dewetting of thin polymer films*. Soft Matter, 2008. **4**(10): p. 2086-2097.
100. Mukherjee, R., M. Gonuguntla, and A. Sharma, *Meso-patterning of thin polymer films by controlled dewetting: From nano-droplet arrays to membranes*. Journal of nanoscience and nanotechnology, 2007. **7**(6): p. 2069-2075.
101. Zhang, X., F. Xie, and O.K. Tsui, *Microscopic surface patterning by rubbing induced dewetting*. Polymer, 2005. **46**(19): p. 8416-8421.
102. Julthongpiput, D., et al., *Pattern-directed to isotropic dewetting transition in polymer films on micropatterned surfaces with differential surface energy contrast*. Soft Matter, 2007. **3**(5): p. 613-618.
103. Luo, C., et al., *Ordered droplet formation by thin polymer film dewetting on a stripe-patterned substrate*. Journal of colloid and interface science, 2004. **269**(1): p. 158-163.
104. Xing, R., et al., *Dewetting of polymethyl methacrylate on the patterned elastomer substrate by solvent vapor treatment*. Polymer, 2007. **48**(12): p. 3574-3583.
105. Lee, F.K., et al., *Continuous liquid crystal pretilt control through textured substrates*. Applied physics letters, 2004. **85**(23): p. 5556-5558.
106. Li, Z., et al., *Polymer thin films on patterned Si surfaces*. Macromolecules, 1998. **31**(6): p. 1915-1920.
107. Braun, H.-G. and E. Meyer, *Thin microstructured polymer films by surface-directed film formation*. Thin Solid Films, 1999. **345**(2): p. 222-228.
108. Meyer, E. and H.-G. Braun, *Controlled dewetting processes on microstructured surfaces-a new procedure for thin film microstructuring*. Macromolecular Materials and Engineering, 2000. **276**(1): p. 44-50.
109. Quéré, D., *Wetting and roughness*. Annu. Rev. Mater. Res., 2008. **38**: p. 71-99.
110. Seemann, R., et al., *Droplet based microfluidics*. Reports on progress in physics, 2011. **75**(1): p. 016601.
111. Chen, Y., C. Helm, and J. Israelachvili, *Molecular mechanisms associated with adhesion and contact angle hysteresis of monolayer surfaces*. The journal of physical chemistry, 1991. **95**(26): p. 10736-10747.
112. Rauscher, M. and S. Dietrich, *Nano-droplets on structured substrates*. Soft matter, 2009. **5**(16): p. 2997-3001.
113. Varagnolo, S., et al., *Tuning drop motion by chemical patterning of surfaces*. Langmuir, 2014. **30**(9): p. 2401-2409.
114. Beltrame, P., P. Hänggi, and U. Thiele, *Depinning of three-dimensional drops from wettability defects*. EPL (Europhysics Letters), 2009. **86**(2): p. 24006.
115. Herde, D., et al., *Driven large contact angle droplets on chemically heterogeneous substrates*. EPL (Europhysics Letters), 2012. **100**(1): p. 16002.
116. Thiele, U. and E. Knobloch, *On the depinning of a driven drop on a heterogeneous substrate*. New Journal of Physics, 2006. **8**(12): p. 313.
117. Thiele, U. and E. Knobloch, *Driven drops on heterogeneous substrates: Onset of sliding motion*. Physical review letters, 2006. **97**(20): p. 204501.
118. Leopoldes, J. and D. Bucknall, *Droplet spreading on microstriped surfaces*. The Journal of Physical Chemistry B, 2005. **109**(18): p. 8973-8977.
119. Kusumaatmaja, H. and J. Yeomans, *Modeling contact angle hysteresis on chemically patterned and superhydrophobic surfaces*. Langmuir, 2007. **23**(11): p. 6019-6032.
120. Morita, M., et al., *Macroscopic-wetting anisotropy on the line-patterned surface of fluoroalkylsilane monolayers*. Langmuir, 2005. **21**(3): p. 911-918.

121. Suzuki, S., et al., *Sliding behavior of water droplets on line-patterned hydrophobic surfaces*. Applied Surface Science, 2008. **254**(6): p. 1797-1805.
122. Elloumi-Hannachi, I., et al., *Portable microcontact printing device for cell culture*. Biomaterials, 2010. **31**(34): p. 8974-8979.
123. Deruelle, M., et al., *Some remarks on JKR experiments*. Journal of adhesion science and technology, 1998. **12**(2): p. 225-247.
124. Deruelle, M., L. Leger, and M. Tirrell, *Adhesion at the solid-elastomer interface: influence of the interfacial chains*. Macromolecules, 1995. **28**(22): p. 7419-7428.
125. Maugis, D. and M. Barquins, *Fracture mechanics and adherence of viscoelastic solids*, in *Adhesion and adsorption of polymers*. 1980, Springer. p. 203-277.
126. Hertz, H., *The principles of mechanics presented in a new form*. 1899: Courier Corporation.
127. Binnig, G., et al., *Atomic resolution with atomic force microscope*. EPL (Europhysics Letters), 1987. **3**(12): p. 1281.
128. Binnig, G., C.F. Quate, and C. Gerber, *Atomic force microscope*. Physical review letters, 1986. **56**(9): p. 930.
129. Maivald, P., et al., *Using force modulation to image surface elasticities with the atomic force microscope*. Nanotechnology, 1991. **2**(2): p. 103.
130. Magonov, S., V. Elings, and M.-H. Whangbo, *Phase imaging and stiffness in tapping-mode atomic force microscopy*. Surface science, 1997. **375**(2-3): p. L385-L391.
131. Burnham, N.A. and R.J. Colton, *Measuring the nanomechanical properties and surface forces of materials using an atomic force microscope*. Journal of Vacuum Science & Technology A: Vacuum, Surfaces, and Films, 1989. **7**(4): p. 2906-2913.
132. Rosa-Zeiser, A., et al., *The simultaneous measurement of elastic, electrostatic and adhesive properties by scanning force microscopy: pulsed-force mode operation*. Measurement Science and Technology, 1997. **8**(11): p. 1333.
133. Pittenger, B., N. Erina, and C. Su, *Quantitative mechanical property mapping at the nanoscale with PeakForce QNM*. Application Note Veeco Instruments Inc, 2010.
134. Voss, A., R.W. Stark, and C. Dietz, *Surface versus volume properties on the nanoscale: Elastomeric polypropylene*. Macromolecules, 2014. **47**(15): p. 5236-5245.
135. Owens, D.K. and R.C. Wendt, *Estimation of the surface free energy of polymers*. Journal of Applied Polymer Science, 1969. **13**(8): p. 1741-1747.
136. Jansen, H.P., et al., *Simulating anisotropic droplet shapes on chemically striped patterned surfaces*. Langmuir, 2011. **28**(1): p. 499-505.
137. Drelich, J., et al., *Contact angles for liquid drops at a model heterogeneous surface consisting of alternating and parallel hydrophobic/hydrophilic strips*. Langmuir, 1996. **12**(7): p. 1913-1922.
138. Pompe, T. and S. Herminghaus, *Three-phase contact line energetics from nanoscale liquid surface topographies*. Physical review letters, 2000. **85**(9): p. 1930.
139. Moffat, J.R., K. Sefiane, and M.E.R. Shanahan, *Effect of TiO₂ Nanoparticles on Contact Line Stick-Slip Behavior of Volatile Drops*. The Journal of Physical Chemistry B, 2009. **113**(26): p. 8860-8866.
140. Mittal, K.L., *Contact Angle, Wettability and Adhesion, Volume 6*. 2009: CRC Press.
141. Duursma, G., K. Sefiane, and S. David, *Advancing and receding contact lines on patterned structured surfaces*. Chemical Engineering Research and Design, 2010. **88**(5): p. 737-743.
142. Shahsavan, H., *Biomimetic Micro/nano-Structured Surfaces: A Potential Tool for Tuning of Adhesion and Friction*. 2012.
143. Chen, N., et al., *Adhesion and friction of polymer surfaces: the effect of chain ends*. Macromolecules, 2005. **38**(8): p. 3491-3503.
144. Burnham, N.A., R.J. Colton, and H.M. Pollock, *Interpretation issues in force microscopy*. Journal of Vacuum Science & Technology A: Vacuum, Surfaces, and Films, 1991. **9**(4): p. 2548-2556.

145. Maboudian, R. and R.T. Howe, *Critical review: Adhesion in surface micromechanical structures*. Journal of Vacuum Science & Technology B: Microelectronics and Nanometer Structures Processing, Measurement, and Phenomena, 1997. **15**(1): p. 1-20.
146. Singh, R.A., et al., *Nano-scale adhesion and friction in Si-wafer with the tip size using AFM*. KSTLE Intl. Jl, 2004. **5**(1): p. 1-6.
147. Singh, R.A., et al., *Friction behaviour of chemical vapor deposited self-assembled monolayers on silicon wafer*. Wear, 2007. **262**(1): p. 130-137.
148. Lee, S., et al., *The influence of packing densities and surface order on the frictional properties of alkanethiol self-assembled monolayers (SAMs) on gold: a comparison of SAMs derived from normal and spiroalkanedithiols*. Langmuir, 2000. **16**(5): p. 2220-2224.
149. Shon, Y.-S., et al., *Spiroalkanedithiol-based SAMs reveal unique insight into the wettabilities and frictional properties of organic thin films*. Journal of the American Chemical Society, 2000. **122**(31): p. 7556-7563.
150. Camillone III, N., et al., *Surface structure and thermal motion of n-alkane thiols self-assembled on Au (111) studied by low energy helium diffraction*. The Journal of chemical physics, 1991. **94**(12): p. 8493-8502.
151. Clear, S.C. and P.F. Nealey, *Lateral force microscopy study of the frictional behavior of self-assembled monolayers of octadecyltrichlorosilane on silicon/silicon dioxide immersed in n-alcohols*. Langmuir, 2001. **17**(3): p. 720-732.
152. Moser, A. and C. Eckhardt, *A method for reliable measurement of relative frictional properties of different self-assembled monolayers using frictional force microscopy*. Thin Solid Films, 2001. **382**(1): p. 202-213.
153. Ren, S., S. Yang, and Y. Zhao, *Micro-and macro-tribological study on a self-assembled dual-layer film*. Langmuir, 2003. **19**(7): p. 2763-2767.
154. Ren, S., et al., *Friction and wear studies of octadecyltrichlorosilane SAM on silicon*. Tribology Letters, 2002. **13**(4): p. 233-239.
155. Aoike, T., et al., *Comparison of macro-and nanotribological behavior with surface plastic deformation of polystyrene*. Langmuir, 2001. **17**(7): p. 2153-2159.
156. SAHLI, R., *Mise en glissement des interfaces multi-contacts élastomères : étude expérimentale par visualisation in situ*. École Centrale de Lyon, 2017.
157. Mate, C.M., et al., *Atomic-scale friction of a tungsten tip on a graphite surface*, in *Scanning Tunneling Microscopy*. 1987, Springer. p. 226-229.
158. Riedo, E., F. Lévy, and H. Brune, *Kinetics of capillary condensation in nanoscopic sliding friction*. Physical review letters, 2002. **88**(18): p. 185505.
159. Archard, J. *Elastic deformation and the laws of friction*. in *Proceedings of the Royal Society of London A: Mathematical, Physical and Engineering Sciences*. 1957. The Royal Society.
160. Yoon, E.-S., et al., *The effect of contact area on nano/micro-scale friction*. Wear, 2005. **259**(7): p. 1424-1431.
161. Bowden, F., et al., *The Friction and Lubrication of Solids The Friction and Lubrication of Solids Clarendon*. 1950, Oxford.
162. Angst, D.L. and G.W. Simmons, *Moisture absorption characteristics of organosiloxane self-assembled monolayers*. Langmuir, 1991. **7**(10): p. 2236-2242.
163. Xiao, X., et al., *Chain length dependence of the frictional properties of alkylsilane molecules self-assembled on mica studied by atomic force microscopy*. Langmuir, 1996. **12**(2): p. 235-237.
164. Brown, H., *Chain Pullout and Mobility Effects in*. Science, 1994. **263**: p. 11.
165. Galliano, A., S. Bistac, and J. Schultz, *Adhesion and friction of PDMS networks: molecular weight effects*. Journal of colloid and interface science, 2003. **265**(2): p. 372-379.
166. Hsu, S.M., *Nano-lubrication: concept and design*. Tribology International, 2004. **37**(7): p. 537-545.

167. Singh, R.A., et al., *A comparative study of micro-friction properties of Si-wafer and DLC and DMDC self-assembled monolayer coated on Si-wafer*. 한국윤활학회 학술대회, 2005: p. 49-55.
168. Tupper, K.J. and D.W. Brenner, *Molecular dynamics simulations of friction in self-assembled monolayers*. Thin Solid Films, 1994. **253**(1-2): p. 185-189.
169. Kendall, K., *Inadequacy of Coulomb's friction law for particle assemblies*. Nature, 1986. **319**(6050): p. 203-205.
170. Zhou, Y., et al., *Compositional mapping of micropatterned, mixed self-assembled monolayers by lateral force microscopy*. Langmuir, 1998. **14**(3): p. 660-666.
171. Li, Y. and D. Li, *Experimental studies on relationships between the electron work function, adhesion, and friction for 3d transition metals*. Journal of applied physics, 2004. **95**(12): p. 7961-7965.
172. Reiter, G. *Deriving molecular parameters of interfaces between chemically identical polymers from macroscopically observed phenomena*. in *Macromolecular symposia*. 2005. Wiley Online Library.
173. Reiter, G. and R. Khanna, *Kinetics of autophobic dewetting of polymer films*. Langmuir, 2000. **16**(15): p. 6351-6357.
174. Reiter, G. and R. Khanna, *Real-time determination of the slippage length in autophobic polymer dewetting*. Physical review letters, 2000. **85**(13): p. 2753.
175. Mülhaupt, R., *Hermann Staudinger and the origin of macromolecular chemistry*. Angewandte Chemie International Edition, 2004. **43**(9): p. 1054-1063.
176. Chowdhury, M., *Thin Polymer Films Out of Thermodynamic Equilibrium*. 2012, PhD thesis, Albert-Ludwigs-Universität Freiburg, Freiburg.
177. De Gennes, P.-G., *Scaling concepts in polymer physics*. 1979: Cornell university press.
178. Jones, R.A., *Soft condensed matter*. Vol. 6. 2002: Oxford University Press.
179. Edwards, S.F., *The theory of polymer dynamics*. 1986: Oxford Univ. Press.
180. de Gennes, P.-G., *Reptation of a polymer chain in the presence of fixed obstacles*. Journal of chemical physics, 1971. **55**: p. 572-579.
181. Brandrup, J. and E. Immergut, *Polymer handbook ed*. 1989: publisher not identified.
182. Adamson, A. and A. Gast, *Chemistry of Surfaces*. 1997, John Wiley & Sons, New York, NY, USA.
183. Charru, F., *Hydrodynamic instabilities*. Vol. 37. 2011: Cambridge University Press.
184. Eggers, J. and E. Villermaux, *Physics of liquid jets*. Reports on progress in physics, 2008. **71**(3): p. 036601.
185. Magnus, G., *Hydraulische untersuchungen*. Annalen der Physik, 1855. **171**(5): p. 1-59.
186. Savart, F., *Mémoire sur la constitution des veines liquides lancées par des orifices circulaires en mince paroi*. Ann. Chim. Phys, 1833. **53**(337): p. 1833.
187. Plateau, J., *Mémoire sur les phénomènes que présente une masse liquide et soustraite à l'action de la pesanteur*. Nouveaux mémoires de l'Académie Royale des Sciences et Belles-Lettres de Bruxelles, 1843. **16**: p. 1-1.
188. Rayleigh, L., *XVI. On the instability of a cylinder of viscous liquid under capillary force*. The London, Edinburgh, and Dublin Philosophical Magazine and Journal of Science, 1892. **34**(207): p. 145-154.
189. Rayleigh, L., *On the stability, or instability, of certain fluid motions*. Proceedings of the London Mathematical Society, 1879. **1**(1): p. 57-72.
190. Strutt, J.W. and L. Rayleigh, *On the instability of jets*. Proc. London Math. Soc, 1878. **10**(4).
191. Howard, L.N., *Hydrodynamic and Hydromagnetic Stability*. By S. CHANDRASEKHAR. Clarendon Press: Oxford University Press, 1961. 652 pp. £5. 5s. Journal of Fluid Mechanics, 1962. **13**(1): p. 158-160.
192. Eggers, J., *Nonlinear dynamics and breakup of free-surface flows*. Reviews of modern physics, 1997. **69**(3): p. 865.

193. Merrington, A. and E. Richardson, *The break-up of liquid jets*. Proceedings of the Physical Society, 1947. **59**(1): p. 1.
194. Weast, R., et al., *CRC Handbook of Chemistry and Physics*, CRC Press, Boca Raton, 1989, p. B196 F. **187**.
195. Seemann, R., S. Herminghaus, and K. Jacobs, *Shape of a liquid front upon dewetting*. Physical Review Letters, 2001. **87**(19): p. 196101.
196. Vilmin, T. and E. Raphaël, *Dewetting of thin viscoelastic polymer films on slippery substrates*. EPL (Europhysics Letters), 2005. **72**(5): p. 781.
197. Gabriele, S., et al., *Disentanglement time of polymers determines the onset of rim instabilities in dewetting*. Physical review letters, 2006. **96**(15): p. 156105.
198. de Gennes, P.-G., *Écoulements viscométriques de polymères enchevêtrés*, in *Simple Views On Condensed Matter*. 2003, World Scientific. p. 203-205.
199. Seemann, R., S. Herminghaus, and K. Jacobs, *Gaining control of pattern formation of dewetting liquid films*. Journal of Physics: Condensed Matter, 2001. **13**(21): p. 4925.
200. Brochard-Wyart, F., et al., *Wetting and slippage of polymer melts on semi-ideal surfaces*. Langmuir, 1994. **10**(5): p. 1566-1572.
201. Brochard-Wyart, F., et al., *Dewetting of supported viscoelastic polymer films: Birth of rims*. Macromolecules, 1997. **30**(4): p. 1211-1213.
202. Maoz, R. and J. Sagiv, *On the formation and structure of self-assembling monolayers. I. A comparative atr-wettability study of Langmuir—Blodgett and adsorbed films on flat substrates and glass microbeads*. Journal of Colloid and Interface Science, 1984. **100**(2): p. 465-496.
203. Brenner, M.P. and D. Gueyffier, *On the bursting of viscous films*. Physics of Fluids, 1999. **11**: p. 737-739.
204. Debrégeas, G., P. Martin, and F. Brochard-Wyart, *Viscous bursting of suspended films*. Physical review letters, 1995. **75**(21): p. 3886.
205. Young, T., *An essay on the cohesion of fluids*. Philosophical Transactions of the Royal Society of London, 1805. **95**: p. 65-87.
206. Redon, C., F. Brochard-Wyart, and F. Rondelez, *Dynamics of dewetting*. Physical review letters, 1991. **66**(6): p. 715.
207. Bonn, D., et al., *Wetting and spreading*. Reviews of modern physics, 2009. **81**(2): p. 739.
208. Redon, C., J. Brzoska, and F. Brochard-Wyart, *Dewetting and slippage of microscopic polymer films*. Macromolecules, 1994. **27**(2): p. 468-471.
209. Bäümchen, O. and K. Jacobs, *Slip effects in polymer thin films*. Journal of Physics: Condensed Matter, 2009. **22**(3): p. 033102.
210. Reiter, G., et al., *Dewetting as an investigative tool for studying properties of thin polymer films*. The European Physical Journal-Special Topics, 2009. **166**(1): p. 165-172.
211. Petitet, G. and M. Barquins, *Matériaux caoutchouteux: morphologies, formulations, adhérence, glissance et usure*. 2008: PPUR presses polytechniques.
212. Schallamach, A., *A theory of dynamic rubber friction*. Wear, 1963. **6**(5): p. 375-382.
213. Grosch, K. *The relation between the friction and visco-elastic properties of rubber*. in *Proceedings of the Royal Society of London A: Mathematical, Physical and Engineering Sciences*. 1963. The Royal Society.
214. Reiter, G. and A. Sharma, *Auto-optimization of dewetting rates by rim instabilities in slipping polymer films*. Physical review letters, 2001. **87**(16): p. 166103.
215. Al Akhrass, S., *Démouillage des films minces viscoélastique sur substrats glissants et déformables*. 2007, Université de Haute Alsace-Mulhouse.

Table of Figures

Figure 1. 1 A water strider. The membrane-like nature of water due to its surface tension is clearly seen. The behavior is assisted by the hydrophobic nature of the insect's tentacles. 14

Figure 1. 2 The main features of classical contact mechanics theories Hertz, JKR and DMT. 16

Figure 1. 3 (a) A small droplet in equilibrium over a horizontal surface: (b) and (c) correspond to partial wetting, the trend towards wetting being stronger in (c) than (b). (d) Corresponds to complete wetting $\theta_{eq} = 0$ 18

Figure 1. 4 The contact angle on geometrically and chemically rough surfaces. (a) Wenzel state (b) Cassie-Baxter state. 20

Figure 1. 5 (a) Schematic of spherical probe contacting polymer surface decorated with low-aspect ratio posts. (b) Contact area image of spherical probe and patterned surface. (c-d) corresponds Normalized $Wadh$ as a function of post radius, r_P , for two differently spaced patterns: $L = 50 \mu m$ and $L = 500 \mu m$. The patterns with $L = 50 mm$ have significantly lower values of $Wadh$. Maximum contact area images for $L = 500 mm$ (top) and $L = 50 \mu m$ (bottom) are on right. 24

Figure 1. 6 (a) Schematic representation of the experimental setup. (b-c) microscopy images of the contacts on substrates with holes of various depths and for a positive load $F = 0.6 mN$. The contact is intimate for $h < h_c$ (b), and suspended for $h > h_c$. (c) The white bar represents 50 mm. 25

Figure 1. 7 AFM-PFM scans of a heterogeneous micro-contact printed pattern on a SiO₂ surface. The APS was solution deposited, followed by ODTs micro-contact printing. Scan width 10 μm 26

Figure 1. 8 The surface textures include (a) three groove widths and (b) three sizes of quadratic depressions, all with a 25% surface coverage (SEM). (d-e) show the friction coefficient in dry sliding between the steel ball and the TiN coated surfaces. (d) Two parallel tests on the flat surface. (e) All types of textured surfaces, including grooves (open circles) and a square depression (black squares) of three sizes each. 27

Figure 1. 9 (a) LFM image and (b) frictional curve of DTMS/FOETMS monolayer (c) Frictional direction of two-component micro patterned organosilane monolayer. 28

Figure 1. 10 (a) TMR (Trace minus Retrace) as a function of applied external load for different NH₂ surface fraction for micro and nano-patterned binary NH₂/CH₃ surfaces. (b) Friction coefficient versus NH₂ surface fraction for micro and nano-patterned binary NH₂/CH₃ surfaces. 28

Table of Figures

Figure 1. 11 (a) Different shapes of the effective interface potential ϕh associated with different wetting conditions. Curve (1) characterizes a stable liquid film. Curve (2) represents a metastable, curve (3) and (4) an unstable situation. (b) Effective interface potential ϕh (solid line) and its second derivative $\phi''h$ (dashed line) for a liquid polystyrene PS (2k) film prepared on a Si wafer with a 1.7nm SiO₂ layer. The sign reversal of $\phi''h$ characterizes the stability of the film. The hatched rectangle indicates typical experimental errors of the contact angle measurement and the determination of the equilibrium film thickness h_{eq} 30

Figure 1. 12 Different velocity profiles in the vicinity of the solid/liquid interface and illustration of the slip (extrapolation) length b . The situation of (apparent) slip is illustrated on the right: according to a thin liquid layer of thickness z_0 that obtains a significantly reduced viscosity, the slip velocity $u_{xz} = 0$ is zero, but a substantial slip length is measured. 31

Figure 1. 13 Optical micrographs (size of each: 240 x 200 μm^2) showing dewetting of a thin film of polystyrene ($M_w = 4840 \text{ kg/mol}$, $h = 40 \text{ nm}$) nucleation and growth on a silicon substrate coated with a monolayer of adsorbed PDMS ($M_w = 139 \text{ kg/mol}$, thickness = 11 nm). The temperature of dewetting is 180 °C. At the end, a multitude of dewetting droplets were arranged in polygons. The time between images is about 30 s. 33

Figure 1. 14 Typical examples for holes and the corresponding rim formed in a 24 nm thick PS film. This film is thick enough for holes being separated by several μm on average. (a) Optical micrograph after annealing for 80 min at 120 °C. AFM images (b) and (c) focus on the asymmetric shape of the rim. The length of the bar represents 5 μm in each case. (d) Cross sections through holes in a 20 nm thick PS film after annealing for 1, 5, 40, and 80 min at 120 \pm C, respectively. Note the highly asymmetric shape of the rim. 34

Figure 1. 15 3D-view (measured by AFM) of a section of a typical hole obtained by dewetting a polystyrene film on a PDMS-coated substrate at temperatures close to the glass transition of PS. $h(x, t)$ is the profile of the film, h_0 is the initial height of the film, H is the height of the front, R is the dewetted distance, W is the width of the rim, and $v(x, t)$ is the velocity inside the film. 35

Figure 1. 16 (a) SFM Tapping ModeTM topography images of a thin PS film ($M_w = 100 \text{ kDa}$, $t_{av} = 5 \text{ nm}$) on a corrugated silicon substrate at 150 °C for 3 h. (b) Average line scan along the horizontal taken from image. (c) The solid line is the experimental result. The dashed line depicts the position of the substrate surface. 36

Figure 1. 17 (a) A floated PS film conformally adhering to a topographically patterned substrate, comprising an array of square pillars (inset a_1). Inset (a_2) shows the line profile of the substrate and the film. (b) A perfectly filled and ordered dewetted structure resulting from the dewetting of a 24 nm -thick film on the substrate shown in inset (a_1). (c) A 24 nm-thick floated PS film focally adhering to the same substrate as shown in (a_1). Inset shows the film (dashed line) in contact with the raised protrusions of the substrate only and freely hanging over other intervening areas. (d) The dewetted droplets are positioned on top of each pillar roof. (e) Imperfect ordering with some missing droplets for an 11 nm film, (f) perfectly ordered but underfilled structure formation for a 17 nm -thick film, and (g) distorted, overfilled structure with occasional oversized or interconnected droplets for a 31 nm-thick PS film. 37

Table of Figures

Figure 1. 18 Library of the late stage morphology of the droplet arrays with pattern dimension. OM images and insets show transition from the doublet state (15-12 μm), to coalescence (9 μm), confinement (6 and 3 μm), and a heterogeneous morphology (1 μm) with bridging over multiple bands. Dashed lines (insets) indicate registry with the underlying chemical pattern period. AFM images (9 and 6 μm) highlight control of droplet size and spatial position..... 38

Figure 1. 19 (a) Topographic AFM image ($25 \times 25 \mu\text{m}^2$) of holes formed in a ca. 15 nm thick PS120k film. The height range is 100 nm. Holes are circular with both a diameter and a surface distribution identical to that of the imprinted domains pattern. (b) Topographic AFM image ($30 \times 30 \mu\text{m}^2$) of droplets formed in a ca. 50 nm thick PS120k film. The height range is 250 nm. The circular droplets with a diameter identical to that of the imprinted domains are distributed regularly on the substrate. (c) Topographic AFM image ($30 \times 30 \mu\text{m}^2$) of patterns formed in a ca. 90 nm thick PS120k film. The height range is 40 nm. Circular toroids with a diameter identical to that of the imprinted domains are distributed regularly on the substrate. These toroids at the periphery of the imprinted domains were generated by polymers remaining after dewetting at the boundaries of the domains..... 39

Figure 2. 1 (a) Master pattern development process using a photoresist. (b) Subsequent generation of the PDMS replication stamp. (c) Printing of self-assembled monolayers of trichlorosilane on the surface using μCP 43

Figure 2. 2 Optical microscopic images of the PDMS stamps used for μCP experiments. (a) 16 μm spherical stamp, (b) 113 μm spherical stamp, (c) 10 μm linear stamp and (d) 45 μm linear stamp..... 44

Figure 2. 3 Schematic outline of the procedure for patterning of alkylsiloxanes on the silicon surface. 45

Figure 2. 4 Schematic outline of the procedure for grafting PDMS on the MTS/Si-OH patterned surface. 46

Figure 2. 5 A mini microcontact printer device. (a) Three-Dimensional Computer graphic of the components of the $M\mu\text{CP}$. (b) Photograph of the $M\mu\text{CP}$ 47

Figure 2. 6 Optical micrographs showing a typical real-time dewetting of a PS film ($40 \pm 0.2 \text{ nm}$) on a Si/SiO₂ patterned substrate. (a) Circular Patches of MTCS. (b) Linear Patches of MTCS. 48

Figure 2. 7 (a) Optical microscopic image of the PDMS stamps used for μCP experiments. 21 μm circular (b) Optical microscopic images of a 21 μm sized pattern of a dewetted PS film on a Si/SiO₂ patterned substrate. (c) A contrasted optical microscopic images of a 21 μm sized pattern of a dewetted PS film on a Si/SiO₂ patterned substrate. 48

Figure 2. 8 On the left side, variation of fraction area as function of pattern size before stamp printing; (a-c) corresponds to an example of a selection on stamp of size 128 and 45 μm respectively circular and linear patterns that was made to measure surface. On the right side: Variation of fraction area as

Table of Figures

<i>function of pattern size after stamp printing; (b-d) corresponds to an example of a selection on patterned surface with stamps of size 128 and 45 μm that was made to measure surface ratio.</i>	49
<i>Figure 2. 9 Variation of fraction area as function of pattern size before and after stamp printing.</i>	50
<i>Figure 2. 10 (a) Three-Dimensional Computer graphic of the components of the JKR machine. (b) Photograph the JKR device.</i>	51
<i>Figure 2. 11 A Photograph of a JKR measurement on a normal glass slide</i>	52
<i>Figure 2. 12 Experimental data for a compression/decompression cycle on a glass slide. (a) The contact radius a versus the pseudo-force F. (b) The pseudo-contact radius ($A_n = a^3 26\pi R$) versus the pseudo-force $F_n = F 6\pi a^3$</i>	54
<i>Figure 2. 13 Force versus Separation plot</i>	55
<i>Figure 2. 14 (a) The left side shows several water contact angle measurements on substrate before and after treatment; (1) Silicon wafer, (2) Silicon grafted with adsorbed PDMS, (3) Silicon with self-assembled monolayer OTS, and (4) Silicon with self-assembled monolayer MTS. (b) The right side illustrate, water contact angle variation versus surface treatment.</i>	57
<i>Figure 2. 15 (a) Schematic of a circular patterned surface of MTS/Si-OH. (b) Schematic of a linear patterned surface of MTS/Si-OH. Notations D and L denote the patterns size and pitch.</i>	58
<i>Figure 2. 16 (a) Water contact angle of the 128 μm circular pattern. (b) Temporal evolution of the advancing and receding contact angles for water drops of varying drop base diameter (1-6 mm).</i>	59
<i>Figure 2. 17 (a) Variation of water contact angle as function of pattern size versus real stamp size. (b) The evolution of the equilibrium contact angle, hysteresis and Cassie Baxter predicted value as function of the pattern, size.....</i>	59
<i>Figure 2. 18 Temporal evolution of the contact angle and the drop base diameter for an advancing and receding stage experiments on circular patterned surfaces.</i>	60
<i>Figure 2. 19 Variation of water contact angle hysteresis versus real stamp size. (a) Circular patches. (b) Linear patches.</i>	62
<i>Figure 2. 20 Temporal evolution of the contact angle and the drop base diameter for an advancing and receding stage experiments on linear patterned surfaces.</i>	63

Table of Figures

Figure 2. 21 (a) Young adhesion energy as function of the circular pattern size. (b) Young adhesion energy as function of the linear strips size for the MTS/Si-OH systems.	65
Figure 2. 22 (a) Normalized adhesion energy as function of the parameter α for the different circular patterned systems. (b) Normalized adhesion energy as function of the pattern size for the different linear patterned surfaces for the MTS/Si-OH systems.	65
Figure 2. 23 (a-b) Illustration of the contact line pinning for the discrete circular and linear patterns of the system (MTS/Si-OH).	66
Figure 2. 24 Experimental data for a compression/decompression cycle on a several reference surfaces. Where the force F was plotted as a function of the contact radius (a).	68
Figure 2. 25 Experimental data for a compression/decompression cycle on a several reference surfaces. Where the pseudo-force $F_n = F_0 \pi a^3$ was plotted as a function of the pseudo-contact radius ($A_n = a^3 / 26 \pi R$).	69
Figure 2. 26 (a) Force–displacement curves for the smooth non-patterned surfaces. (a) Pull-off Force as function as function of the smooth non-patterned systems.	70
Figure 2. 27 Micrographs of the contact on substrates covered with linear strips of various patterns seize where the contact can be intimate.	71
Figure 2. 28 Experimental data for a compression/decompression cycle on the (MTS/Si-OH) patterned surfaces. Where of the pseudo-force (F_n) was plotted as a function the pseudo-contact radius (A_n).	72
Figure 2. 29 (a) Adhesion response as function of the pattern size for the MTS/Si-OH system. (b) Pull-off force as function of pattern size.	73
Figure 2. 30 2D AFM images of the Topography ($5 \times 5 \mu\text{m}^2$, $60 \times 60 \mu\text{m}^2$) of $10 \mu\text{m}$ linear strips (MTS/Si-OH).	73
Figure 2. 31 Micrographs of the contact on substrates covered with linear strips of various patterns seize where the contact can be intimate.	74
Figure 2. 32 Experimental data for a compression/decompression cycle on the (MTS/PDMS) patterned surfaces. Where the pseudo-contact radius (F_n) was plotted as a function of the pseudo-force (A_n).	75
Figure 2. 33 (a) Adhesion response as function of the pattern size for the MTS/Si-OH system. (b) Pull-off force as function of pattern size.	76

Table of Figures

Figure 2. 34 AFM images ($60 \times 60 \mu\text{m}^2$) of the different smooth substrates.....	77
Figure 2. 35 (a) Representative force-displacement curves for the different smooth substrate. (b) 2D AFM images of the topography and the adhesion of the different smooth substrates ($5 \times 5 \mu\text{m}^2$).....	78
Figure 2. 36 Adhesion force of the different non-patterned substrates.....	79
Figure 2. 37 (a) 2D and 3D AFM images of topography and adhesion ($60 \times 60 \mu\text{m}^2$) of the $10 \mu\text{m}$ patterned surface for the MTS/Si-OH system. (b) Adhesion force as function of pattern size for the MTS/Si-OH system.....	81
Figure 2. 38 (a) 2D and 3D AFM images of topography and adhesion ($20 \times 20 \mu\text{m}^2$, $60 \times 60 \mu\text{m}^2$) of the $10 \mu\text{m}$ patterned surface for the MTS/PDMS system. (b) Adhesion force as function of pattern size for the MTS/PDMS system.....	82
Figure 2. 39 Normalized Adhesion force as function of the pattern size for the MTS/Si-OH patterned system.....	83
Figure 2. 40 Normalized Adhesion force as function of the pattern size for the MTS/PDMS patterned system.....	84
Figure 3. 1 Three-Dimensional Computer graphic of the components of the Friction machine.....	88
Figure 3. 2 A micrograph of a friction measurement.....	89
Figure 3. 3 The temporal evolution of the tangential force was and the contact area of an adsorbed layer of PDMS. The load used here is $2,117 \text{ N}$ and the velocity is $0,1 \text{ mm/s}$	89
Figure 3. 4 A schematic of the experimental friction force.....	90
Figure 3. 5 (a) A typical friction force image from a Si tip scanned over an area consisting of two materials, graphene on A and SiO_2 on B, which exhibit distinct frictional behaviors. Lower brightness corresponds to lower friction. (b) A typical friction loop taken from the red dash line in (a). Black arrows indicate the scan direction.....	91
Figure 3. 6 (a) Initial contact before the sample is sheared relative to beads (the area is nearly circular $F=0$). (b) Contact area during sliding ($F=F_s$).....	92

Table of Figures

Figure 3. 7 (a-b) The temporal evolution of the lateral force and the real contact using several load for the different smooth surfaces.	93
Figure 3. 8 The real contact as function of the lateral force of for the different smooth surfaces for the different smooth surfaces.	94
Figure 3. 9 The maximum static friction F_s versus is the real contact area A_{sr} for different smooth surfaces.	95
Figure 3. 10 critical shear stress of a PDMS bead for the different non-patterned surfaces	96
Figure 3. 11 The temporal evolution of the static friction F and the real contact area A_r for the different Patterns sizes of the MTS/Si-OH surfaces.	97
Figure 3. 12 critical shear stress of a PDMS bead for the different Patterns sizes of the MTS/Si-OH surfaces. The dashed lines represents the average values of the critical shear stress of the MTS and Si-OH smooth surfaces.	98
Figure 3. 13 Micrographs of the contact on substrates covered with linear strips of various patterns size for the MTS/PDMS substrates.	99
Figure 3. 14 The temporal evolution of the static friction F and the real contact area A_r for different Patterns sizes of the MTS/PDMS surfaces.	99
Figure 3. 15 The maximum static friction F_s versus is the real contact area A_{sr} for (10, 26, 45 μm) patterned surfaces and the MTS, Si-OH smooth surfaces.	100
Figure 3. 16 Average critical shear stress of a PDMS bead for the different Patterns sizes of the MTS/PDMS surfaces. The dashed lines represents the average values of the critical shear stress of the MTS and PDMS smooth surfaces.	100
Figure 3. 17 2D AFM images of the Topography (60 \times 60 μm^2) for the different non-patterned surfaces. The different Patterns sizes of the MTS/PDMS surfaces.	102
Figure 3. 18 Lateral force friction as a function for the applied normal load for the different non-patterned surfaces	102
Figure 3. 19 Relative coefficient of friction for the different non-patterned surfaces.....	103
Figure 3. 20 2D AFM images of the Topography (60 \times 60 μm^2 , 120 \times 120 μm^2) for the different patterned surfaces (MTS/Si-OH).	104

Table of Figures

Figure 3. 21 (a-b) 2D AFM images of the Friction ($60 \times 60 \mu\text{m}^2$) of the perpendicular and parallel scanning respectively of the of Si_3N_4 tip to the $10 \mu\text{m}$ linear strips. (c) Friction loop of the perpendicular parallel sliding for the trace and retrace sections. 105

Figure 3. 22 (a) Force friction as a function for the applied normal load for the perpendicular and parallel scanning of the of Si_3N_4 tip to the $10 \mu\text{m}$ linear strips. (b) Relative coefficient of friction of the sliding of the Si_3N_4 tip on the different Patterns sizes of the MTS/Si-OH surfaces. The dashed lines represents the average values of the relative coefficient friction of the MTS and Si-OH smooth surfaces. 106

Figure 3. 23 Relative coefficient of friction of a Si_3N_4 tip for the different Patterns sizes of the MTS/Si-OH surfaces. The dashed lines represents the average values of the relative coefficient friction of the MTS and Si-OH smooth surfaces. 106

Figure 3. 24 2D AFM images of the Topography ($60 \times 60 \mu\text{m}^2, 120 \times 120 \mu\text{m}^2$) for the different patterned surfaces (MTS/PDMS). 108

Figure 3. 25 (a) 2D AFM images of the Friction ($60 \times 60 \mu\text{m}^2, 120 \times 120 \mu\text{m}^2$) of the Si_3N_4 tip on the $10 \mu\text{m}$ and $26 \mu\text{m}$ linear strips respectively. (b) Friction loop of the perpendicular parallel sliding for the trace and retrace sections of the $10 \mu\text{m}$ linear pattern. 109

Figure 3. 26 (a) Force friction as a function for the applied normal load for to different patterned substrates. (b) Relative coefficient of friction of the sliding of the Si_3N_4 tip on the different Patterns sizes of the MTS/PDMS surfaces. The dashed lines represents the average values of the relative coefficient friction of the MTS and PDMS smooth surfaces. 110

Figure 4. 1 Schematic of a polymer chain at different length scales with (a) is the monomer length, (b) is the persistence length (real chain), (N) is the number of segments, (R) is the end to end distance of a polymer chain and R_g is the radius of gyration. 115

Figure 4. 2 Schematic creep and recovery of a polymeric system under a constant stress at time zero. 116

Figure 4. 3 Schematic of chain segment AB in dens rubber. The blue chain is undergoing reptation inside the tube while other green chains. The redline shows the primitive path. 117

Figure 4. 4 Explanation of the stress relaxation after a large step strain. (a) Before deformations the conformation on the primitive chain is in equilibrium ($t=-0$). (b) Immediately after deformation, the primitive chain is in the affinely deformed conformation ($t=+0$). (c) After time τ_e the primitive chain contracts along the tube and recovers the equilibrium contour length ($t=\tau_e$). (d) After the time τ_d , the

Table of Figures

<i>primitive chain leaves the deformed tube by reptation ($t=\tau d$). The oblique lines indicate the deformed part of the tube.....</i>	<i>118</i>
<i>Figure 4. 5 Chemical formula of styrene monomer.</i>	<i>119</i>
<i>Figure 4. 6 Chemical formula of two dimethylsiloxane units.....</i>	<i>119</i>
<i>Figure 4. 7 (a) Water jet falling from a faucet (b) Dimensionless growth rate of sinusoidal perturbations on a cylinder as a function of the dimensionless wave number kh_0. The solid line represents Rayleigh's theory for inviscid flow.</i>	<i>120</i>
<i>Figure 4. 8 Optical micrograph of a supported liquid cylinder decaying into droplets via the Rayleigh-Plateau instability. This is an example of our dewetting experiments of a PS film on a textured surfaces.</i>	<i>122</i>
<i>Figure 4. 9 Optical micrograph ($842 \mu\text{m} \times 660 \mu\text{m}$) of the dewetting dynamic of a 195 nm thick PS (137k) performed at 180 °C for different patterned substrates.</i>	<i>123</i>
<i>Figure 4. 10 Optical micrograph of the dewetting dynamic defining the averaged dewetting distance $d_{Average}$ and the rim width $W_{Average}$.</i>	<i>124</i>
<i>Figure 4. 11 (a) Temporal evolution of the dewetting distance of a PS film (195 nm $M_w = 139\,000 \text{ g/mol}$) on top of a MTS/Si-OH patterned substrates (10, 26 and 45 μm). (b) Velocity dewetting as a function of time for the same conditions as described in (a). The lines are guideline for eyes. (c) Temporal evolution of the rim width.</i>	<i>125</i>
<i>Figure 4. 12 Optical micrograph of the dewetting dynamic of a 195 nm thick PS (137k) on top of a 10 μm MTS/Si-OH patterned substrates illustrating the different regimes of the dewetting experiments.</i>	<i>126</i>
<i>Figure 4. 13 Optical micrograph of the dewetting dynamic defining the different parameter used in this section.....</i>	<i>127</i>
<i>Figure 4. 14 (a) Temporal evolution of the dewetting distance (d) of the "Tip" and "Finger" rim regions of a 195 nm PS(137k) thick film dewetted on top of a 10 μm MTS/Si-OH patterned substrates. (b) Temporal evolution of the dewetting velocity (V) on double logarithmic scales.</i>	<i>128</i>
<i>Figure 4. 15 (a-c) Temporal evolution of the dewetting distance (d) of the "Tip" and "Finger" rim regions of a 195 nm PS(137k) thick film dewetted on top of 26 and 45 μm MTS/Si-OH patterned substrates. (b-d) Temporal evolution of the dewetting velocity (V) on double logarithmic scales of 26 and 45 μm.</i>	<i>129</i>

Table of Figures

- Figure 4. 16 (a-c) Temporal evolution of the rim width (W) of thicker (Tip) and thinner (Finger) rim regions of a 195 nm PS(137k) film on top of a 10,26 μm and 46 μm MTS/Si-OH patterned substrates respectively. Dewetting experiments performed at 180 °C..... 131
- Figure 4. 17 (a-c) Temporal evolution of the wavelength $\lambda(t)$ presented for the different patterned surfaces. $\lambda(t)$ is defined as the length between successive thicker regions with the part at early stage following the solid curve. The system is a 195 nm thick PS(137k). Dewetting experiments performed at 180 °C..... 132
- Figure 4. 18 Schematic of the competition between slip and no slip behavior induced by the introduction of (-CH₃/-OH) system on the surface. Where the velocity dewetting at the finger region is faster compared to V at the tip zone and the friction of the -OH layer is higher compared to the -CH₃ zone 135
- Figure 4. 19 (a) Optical micrograph of the droplet detachment instabilities of a 248 nm thick PS (137k) on top of a different patterned substrates. (b) Primary droplets diameters as function of the varying PS thicknesses for the different textured systems..... 136
- Figure 4. 20 Optical micrographs of the droplet detachment instabilities of a 311 nm thick PS (137k) on top of a different patterned substrates illustrating the primary and secondary droplets. 137
- Figure 4. 21 Optical micrograph of the dewetting dynamic defining the averaged dewetting distance $d_{Average}$ and the rim width $W_{Average}$ 138
- Figure 4. 22 Optical micrograph of the dewetting dynamic of a 195, 248 and 311 nm PS (137k) performed at 180 °C for different patterned substrates. (842 μm \times 660 μm and 336 μm \times 263 μm) 139
- Figure 4. 23 (a) Temporal evolution of the dewetting distance (d) of a varying PS film ranging from 195 nm up to 311 nm on top of a 45 μm MTS/Si-OH patterned substrate. (b) Temporal evolution of the velocity dewetting (V) of a varying PS film ranging from 195 nm up to 311 nm on top of a 45 μm MTS/Si-OH patterned substrate. (c) Temporal evolution of the rim width (W) of a varying PS film ranging from 195 nm up to 311 nm on top of a 45 μm MTS/Si-OH patterned substrates. 140
- Figure 4. 24 The growth of the maximum dewetting distance (d_{max}) at the hydrophilic zone of the different patterned systems as function of the PS film. 141
- Figure 4. 25 Droplets diameter and distance between droplets as function of the varying PS thicknesses for the different textured systems..... 142
- Figure 4. 26 Finger length as function of the varying PS thicknesses for the different textured systems. 143
- Figure 4. 27 Optical micrograph (842 μm \times 660 μm) of the dewetting dynamic of a 248 nm thick PS (137k) performed at 180 °C for different patterned substrates 144

Table of Figures

Figure 4. 28 Optical micrograph ($842 \mu\text{m} \times 660 \mu\text{m}$) of the dewetting dynamic defining the different parameter used in this part.	144
Figure 4. 29 Temporal evolution of the hole radius (R) of the different patterned systems.	145
Figure 4. 30 Temporal evolution of the hole radius R_{finger} and R_{tip} of the $45 \mu\text{m}$ patterned system.	145
Figure 4. 31 A comparison of the temporal evolution of the dewetting distance (d) and the hole radius (R) for the different patterned systems.	146
Figure 4. 32 Schematic of the dewetting dynamic of a 311 nm thick PS (137k) on top of a $10 \mu\text{m}$ MTS/Si-OH patterned substrates illustrating the different regimes of the dewetting experiments, defined by the relation between dewetting velocity and rim width.	147
Figure 4. 33 Optical micrograph ($842 \mu\text{m} \times 660 \mu\text{m}$) of the dewetting dynamic of a 500 nm thick PDMS (139k) performed at 150°C on top of a homogenous PDMS absorbed layer and of a $10 \mu\text{m}$ MTS/PDMS patterned surface. ($336 \mu\text{m} \times 263 \mu\text{m}$) micrograph correspond the $45 \mu\text{m}$ patterned substrates MTS/PDMS.	149
Figure 4. 34 Optical micrograph of the dewetting dynamic defining the averaged dewetting distance $d_{Average}$ and the rim width $W_{Average}$	149
Figure 4. 35 (a) Temporal evolution of the dewetting distance (d) of a PDMS film (500 nm $M_w = 139\,000 \text{ g/mol}$) on top of a homogenous PDMS absorbed layer and of a $10, 45 \mu\text{m}$ MTS/PDMS patterned system at 150°C . (b) Dewetted distance (d) as a function of time on double logarithmic scales for the same conditions as described in (a).	150
Figure 4. 36 (a) Temporal evolution of the rim width (W) of a PDMS film (500 nm $M_w = 139\,000 \text{ g/mol}$) on top of a homogenous PDMS absorbed layer and of a $10, 45 \mu\text{m}$ MTS/PDMS patterned system. The temperature was 150°C . (b) Rim width (W) as a function of time on double logarithmic scales for the same conditions as described in (a).	151
Figure 4. 37 Optical micrograph of the autophobic dewetting dynamic illustrating the anchoring phenomena of the PDMS film on the MTYS patterned layer.	152
Figure 4. 38 Temporal evolution of the dewetting velocity (V) on double logarithmic scales for the same conditions as described in the legend of Fig.4.30.a.	153
Figure 4. 39 (a) Temporal evolution of the contact angle (θ) as determined from eq 4.13. (b) Temporal evolution of the contact angle (θ) on double logarithmic scales. The straight lines are guideline for eyes.	154

Table of Figures

Figure 4. 40 Slippage length a function of time on double logarithmic scales. The dotted lines are guideline for eyes.	155
Figure 4. 41 Dewetting velocity (V) as a function of the rim width (W) of a homogenous PDMS absorbed layer and of a 10, 45 μm MTS/PDMS patterned system at 150°C. The straight lines are guideline for eyes.	156
Figure 4. 42 (a) Slippage length (b) as a function of dewetting velocity (V). (b) Slippage length (b), as a function of rim width (W).	157
Figure 4. 43 2D AFM images of the Topography ($60 \times 60 \mu\text{m}^2, 120 \times 120 \mu\text{m}^2$) of the several non-covered Zone for the different patterned surfaces (MTS/Si-OH). The red circle presents the non-covered zone on the MTS patterns.	158
Figure 5. 1 Schematic representation of the rim forming in the middle of dewetting of a thin liquid film. Hence, an Illustration of the rim width w , the distance x_0 for a given film thickness h and hole radius R (or dewetted distance D of a straight front).	163
Figure 5. 2 Schematic presentation of late stages of dewetting of Newtonian fluid on a substrate with (a) a non-slip and (b) a slip boundary condition.	165
Figure 5. 3 Schematic of the fabrication processes of the thick PDMS surfaces	166
Figure 5. 4 (a-b) Temporal evolution of the lateral force and the real contact using several load for a smooth surface of an 11 nm adsorbed PDMS coated layer.	167
Figure 5. 5 (a-b) real contact area versus lateral force using several load for a homogenous surface of an 11 nm adsorbed PDMS coated layer.	168
Figure 5. 6 (a) The maximum static friction F_s versus is the real contact area A_{sr} for the different thickness of the PDMS cross-linked layer. The straight lines are the fits data using the following equation $F_s = \epsilon_s A_{sr}$. (b) Critical shear stress ϵ_s , averaged over the whole time and load range of the experiment, as a function of coated layer thickness h . The line is a guideline for eyes.	168
Figure 5. 7 (a) Young modulus as function of the PDMS thickness. (b) Tangential stiffness as function of the PDMS thickness.	169
Figure 5. 8 Schematic of the friction test between a PDMS bead and a thin cross-linked PDMS layer $0 > h > 500 \mu\text{m}$	170

Table of Figures

- Figure 5. 9 Schematic of the friction test between a PDMS bead and a thick cross-linked PDMS layer $h < 500 \mu\text{m}$ 170
- Figure 5. 10 Critical shear stress ϵ_s , as a function of the sliding velocity V for a thickness $h = 4,65 \mu\text{m}$ and a load $P = 1,1 \text{ N}$. The straight line is a guideline for eyes. 171
- Figure 5. 11 Schematic of the model proposed by Scheibert and Sahli. (a) Correspond to the first regime thinner thickness $h_a < 0,25$. (b) Correspond to the second regime thicker thickness $h_a > 1,8$. The deformed volume V_p is presented by the grey zones..... 172
- Figure 5. 12 Optical micrograph of the dewetting of a 500 nm PDMS (139k) at 150 °C for different cross-linked PDMS coated layer ($336 \mu\text{m} \times 263 \mu\text{m}$)..... 172
- Figure 5. 13 Optical micrograph of the dewetting of a 500 nm PDMS film at 150 °C on of the 274 nm cross-linked PDMS coated layer..... 173
- Figure 5. 14 (a) Temporal evolution of the dewetting distance of a PDMS film (500 nm $M_w = 139\,000 \text{ g/mol}$) on top of a cross-linked PDMS coted layer of a varying thickness ranging from (30 nm up to 1,8 μm) at 150°C. (from (0 to 1400 S) (b) Dewetted distance as a function of time from (2000 to 10000 S) . (c) Temporal evolution of the dewetting velocity on double logarithmic scales. (d) Temporal evolution of the rim width for the same conditions as Fig.5.14 (a)..... 174
- Figure 5. 15 (a) Temporal evolution of the contact angle as determined from eq 5.11 of a PDMS film (500 nm $M_w = 139\,000 \text{ g/mol}$) on top of a cross-linked PDMS of a varying thickness ranging from (30 nm up to 1,8 μm) at 150°C. (b) Temporal evolution of the contact angle on double logarithmic scales. The straight lines are guideline for eyes. 175
- Figure 5. 16 (a) Temporal evolution of the slippage length as determined from eq 5.13 of a PDMS film (500 nm $M_w = 139\,000 \text{ g/mol}$) on top of a cross-linked PDMS coted layer of a varying thickness ranging from (30 nm up to 1,8 μm) at 150°C. The dotted lines are guideline for eyes. (b) Slippage length as determined from eq 5.13, deduced over the time range of 100 s, 1000s and 6000 s respectively, as a function of coated layer thickness on double logarithmic scales. 177
- Figure 5. 17 Dewetting velocity as a function of the rim width of a varying thickness of a cross-linked PDMS layer ranging from (30 nm up to 1,8 μm) at 150°C. The straight lines are guideline for eyes.... 178
- Figure 5. 18 Schematic presentation of late stages of dewetting of a PDMS film on a substrate of a cross-linked PDMS coated layer of a thin thickness (30 nm up to 270 nm). 179
- Figure 5. 19 Schematic presentation of late stages of dewetting of a PDMS film on a substrate of a cross-linked PDMS coated layer of a thin thickness (490 nm up to 1,8 μm)..... 179

Table of Figures

Figure 5. 20 (a) Slippage length as a function of dewetting velocity width of a varying thickness of of a cross-linked PDMS layer ranging from (30 nm up to 1,8 μm) at 150°C. (b) Slippage length (b) as a function of rim width (W) for the same conditions as 5.23. (a) 180

Figure 5. 21 Interfacial friction coefficient (ξ) as determined following the equation $\xi = \eta/b$ of a PDMS film (500 nm $M_w = 139\ 000\ \text{g/mol}$ $\eta = 90\ \text{Pa s}$) on top of a cross-linked PDMS coated layer of a varying thickness ranging from (30 nm up to 1,8 μm) at 150°C, deduced over the time range of 100 s, 1000s and 6000 s respectively, as a function of coated layer thickness. 181

Table of Tables

Table 1 The main types of nonspecific intermolecular and surface forces..... 13

Table 2 Wetting Behavior of a Water Droplet on non-patterned Surfaces 57

Table 3 Adhesive behavior of PDMS bead and the different non-patterned surfaces..... 70